MICROFLUIDIC PLATFORMS FOR THE CHARACTERIZATION OF *IN MESO* MEMBRANE PROTEIN CRYSTALLIZATION

BY

SARAH LOUISE PERRY

DISSERTATION

Submitted in partial fulfillment of the requirements
for the degree of Doctor of Philosophy in Chemical Engineering
in the Graduate College of the
University of Illinois at Urbana-Champaign, 2010

Urbana, Illinois

Doctoral Committee:

Professor Paul J.A. Kenis, Chair
Professor Charles F. Zukoski
Assistant Professor Brendan A. Harley
Professor Robert B. Gennis

Abstract

Membrane proteins, which reside in the membranes of cells, play a critical role in many important biological processes including cellular signaling, immune response, and material and energy transduction. Because of their key role in maintaining the environment within cells and facilitating intercellular interactions, understanding the function of these proteins is of tremendous medical and biochemical significance. Indeed, the malfunction of membrane proteins has been linked to numerous diseases including diabetes, cirrhosis of the liver, cystic fibrosis, cancer, Alzheimer's disease, hypertension, epilepsy, cataracts, tubulopathy, leukodystrophy, Leigh syndrome, anemia, sensorineural deafness, and hypertrophic cardiomyopathy.[1-3] However, the structure of many of these proteins and the changes in their structure that lead to disease-related malfunctions are not well understood. Additionally, at least 60% of the pharmaceuticals currently available are thought to target membrane proteins, despite the fact that their exact mode of operation is not known.[4-6]

Developing a detailed understanding of the function of a protein is achieved by coupling biochemical experiments with knowledge of the structure of the protein. Currently the most common method for obtaining three-dimensional structure information is X-ray crystallography. However, no *a priori* methods are currently available to predict crystallization conditions for a given protein.[7-14] This limitation is currently overcome by screening a large number of possible combinations of precipitants, buffer, salt, and pH conditions to identify conditions that are conducive to crystal nucleation and growth.[7,9,11,15-24] Unfortunately, these screening efforts are often limited by difficulties associated with quantity and purity of available protein samples.

While the two most significant bottlenecks for protein structure determination in general are the (i) obtaining sufficient quantities of high quality protein samples and (ii) growing high quality protein crystals that are suitable for X-ray structure determination,[7,20,21,23,25-47] *membrane* proteins present additional challenges. For crystallization it is necessary to extract the membrane proteins from the cellular membrane. However, this process often leads to denaturation. In fact, membrane proteins have proven to be so difficult to crystallize that of the more than 66,000 structures deposited in the Protein Data Bank,[48] less than 1% are for membrane proteins, with even fewer present at high resolution (< 2Å)[4,6,49] and only a handful are human membrane proteins.[49] A variety of strategies including detergent solubilization[50-53] and the use of artificial membrane-like environments have been developed to circumvent this challenge.[43,53-55]

In recent years, the use of a lipidic mesophase as a medium for crystallizing membrane proteins has been demonstrated to increase success for a wide range of membrane proteins, including human receptor proteins.[54,56-62] This *in meso* method for membrane protein crystallization, however, is still by no means routine due to challenges related to sample preparation at sub-microliter volumes and to crystal harvesting and X-ray data collection. *This dissertation presents various aspects of the development of a*

microfluidic platform to enable high throughput in meso membrane protein crystallization at a level beyond the capabilities of current technologies.

Microfluidic platforms for protein crystallization and other lab-on-a-chip applications have been well demonstrated.[9,63-66] These integrated chips provide fine control over transport phenomena and the ability to perform high throughput analyses via highly integrated fluid networks. However, the development of microfluidic platforms for *in meso* protein crystallization required the development of strategies to cope with extremely viscous and non-Newtonian fluids. A theoretical treatment of highly viscous fluids in microfluidic devices is presented in Chapter 3, followed by the application of these strategies for the development of a microfluidic mixer capable of preparing a mesophase sample for *in meso* crystallization at a scale of less than 20 nL in Chapter 4. This approach was validated with the successful on chip *in meso* crystallization of the membrane protein bacteriorhodopsin. *In summary, this is the first report of a microfluidic platform capable of performing in meso crystallization on-chip, representing a 1000x reduction in the scale at which mesophase trials can be prepared.*

Once protein crystals have formed, they are typically harvested from the droplet they were grown in and mounted for crystallographic analysis. Despite the high throughput automation present in nearly all other aspects of protein structure determination, the harvesting and mounting of crystals is still largely a manual process. Furthermore, during mounting the fragile protein crystals can potentially be damaged, both from physical and environmental shock. *To circumvent these challenges an X-ray transparent microfluidic device architecture was developed to couple the benefits of scale, integration, and precise fluid control with the ability to perform in situ X-ray analysis (Chapter 5).* This approach was validated successfully by crystallization and subsequent on-chip analysis of the soluble proteins lysozyme, thaumatin, and ribonuclease A and will be extended to microfluidic platforms for *in meso* membrane protein crystallization. The ability to perform *in situ* X-ray analysis was shown to provide extremely high quality diffraction data, in part as a result of not being affected by damage due to physical handling of the crystals.

As part of the work described in this thesis, a variety of data collection strategies for *in situ* data analysis were also tested, including merging of small slices of data from a large number of crystals grown on a single chip, to allow for diffraction analysis at *biologically relevant temperatures*. While such strategies have been applied previously,[57,59,61,67] they are potentially challenging when applied via traditional methods due to the need to grow and then mount a large number of crystals with minimal crystal-to-crystal variability. The integrated nature of microfluidic platforms easily enables the generation of a large number of reproducible crystallization trials. This, coupled with *in situ* analysis capabilities has the potential of being able to acquire high resolution structural data of proteins at biologically relevant conditions for which only small crystals, or crystals which are adversely affected by standard cryocooling techniques, could be obtained (Chapters 5 and 6).

While the main focus of protein crystallography is to obtain three-dimensional protein structures, the results of typical experiments provide only a static picture of the protein. The use of polychromatic or Laue X-ray diffraction methods enables the collection of time resolved structural information. These experiments are very sensitive to crystal quality, however, and often suffer from severe radiation damage due to the intense polychromatic X-ray beams. Here, as before, the ability to perform *in situ* X-ray analysis on many small protein crystals within a microfluidic crystallization platform has the potential to overcome these challenges. An automated method for collecting a "single-shot" of data from a large number of crystals was developed in collaboration with the BioCARS team at the Advanced Photon Source at Argonne National Laboratory (Chapter 6). *The work described in this thesis shows that, even more so than for traditional structure determination efforts, the ability to grow and analyze a large number of high quality crystals is critical to enable time resolved structural studies of novel proteins.*

In addition to enabling X-ray crystallography experiments, the development of X-ray transparent microfluidic platforms also has tremendous potential to answer other scientific questions, such as unraveling the mechanism of *in meso* crystallization. For instance, the lipidic mesophases utilized during *in meso* membrane protein crystallization can be characterized by small angle X-ray diffraction analysis. *Coupling in situ analysis with microfluidic platforms capable of preparing these difficult mesophase samples at very small volumes has tremendous potential to enable the high throughput analysis of these systems on a scale that is not reasonably achievable using conventional sample preparation strategies* (Chapter 7). In collaboration with the LS-CAT team at the Advanced Photon Source, an experimental station for small angle X-ray analysis coupled with the high quality visualization capabilities needed to target specific microfluidic samples on a highly integrated chip is under development. Characterizing the phase behavior of these mesophase systems and the effects of various additives present in crystallization trials is key for developing an understanding of how *in meso* crystallization occurs. *A long term goal of these studies is to enable the rational design of in meso crystallization experiments so as to avoid or limit the need for high throughput screening efforts.*

In summary, this thesis describes the development of microfluidic platforms for protein crystallization with *in situ* analysis capabilities. Coupling the ability to perform *in situ* analysis with the small scale, fine control, and the high throughput nature of microfluidic platforms has tremendous potential to enable a new generation of crystallographic studies and facilitate the structure determination of important biological targets. The development of platforms for *in meso* membrane protein crystallization is particularly significant because they enable the preparation of highly viscous mixtures at a previously unachievable scale. Work in these areas is ongoing and has tremendous potential to improve not only current the methods of protein crystallization and crystallography, but also to enhance our knowledge of the structure and function of proteins which could have a significant scientific and medical impact on society as a whole. The microfluidic technology described in this thesis has the potential to significantly advance our understanding of the structure and function of membrane proteins, thereby aiding the elucidation of human biology, the development of pharmaceuticals with fewer side effects for a wide range of diseases.

References

(1) Quick, M.; Javitch, J. A. *P Natl Acad Sci USA* **2007**, *104*, 3603.

(2) Trubetskoy, V. S.; Burke, T. J. *Am Lab* **2005**, *37*, 19.

(3) Pecina, P.; Houstkova, H.; Hansikova, H.; Zeman, J.; Houstek, J. *Physiol Res* **2004**, *53*, S213.

(4) Arinaminpathy, Y.; Khurana, E.; Engelman, D. M.; Gerstein, M. B. *Drug Discovery Today* **2009**, *14*, 1130.

(5) Overington, J. P.; Al-Lazikani, B.; Hopkins, A. L. *Nat Rev Drug Discov* **2006**, *5*, 993.

(6) Dauter, Z.; Lamzin, V. S.; Wilson, K. S. *Current Opinion in Structural Biology* **1997**, *7*, 681.

(7) Hansen, C.; Quake, S. R. *Current Opinion in Structural Biology* **2003**, *13*, 538.

(8) Govada, L.; Carpenter, L.; da Fonseca, P. C. A.; Helliwell, J. R.; Rizkallah, P.; Flashman, E.; Chayen, N. E.; Redwood, C.; Squire, J. M. *J Mol Biol* **2008**, *378*, 387.

(9) Hansen, C. L.; Skordalakes, E.; Berger, J. M.; Quake, S. R. *P Natl Acad Sci USA* **2002**, *99*, 16531.

(10) Leng, J.; Salmon, J.-B. *Lab Chip* **2009**, *9*, 24.

(11) Zheng, B.; Gerdts, C. J.; Ismagilov, R. F. *Current Opinion in Structural Biology* **2005**, *15*, 548.

(12) Lorber, B.; Delucas, L. J.; Bishop, J. B. *J Cryst Growth* **1991**, *110*, 103.

(13) Talreja, S.; Perry, S. L.; Guha, S.; Bhamidi, V.; Zukoski, C. F.; Kenis, P. J. A. *The Journal of Physical Chemistry B* **2010**, *114*, 4432.

(14) Chayen, N. E. Current Opinion in Structural Biology **2004**, 14, 577.

(15) He, G. W.; Bhamidi, V.; Tan, R. B. H.; Kenis, P. J. A.; Zukoski, C. F. *Cryst Growth Des* **2006**, *6*, 1175.

(16) Zheng, B.; Tice, J. D.; Roach, L. S.; Ismagilov, R. F. *Angew Chem Int Edit* **2004**, *43*, 2508.

(17) Li, L.; Mustafi, D.; Fu, Q.; Tereshko, V.; Chen, D. L. L.; Tice, J. D.; Ismagilov, R. F. *P Natl Acad Sci USA* **2006**, *103*, 19243.

(18) Song, H.; Chen, D. L.; Ismagilov, R. F. *Angew Chem Int Edit* **2006**, *45*, 7336.

(19) van der Woerd, M.; Ferree, D.; Pusey, M. *Journal of Structural Biology* **2003**, *142*, 180.

(20) Ng, J. D.; Gavira, J. A.; Garcia-Ruiz, J. M. *Journal of Structural Biology* **2003**, *142*, 218.

(21) Talreja, S.; Kenis, P. J. A.; Zukoski, C. F. *Langmuir* **2007**, *23*, 4516.

(22) Hansen, C. L.; Quake, S. R.; Berger, J. M. US, 2007.

(23) Newman, J.; Fazio, V. J.; Lawson, B.; Peat, T. S. *Cryst Growth Des* **2010**, *10*, 2785.

(24) Newman, J.; Xu, J.; Willis, M. C. *Acta Crystallographica Section D* **2007**, *63*, 826.

(25) Collingsworth, P. D.; Bray, T. L.; Christopher, G. K. *J Cryst Growth* **2000**, *219*, 283.

(26) Durbin, S. D.; Feher, G. *Annu Rev Phys Chem* **1996**, *47*, 171.

(27) Talreja, S.; Kim, D. Y.; Mirarefi, A. Y.; Zukoski, C. F.; Kenis, P. J. A. *J Appl Crystallogr* **2005**, *38*, 988.

(28) Yoshizaki, I.; Nakamura, H.; Sato, T.; Igarashi, N.; Komatsu, H.; Yoda, S. *J Cryst Growth* **2002**, *237*, 295.

(29) Anderson, M. J.; Hansen, C. L.; Quake, S. R. *P Natl Acad Sci USA* **2006**, *103*, 16746.

(30) Hansen, C. L.; Sommer, M. O. A.; Quake, S. R. *P Natl Acad Sci USA* **2004**, *101*, 14431.

(31) Lounaci, M.; Rigolet, P.; Abraham, C.; Le Berre, M.; Chen, Y. *Microelectron Eng* **2007**, *84*, 1758.

(32) Zheng, B.; Roach, L. S.; Ismagilov, R. F. *J Am Chem Soc* **2003**, *125*, 11170.

(33) Zhou, X.; Lau, L.; Lam, W. W. L.; Au, S. W. N.; Zheng, B. *Anal. Chem.* **2007**.

(34) Cherezov, V.; Caffrey, M. *J Appl Crystallogr* **2003**, *36*, 1372.

(35) Qutub, Y.; Reviakine, I.; Maxwell, C.; Navarro, J.; Landau, E. M.; Vekilov, P. G. *J Mol Biol* **2004**, *343*, 1243.

(36) Rummel, G.; Hardmeyer, A.; Widmer, C.; Chiu, M. L.; Nollert, P.; Locher, K. P.; Pedruzzi, I.; Landau, E. M.; Rosenbusch, J. P. *Journal of Structural Biology* **1998**, *121*, 82.

(37) Gavira, J. A.; Toh, D.; Lopez-Jaramillo, J.; Garcia-Ruiz, J. M.; Ng, J. D. *Acta Crystallogr D* **2002**, *58*, 1147.

(38) Stevens, R. C. Current Opinion in Structural Biology **2000**, 10, 558.

(39) Baker, M. *Nat Methods* **2010**, *7*, 429.

(40) McPherson, A. In *Current Topics in Membranes, Volume 63*; Volume 63 ed.; DeLucas, L., Ed.; Academic Press: 2009, p 5.

(41) Gabrielsen, M.; Gardiner, A. T.; Fromme, P.; Cogdell, R. J. In *Current Topics in Membranes, Volume 63*; Volume 63 ed.; DeLucas, L., Ed.; Academic Press: 2009, p 127.

(42) Page, R. In *Methods in Molecular Biology: Structural Proteomics - High Throughput Methods*; Kobe, B., Guss, M., Huber, T., Eds.; Humana Press: Totowa, NJ, 2008; Vol. 426, p 345.

(43) Caffrey, M. *Ann Rev Biophys* **2009**, *38*, 29.

(44) Doerr, A. *Nat Methods* **2006**, *3*, 244.

(45) Brostromer, E.; Nan, J.; Li, L.-F.; Su, X.-D. *Biochemical and Biophysical Research Communications* **2009**, *386*, 634.

(46) Li, G.; Chen, Q.; Li, J.; Hu, X.; Zhao, J. *Anal Chem* **2010**, *82*, 4362.

(47) Jia, Y.; Liu, X.-Y. *The Journal of Physical Chemistry B* **2006**, *110*, 6949.

(48) RCSB Protein Data Bank. http://www.rcsb.org/ (July 11, 2010).

(49) Membrane Proteins of Known 3D Structure. http://blanco.biomol.uci.edu/Membrane_Proteins_xtal.html (July 11, 2010).

(50) Michel, H. *Trends Biochem Sci* **1983**, *8*, 56.

(51) Rosenbusch, J. P. *Journal of Structural Biology* **1990**, *104*, 134.

(52) Garavito, R. M.; Picot, D. *Methods* **1990**, *1*, 57.

(53) Kulkarni, C. V. 2010; Vol. 12, p 237.

(54) Landau, E. M.; Rosenbusch, J. P. *P Natl Acad Sci USA* **1996**, *93*, 14532.

(55) Pebay-Peyroula, E.; Rummel, G.; Rosenbusch, J. P.; Landau, E. M. *Science* **1997**, *277*, 1676.

(56) Cherezov, V.; Liu, W.; Derrick, J. P.; Luan, B.; Aksimentiev, A.; Katritch, V.; Caffrey, M. *Proteins: Structure, Function, and Bioinformatics* **2008**, *71*, 24.

(57) Cherezov, V.; Rosenbaum, D. M.; Hanson, M. A.; Rasmussen, S. G. F.; Thian, F. S.; Kobilka, T. S.; Choi, H. J.; Kuhn, P.; Weis, W. I.; Kobilka, B. K.; Stevens, R. C. *Science* **2007**, *318*, 1258.

(58) Cherezov, V.; Yamashita, E.; Liu, W.; Zhalnina, M.; Cramer, W. A.; Caffrey, M. *J Mol Biol* **2006**, *364*, 716.

(59) Jaakola, V. P.; Griffith, M. T.; Hanson, M. A.; Cherezov, V.; Chien, E. Y. T.; Lane, J. R.; IJzerman, A. P.; Stevens, R. C. *Science* **2008**, *322*, 1211.

(60) Rosenbaum, D. M.; Cherezov, V.; Hanson, M. A.; Rasmussen, S. G. F.; Thian, F. S.; Kobilka, T. S.; Choi, H. J.; Yao, X. J.; Weis, W. I.; Stevens, R. C.; Kobilka, B. K. *Science* **2007**, *318*, 1266.

(61) Wacker, D.; Fenalti, G.; Brown, M. A.; Katritch, V.; Abagyan, R.; Cherezov, V.; Stevens, R. C. *J Am Chem Soc* **2010**, *132*, 11443.

(62) Höfer, N.; Aragão, D.; Caffrey, M. *Biophys J* **2010**, *99*, L23.

(63) Li, L.; Ismagilov, R. F. *Ann Rev Biophys* **2010**.

(64) Pal, R.; Yang, M.; Lin, R.; Johnson, B. N.; Srivastava, N.; Razzacki, S. Z.; Chomistek, K. J.; Heldsinger, D. C.; Haque, R. M.; Ugaz, V. M.; Thwar, P. K.; Chen, Z.; Alfano, K.; Yim, M. B.; Krishnan, M.; Fuller, A. O.; Larson, R. G.; Burke, D. T.; Burns, M. A. *Lab Chip* **2005**, *5*, 1024.

(65) Jayashree, R. S.; Gancs, L.; Choban, E. R.; Primak, A.; Natarajan, D.; Markoski, L. J.; Kenis, P. J. A. *J Am Chem Soc* **2005**, *127*, 16758.

(66) Wootton, R. C. R.; deMello, A. J. *Chem Commun* **2004**, 266.

(67) McPherson, A. *J Appl Crystallogr* **2000**, *33*, 397.

Acknowledgements

All of my thanks, love, and appreciation to my friends and family who supported me during my graduate studies. The help and support that my mother and father have given me has been particularly invaluable.

I would also like to thank my advisor, Prof. Paul Kenis for his support over the years. When I joined the group Prof. Kenis gave me the goal of creating a microfluidic platform for performing *in meso* crystallization. However, from that original goal he allowed me to develop the project as my own. Knowing that I had a goal of pursuing a career in academia, Prof. Kenis further helped me to develop my research skills by writing grant proposals to further both my training and my research. With all of this preparation I hope that my future career will be as successful as Prof. Kenis' has been.

My groupmates have also been invaluable, not only for assistance in the lab, but also for insightful conversations. Joshua Tice and Dr. Benjamin Schudel were particularly helpful in learning about microfluidics and designing devices. Also, my research could not have progressed to the level it is today without the assistance of three undergraduate students, Andrew Choi, Tom Bassett, and in particular Griffin Roberts. Griffin helped to develop the original lipid mixer, Andrew began some of the work on X-ray compatible microfluidic chips, and Tom helped to develop a database for understanding the effects of additives on mesophase behavior. Much of the research described here will be carried on by Sudipto Guha, Daria Khvostichenko and Dr. Ashtamurthy Pawate. I thank them for their help and wish them the best of luck as they continue on.

A variety of other people have been key in the development of various aspects of this work. Dr. Deborah Berthold from Prof. Chad Rienstra's lab was a tremendous help in teaching me about protein expression and purification. Prof. Bob Gennis, Prof. Satish Nair and their students were also very helpful in working with various novel proteins and learning about protein crystallography. Prof. Jon Higdon was also invaluable in his assistance with understanding the physics behind viscous fluid flow and mixing, as was Ashlee Ford for her help with MATLAB.

The collaborative efforts of Dr. Howard Robinson, Dr. Alexei Soares, Dr. Vivian Stojanoff, and Dr. Jean Jakoncic at the National Synchrotron Light Source at Brookhaven National Laboratory as well as Dr. Joseph Brunzelle, Dr. Spencer Anderson, and Dr. Elena Kondrashkina with the Life Sciences Collaborative Access Team (LS-CAT) and Dr. Zhong Ren with the BioCARS group at the Advanced Photon Source at Argonne National Laboratory and Dr. Danielle Gray at the George L. Clark X-ray Facility at the University of Illinois helped to make this work possible.

Funding for this work was provided by various grants from the National Institutes of Health (R21 GM075930-01 and R01 GM086727), including an NIH Kirschstein Predoctoral Fellowship (F31 EB008330) and a critical research initiative grant (Campus Research Board, UIUC).

Table of Contents

Chapter 1. Introduction 1

1.1 Protein Crystallization 1

1.1.1 The Challenge of Crystallizing Membrane Proteins 3

1.2 Traditional Methods for Protein Crystallization 4

1.3 Microfluidic Platforms for Protein Crystallization 7

1.3.1 Fabrication of Microfluidic Systems 7

1.3.2 Examples of Microfluidic Platforms for Protein Crystallization 8

1.4 Protein Crystallography 13

1.5 Traditional Methods for Protein Crystallography 15

1.6 Microfluidic Methods for *In Situ* Protein Crystallography 16

1.7 Summary and Key Remaining Challenges 19

1.8 References 20

Chapter 2. *In Meso* Membrane Protein Crystallization 27

2.1 The Challenge of Amphiphilic Membrane Proteins 27

2.2 The *In Meso* Membrane Protein Crystallization Method 30

2.3 Current Mechanistic Understanding of *In Meso* Membrane Protein Crystallization 33

2.4 The Role of Lipid Phase Behavior in *In Meso* Membrane Protein Crystallization 34

2.4.1 The Phase Behavior of MAG/Water Systems 36

2.4.2 The Effect of Additives on the Phase Behavior of MAG/Water Systems 38

2.5 Key Challenges 46

2.6 References 47

Chapter 3. Overcoming the Challenge of Pumping Viscous Fluids at the Microscale 54

3.1 Introduction 55

3.2 Theory 56

3.2.1 The Effect of Valve Membrane Actuation on Pressure-Driven Flow in a Rigid Channel 56

3.2.2 The Effect of Channel Deformation on Viscous Flow 58

3.3 Design Rules 65

3.3.1 Effective Pneumatic Valves for Pumping Viscous Fluids 65

3.3.2 Steady-State Pumping in a Microfluidic Channel 67

3.3.3 Precise Metering Operations 67

3.3.4 Applications of the Design Rules 71

3.4 Conclusions 77

3.5 Acknowledgements 78

3.6 References 78

Chapter 4. Design and Application of Microfluidic Platforms for *In Meso* Membrane Protein Crystallization 79
4.1 Introduction 80
4.2 Materials and Methods 82
4.2.1 Device Fabrication and Operation 82
4.2.2 Crystallization Experiments 82
4.2.3 Protein, Lipid, and Precipitant Solutions 83
4.3. Results and Discussion 84
4.3.1 Design and Operation 84
4.3.2 Validation of the Platform Using Bacteriorhodopsin as a Model Protein 90
4.4. Conclusions 92
4.5 Acknowledgements 93
4.6 References 93
Chapter 5. Design and Application of Microfluidic Platforms for *In Situ* Protein Crystallography 98
5.1 Introduction 99
5.2 Materials and Methods 99
5.2.1 Device Fabrication 99
5.2.2 Protein and Precipitant Solutions 101
5.2.3 Crystallization Experiments 102
5.2.4 X-ray Diffraction Experiments 103
5.2.5 Analysis of X-ray Diffraction Data 104
5.3 Results and Discussion 104
5.3.1 Characterization of Device Materials 104
5.3.2 Device Fabrication and Characterization 107
5.3.3 Validation of Device Architecture with Single Microfluidic Well Configuration: Crystallization of Soluble Proteins 109
5.3.4 X-ray Transparent Microfluidic Array Chips for the Crystallization of Soluble Proteins 113
5.3.5 X-ray Transparent Devices for the *In Meso* Crystallization and Study of Membrane Proteins 124
5.4 Conclusions 126
5.5 Acknowledgements 126
5.6 References 127
Chapter 6. Microfluidic Platforms for *In Situ* Laue Crystallography 133
6.1 Introduction 134
6.2 Materials and Methods 136
6.2.1 Device Fabrication and Operation 136
6.2.2 Protein and Precipitant Solutions 136
6.2.3 Crystallization Experiments 136
6.2.4 X-ray Diffraction Experiments 136
6.2.5 Analysis of X-ray Diffraction Data 137
6.3 Results and Discussion 139

6.3.1 Proof-of-Concept On-Chip Laue Diffraction Experiments 139
6.3.2 *In Situ* Single-Shot Laue Structure Determination of Crystals Grown in a Microfluidic Chip 141
6.4 Conclusions 145
6.5 Acknowledgements 146
6.6 References 146

Chapter 7. Microfluidic Platforms for *In Situ* Analysis of Lipid Phase Behavior 149
7.1 Introduction 150
7.2 Materials and Methods 152
7.2.1 Device Fabrication and Operation 152
7.2.2 Chemicals and Solutions 152
7.2.3 Sample Thickness Experiments 153
7.2.4 *In Situ* Analysis of Phase Behavior on a Microfluidic Chip 153
7.2.5 Small Angle X-ray Diffraction Experiments 154
7.2.6 Analysis of Small Angle X-ray Diffraction Data 155
7.3 Results and Discussion 156
7.3.1 Development of Small Angle X-ray Analysis Capabilities at LS-CAT with High Resolution Sample Visualization Capabilities 156
7.3.2 Proof-of-Concept Experiments: Signal Intensity as a Function of Sample Thickness 157
7.3.3 Design of Microfluidic Chips for Phase Diagram Determination 162
7.3.4 Validation of Platform by *In Situ* Analysis of Phase Behavior 163
7.4 Conclusions 167
7.5 Acknowledgements 167
7.6 References 168

Chapter 8. Summary of Accomplishments and Future Directions 171
8.1 Introduction 171
8.2 Microfluidic Platforms for Protein Crystallization 171
8.2.1 Microfluidic Platforms for the Crystallization of Solubilized Proteins 171
8.2.2 Microfluidic Platforms for the *In Meso* Crystallization of Membrane Proteins 172
8.3 X-ray Transparent Microfluidic Devices for *In Situ* Protein Crystallography 173
8.3.1 Microfluidic Platforms for Crystal Quality Screening and Structure Determination 173
8.3.2 Microfluidic Platforms for Laue Crystallography 173
8.4 Microfluidic Platforms for the Preparation and *In Situ* Analysis of Aqueous/Lipid Phase Behavior 174
8.5 Conclusions 174
8.6 References 175

Appendix. Overcoming the Challenge of Pumping Viscous Fluids at the Microscale 176
Appendix A.1 Typical Values of β for Microfluidic Channels 176
Appendix A.2 Determination of Constants for 2nd Order Polynomial Fit for Time 177

Appendix A.3 Determination of a Graduated Mesh 177
Appendix A.4 Development of a Differential Equation with an Analytical Solution for Code Debugging 178
Appendix A.5 Derivation of the Displacement of an Infinite Slab from a Point Pressure Source 178
Appendix A.6 MATLAB Code 180
References 189

Chapter 1

Introduction

Proteins are a class of biological macromolecules which play crucial roles in the internal machinery of a cell. These proteins are composed of long chains of amino acids, the sequence for which is encoded by the DNA of a cell. While genome[1,2] and protein sequencing efforts[3] have provided information about the primary structure of proteins and the genes that encode them, this information is obtained without any knowledge of the actual function of the protein. Efforts to determine the mechanism whereby a protein performs a particular function involve coupling biochemical analyses with knowledge of the three-dimensional structure of the protein.

In 2000, the National Institutes of Health (NIH) launched the Protein Structure Initiative (PSI) with the goal of obtaining the three-dimensional structures of 10,000 proteins within a decade.[4] One of the major achievements of this concerted effort was the development of improved, and often automated, high throughput methodologies for the cloning, expression, and purification of protein targets.[5] A particular focus included the production of membrane protein samples for structure determination. Membrane proteins are especially challenging because of their amphiphilic nature and the fact that they are grown within the confines of cellular membranes. Once a sufficient quantity of high quality protein is obtained, protein structure determination is then pursued mainly by protein crystallography, though alternative techniques such as nuclear magnetic resonance (NMR) and electron microscopy are achieving increasing levels of success.[6,7] Despite advances associated with protein expression and purification, the two most significant bottlenecks for protein structure determination continue to be the (i) obtaining sufficient quantities of high quality protein samples and (ii) growing high quality protein crystals.[7-33]

1.1 Protein Crystallization

The human genome has been estimated to encode for ~30,000 proteins of which roughly a third each are thought to be (i) soluble or globular proteins responsible for functions within the organism, (ii) membrane-bound proteins typically responsible for signaling and material and energy transduction across the cell membrane,[7,34-39] and (iii) proteins with no intrinsic structure.[40] Because protein crystallography requires the formation of crystals with repeating units of the protein in identical conformations, it is only the structured soluble and membrane proteins to which this method can be applied.

Crystallization is a technique that has long been used as a purification procedure because crystals naturally exclude contaminants. First a solution of the species of interest is made under conditions

favoring dissolution. Crystallization is then achieved by altering the solution conditions so as to decrease the solubility of the desired product to the point where it will precipitate out of solution creating a solid crystalline form. This decrease in solubility is typically achieved by changes in temperature, concentration, or by the addition of a precipitating agent such as a salt, an osmotically active molecule such as polyethylene glycol, or an anti-solvent.[41] The growth of high quality protein crystals for X-ray analysis is achieved in a similar fashion; first through the identification of crystal forming conditions,[10,14,23,42-49] followed by optimization of crystallization conditions to produce the highest quality crystals.[8,9,13-15,22,23,45,46,48,50-60]

One of the main bottlenecks associated with protein crystallography is the identification of crystal forming conditions.[8-27,29,30,32,33,61] Unfortunately, no methods currently exist to predict crystallization conditions *a priori*.[14,42,45,62-66] Consequently, sparse matrix screening approaches have been adopted in order to explore multidimensional chemical space.[14,25,30-33,42,43,45,49,61,67,68] In a sparse matrix screen a large number of possible combinations of precipitants with different buffer and pH conditions are screened to identify conditions that are conducive to crystal nucleation and growth.[10,14,23,31,42-49,68] However, while sparse matrix screening approaches provide a way to survey a wide range of chemical space, additional considerations such as the kinetic changes of species concentration with time are critical for controlling the nucleation and growth of crystals. The exploration of chemical space and the impact of kinetic factors can be illustrated by examining the solubility phase diagram associated with crystallization and, once understood, can be affected by the choice of crystallization technique used.

Figure 1.1 shows a generalized two-dimensional phase diagram, showing the conditions for crystallization as a function of protein and precipitant concentration. However, determination and optimization of an actual crystallization condition can involve a large number of parameters including temperature, ionic strength, buffer identity and pH, additives, and protein purity. For membrane proteins additional parameters such as detergent or lipid identity and concentration can also have a very significant effect.[69] Furthermore, the areas of the phase diagram that are conducive for crystallization may be discontinuous, requiring extensive mapping out of phase behavior or special consideration during crystallization trials.[61]

The portions of the phase diagram associated with crystallization can be divided into four regions (Figure 1.1).[25,41,70] The solubility boundary separates the undersaturated region, where any crystals present would dissolve, from regions of supersaturation where crystal growth is possible. Within this supersaturated region there are three zones: (1) the nucleation or labile zone, (2) the metastable zone, and (3) the precipitation zone. In the nucleation zone the level of supersaturation is high enough to induce the nucleation of new crystals and to support subsequent crystal growth. The metastable zone is at a lower level of supersaturation compared to the nucleation zone. Thus while the level of supersaturation is not high enough to support the formation of new nuclei, growth of existing crystals is possible. In the precipitation zone the level of supersaturation is very high, resulting in fast nucleation

and growth. These processes occur so quickly that the resulting solid is amorphous rather than crystalline. Thus, for a crystal to nucleate and grow, the solution needs to reach the nucleation zone first, after which it can continue to grow in either the metastable or the nucleation zone. A wide variety of crystallization techniques to achieve first nucleation and then crystal growth have been developed over the years. These are described in detail in Section 1.2.

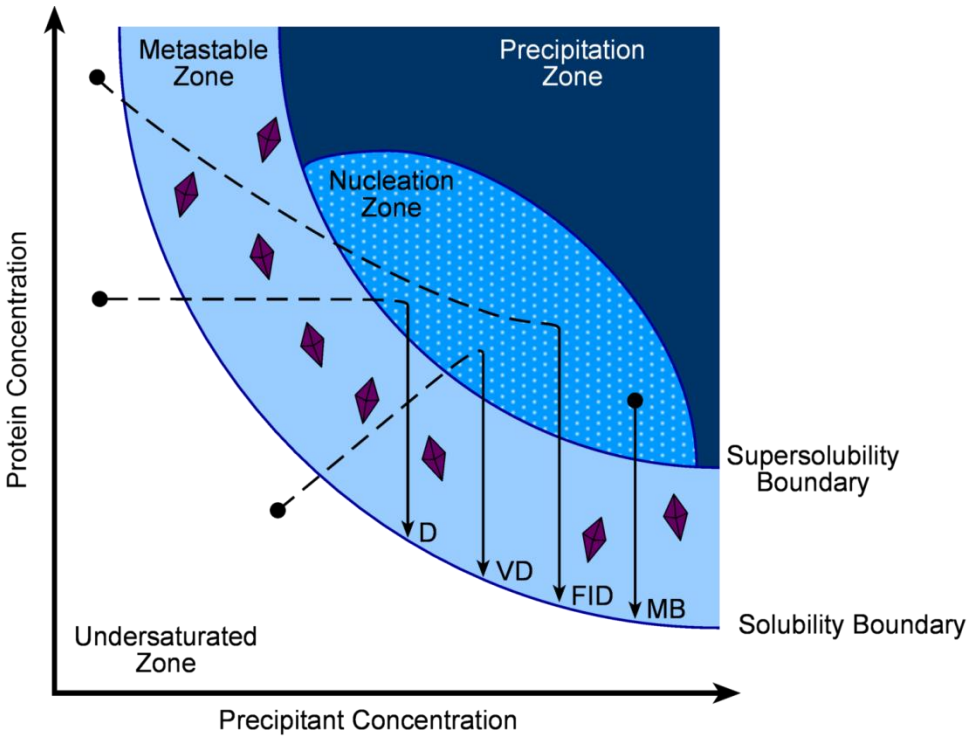

Figure 1.1. A generalized depiction of the solubility phase diagram for protein crystallization. The solubility boundary defines the undersaturated from the metastable zone. While crystal growth is possible in the metastable zone, higher levels of supersaturation are required for nucleation, as indicated by the nucleation zone. At even higher levels of supersaturation, in the precipitation zone, the driving force to precipitate protein from solution is so high that there is not time for the formation of a crystalline solid, and an amorphous precipitate results. Thus for crystallization to occur the concentration of the solution must be such that the nucleation zone can be accessed, though subsequent crystal growth can occur in the metastable zone. Dynamic pathways for various common crystallization techniques are shown. D = dialysis, VD = vapor diffusion, FID = free interface diffusion, and MB = microbatch. (Image adapted from Chayen and Saridakis, 2008).[70]

1.1.1 The Challenge of Crystallizing Membrane Proteins

While crystallization and structure determination of soluble proteins has been progressing swiftly, the structure determination of membrane proteins has lagged behind. The amphiphilic nature of membrane proteins coupled with limited availability has hampered crystallization efforts.[26,39,71] Amphiphilicity in particular is a challenge because crystal growth occurs from a solution of protein and dissolution occurs as an interaction of molecules with a like solvent (i.e. polar – polar or apolar – apolar). Because membrane proteins have both hydrophobic and hydrophilic portions they will not readily dissolve into either a polar or an apolar solvent on their own. To counteract this difficulty a variety of strategies have been developed such as (i) the *in surfo* detergent solubilization method which encapsulates the hydrophobic portions of the membrane protein in a detergent micelle to allow for dissolution,[36,39,72,73] or (ii)

the *in meso* method which maintains the membrane protein in a membrane-like environment (see Chapter 2).[28,39,74,75] Despite these strategies, membrane proteins have proven to be so difficult to crystallize that 25 years passed between the first structure determination of a soluble protein[76,77] and that of a membrane protein.[78,79] Furthermore, of the more than 66,000 structures deposited in the Protein Databank,[6] less than 1% are for membrane proteins, with even fewer present at high resolution (< 2Å).[80-82] Of these known structures, only 15 are unique human membrane proteins (Figure 1.2).[80] This disparity exists despite genomic analyses indicating that the number of soluble and membrane proteins should be similar.[34,83] Even more critically, the malfunction of membrane proteins has been linked to a variety of diseases including diabetes, cirrhosis of the liver, cystic fibrosis, cancer, Alzheimer's disease, hypertension, epilepsy, cataract, tubulopathy, leukodystrophy, Leigh syndrome, anemia, sensorineural deafness, and hypertrophic cardiomyopathy,[37,38,84] though the structure of many of these proteins and the corresponding malfunctions are not understood. Furthermore, at least 60% of the drugs currently available are thought to target membrane proteins, the influence of a vast majority of which has only been guessed at because of a lack of structural information.[81,82,85]

In the following sections the traditional methods for protein crystallization will be discussed first (Section 1.2), followed by adaptations of these methods for use in microfluidic platforms for protein crystallization (Section 1.3). The work presented in both of these sections is applicable to soluble proteins and to analogous strategies for the *in surfo* crystallization of membrane proteins.[26,73] A more detailed description of the challenges associated with amphiphilic membrane proteins and the *in meso* crystallization of membrane proteins will be considered in Chapter 2. Both traditional (Section 1.5) and microfluidic (Section 1.6) methods for X-ray crystallography will then be discussed in regards to obtaining structural information.

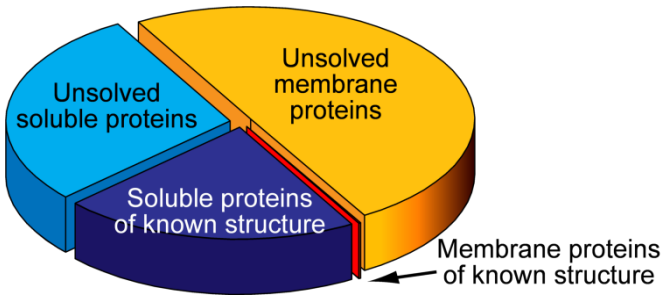

Figure 1.2. Pie chart indicating the number of soluble and membrane proteins of known and unknown structure.[6,34,80]

1.2 Traditional Methods for Protein Crystallization

Within the context of a sparse matrix approach where the identity of various precipitating agents are screened, a variety of crystallization methods have been developed which provide varying degrees of control over the concentration of the protein/precipitant mixture over time.[86] The four most common techniques for protein crystallization are; (1) microbatch, (2) vapor diffusion, (3) dialysis, and (4) free interface diffusion. Each of these techniques controls the change of concentration within the

protein/precipitant solution differently, though with allowances for the different dynamics of each method, converting between techniques is possible.[87-89]

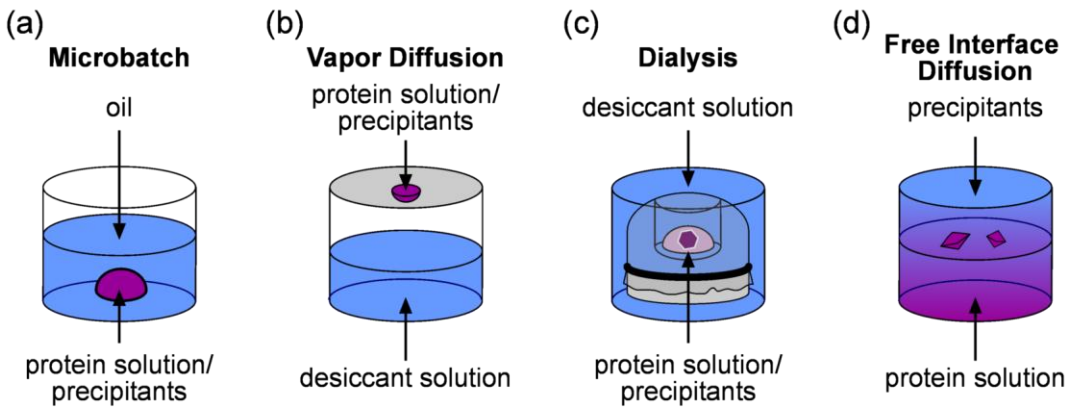

Figure 1.3. Schematic depiction of the generalized setups of typical traditional crystallization methods. **(a)** Microbatch, **(b)** the hanging drop configuration of a vapor diffusion setup, **(c)** a dialysis button, and **(d)** free interface diffusion are depicted.

Microbatch methods are based on the idea of identifying an initial condition which leads to crystallization.[61] A small drop of protein solution is combined with precipitants or other additives and then incubated under Paraffin oil so as to prevent evaporation (Figure 1.3a).[86,90,91] Thus the supersaturation of the droplet is constant with time and the conditions in the droplet will only change if the protein comes out of solution, either as a crystal or as an amorphous solid. In reference to the phase diagram shown in Figure 1.1, crystals would only be observed if the initial combination of protein and precipitants resulted in a supersaturation high enough to be in the nucleation zone. In a slight modification to this technique a mixture of Paraffin and silicon oils is used in the experiment. This combination of oils is permeable to water vapor and would allow for the permeation of water from the sample and a change in concentration.[92] In this variation, unless the experiment is performed under controlled environmental conditions to limit the extent of removal of water, the permeation of water away from the protein droplet will occur until the sample has completely dried out. Microbatch crystallization is typically performed in well plates for high throughput analysis.

Whereas microbatch crystallization involved a search for appropriate initial conditions, vapor diffusion, dialysis, and free interface diffusion methods are more dynamic, searching for a path through the phase diagram which leads to crystallization.[91] Vapor diffusion is the most widely used protein crystallization technique[25,26,41,87,93,94] and can be performed in a variety of geometries including hanging, sitting, and sandwich drop configurations.[25,26,30,41,86,95] A droplet containing a mixture of protein and precipitants is placed in a sealed environment to equilibrate with a larger reservoir of the precipitant solution (Figure 1.3b). Evaporation from the droplet will then take place until equilibrium is reached. In this method a single droplet is able to traverse a range of protein concentration values starting from an undersaturated solution, as indicated in Figure 1.1. The concentration of the droplet will continue to increase until either equilibrium is reached or the protein comes out of solution. Thus vapor diffusion is a more flexible

technique than microbatch, with a higher probability of obtaining crystals from a single set of crystallization conditions. However, setting up vapor diffusion trials is more intensive than microbatch because of the need to individually seal each crystallization compartment.

In dialysis the protein and precipitant solutions are separated by a dialysis membrane which is impermeable to the protein, but not to the precipitant (Figure 1.3c).[26,61] As the concentration of precipitant changes with time the concentration of protein will remain constant until it comes out of solution. The advantage of this technique is that the dialysis membranes allow for bidirectional changes in the concentration of precipitant species without significantly affecting the protein concentration (Figure 1.1). One could perform both salting in and salting out experiments, or sample a wide range of pH values.[41,86] While this method has similar flexibility to vapor diffusion, setting up crystallization trials is very intensive and is typically done using dialysis buttons,[86] though recently high throughput wellplates for dialysis have been developed.[96]

In free interface diffusion a path through the phase diagram is traversed by allowing diffusion between a protein and a precipitant solution. Initially the protein and precipitant solutions are placed into contact along a clearly defined interface. The subsequent diffusion of protein into the precipitant solution and vice versa then creates a gradient of concentrations along which crystallization can occur (Figure 1.3d).[61] As the protein begins to diffuse into the precipitant solution the experiment samples conditions of low protein concentration and high precipitant concentration. However, smaller precipitant molecules will tend to diffuse more quickly than larger proteins, allowing the experiment to also sample conditions of high protein and low precipitant concentration. This flexibility gives free interface diffusion trials a tremendous capacity to sample a wide range of phase space in search of appropriate crystallization conditions (Figure 1.1). From an optimization perspective, protein crystals will grow along the length of the gradient, changing from showers of very small crystals or amorphous precipitates where the supersaturation is high enough to be significantly into the nucleation zone or into the precipitation zone to single larger crystals where the concentration is such that only a few nucleation events are adequate to lower the level of supersaturation from the nucleation zone into the metastable zone. Despite its strengths, free interface diffusion is not commonly used on the macroscale due to difficulties in preventing convectional mixing in large scale devices. It has, however, been used in microgravity experiments,[59,60,97,98] and is ideally suited for scaling down to microscale dimensions where the geometries prohibit convectional mixing. This technique and the related counter-diffusion method will be discussed further with respect to microfluidic strategies for protein crystallization in Section 1.3.

The development of high throughput methods for preparing crystallization trials have developed to the point where an individual crystallization trial can be set up at volumes <50 nL in a fully automated fashion.[88] Automated fluid handling robots have become a major workhorse of both high throughput crystallography facilities as well as smaller structural biology laboratories, with a single unit capable of setting up over 400,000 individual trials per month, or 500-600 trials per hour.[4,24] Despite these advances

there is still potential to scale down the volume of crystallization trials further, to the <1nL range, through the use of microfluidics.

1.3 Microfluidic Platforms for Protein Crystallization

Efforts in developing microfluidic platforms for protein crystallization have focused on utilizing the high-throughput capability of microfluidic networks to screen a large number of crystallization conditions while relying on miniaturization to reduce the amount of sample needed per experiment. Additionally, microfluidics can provide unique experimental approaches that would be difficult or impossible to implement on a larger scale.[61,89] While the majority of these efforts have focused on miniaturizing traditional methods for crystallization including microbatch,[17,18,32,44-47,54,99-116] and vapor diffusion,[16,44,51-53,56,117,118] others such as those focused on platforms for counter-diffusion[22,23,59,60,119-126] and free interface diffusion[14,22,23,42,51,61,99,119-122,124-128] have taken further advantage of the lack of convection and turbulence at the microscale to enable their technology. In the subsequent examples microfluidics has been defined as any system where the characteristic dimension of the system is < 1 mm, such that turbulent effects can be neglected. These "microfluidic" systems include examples ranging from simple capillaries, to nanoliter-scale droplets contained by two-phase flow, to highly integrated microfluidic networks created by multilayer soft lithography.

1.3.1 Fabrication of Microfluidic Systems

Soft lithography and replica molding have facilitated the development of a wide range of microfluidic technologies ranging from simple single layer devices to complex microfluidic networks.[129] While fabrication methods such as hot embossing can be used to define device structures, soft lithography has the benefit of rapid prototyping for faster cycle time from concept to device. A device design can be created in a computer aided design program and then printed on a high resolution transparency to serve as a mask. A master for replica molding can then be fabricated from photoresist on a silicon wafer using standard photolithographic techniques. Device fabrication is achieved by replica molding from a master. While a wide variety of materials including glass and various polymers have been used for simple structures, the use of elastomeric materials such as polydimethylsiloxane (PDMS) allows for the integration of valves and pumping mechanisms[130-132] and is capable of replicating features down to sub-micrometer length scales.[133] Valving of fluid lines can be accomplished by the creation of a multi-layer device where a thin membrane can be pneumatically deflected by either positive pressure to seal off flow in the fluid layer below in an actuate-to-close configuration[130] (Figure 1.4a) or negative pressure to allow flow in an actuate-to-open configuration (Figure 1.4b).[131,134] A pump can be fabricated by placing a series of valves in series and actuating them a peristaltic fashion.[130,132]

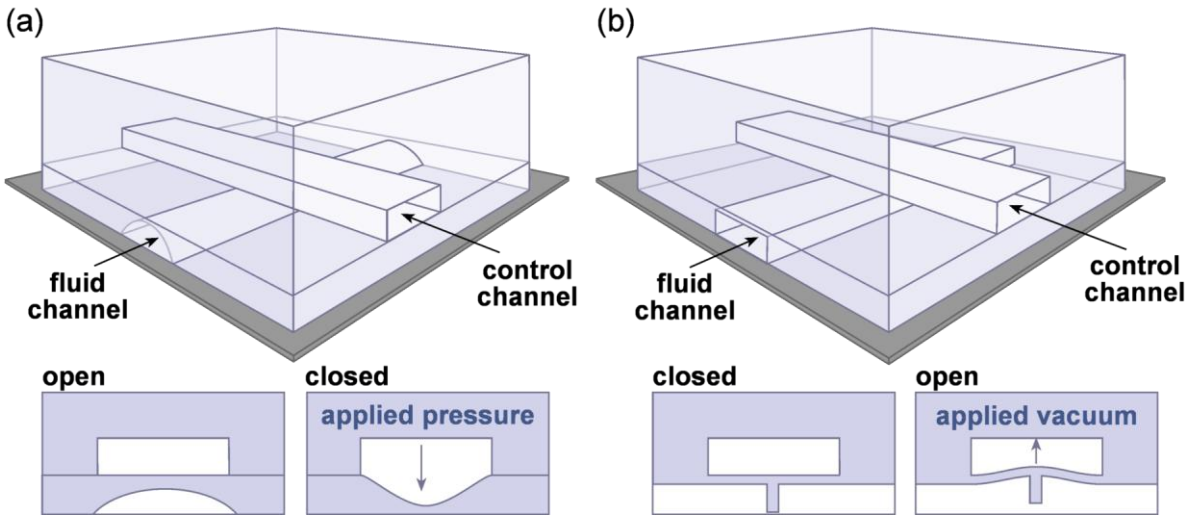

Figure 1.4. Schematic showing operation of microfluidic valves by deflection of a thin membrane by **(a)** positive pressure in an actuate-to-close configuration, or **(b)** negative pressure in an actuate-to-open configuration.

1.3.2 Examples of Microfluidic Platforms for Protein Crystallization

In applying a microfluidic approach to microbatch crystallization the major benefit comes from the small volumes of fluid used. Whereas the volume of fluid dispensed can be easily controlled for the traditional scale of crystallization trials, metering and controlling nanoliter-scale or smaller volumes is a significant consideration on the microfluidic scale. The simplest method for metering fluids is filling of a geometrically defined volume. Individual fluids can be loaded into a series of wells by either positive[99,135] or negative pressure.[18] For a crystallization trial, wells containing protein solution must be brought into contact with those containing precipitant solutions. In a very simple example, a series of wells on the glass bottom half of a device were aligned with a PDMS slab containing connecting channels. Having degassed the PDMS slab by exposure to vacuum, the material retained enough internal pressure to fill the wells with either a protein or a precipitant solution. Similar to traditional microbatch experiments, a silicone oil was used to protect filled wells as the PDMS slab was removed (Figure 1.5a). Two half devices, one containing protein and the other containing precipitant solutions were then aligned under oil and allowed to incubate (Figure 1.5b).[18]

A similar but more elegant microfluidic solution, termed SlipChip, begins with the various wells and connecting channels present in two half devices. The two halves of the device can be slipped relative to each other to align wells and channels for loading of protein and precipitants and then to align and seal off wells to form a crystallization trial (Figure 1.6).[99,135]

An alternative method of defining and controlling nanoliter volumes of fluid involves the use of two-phase flow.[17,44-47,54,93,100-106,108,110,112,136-138] By carefully controlling surface tension a series of droplets can be formed at a T junction where a carrier stream such as a fluorinated oil is used to disperse aqueous droplets (Figure 1.7a). An advantage of this method over more static well-based strategies for microbatch crystallization is that the composition of an individual droplet can be easily varied by changing

the flowrates of the various components over time (buffer, protein, precipitant, etc.). Thus instead of merely screening a single protein/precipitant combination, the droplet-based approach allows for sub-screening of a wide range of concentrations for each individual precipitant. This allows for the simultaneous screening and optimization of crystallization conditions (Figure 1.7b). The scale and ease of this method also vastly outstrips the current speed with which traditional microbatch trials can be set up. Instead of 500-600 trials per hour at 50 nL/trial, using 25-30 µL of protein,[4,24] the droplet-based approach is capable of setting up 1300 trials in less than 20 minutes using only 10 µL of protein.[46,61]

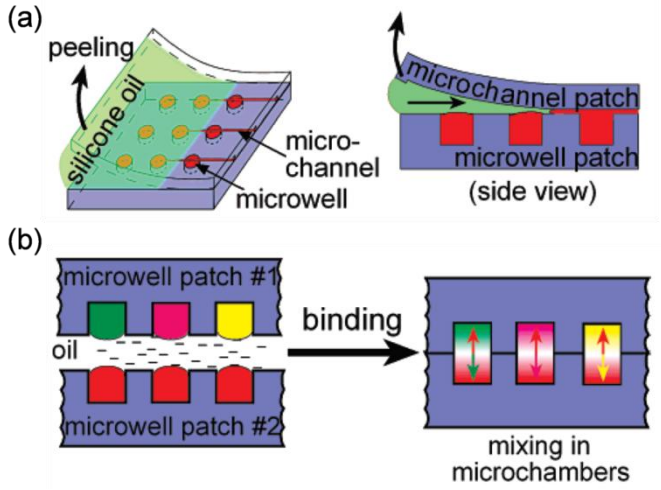

Figure 1.5. (a) Schematic illustration of the process of removing the PDMS microchannel from a filled series of microwells. Silicone oil has been applied to protect the microwells from evaporative losses. **(b)** Illustration of the aligning of two half-devices under oil followed by diffusive mixing and incubation. (Figure adapted from Zhou *et al.*, 2007).[18]

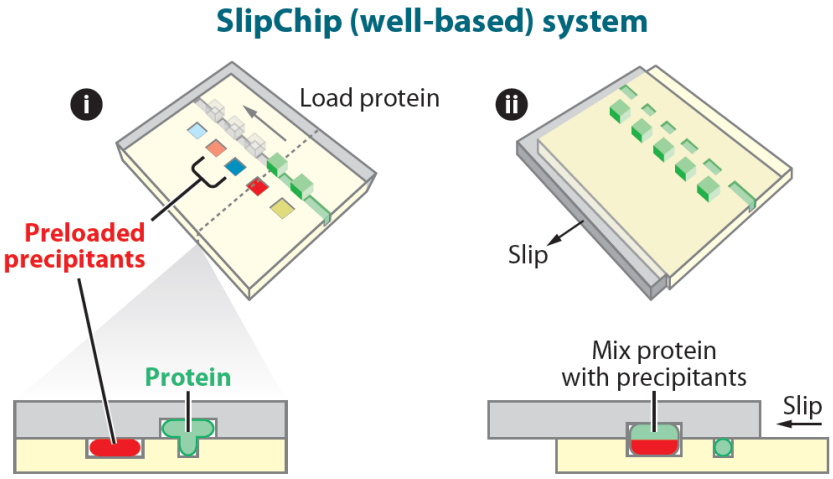

Figure 1.6. Schematic depiction of filling of the protein precipitant solutions. Slipping of the chip allows for mixing by diffusion. (Image adapted from Li and Ismagilov, 2010).[61]

While vapor diffusion at the macroscale involves controlling composition based on vapor/liquid equilibrium, we will expand our consideration of this technique at the microscale to include diffusion of solvent through any medium. One of the difficulties in scaling down vapor diffusion while maintaining a vapor/liquid equilibrium is the difficulty in controlling separate volumes of fluid with merely an air gap.

This can be a particular challenge in screening for crystallization conditions where the various chemicals present can create vastly different wetting properties and for membrane proteins where the presence of detergents significantly affects wetting.[46]

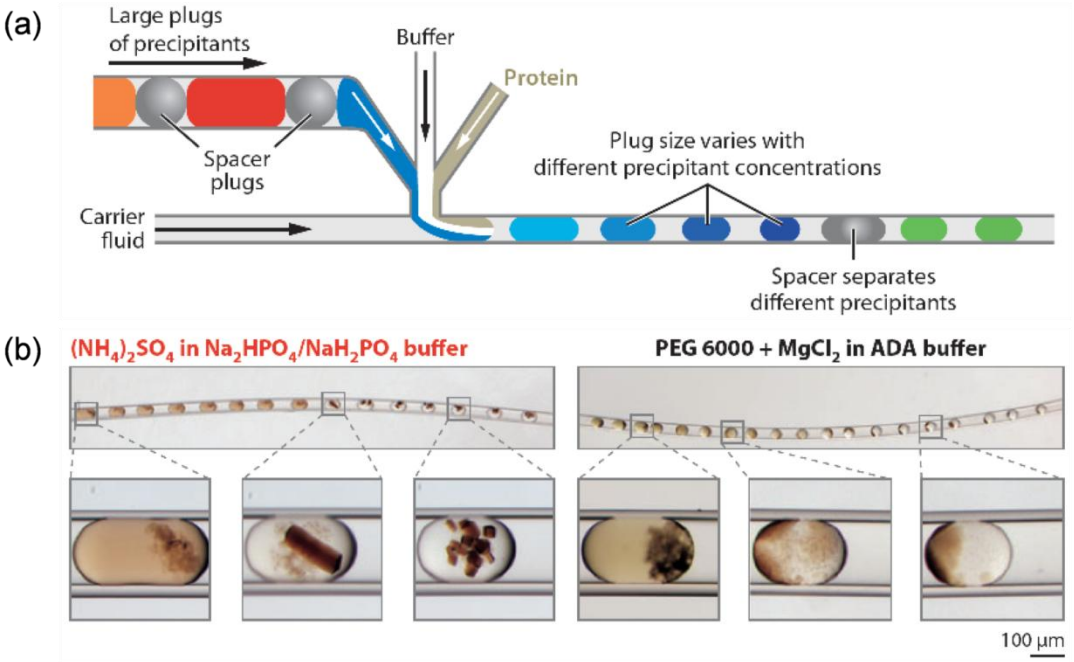

Figure 1.7. A droplet-based microfluidic approach to microbatch crystallization. **(a)** A schematic illustration of the droplet formation process where various precipitants combine with buffer and protein solution in various ratios. **(b)** Optical micrographs of crystallization results for photosynthetic reaction center from *Blastochloris viridis* at two different crystallization conditions. (Figure adapted from Li and Ismagilov, 2010).[61]

Lounaci and coworkers have demonstrated two examples of traditional microscale vapor diffusion. Reservoirs containing the crystallization and reservoir solutions are separated by a microchannel through which vapor/liquid equilibrium is established.[16,117] A secondary challenge with this method is the fact that in order for the two liquids to be in vapor contact with each other they cannot be isolated from the device materials or the external environment. While PDMS has many benefits for microfluidic devices, including air permeability which allows for dead-filling of chambers, this same air permeability means that the PDMS is capable of both solvent absorption and evaporative solvent loss. This can be controlled to a certain extent by controlling the environment around the device, but provides an additional complication.

The droplet-based methods described earlier with respect to microbatch can be modified for vapor diffusion-type experiments. Two phase flow can be used to generate and control individual crystallization trials while reservoir solutions are used to osmotically control the composition of the droplets by solvent diffusion through the carrier stream. This strategy has been applied in several ways, the first of which is to generate a set of alternating droplets of a crystallization trial and "reservoir" droplet which acts as an osmotic bath.[44] An alternative approach is to separate the crystallization trials and reservoir solutions in separate layers of the device.[53,56,118,137,138] This strategy has the added benefit of allowing dynamic control over the composition of the reservoir solutions with time. In fact, this has been used to decouple the

nucleation and growth of crystals. By initially using a reservoir solution of high concentration Fraden and coworkers were able to first drive nucleation by concentrating the droplet until it reached the labile zone. Subsequent lowering of the concentration in the reservoir caused the concentration of the droplet to decrease to the point where nuclei smaller than a critical radius dissolved and crystal growth on the remaining nuclei could proceed (Figure 1.8).[56,118]

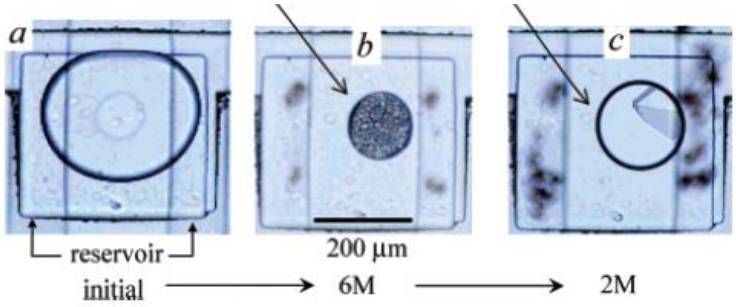

Figure 1.8. A crystallization droplet contained by a carrier fluid and connected to an osmotic reservoir. **(a)** The initial state of the droplet. **(b)** The droplet after equilibrating with a high concentration salt reservoir. The volume of the droplet has shrunk and nucleation can be seen. **(c)** The droplet after subsequent equilibration with a reservoir of lower salt concentration. The droplet has increased in size with rehydration and many of the nuclei have dissolved, allowing for the formation of one single crystal. (Figure adapted from Shim *et al.*, 2007).[56]

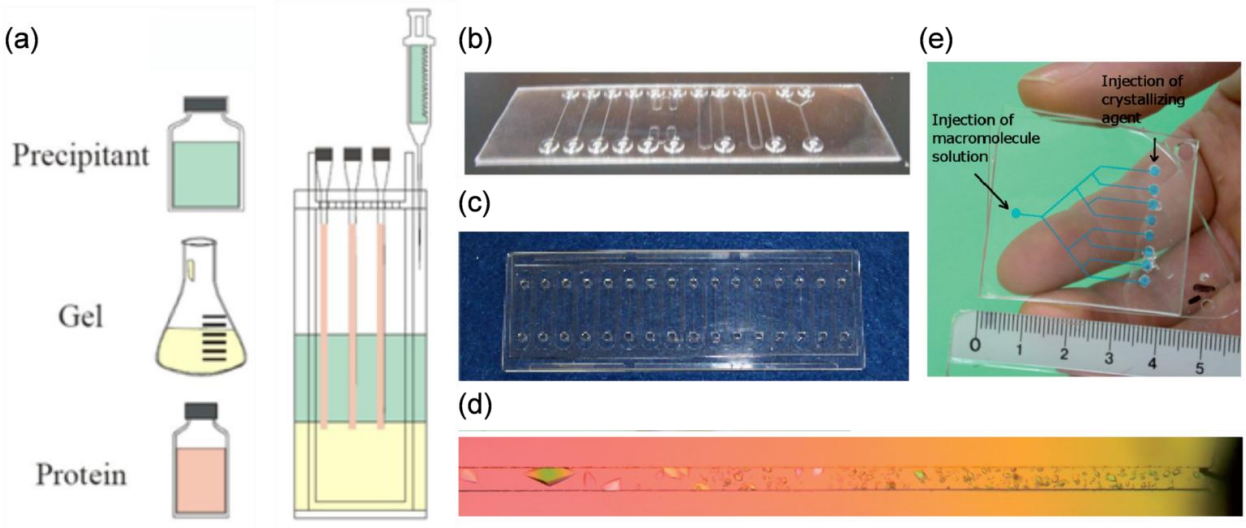

Figure 1.9. (a) Schematic of a gel acupuncture experimental setup for counter-diffusion. The protein is loaded into capillaries and then punctured into a gel which prevents protein diffusion but through which precipitants can diffuse. (Figure adapted from Garcia-Ruiz *et al.,* 2002).[120] **(b)** A counter-diffusion chip fabricated out of cyclic olefin copolymer (COC) by Greiner Bio-One. (Figure adapted from Ng *et al.*, 2008).[122] **(c)** A counter-diffusion chip manufactured by Microlytic. (Figure adapted from http://www.microlytic.com).[139] **(d)** A typical crystal growth profile in a counter-diffusion experiment using the device from **(e)** ranging from small crystals or amorphous precipitates on the right side which is closest to the precipitant reservoir to large single crystals on the left where lower levels of supersaturation are present.[124] **(e)** A multichannel counter-diffusion chip fabricated out of COC. (Figures adapted from Dhouib *et al.*, 2009).[124]

Free interface diffusion and counter-diffusion are the two crystallization methods most closely associated with microfluidic crystallization. Counter-diffusion localizes the protein solution in a capillary or a microfluidic channel, oftentimes immobilized in a gel to reduce convective effects. After filling the capillary or channel with protein solution, the precipitant solution is then introduced at one end. The

precipitant solution then diffuses into the protein solution, creating a concentration gradient (Figure 1.9).[22,23,26,59,60,93,98,119-126,139] Free interface diffusion, on the other hand, establishes an interface between a protein and precipitant solution where diffusion of both species can occur.[14,22,23,42,51,61,98,99,119-122,124-128] Unlike counter-diffusion where a gel can be used to stabilize the protein solution and prevent convection, free interface diffusion requires either the convection-free conditions present in microfluidics or a zero-gravity environment to be fully realized.

Though elegant solutions such as the Slip-Chip have been recently developed,[61,99] the free interface diffusion technique was truly enabled by multilayer microfluidic technology and the active valving and fluid control it provided (Section 1.3.1, Figure 1.4). These valves were required because of the need to establish a clean interface between the protein and precipitant solutions and prevent premature contact during device filling. In one of the best known examples, Quake and coworkers reported a microfluidic free interface diffusion crystallization platform comprised of an array of 144 10 nL chambers, capable of screening 48 precipitants, each at three different precipitant-to-protein ratios (Figure 1.10).[42,49,51,140] Pneumatic valves were used to isolate the chambers containing protein and precipitant solutions from each other during filling and then released to allow diffusion. This method has been used to crystallize a number of novel targets,[13,127,141] and has been commercialized by Fluidigm Corporation.[29,89,98,142]

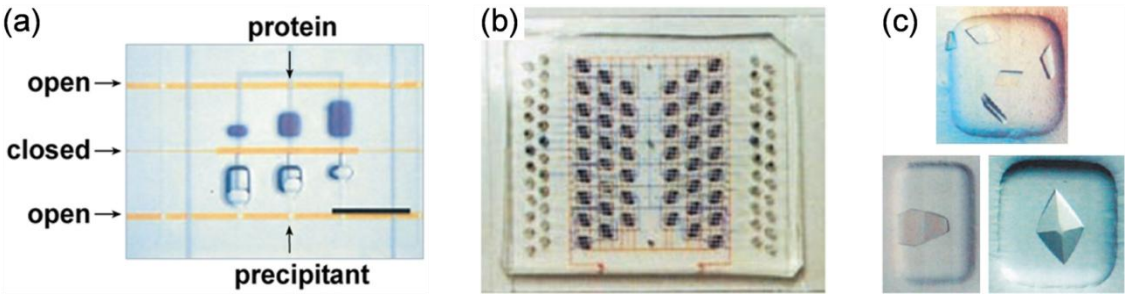

Figure 1.10. **(a)** Optical micrograph of a portion of a microfluidic device showing a set of three chambers used to create differing protein/precipitant ratios for free interface diffusion crystallization. **(b)** A photograph of an integrated array chip containing 48 sets of three wells, each capable of screening a separate precipitant. **(c)** Optical micrographs of protein crystals of type II topoisomerase ATPase domain/ADP (top), lysozyme (bottom left), thaumatin (bottom right) grown on-chip. (Figure adapted from Hansen *et al.*, 2002).[42]

The advantage of both counter-diffusion and free interface diffusion as crystallization techniques is the range of phase space covered by a single trial. Hybrid strategies that combine free interface diffusion with the osmotic control of vapor diffusion have also been reported to further extend this range.[51]

Beyond conversion of existing crystallization to the microscale, microfluidic technology has also enabled high throughput pre-crystallization screening efforts. Whereas crystallization screening experiments may need to incubate for days or weeks, a fast "solubility fingerprint" can be obtained in order to narrow down the window of phase space for further examination. A highly integrated microfluidic chip was developed by the Quake group to efficiently meter in varying amounts of different precipitants or buffers, mix them quickly with the protein solution, and then examine the resulting droplet for precipitation (Figure 1.11).[15] The formulator can also be coupled with an osmotic bath for long term storage and

incubation of droplets.[53] This strategy has been used numerous times as a pre-screening method which helped to provide insight towards a more rational design of subsequent crystallization experiments.[13,141,143]

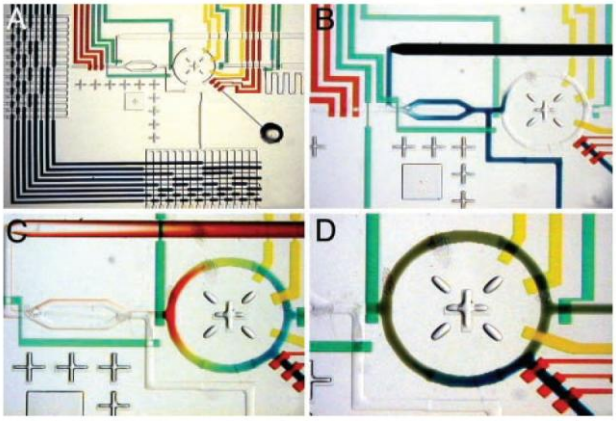

Figure 1.11. **(a)** Optical micrographs of the microfluidic formulator and accompanying ring mixer used to screen for solubility. **(b)** Metering of a chemical (blue) into the ring mixer. **(c)** The ring mixer filled with several different chemicals, as indicated by the different colors present. **(d)** The well mixed trial after ring mixer operation. (Figure adapted from Hansen *et al.*, 2004).[15]

In summary, microfluidic strategies have been developed for a wide variety of crystallization methods. While the application of these methods to membrane proteins in particular was not discussed, their efficacy has been demonstrated in many cases. One of the major challenges in adapting these platforms for the crystallization of membrane proteins is controlling wetting and surface properties of the devices in the presence of detergents and other amphiphiles. This is a challenge not only from a fluid handling perspective, but also with respect to the crystallization trial itself.[61] Because detergents and amphiphiles are critical for the solubilization and stabilization of membrane proteins unanticipated variations in their concentration due to adsorption onto the surface of the device could adversely affect a crystallization trial. Another challenge that will be addressed in Chapters 3 and 4 is the ability of microfluidics to work with highly viscous fluids, such as the lipidic mesophases used for *in meso* crystallization (Chapter 2).

1.4 Protein Crystallography

While obtaining high quality crystals is one of the major bottlenecks associated with structural biology,[8-28,30-33,61,82] the harvesting and X-ray analysis of these crystals is also non-trivial.[31,144] Protein crystallography makes use of the diffraction of X-rays through the lattice of the crystal. The theoretical resolution limit on the level of structural detail that can be resolved by diffraction is equal to half of the wavelength of light used to probe the sample.[41] Thus in order to extract atomic detail about the structure of a protein it is necessary to use X-ray radiation, the characteristic wavelengths for which are ~1Å. In a typical crystallography experiment a crystal is exposed to a beam of X-rays and the subsequent diffraction image is recorded (Figure 1.12). To fully characterize the molecular structure of the crystal the sample is rotated and additional diffraction images are taken. The resultant diffraction data can then be

analyzed and a map of the electronic density present within the crystal extracted. The three dimensional structure of a protein can be drawn from these electronic density maps.

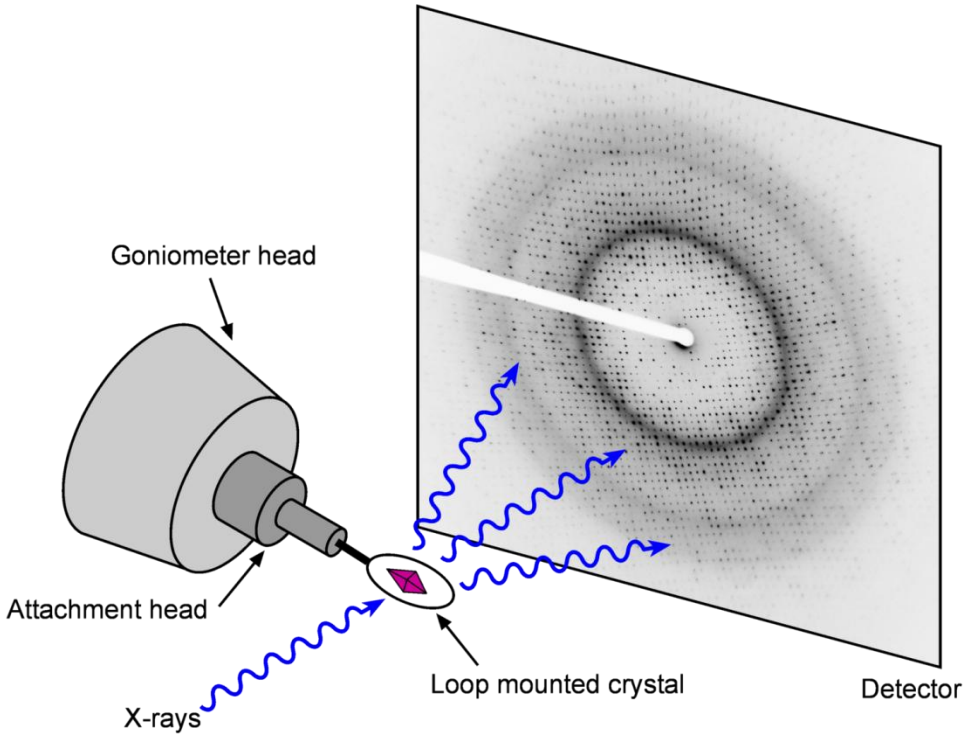

Figure 1.12. Schematic depiction of a protein crystallography setup. A loop mounted crystal has been placed on the goniometer and is exposed to the incident X-ray beam. The resultant diffraction pattern is recorded on a detector. The displayed diffraction pattern was taken of a thaumatin crystal under cryogenic conditions at the 21-ID-F beamline at the LS-CAT at the Advanced Photon Source (APS) at Argonne National Lab.

The strength and quality of the diffraction signal observed from a protein is a strong function of the internal perfection of the crystal, and cannot be determined by optical inspection.[93] While the common perception may be that crystals have a rigid internal order, as is true for ionic crystals such as NaCl or crystals of smaller organic molecules, the strength of this ordering is much weaker in protein crystals due to a smaller number of stabilizing lattice contacts relative to the total number of atoms present.[25,41] This problem is particularly exacerbated for crystals of membrane proteins grown *in surfo* where the protective band of detergent necessary for solubilizing the proteins interferes with intermolecular contacts.[145] An additional challenge in dealing with protein crystals is their high solvent content. Protein crystals typically contain 30 to 70% water, with some examples showing a water content as high as 95%.[25,41,105,145-162] The fragility and high solvent content means that protein crystals can not only be easily damaged by physical handling, but are also very susceptible to changes in their environment, dehydration in particular.[28,29,48,51,63,98,141,162,163]

As a result of this fragility and the need to insulate protein crystals from environmental effects, methods for harvesting and mounting crystals are a significant consideration for a crystallography experiment. Section 1.5 presents traditional methods for harvesting and mounting protein crystals as well

as addressing strategies for minimizing radiation damage. Section 1.6 discusses microfluidic strategies for protein crystallography that do not require harvesting crystals from a microfluidic device.

1.5 Traditional Methods for Protein Crystallography

Having overcome the challenges associated with growing high quality protein crystals, the geometry and materials of most crystallization setups prevent or limit *in situ* analysis of undisturbed crystals.[164-168] The limitations of crystallization trays come both from the geometry of the plates, the proximity of crystallization droplets and reservoir solutions, and the significant attenuation and scatter that would result from both the materials of the tray and the liquid surrounding the crystal. Therefore harvesting individual crystals has proven necessary for any significant level of X-ray analysis.

Harvesting and mounting of protein crystals is performed using either a crystal loop (Figure 1.13a) or a crystal mount (Figure 1.13b).[71,169-172] Once isolated, handling and mounting of the crystal depends on how the X-ray analysis is going to be performed. Initial screening to examine crystal quality was historically performed at room temperature, and while the collection of a complete dataset for structural analysis can be done at ambient conditions, it is more common to collect data at cryogenic conditions to minimize radiation damage and decrease molecular motion.[147,162,173-175] While a vast majority of crystallography experiments today are done completely under cryogenic conditions, some crystals and some crystallography experiments are not amenable to cryocooling and thus mounting is still done under ambient conditions.[162,176-180]

One of the big challenges in mounting a protein crystal at ambient conditions is the need to protect it against environmental shock and dehydration. Historically this has been done by mounting the crystal against the wall of a thin glass or quartz capillary using the surface tension of a thin film of mother liquor from the crystallization droplet.[169,181,182] However, this method for mounting crystals is very challenging and has a series of disadvantages: (i) Fragile crystals must be carefully manipulated and may tend to conform to the cylindrical shape of the capillary, thereby increasing the crystal mosaicity. (ii) Optical observations of a crystal in a capillary are hindered by scattering from both the capillary itself and the capillary-liquid interface. (iii) The capillary itself results in significant signal attenuation, the effects of which may be non-uniform due to different path lengths through both the capillary and the liquid holding the capillary in place. (iv) Finally, capillary mounting methods are poorly suited for cryocooling due to the significant air gap and poor heat conduction.[169] While some of these challenges can be overcome by the use of flattened capillaries or more advanced materials,[169,183] mounting crystals remains a challenge. More recent methods for crystal mounting at room temperature couple the idea of a capillary containing a humidifying volume of mother liquor with crystal mounts that were originally developed for cryogenic data collection (Figure 1.13c).[172,175,184,185]

Sample mounting for cryogenic data collection has the distinct advantage of avoiding concerns of crystal dehydration. Crystals are harvested either in a thin loop that holds the crystal in place via surface tension (Figure 1.13a)[147,169] or by a thin plastic material which supports the crystal directly (Figure

1.13b).[170-172,184] The goal here, as in room temperature mounting is to minimize both the scattering contribution of the mount itself and to minimize the volume of liquid remaining around the crystal. Once mounted, the crystals are then plunged into a cryogen such as liquid nitrogen, a cold nitrogen gas stream, or liquid propane which cools the sample at a rate fast enough to vitrify the sample into an amorphous solid, avoiding the formation of ice. However, the cooling rate necessary for vitrification is strongly dependent upon solution conditions. Most crystals must be grown or treated with a cryoprotectant solution to help prevent the formation of ice during cryocooling.[67,147,162,175]

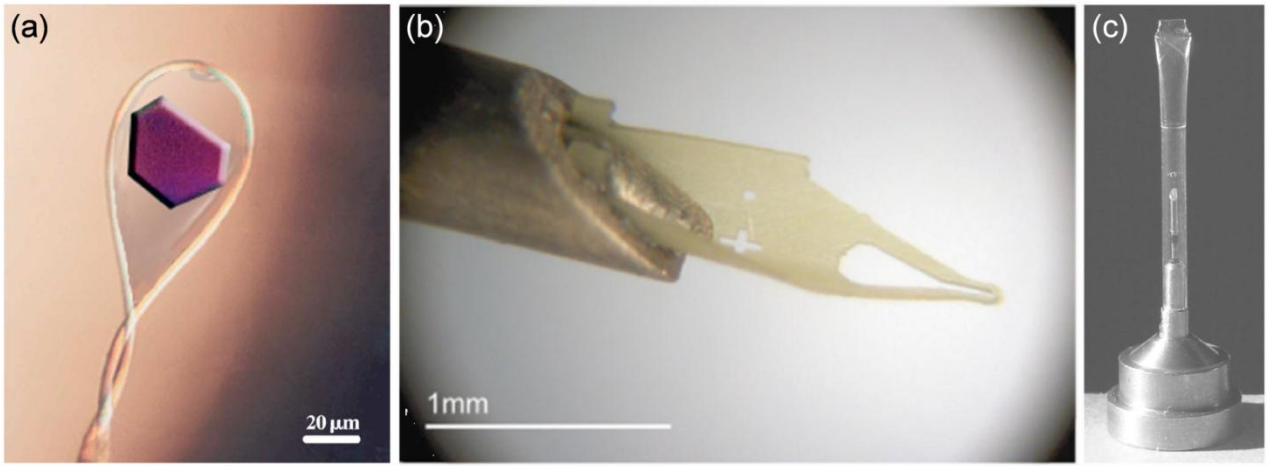

Figure 1.13. (a) An optical micrograph of a crystal of the membrane protein of bacteriorhodopsin mounted in a traditional crystal loop. **(b)** An image of a polyimide-based crystal mount from Mitegen.[172] **(c)** A photograph of a mounting setup for room temperature analysis. The crystal is harvested using a standard mount as in **(b)** and protected from dehydration by a thin plastic capillary containing a small amount of mother liquor. (Figures adapted from Qutub *et al*., 2004, Thorne *et al*., 2003, and Kalinin *et al*., 2005).[20,170,184]

The methods for mounting crystals both at ambient and at cryogenic conditions require significant skill in manipulating small, fragile samples under a microscope. These difficulties in handling are further compounded by the need to minimize handling time to avoid damaging the already sensitive crystals via environmental shock. Additionally, as structural biology efforts continue, the remaining targets of interest are increasingly likely to be proteins which have resisted crystallization and analysis previously, and may only be available in miniscule quantities. Crystallization trials for these difficult proteins may need to be performed at a very small volumetric scale and may produce only microcrystals. While brighter X-ray sources and more tightly focused beams have enabled analysis of tiny, sub-10 µm crystals,[21,24,144,186] the handling and mounting of these crystals remains a challenge.[144]

1.6 Microfluidic Methods for *In Situ* Protein Crystallography

As discussed in Section 1.3, a variety of microfluidic strategies for protein crystallization have been developed. While much of the application focus for microfluidics in structural biology has been on the screening and optimization of crystallization conditions, mounting of crystals for analysis represents the only fully manual step remaining in the structure determination pipeline.[14,23,48,55] Coupling *in situ* X-ray analysis with the high throughput screening ability of these platforms has tremendous potential not only to

decouple physical handling and environmental effects from crystal quality studies but also to enable the structure determination of otherwise recalcitrant targets.[28,29,51,63,93,125,141]

The main consideration for enabling *in situ* analysis is simply minimizing the signal attenuation and scattering profile from the microfluidic device materials, as in traditional room temperature sample mounting. However, unlike traditional mounting strategies, *in situ* analysis prevents removal of the surrounding mother liquor from the crystal. Nevertheless, the benefits of avoiding sample handling have the potential to outweigh the additional scatter and signal attenuation resulting from this liquid. Additional considerations for *in situ* analysis involve limitations on the device geometry with respect to sample mounting, translation, and rotation as well as cooling for cryogenic data collection, and the addition of various additives such as cryoprotectants or heavy atom solutions for *ab initio* structure determination.[9,13,22,23,28,51,98,120,125,126,147,162,165,175,187-190]

Within the realm of microfluidic crystallization methods, those performed in capillaries are the simplest to use for *in situ* analysis because very little adaptation is necessary to mount the sample for analysis. In the counter-diffusion method crystals are grown within an X-ray capillary.[22,23,93,98,119-121,123,191] The use of a gel within a capillary helps to completely eliminate both convective effects and the potential for crystals to move within the capillary.[22,23,98,119,120] While crystals grown via this method can be mounted directly for analysis at room temperature, cryogenic data collection requires the addition of a cryoprotectant. Because the cryoprotectant solution is added separately, rather than mixed in with the gel, the diffusive time necessary for crystals along the length of the capillary to become adequately cryoprotected can be significant.[23,93,98,119,120] A similar strategy can be used to add not only cryoprotectant, but other additives such as heavy atoms for *ab initio* structure determination.[22,23,93,98]

Crystallization in droplets can also be easily adapted for *in situ* analysis. Droplet incubation is typically done in either a glass capillary or plastic tubing, thus mounting of samples is similar to traditional capillary-based experiments.[44-47,93,100,102,104,105,110,112,140] In this example, unless the cryoprotectant is capable of diffusing through the fluorinated carrier, it would be necessary to grow the crystals under cryoprotected conditions.

Despite the fact that X-ray capillaries have a long history of use in crystallography, the capillary or tube geometry which is most efficient for crystallization trials is most likely not optimal for diffraction experiments, particularly under cryogenic conditions. For crystallization trials a long tube or capillary is desirable either to establish a long diffusive path for counter-diffusion, or to contain many droplets. However, for cryogenic data collection it is necessary not only to flash-cool the crystal of interest, but also to maintain the temperature of the crystal and the surrounding materials in order to prevent the formation of ice during data collection. To this end a coaxial laminar stream of cold nitrogen surrounded by warm dry air is used to constantly cool the sample and prevent ice formation once mounted for analysis. This cryostream is only a few millimeters in diameter and would only be able to cool a small section of a long capillary. The remaining portions of the capillary will act as a heat sink, conducting heat towards the

crystal at a rate which the cryostream may or may not be able to overcome. Therefore for long capillaries the chance for ice formation and poor cryocooling is substantially larger. To overcome these problems or geometric limitations in mounting, a large the capillary could possibly be trimmed down to merely the section of interest.[23,93]

In situ crystallography has also been demonstrated for simple counter-diffusion and droplet-based microfluidic crystallization chips where the microfluidic channel has been molded into a planar plastic substrate.[98,110,122,124,126,139] In these examples the crystallization method itself has not changed, though the physical geometry of the chip has been modified. For instance, in the counter-diffusion chip shown in

Figure 1.9e, a branching design was used to simplify loading of protein solution and minimize losses.[124,126] In another example the CrystalCard manufactured by deCODE Biosystems combines a microfluidic droplet formulator and storage channel onto a single plastic chip, improving ease of use (Figure 1.14).[110] In all of these cases the chip was fabricated from relatively thin organic plastic materials in order to minimize X-ray attenuation and scatter. While *in situ* crystallography has been demonstrated for all of these microfluidic platforms, it has been limited to noncryogenic conditions due to even more significant geometric limitations in cooling than those discussed previously in reference to long capillaries.

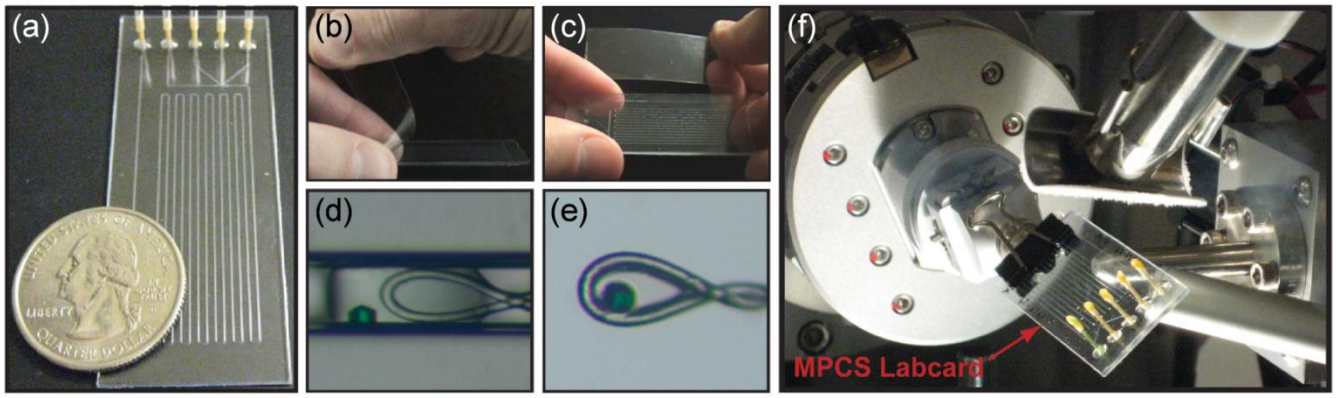

Figure 1.14. **(a)** A picture of the plastic CrystalCard produced by deCODE Biosystems, combining a microfluidic formulator and a winding storage channel. **(b-c)** The thin plastic cover being removed from the CrystalCard. **(d-e)** Optical micrographs of a crystal grown on-chip being harvested with a cryoloop. **(f)** A picture of the CrystalCard mounted on the goniometer head of an X-ray source for *in situ* analysis. (Figure adapted from Gerdts *et al.*, 2008).[110]

In situ analysis has been demonstrated for a range of different platforms, but it has been mostly limited to simple microfluidic geometries. For multilayer microfluidic devices such as the free interface diffusion chip developed by Quake and coworkers (Figure 1.10) it is necessary to use an elastomeric material such as polydimethylsiloxane (PDMS) to enable valve actuation.[13,14,42,51,130,141] PDMS, however, is a silicon-based polymer, resulting in significantly higher X-ray attenuation than organic polymers.[192] Thus when performing *in situ* analysis of crystals grown in a chip made of PDMS, the thickness of the material becomes a significant consideration.

While the functional areas of a multilayer microfluidic device (the fluid and control lines) are typically only 10 – 100 µm thick, typical fabrication procedures result in a much thicker device, up to several

millimeters, in order to provide stability and facilitate connections between the chip and external pressure control lines. Therefore in order to perform *in situ* analysis of crystals grown in a PDMS-based free interface diffusion chip a section of the device of interest needed to be punched out and then excess material needed to be trimmed away.[29,51] The resulting sample was small enough to allow both room temperature and cryogenic data collection. Although this strategy has been successful in several cases,[13,51] including the first *in situ* structure determination of a novel crystallization target using a microfluidic platform for protein crystallization,[141] it still involves significant manual sample handling and the potential for damaging crystals.

One potentially interesting application for *in situ* analysis using a multilayer microfluidic device would be for real-time crystallographic analysis that takes advantage of the active fluid control provided by microfluidic valves. This kind of study could vary from an investigation of the effects of various cryoprotectants on crystal quality to time resolved structural studies as a result of a pH or concentration gradient. However, X-ray transparency must be coupled with active microfluidic valving to enable these experiments. Additionally, geometric considerations associated with mounting the device for analysis, and the subsequent need for translation and rotation during X-ray data collection, must also be dealt with.

In summary, the ability to perform *in situ* X-ray analysis on crystals grown in microfluidic devices has been demonstrated. *In situ* analysis has been shown to allow for data collection from higher quality crystals by avoiding the potential for both physical damage and environmental shock during mounting. However, in designing a microfluidic platform for *in situ* analysis both the properties and dimensions device and the operational needs of the experiment must be carefully considered. As a result of scatter / absorption, device materials can have a significant impact on the quality of X-ray data which can be collected. Additionally, the device geometry can potentially introduce limitations in terms of mounting, translation, rotation, and cryocooling. However, the benefits of microfluidic platforms, both in terms of scale and in terms of precise fluid control, coupled with *in situ* crystallography have tremendous potential to enable the study of small fragile protein crystals for the next generation of structural biology efforts.

1.7 Summary and Key Remaining Challenges

One of the key bottlenecks in the structure determination of proteins still remains identification of appropriate crystallization conditions to grow high quality crystals for X-ray diffraction analysis.[8-25,29-33,61] Because no methods exist to predict crystallization conditions *a priori*, high throughput sparse matrix screening approaches have been adopted in order to screen a wide range of conditions.[14,30-33,42,43,45,49,61,63,68] Microfluidic platforms for crystallization have the potential to facilitate these screening efforts, not only by a reduction of the volumetric scale of the screen, but also through efficient fluid handling and by enabling crystallization methods that cannot be implemented on a larger scale.[14,15,17,32,42,44-46,49,51,53,54,61,99,100,102-105,124,126,193]

While the crystallization and structure determination of both soluble and membrane proteins has been progressing at an exponential rate, the success rate for membrane proteins is significantly slower than

that of their soluble counterparts.[78] The challenge in dealing with these membrane-bound proteins comes from their amphiphilic nature and difficulties in maintaining their functional structure upon removal from the membrane. A variety of methods, including the *in meso* method of crystallization which "solubilizes" the membrane protein in an artificial membrane rather than a detergent micelle, have been developed to overcome these difficulties. An in depth discussion of the *in meso* method will be given in Chapter 2.

Coupled with the need to maintain amphiphilic proteins in a membrane-like environment is the challenge of preparing highly viscous crystallization samples. This challenge presents particular difficulties when trying to adapt it for crystallization in microfluidic platforms. Chapter 3 develops a series of design rules for overcoming the limitations of highly viscous fluids at the microscale and Chapter 4 applies these results for the development of a microfluidic platform for *in meso* membrane protein crystallization.

Although obtaining high quality protein crystals is a significant bottleneck for structural biology efforts,[8-33,61,82] mounting crystals for X-ray analysis is also non-trivial. Membrane proteins in particular have a tendency to form only very small and fragile crystals, and the size of crystals that can be analyzed at current synchrotron facilities is becoming smaller than the crystal size which can be reasonably mounted using present methods.[21,24,144,186] Additionally, protein crystals have a very large solvent content and are particularly susceptible to dehydration and environmental shock once removed from the droplet they were grown in.[32,41,105,145-161] The ability to perform *in situ* crystallographic analysis avoids many of these difficulties and would enable structural studies of difficult proteins by facilitating the analysis of higher quality crystals by avoiding potential damage.[13,44,45,51,100,102,104,105,110,140,141] Coupling the advantages of microfluidic platforms for protein crystallization with *in situ* X-ray analysis has tremendous potential to enable not only traditional structural biology efforts, but also more advanced examinations of protein function through dynamic real-time and time resolved structural studies.

1.8 References

(1) Wu, D. Y.; Hugenholtz, P.; Mavromatis, K.; Pukall, R.; Dalin, E.; Ivanova, N. N.; Kunin, V.; Goodwin, L.; Wu, M.; Tindall, B. J.; Hooper, S. D.; Pati, A.; Lykidis, A.; Spring, S.; Anderson, I. J.; D'haeseleer, P.; Zemla, A.; Singer, M.; Lapidus, A.; Nolan, M.; Copeland, A.; Han, C.; Chen, F.; Cheng, J. F.; Lucas, S.; Kerfeld, C.; Lang, E.; Gronow, S.; Chain, P.; Bruce, D.; Rubin, E. M.; Kyrpides, N. C.; Klenk, H. P.; Eisen, J. A. *Nature* **2009**, *462*, 1056.

(2) NCBI Genome Entrez Database. http://www.ncbi.nlm.nih.gov/sites/genome (May 13, 2010).

(3) Swiss-Prot Protein Knowledgebase. http://ca.expasy.org/sprot/ (May 13, 2010).

(4) Service, R. *Science* **2005**, *307*, 1554.

(5) Mancia, F.; Love, J. *Journal of Structural Biology*, *In Press, Corrected Proof*.

(6) RCSB Protein Data Bank. http://www.rcsb.org/ (July 11, 2010).

(7) Baker, M. *Nat Methods* **2010**, *7*, 429.

(8) Collingsworth, P. D.; Bray, T. L.; Christopher, G. K. *J Cryst Growth* **2000**, *219*, 283.

(9) Durbin, S. D.; Feher, G. *Annu Rev Phys Chem* **1996**, *47*, 171.

(10) Talreja, S.; Kenis, P. J. A.; Zukoski, C. F. *Langmuir* **2007**, *23*, 4516.

(11) Talreja, S.; Kim, D. Y.; Mirarefi, A. Y.; Zukoski, C. F.; Kenis, P. J. A. *J Appl Crystallogr* **2005**, *38*, 988.

(12) Yoshizaki, I.; Nakamura, H.; Sato, T.; Igarashi, N.; Komatsu, H.; Yoda, S. *J Cryst Growth* **2002**, *237*, 295.

(13) Anderson, M. J.; Hansen, C. L.; Quake, S. R. *P Natl Acad Sci USA* **2006**, *103*, 16746.

(14) Hansen, C.; Quake, S. R. *Current Opinion in Structural Biology* **2003**, *13*, 538.

(15) Hansen, C. L.; Sommer, M. O. A.; Quake, S. R. *P Natl Acad Sci USA* **2004**, *101*, 14431.

(16) Lounaci, M.; Rigolet, P.; Abraham, C.; Le Berre, M.; Chen, Y. *Microelectron Eng* **2007**, *84*, 1758.

(17) Zheng, B.; Roach, L. S.; Ismagilov, R. F. *J Am Chem Soc* **2003**, *125*, 11170.

(18) Zhou, X.; Lau, L.; Lam, W. W. L.; Au, S. W. N.; Zheng, B. *Anal. Chem.* **2007**.

(19) Cherezov, V.; Caffrey, M. *J Appl Crystallogr* **2003**, *36*, 1372.

(20) Qutub, Y.; Reviakine, I.; Maxwell, C.; Navarro, J.; Landau, E. M.; Vekilov, P. G. *J Mol Biol* **2004**, *343*, 1243.

(21) Rummel, G.; Hardmeyer, A.; Widmer, C.; Chiu, M. L.; Nollert, P.; Locher, K. P.; Pedruzzi, I.; Landau, E. M.; Rosenbusch, J. P. *Journal of Structural Biology* **1998**, *121*, 82.

(22) Gavira, J. A.; Toh, D.; Lopez-Jaramillo, J.; Garcia-Ruiz, J. M.; Ng, J. D. *Acta Crystallogr D* **2002**, *58*, 1147.

(23) Ng, J. D.; Gavira, J. A.; Garcia-Ruiz, J. M. *Journal of Structural Biology* **2003**, *142*, 218.

(24) Stevens, R. C. *Current Opinion in Structural Biology* **2000**, *10*, 558.

(25) McPherson, A. In *Current Topics in Membranes, Volume 63*; Volume 63 ed.; DeLucas, L., Ed.; Academic Press: 2009, p 5.

(26) Gabrielsen, M.; Gardiner, A. T.; Fromme, P.; Cogdell, R. J. In *Current Topics in Membranes, Volume 63*; Volume 63 ed.; DeLucas, L., Ed.; Academic Press: 2009, p 127.

(27) Page, R. In *Methods in Molecular Biology: Structural Proteomics - High Throughput Methods*; Kobe, B., Guss, M., Huber, T., Eds.; Humana Press: Totowa, NJ, 2008; Vol. 426, p 345.

(28) Caffrey, M. *Ann Rev Biophys* **2009**, *38*, 29.

(29) Doerr, A. *Nat Methods* **2006**, *3*, 244.

(30) Brostromer, E.; Nan, J.; Li, L.-F.; Su, X.-D. *Biochemical and Biophysical Research Communications* **2009**, *386*, 634.

(31) Newman, J.; Fazio, V. J.; Lawson, B.; Peat, T. S. *Cryst Growth Des* **2010**, *10*, 2785.

(32) Li, G.; Chen, Q.; Li, J.; Hu, X.; Zhao, J. *Anal Chem* **2010**, *82*, 4362.

(33) Jia, Y.; Liu, X.-Y. *The Journal of Physical Chemistry B* **2006**, *110*, 6949.

(34) Wallin, E.; von Heijne, G. *Protein Sci* **1998**, *7*, 1029.

(35) Willis, M. S.; Koth, C. M. In *Methods in Molecular Biology: Structural Proteomics - High Throughput Methods*; Kobe, B., Guss, M., Huber, T., Eds.; Humana Press: Totowa, NJ, 2008; Vol. 426, p 277.

(36) Michel, H. *Trends Biochem Sci* **1983**, *8*, 56.

(37) Quick, M.; Javitch, J. A. *P Natl Acad Sci USA* **2007**, *104*, 3603.

(38) Trubetskoy, V. S.; Burke, T. J. *Am Lab* **2005**, *37*, 19.

(39) Kulkarni, C. V. 2010; Vol. 12, p 237.

(40) Wootton, J. C. *Current Opinion in Structural Biology* **1994**, *4*, 413.

(41) McPherson, A. *Crystallization of Biological Macromolecules*; CSHL Press, 1999.

(42) Hansen, C. L.; Skordalakes, E.; Berger, J. M.; Quake, S. R. *P Natl Acad Sci USA* **2002**, *99*, 16531.

(43) He, G. W.; Bhamidi, V.; Tan, R. B. H.; Kenis, P. J. A.; Zukoski, C. F. *Cryst Growth Des* **2006**, *6*, 1175.

(44) Zheng, B.; Tice, J. D.; Roach, L. S.; Ismagilov, R. F. *Angew Chem Int Edit* **2004**, *43*, 2508.

(45) Zheng, B.; Gerdts, C. J.; Ismagilov, R. F. *Current Opinion in Structural Biology* **2005**, *15*, 548.
(46) Li, L.; Mustafi, D.; Fu, Q.; Tereshko, V.; Chen, D. L. L.; Tice, J. D.; Ismagilov, R. F. *P Natl Acad Sci USA* **2006**, *103*, 19243.
(47) Song, H.; Chen, D. L.; Ismagilov, R. F. *Angew Chem Int Edit* **2006**, *45*, 7336.
(48) van der Woerd, M.; Ferree, D.; Pusey, M. *Journal of Structural Biology* **2003**, *142*, 180.
(49) Hansen, C. L.; Quake, S. R.; Berger, J. M. US, 2007.
(50) Chan, P. H.; Su, Y. C. *J Micromech Microeng* **2007**, *17*, 642.
(51) Hansen, C. L.; Classen, S.; Berger, J. M.; Quake, S. R. *J Am Chem Soc* **2006**, *128*, 3142.
(52) Korczynska, J.; Hu, T. C.; Smith, D. K.; Jenkins, J.; Lewis, R.; Edwards, T.; Brzozowski, A. M. *Acta Crystallogr D* **2007**, *63*, 1009.
(53) Lau, B. T. C.; Baitz, C. A.; Dong, X. P.; Hansen, C. L. *J Am Chem Soc* **2007**, *129*, 454.
(54) Zheng, B.; Ismagilov, R. F. *Angew Chem Int Edit* **2005**, *44*, 2520.
(55) Cherezov, V.; Peddi, A.; Muthusubramaniam, L.; Zheng, Y. F.; Caffrey, M. *Acta Crystallogr D* **2004**, *60*, 1795.
(56) Shim, J. U.; Cristobal, G.; Link, D. R.; Thorsen, T.; Jia, Y.; Piattelli, K.; Fraden, S. *J Am Chem Soc* **2007**, *129*, 8825.
(57) Faham, S.; Bowie, J. U. *J Mol Biol* **2002**, *316*, 1.
(58) Faham, S.; Boulting, G. L.; Massey, E. A.; Yohannan, S.; Yang, D.; Bowie, J. U. *Protein Sci* **2005**, *14*, 836.
(59) Garcia-Ruiz, J. M.; Otalora, F.; Novella, M. L.; Gavira, J. A.; Sauter, C.; Vidal, O. *J Cryst Growth* **2001**, *232*, 149.
(60) Sauter, C.; Otalora, F.; Gavira, J. A.; Vidal, O.; Giege, R.; Garcia-Ruiz, J. M. *Acta Crystallogr D* **2001**, *57*, 1119.
(61) Li, L.; Ismagilov, R. F. *Ann Rev Biophys* **2010**.
(62) Govada, L.; Carpenter, L.; da Fonseca, P. C. A.; Helliwell, J. R.; Rizkallah, P.; Flashman, E.; Chayen, N. E.; Redwood, C.; Squire, J. M. *J Mol Biol* **2008**, *378*, 387.
(63) Leng, J.; Salmon, J.-B. *Lab Chip* **2009**, *9*, 24.
(64) Lorber, B.; Delucas, L. J.; Bishop, J. B. *J Cryst Growth* **1991**, *110*, 103.
(65) Talreja, S.; Perry, S. L.; Guha, S.; Bhamidi, V.; Zukoski, C. F.; Kenis, P. J. A. *The Journal of Physical Chemistry B* **2010**, *114*, 4432.
(66) Chayen, N. E. *Current Opinion in Structural Biology* **2004**, *14*, 577.
(67) Newby, Z. E. R.; O'Connell, J. D.; Gruswitz, F.; Hays, F. A.; Harries, W. E. C.; Harwood, I. M.; Ho, J. D.; Lee, J. K.; Savage, D. F.; Miercke, L. J. W.; Stroud, R. M. **2009**, *4*, 619.
(68) Newman, J.; Xu, J.; Willis, M. C. *Acta Crystallographica Section D* **2007**, *63*, 826.
(69) Hunte, C.; Richers, S. *Current Opinion in Structural Biology* **2008**, *18*, 406.
(70) Chayen, N. E.; Saridakis, E. **2008**, *5*, 147.
(71) Nollert, P.; Navarro, J.; Landau, E. M. *Method Enzymol* **2002**, *343*, 183.
(72) Rosenbusch, J. P. *Journal of Structural Biology* **1990**, *104*, 134.
(73) Garavito, R. M.; Picot, D. *Methods* **1990**, *1*, 57.
(74) Landau, E. M.; Rosenbusch, J. P. *P Natl Acad Sci USA* **1996**, *93*, 14532.
(75) Pebay-Peyroula, E.; Rummel, G.; Rosenbusch, J. P.; Landau, E. M. *Science* **1997**, *277*, 1676.
(76) Kendrew, J. C.; Bodo, G.; Dintzis, H. M.; Parrish, R. G.; Wyckoff, H.; Phillips, D. C. **1958**, *181*, 662.
(77) Kendrew, J. C.; Dickerson, R. E.; Strandberg, B. E.; Hart, R. G.; Davies, D. R.; Phillips, D. C.; Shore, V. C. *Nature* **1960**, *185*, 422.
(78) White, S. H. *Protein Sci* **2004**, *13*, 1948.
(79) Deisenhofer, J.; Epp, O.; Miki, K.; Huber, R.; Michel, H. *Nature* **1985**, *318*, 618.

(80) Membrane Proteins of Known 3D Structure. http://blanco.biomol.uci.edu/Membrane_Proteins_xtal.html (July 11, 2010).

(81) Arinaminpathy, Y.; Khurana, E.; Engelman, D. M.; Gerstein, M. B. *Drug Discovery Today* **2009**, *14*, 1130.

(82) Dauter, Z.; Lamzin, V. S.; Wilson, K. S. *Current Opinion in Structural Biology* **1997**, *7*, 681.

(83) Seddon, A. A.; Curnow, P.; Booth, P. J. *Bba-Biomembranes* **2004**, *1666*, 105.

(84) Pecina, P.; Houstkova, H.; Hansikova, H.; Zeman, J.; Houstek, J. *Physiol Res* **2004**, *53*, S213.

(85) Overington, J. P.; Al-Lazikani, B.; Hopkins, A. L. *Nat Rev Drug Discov* **2006**, *5*, 993.

(86) *Crystal Growth Techniques*; Hampton Research, 2001.

(87) Chayen, N. E. *Acta Crystallogr D* **1998**, *54*, 8.

(88) Luft, J. R.; Collins, R. J.; Fehrman, N. A.; Lauricella, A. M.; Veatch, C. K.; DeTitta, G. T. *Journal of Structural Biology* **2003**, *142*, 170.

(89) May, A. P.; Segelke, B. W. In *Methods in Molecular Biology: Structural Proteomics - High Throughput Methods*; Kobe, B., Guss, M., Huber, T., Eds.; Humana Press: Totowa, NJ, 2008; Vol. 426, p 387.

(90) Chayen, N. E.; Stewart, P. D. S.; Blow, D. M. *J Cryst Growth* **1992**, *122*, 176.

(91) Chayen, N. E.; Stewart, P. D. S.; Maeder, D. L.; Blow, D. M. *J Appl Crystallogr* **1990**, *23*, 297.

(92) Brumshtein, B.; Greenblatt, H. M.; Futerman, A. H.; Silman, I.; Sussman, J. L. *J Appl Crystallogr* **2008**, *41*, 969.

(93) Ng, J. D.; Stevens, R. C.; Kuhn, P. In *Methods in Molecular Biology: Structural Proteomics - High Throughput Methods*; Kobe, B., Guss, M., Huber, T., Eds.; Humana Press: Totowa, NJ, 2008; Vol. 426, p 363.

(94) Johansson, L. C.; Wöhri, A. B.; Katona, G.; Engström, S.; Neutze, R. *Current Opinion in Structural Biology* **2009**, *19*, 372.

(95) Hampel, A.; Labanaus.M; Connors, P. G.; Kirkegar.L; Rajbhand.Ul; Sigler, P. B.; Bock, R. M. *Science* **1968**, *162*, 1384.

(96) XZ™ Dialysis Plate for Crystallography and Sample Preparation. http://www.gnbiosystems.com/ (June 14, 2010).

(97) Kundrot, C. E.; Judge, R. A.; Pusey, M. L.; Snell, E. H. *Cryst Growth Des* **2001**, *1*, 87.

(98) Otálora, F.; Gavira, J. A.; Ng, J. D.; García-Ruiz, J. M. *Progress in Biophysics and Molecular Biology* **2009**, *101*, 26.

(99) Li, L.; Du, W.; Ismagilov, R. F. *J Am Chem Soc* **2009**.

(100) Zheng, B.; Tice, J. D.; Ismagilov, R. F. *Adv Mater* **2004**, *16*, 1365.

(101) Zheng, B.; Tice, J. D.; Ismagilov, R. F. *Anal Chem* **2004**, *76*, 4977.

(102) Yadav, M. K.; Gerdts, C. J.; Sanishvili, R.; Smith, W. W.; Roach, L. S.; Ismagilov, R. F.; Kuhn, P.; Stevens, R. C. *J Appl Crystallogr* **2005**, *38*, 900.

(103) Chen, D. L.; Gerdts, C. J.; Ismagilov, R. F. *J Am Chem Soc* **2005**, *127*, 9672.

(104) Chen, D. L. L.; Ismagilov, R. F. *Curr Opin Chem Biol* **2006**, *10*, 226.

(105) Gerdts, C. J.; Tereshko, V.; Yadav, M. K.; Dementieva, I.; Collart, F.; Joachimiak, A.; Stevens, R. C.; Kuhn, P.; Kossiakoff, A.; Ismagilov, R. F. *Angew Chem Int Edit* **2006**, *45*, 8156.

(106) Chen, D. L. L.; Li, L.; Reyes, S.; Adamson, D. N.; Ismagilov, R. F. *Langmuir* **2007**, *23*, 2255.

(107) Laval, P.; Salmon, J. B.; Joanicot, M. *J Cryst Growth* **2007**, *303*, 622.

(108) Dombrowski, R. D.; Litster, J. D.; Wagner, N. J.; He, Y. *Chem Eng Sci* **2007**, *62*, 4802.

(109) Maki, S.; Murai, R.; Yoshikawa, H. Y.; Kitatani, T.; Nakata, S.; Kawahara, H.; Hasenaka, H.; Kobayashi, A.; Okada, S.; Sugiyama, S.; Adachi, H.; Matsumura, H.; Takano, K.; Murakami, S.; Inoue, T.; Sasaki, T.; Mori, Y. *J Synchrotron Radiat* **2008**, *15*, 269.

(110) Gerdts, C. J.; Elliott, M.; Lovell, S.; Mixon, M. B.; Napuli, A. J.; Staker, B. L.; Nollert, P.; Stewart, L. *Acta Crystallographica Section D* **2008**, *64*, 1116.

(111) Salmon, J.-B.; Leng, J. *Comptes Rendus Chimie* **2009**, *12*, 258.
(112) Kreutz, J. E.; Li, L.; Roach, L. S.; Hatakeyama, T.; Ismagilov, R. F. *J Am Chem Soc* **2009**, *131*, 6042.
(113) Du, W.; Li, L.; Nichols, K. P.; Ismagilov, R. F. *Lab Chip* **2009**, *9*, 2286.
(114) Pang, Y.; Liu, J.; Li, H.; Lin, J. *Science in China Series B: Chemistry* **2009**, *52*, 1014.
(115) Luft, J. R.; Rak, D. M.; DeTitta, G. T. *J Cryst Growth* **1999**, *196*, 450.
(116) Steinert, C. P.; Mueller-Dieckmann, J.; Weiss, M.; Roessle, M.; Zengerle, R.; Koltay, P. In *Future Generation Communication and Networking* 2007, p 561.
(117) Lounaci, M.; Rigolet, P.; Casquillas, G. V.; Huang, H. W.; Chen, Y. *Microelectron Eng* **2006**, *83*, 1673.
(118) Shim, J. U.; Cristobal, G.; Link, D. R.; Thorsen, T.; Fraden, S. *Cryst Growth Des* **2007**, *7*, 2192.
(119) Lopez-Jaramillo, F. J.; Garcia-Ruiz, J. M.; Gavira, J. A.; Otalora, F. *J Appl Crystallogr* **2001**, *34*, 365.
(120) Garcia-Ruiz, J. M.; Gonzalez-Ramirez, L. A.; Gavira, J. A.; Otalora, F. *Acta Crystallogr D* **2002**, *58*, 1638.
(121) Bolanos-Garcia, V. M. *J Cryst Growth* **2003**, *253*, 517.
(122) Ng, J. D.; Clark, P. J.; Stevens, R. C.; Kuhn, P. *Acta Crystallographica Section D* **2008**, *64*, 189.
(123) Ng, J. D.; Garcia-Ruiz, J. M.; Gavira-Gallardo, J. A.; Wells, M.; Jenkins, G. US, 2006.
(124) Dhouib, K.; Malek, C. K.; Pfleging, W.; Gauthier-Manuel, B.; Duffait, R.; Thuillier, G.; Ferrigno, R.; Jacquamet, L.; Ohana, J.; Ferrer, J.-L.; Theobald-Dietrich, A.; Giege, R.; Lorber, B.; Sauter, C. *Lab Chip* **2009**, *9*, 1412.
(125) Sugahara, M.; Kageyama, Y.; Kunishima, N. *J Appl Crystallogr* **2009**, *42*, 129.
(126) Sauter, C.; Dhouib, K.; Lorber, B. *Crystal Growth and Design* **2007**, *7*, 2247.
(127) Kothe, M.; Kohls, D.; Low, S.; Coli, R.; Cheng, A. C.; Jacques, S. L.; Johnson, T. L.; Lewis, C.; Loh, C.; Nonomiya, J.; Sheils, A. L.; Verdries, K. A.; Wynn, T. A.; Kuhn, C.; Ding, Y. H. *Biochemistry-Us* **2007**, *46*, 5960.
(128) Sugahara, M.; Asada, Y.; Morikawa, Y.; Kageyama, Y.; Kunishima, N. *Acta Crystallogr D* **2008**, *64*, 686.
(129) Xia, Y. N.; Whitesides, G. M. *Angew Chem Int Edit* **1998**, *37*, 551.
(130) Unger, M. A.; Chou, H. P.; Thorsen, T.; Scherer, A.; Quake, S. R. *Science* **2000**, *288*, 113.
(131) Schudel, B. R.; Choi, C. J.; Cunningham, B. T.; Kenis, P. J. A. *Lab Chip* **2009**, *9*, 1676.
(132) Chou, H. P.; Unger, M. A.; Quake, S. R. *Biomedical Microdevices* **2001**, *3*, 323.
(133) Rogers, J. A.; Nuzzo, R. G. *Materials Today* **2005**, *8*, 50.
(134) Grover, W. H.; Skelley, A. M.; Liu, C. N.; Lagally, E. T.; Mathies, R. A. *Sensor Actuat B-Chem* **2003**, *89*, 315.
(135) Li, L.; Du, W.; Ismagilov, R. *J Am Chem Soc* **2009**.
(136) Laval, P.; Lisai, N.; Salmon, J. B.; Joanicot, M. *Lab Chip* **2007**, *7*, 829.
(137) Selimovic, S.; Gobeaux, F.; Fraden, S. *Lab Chip* **2010**, *10*, 1696.
(138) Selimovic, S.; Jia, Y. W.; Fraden, S. *Cryst Growth Des* **2009**, *9*, 1806.
(139) The Crystal Former. http://www.microlytic.com (June 16, 2010).
(140) Gerdts, C.; Nollert, P. In *Current Topics in Membranes, Volume 63*; Volume 63 ed.; DeLucas, L., Ed.; Academic Press: 2009, p 179.
(141) Anderson, M. J.; DeLaBarre, B.; Raghunathan, A.; Palsson, B. O.; Brunger, A. T.; Quake, S. R. *Biochemistry-Us* **2007**, *46*, 5722.
(142) Fluidigm Corporation. http://www.fluidigm.com/ (June 17, 2010).
(143) Sommer, M. O. A.; Larsen, S. *J Synchrotron Radiat* **2005**, *12*, 779.

(144) Cherezov, V.; Hanson, M. A.; Griffith, M. T.; Hilgart, M. C.; Sanishvili, R.; Nagarajan, V.; Stepanov, S.; Fischetti, R. F.; Kuhn, P.; Stevens, R. C. *Journal of The Royal Society Interface* **2009**, *6*, S587.

(145) Hunte, C.; Michel, H. *Current Opinion in Structural Biology* **2002**, *12*, 503.

(146) Matthews, B. W. *J Mol Biol* **1968**, *33*, 491.

(147) Garman, E. F.; Schneider, T. R. *J Appl Crystallogr* **1997**, *30*, 211.

(148) Asherie, N.; Jakoncic, J.; Ginsberg, C.; Greenbaum, A.; Stojanoff, V.; Hrnjez, B. J.; Blass, S.; Berger, J. *Cryst Growth Des* **2009**.

(149) Pentelute, B. L.; Gates, Z. P.; Tereshko, V.; Dashnau, J. L.; Vanderkooi, J. M.; Kossiakoff, A. A.; Kent, S. B. H. *J Am Chem Soc* **2008**, *130*, 9695.

(150) Cherezov, V.; Yamashita, E.; Liu, W.; Zhalnina, M.; Cramer, W. A.; Caffrey, M. *J Mol Biol* **2006**, *364*, 716.

(151) Cherezov, V.; Clogston, J.; Papiz, M. Z.; Caffrey, M. *J Mol Biol* **2006**, *357*, 1605.

(152) Li, L.; Nachtergaele, S.; Seddon, A. M.; Tereshko, V.; Ponomarenko, N.; Ismagilov, R. F. *J Am Chem Soc* **2008**, *130*, 14324.

(153) Feher, G.; Kam, Z. *Methods in Enzymology* **1985**, *114*, 77.

(154) Abramson, J.; Riistama, S.; Larsson, G.; Jasaitis, A.; Svensson-Ek, M.; Laakkonen, L.; Puustinen, A.; Iwata, S.; Wikstrom, M. *Nat Struct Biol* **2000**, *7*, 910.

(155) Fei, M. J.; Yamashita, E.; Inoue, N.; Yao, M.; Yamaguchi, H.; Tsukihara, T.; Shinzawa-Ito, K.; Nakashima, R.; Yoshikawa, S. *Acta Crystallogr D* **2000**, *56*, 529.

(156) Liu, B.; Chen, Y.; Doukov, T.; Soltis, S. M.; Stout, C. D.; Fee, J. A. *Biochemistry-Us* **2009**, *48*, 820.

(157) Ostermeier, C.; Harrenga, A.; Ermler, U.; Michel, H. *P Natl Acad Sci USA* **1997**, *94*, 10547.

(158) Tsukihara, T.; Aoyama, H.; Yamashita, E.; Tomizaki, T.; Yamaguchi, H.; Shinzawaitoh, K.; Nakashima, R.; Yaono, R.; Yoshikawa, S. *Science* **1995**, *269*, 1069.

(159) Jaakola, V. P.; Griffith, M. T.; Hanson, M. A.; Cherezov, V.; Chien, E. Y. T.; Lane, J. R.; IJzerman, A. P.; Stevens, R. C. *Science* **2008**, *322*, 1211.

(160) Lorber, B.; Witz, J. *Cryst Growth Des* **2008**, *8*, 1522.

(161) Urbani, A.; Gemeinhardt, S.; Warne, A.; Saraste, M. *Febs Lett* **2001**, *508*, 29.

(162) Juers, D. H.; Matthews, B. W. *Q Rev Biophys* **2004**, *37*, 105.

(163) Caffrey, M. *Journal of Structural Biology* **2003**, *142*, 108.

(164) Agirre, J.; Mechaly, A.; Cabo-Bilbao, A.; GuÃ©rin, D. *European Biophysics Journal* **2008**, *37*, 871.

(165) Jacquamet, L.; Ohana, J.; Joly, J.; Borel, F.; Pirocchi, M.; Charrault, P.; Bertoni, A.; Israel-Gouy, P.; Carpentier, P.; Kozielski, F.; Blot, D.; Ferrer, J. L. *Structure* **2004**, *12*, 1219.

(166) Durst, R. D.; He, B. B.; (Bruker Axs, Inc., USA). US, 2003.

(167) Lehmann, C. W.; (Studiengesellschaft Kohle m.b.H., Germany). US, 2003.

(168) McRee, D.; Tari, L.; (Takeda San Diego, Inc., USA). US, 2006.

(169) Teng, T.-Y. *J Appl Crystallogr* **1990**, *23*, 387.

(170) Thorne, R. E.; Stum, Z.; Kmetko, J.; O'Neill, K.; Gillilan, R. *J Appl Crystallogr* **2003**, *36*, 1455.

(171) Thorne, R. E.; Stum, Z.; O'Neill, K.; Kmetko, J.; Cornell Research Foundation, Inc.: US, 2007.

(172) Mitigen. http://www.mitegen.com/ (July 8, 2010).

(173) Garman, E. *Acta Crystallographica Section D* **2010**, *66*, 339.

(174) Nave, C.; Garman, E. F. *J Synchrotron Radiat* **2005**, *12*, 257.

(175) Alcorn, T.; Juers, D. H. *Acta Crystallographica Section D* **2010**, *66*, 366.

(176) Ren, Z.; Bourgeois, D.; Helliwell, J. R.; Moffat, K.; Srajer, V.; Stoddard, B. L. *J Synchrotron Radiat* **1999**, *6*, 891.

(177) Baxter, R. H. G.; Ponomarenko, N.; Å rajer, V.; Pahl, R.; Moffat, K.; Norris, J. R. *P Natl Acad Sci USA* **2004**, *101*, 5982.
(178) Bourgeois, D.; Schotte, F.; Brunori, M.; Vallone, B. *Photoch Photobio Sci* **2007**, *6*, 1047.
(179) Hedman, B.; Hodgson, K. O.; Helliwell, J. R.; Liddington, R.; Papiz, M. Z. *P Natl Acad Sci USA* **1985**, *82*, 7604.
(180) Schlichting, I. *Accounts of Chemical Research* **2000**, *33*, 532.
(181) King, M. *Acta Crystallographica* **1954**, *7*, 601.
(182) Basavappa, R.; Petri, E. T.; Tolbert, B. S. *J Appl Crystallogr* **2003**, *36*, 1297.
(183) Kalinin, Y.; Thorne, R. *Acta Crystallogr D* **2005**, *61*, 1528.
(184) Kalinin, Y.; Kmetko, J.; Bartnik, A.; Stewart, A.; Gillilan, R.; Lobkovsky, E.; Thorne, R. *J Appl Crystallogr* **2005**, *38*, 333.
(185) Mac Sweeney, A.; D'Arcy, A. *J Appl Crystallogr* **2003**, *36*, 165.
(186) Cusack, S.; Belrhali, H.; Bram, A.; Burghammer, M.; Perrakis, A.; Riekel, C. *Nat Struct Biol* **1998**, *5*, 634.
(187) Newman, J. *Acta Crystallogr D* **2006**, *62*, 27.
(188) Benvenuti, M.; Mangani, S. *Nat Protoc* **2007**, *2*, 1633.
(189) Matthews, B. W. *Protein Sci* **2009**, *18*, 1135.
(190) Caffrey, M.; Cherezov, V. **2009**, *4*, 706.
(191) Mirkin, N.; Moreno, A. *J. Mex. Chem. Soc.* **2005**, *49*, 39.
(192) Greaves, E. D.; Manz, A. *Lab Chip* **2005**, *5*, 382.
(193) Hansen, C. L.; Quake, S. R.; Berger, J. M.; California Institute of Technology: US, 2007.

Chapter 2

In Meso Membrane Protein Crystallization

2.1 The Challenge of Amphiphilic Membrane Proteins

Membrane proteins represent one of the most important classes of proteins. These membrane-bound proteins are typically responsible for material and energy transduction across cellular membranes as well as cell signaling.[1-7] Because the function of these proteins is so critical for cellular operation, their malfunction can have serious consequences and has been linked to a variety of diseases including diabetes, cirrhosis of the liver, cystic fibrosis, cancer, Alzheimer's disease, hypertension, epilepsy, cataract, tubulopathy, leukodystrophy, Leigh syndrome, anemia, sensorineural deafness, and hypertrophic cardiomyopathy.[5,6,8] Furthermore, modulation of cellular function by pharmacological treatment of membrane proteins has tremendous therapeutic potential. In fact, at least 60% of the drugs currently available are thought to target membrane proteins.[9-11] In all of these cases, knowledge of the three-dimensional structure of these proteins would dramatically improve our understanding of not only their biological function, but could also allow for the rational design of medical treatments.[12]

Membrane proteins present significant challenges to the study of their function. Obtaining large quantities of membrane proteins through over-expression is often difficult because these proteins are localized within the cellular membrane.[9,12-20] These membranes have a limited capacity and are already crowded with naturally occurring membrane proteins that are necessary for cellular function.[14,21-24] Additionally, different organisms may have different membrane properties. For instance, the simple peripheral inner membrane such as the one in *E. coli* provides a relatively small volume for the sequestration of over-expressed membrane proteins (Figure 2.1a). This is particularly challenging because of the ease by which *E. coli* can otherwise be used for genetic manipulation and protein expression.[18] Other organisms such as *Rhodobacter* have a much larger inner membrane structure, and are therefore able to accommodate much larger quantities of membrane proteins (Figure 2.1b), but might not be as commonly used for protein expression.[14,25] Expression of membrane proteins at too high of a level can also result in aggregation of the expressed protein as inclusion bodies or even cell death,[9,14-18,25-31] and while strategies exist to refold aggregated proteins, there is no guarantee as to the quality of the refolding.[26-28,30] Over-expression of proteins is also often done in a heterologous fashion, leading to additional potential challenges such as misfolding and post-translational modifications when the host organism lacks the necessary cellular machinery or lipid environment to process the protein into its final form.[9,15,16,18,31]

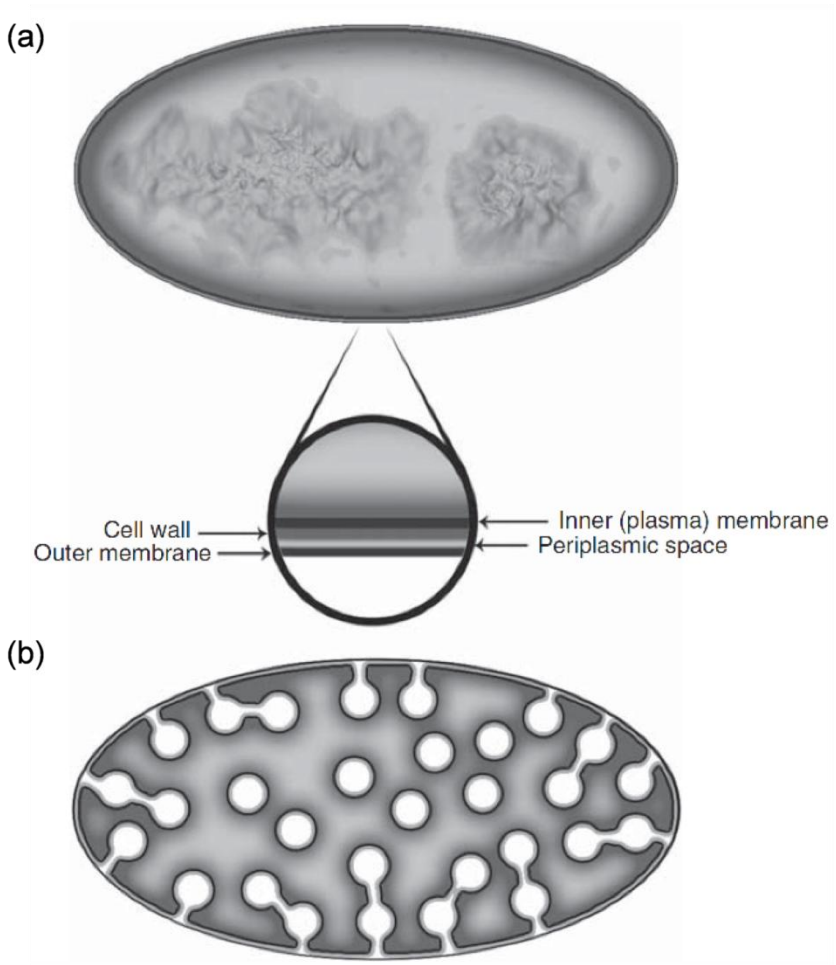

Figure 2.1. Membrane morphologies of prokaryotic cells. **(a)** The volume of the inner membrane in *E. coli* available for accommodating membrane proteins is relatively small (~3%), posing a serious limitation in the available membrane volume for over-expressed membrane proteins. **(b)** Some organisms such as *Rhodobacter* have a much larger inner membrane area and are better able to sequester large quantities of over-expressed membrane proteins. (Figure adapted from Hanson *et al.,* 2009).[14]

In addition to challenges with expression, the amphiphilicity of membrane proteins also causes difficulties with purification and crystallization.[4,20,32-34] Because isolation of cellular membranes from the soluble portions of a cell is relatively straightforward, the main goal of purification is to separate the desired membrane protein from the many other proteins sequestered within the cellular membrane.[18] However, the majority of strategies to perform this separation require the dissolution of these proteins.[4,18,35-38] Because membrane proteins have both hydrophobic and hydrophilic portions they will not readily dissolve into either a polar or an apolar solvent on their own.[13,16,20,34,37,39,40] To overcome this challenge, membrane proteins are typically solubilized in detergent-containing solution.[11-13,16,18-20,31,32,34-37,39,41,42] The use of a detergent solution above the critical micelle concentration (CMC) allows for engulfment of the hydrophobic portion of the membrane protein within a protective detergent micelle while the hydrophilic ends of the protein and the external surface of the detergent micelle present a fully hydrophilic surface. While this detergent micelle is capable of protecting the hydrophobic surface of a membrane protein from deleterious interactions with an aqueous solution, it does not replicate the native

membrane environment of the protein. Many membrane proteins suffer from denaturation upon removal from their native membrane because the solubilizing detergent micelles are unable to maintain the necessary level of lateral pressure on the protein so it can maintain its functional conformation.[6,7,11,12,14,31,34-37,40,42-44]

Although current methods for protein purification may make detergent solubilization of many membrane proteins unavoidable, the time spent in a detergent micelle or in the presence of a particular amphiphile can be limited. For example, long-chain detergents may be more effective at extracting membrane proteins from cellular membranes. However, the long-chain detergent can be exchanged for a shorter chain detergent which is able to better stabilize the protein and/or may be more amenable to crystallization.[18,35,39] Alternatively the solubilizing detergent micelle can be exchanged for a lipidic environment.[7,11,13,16,20,26,27,31,32,36,40,43,45-92] As discussed in Chapter 1, traditional methods for the crystallization of soluble proteins can be easily applied to detergent-solubilized membrane proteins.[4,11,12,31,39,43,93] One of the disadvantages of these *in surfo* methods is that the protective band of detergent also limits the formation of protein-protein crystal contacts,[11,19,31,37,39,47,54,94,95] thereby increasing the potential for crystal fragility and high mosaicity. An analysis of crystal structures shows that *in surfo* grown crystals are typically Type II (Figure 2.2a), with crystal contacts forming almost exclusively from interactions between the polar head-groups of proteins and relatively large cavities between protein molcules.[4,11,16,19,32,37,38,41,50,54,95,96] Type II crystals may suffer from a decreased diffraction signal compared to Type I crystals because of (i) lower packing density and (ii) an increased sensitivity to damage and increased mosaicity from physical handling due to weak crystal contacts.[32,47,50,54]

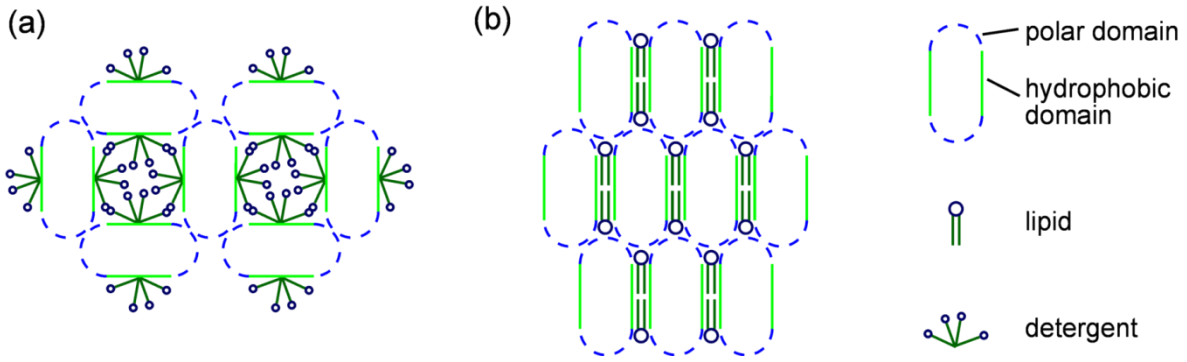

Figure 2.2. Schematic depictions of **(a)** Type II and **(b)** Type I crystals of membrane proteins. Lollipops denote lipids/detergents. Green lines: hydrophobic domains; Blue, dashed lines: polar domains. (Figure adapted from Michel, 1983).[4,16,37,93]

While these *in surfo* methods have proven to be successful in numerous cases,[4,11,16,19,37-39,41,78,85,93-95,97-126] it has been unsuccessful for other proteins, potentially due to the lack of a membrane-like environment.[16,31,37,46,53] To counter this difficulty, several different membrane-based crystallization methods have been developed. These methods include the bicelle method,[11,31,37,43,81,86,96,127-129] where a membrane-like disk of detergent is used to stabilize the proteins, as well as the *in meso,* or lipidic cubic phase (LCP) method,[7,11,13,16,20,26,27,31,32,40,43,45-86,92,130] and the related sponge-phase method[11,32,43,47-52,54,87-

[91,130] where proteins are crystallized directly from lipid bilayers. In Section 2.2 a brief history followed by a detailed description of the *in meso* method for crystallizing membrane proteins is given. Section 2.3 presents the current mechanistic understanding whereby *in meso* crystallogenesis is thought to take place. The relationship between this crystallization technique and the phase behavior of the lipid/water systems used to create the crystallization mesophases is then discussed in Section 2.4. Key challenges related to this method are then addressed in Section 2.5.

2.2 The *In Meso* Membrane Protein Crystallization Method

The *in meso* method for crystallizing membrane proteins was introduced in 1996 by Landau and Rosenbusch with the crystallization of the membrane-bound proton pump bacteriorhodopsin.[7,45] The method utilizes artificial self assembling membranous structures to "solubilize" amphiphilic membrane proteins while maintaining them in a more native environment throughout the entire crystallization process. The *in meso* method relies on the self-assembly of liquid crystalline mesophase structures above a certain limiting concentration of certain lipids in water. The amphiphilic nature of these lipids leads to the formation of various mesophase structures, including lamellar phases, bicontinuous cubic and inverted hexagonal phases (Figure 2.3).[11,26,27,32,66,130-133] Lamellar phases are locally planar lipid bilayer structures with varying degrees of inter-bilayer hydration. On a larger scale these lamellae can exist both as aligned bilayers and as uni-lamellar or multi-lamellar vesicles, though no connectivity exists between the various lamellae.[11,47] Cubic phases can be described as networks of interconnected aqueous channels surrounded by lipid bilayers with negative curvature. These phases are bicontinuous, allowing for diffusion in both the aqueous channels and the curved lipid bilayers. The inverted hexagonal phase consists of highly curved long hexagonally packed rods of lipid surrounding an aqueous core.[11,47] Both lamellar and cubic mesophases are expected to allow for the reconstitution of amphiphilic membrane proteins, whereas the high curvature of the inverted hexagonal phase makes incorporation of membrane proteins less favorable. This kind of phase behavior has been observed for numerous amphiphilic molecules including monoacylgylcerols (MAGs) such as the well-known monoolein (1-monooleoyl-*rac*-glycerol). These MAGs are commonly used for *in meso* crystallization.[26,132] Extensive studies on the phase behavior of different lipids and screening for their suitability for *in meso* crystallization have been performed and will be discussed in Section 2.4.

Crystals of membrane proteins are grown from these lipidic phases as follows: An initial "solution" of protein is obtained by mixing a purified sample of membrane proteins with a MAG at the appropriate composition and temperature for the formation of a cubic phase (typically 60% w/w for monoolein with 40% w/w aqueous solution). Cubic phases are critical for successful *in meso* crystallization.[11,47,53] Crystallization requires first diffusion of a precipitant solution to induce nucleation and then the subsequent diffusion of proteins from a bulk "solution" to the nucleated crystal. While the lamellar and cubic phases are both able to support reconstituted membrane proteins, the onion-like layering of a lamellar phase in a multi-lamellar vesicle would both prevent diffusion of polar precipitants across the

bilayer to induce nucleation and limit the quantity of protein which could diffuse to a growing crystal. However, the bicontinuous nature of a cubic phase allows for free diffusion of precipitant within the aqueous channels and protein diffusion within the cubic bilayer in an analogous fashion to that of a dissolved species in solution. Reconstitution of membrane proteins can be done either from a detergent solubilized protein sample[11,32,47,49,53] or from a highly pure membrane fraction, if such a source is available.[47,53,72] The subsequent addition of an appropriate precipitant is then thought to drive a local phase change from a cubic to a lamellar phase where crystal nucleation and growth can occur (Figure 2.4).[11,32,47,53,55,59,63,75,77,130,134]

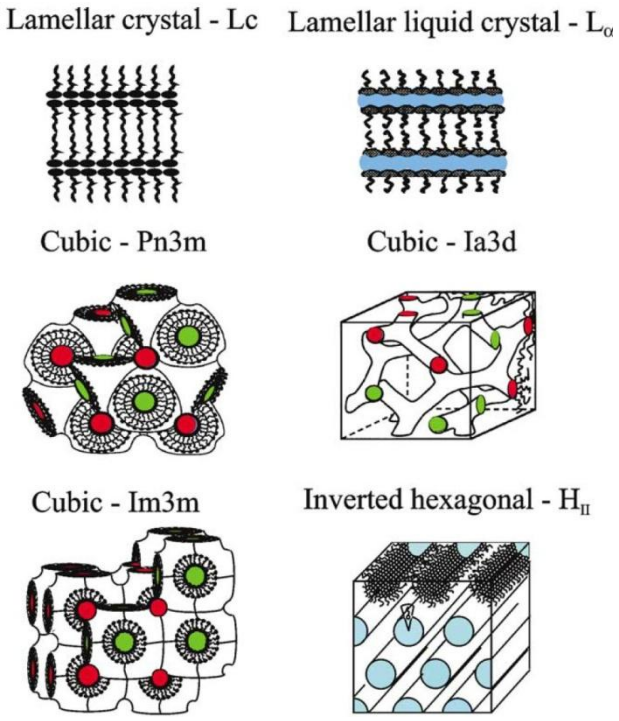

Figure 2.3. Cartoon representations of various phases adopted by lipids. Lipids are shown as lollipops: pop = polar head-group; wiggly stick = apolar chain. The light blue, green, and red colored regions represent water. (Figure adapted from Caffrey, 2003).[26]

This *in meso* crystallization procedure maintains the membrane proteins in an artificial membrane-like environment, thus reducing concerns about protein denaturation. The method has also been shown to be extremely robust with respect to contamination.[62] Furthermore, crystallization from aligned lamellar bilayers facilitates the formation of Type I crystals as a result of side-to-side interactions of the hydrophobic surface of the core of the protein as well as head-to-tail or tail-to-tail interactions between the extra-membranous regions (Figure 2.2b).[4,11,16,26,27,32,37,43,47,48,53,58,77,79,84,86,89,95,96,128,130,135-137] The two major advantages of Type I crystals are (i) an increased number of crystal contacts compared to *in surfo*-grown crystals, particularly with the polar regions of the protein, resulting in the potential for lower mosaicity and decreased fragility and (ii) increased packing density compared to *in surfo*-grown crystals, providing stronger diffracting power.[11,32,47,77,136,137] For example, the packing density of *in meso*-grown light harvesting complex II (LH2) is twice that of *in surfo*-grown crystals.[50,54] Also, the solvent content of

BtuB, an outer membrane cobalamin transporter from *E. coli* grown *in meso* is 53%, similar to what is observed for more robust crystals of soluble proteins, while the solvent content increases to 60% for *in surfo* grown crystals of the same protein.[50,54]

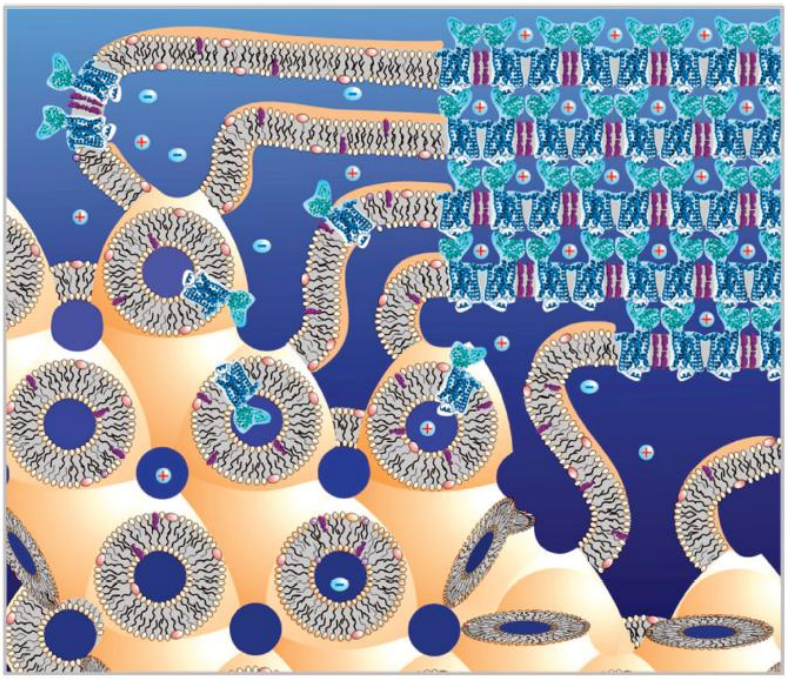

Figure 2.4. Schematic depiction of the proposed *in meso* crystallization process. Membrane proteins are reconstituted into a bicontinuous cubic phase (lower left). Upon the addition of a precipitant such as salt (charged ions are shown) a local lamellar phase forms into which the membrane protein preferentially partitions, resulting in the nucleation and growth of a crystal (upper right). Additional protein diffuses from the cubic phase to the growing crystal through a lamellar conduit. The protein (lysozyme bound β_2-andrenergic receptor, PDB code: 2RH1),[79] monoolein bilayer, and aqueous channels have been drawn to scale. The bilayer thickness is approximately 40Å. (Figure adapted from Caffrey, 2008).[47]

The preparation of aqueous/lipid mesophases, particularly at small volumes is challenging because of the high viscosity of the lipid solution (~30 times higher than the viscoity of water) and the non-Newtonian behavior and the extremely high viscosity (~10^5 times higher than the viscosity of water at the shear rates employed) of the resulting mixture.[11,32,74,138,139] Early on, samples were prepared by repeated centrifugation in a small tube such that the centrifugal forces can be used to fold the mixture over itself along with extended periods of equilibration (Figure 2.5c).[11,42,46,91,133,134,140-152] More recently, a setup involving two microsyringes that are coupled through a small bore connector (Figure 2.5a) was developed,[11,32,49,63,66,68,132,152-157] particularly for crystallization applications where a larger number of samples are needed. Mixing is achieved by repeated actuation of the syringes back and forth such that the high shear stresses experienced by the fluids as they pass through the coupling bore facilitate mixing.

After the crystallization mesophases are prepared in the coupled microsyringes, dispensing of material can be performed either manually or through the use of a robot. Manual dispensing with a 50-step repeat dispenser coupled to a 10 µL syringe (Figure 2.5b,d) enables dispensing of boluses on the order of 70 nL.[32,49,153] Scaling to smaller syringes is not possible due to the high viscosity of the

mesophases. A robotic system has also been developed which is capable of dispensing sub-nL boluses accurately.[32,56,158] Robotically setting up a screen in a 96-well plate takes less than 15 min but the viscous nature of the mesophase first requires precise calibration for dispensing.[158] In all of these cases, however, the flexibility of a crystallization screening experiment is not limited by the size of an individual crystallization trial, but rather the preparative scale at which mixing must be done.

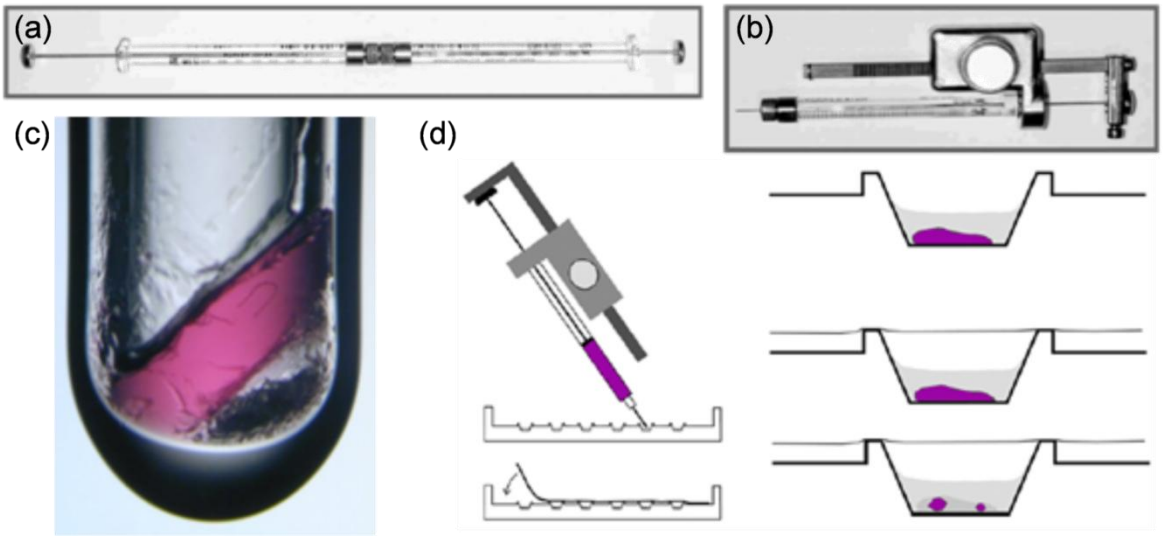

Figure 2.5. Photographs of **(a)** coupled microsyringes used to prepare lipidic membrane protein-containing mesophases by manual actuation; **(b)** manual dispenser used after mixing; and **(c)** mesophase prepared by centrifugation in a test tube from which bacteriorhodopsin crystals were grown. **(d)** Depiction of the preparation of *in meso* crystallization trials. A coupled syringe mixer. A protein-containing mesophase (purple) has been prepared in a coupled-syringe mixer. Dispensing of this mesophase can be done using a dispenser-driven microsyringe as shown. A crystallization tray is prepared first by filling of the wells with a precipitant solution, and subsequent dispensation of a bolus of protein-containing mesophase. The wells are then sealed with tape and allowed to incubate. Over time the formation of crystals will result in the depletion of protein from the bulk of the bolus. (Figures (a) and (b) adapted from Caffrey, 2003. Figures (c) and (d) adapted from Nollert, 2004).[26,46]

Harvesting of *in meso* grown crystals for X-ray analysis is done in much the same manner as with solution-grown crystals. The only major difference in the harvesting procedure is that it is usually necessary to create a path through the viscous mesophase to the crystal in order to minimize damage from physical handling. This can be done manually, through the use of enzymatic hydrolysis, or by dissolution in an oil or detergent solution.[13,32,49,75,159] While it is advantageous to minimize the amount of bulk mesophase harvested along with the crystal, the mesophase has demonstrated cryoprotective abilities, so additional treatments are not typically necessary.[11,26,32,49-52,54,65,67,77,87,89,92,130]

2.3 Current Mechanistic Understanding of *In Meso* Membrane Protein Crystallization

As was described in Section 2.2, *in meso* membrane protein crystallization is thought to occur in the following three steps: (1) reconstitution of the protein, (2) a phase change induced by the addition of a precipitant solution, and (3) crystal nucleation and growth from a lamellar phase. The initial protein-containing mesophase is prepared by mixing a purified sample of membrane protein, typically a detergent

solubilized sample,[32,47,49,53] with a MAG at the appropriate composition and temperature for the formation of a cubic Pn3m phase (typically 60% w/w monoolein with 40% w/w aqueous solution). During preparation the membrane protein along with adventitious detergent and/or lipid molecules are reconstituted into the native-like lipid bilayer environment.[32,66,72,79,80,86,160] The reconstitution of membrane proteins into a bicontinuous cubic phase creates a two-dimensional, membrane-bound analog of solubilized proteins. Within the connected bilayers of the mesophase, membrane proteins are able to diffuse freely within the limited degrees of freedom for motion and curvature imposed by the membranous environment.[32,53,130,136] It has been shown that the ability of reconstituted proteins to diffuse is a necessary but not sufficient condition for crystallogenesis, and that the rate of protein diffusion in the highly curved membranes can be altered based on how various additives such as lipids, detergents, salts, and other crystallization solutions alter the curvature of the mesophase.[136]

The subsequent addition of an appropriate precipitant is then thought to facilitate crystallization in two ways. As in traditional, solution-based crystallization methods the components of the precipitant solution may include salts to screen the repulsive interactions between proteins and/or osmotically active components that may draw the protein molecules together.[26,32,47] The precipitant solution is also thought to drive a local phase change from a cubic to a lamellar phase in or from which crystal nucleation and growth can occur (Figure 2.4).[32,47,53,55,59,63,75,77,130,134] This phase change is the culmination of a variety of effects including kosmotropic and osmotic effects of the precipitants on the mesophase (see Section 2.4.2.1), but also the preference of the reconstituted membrane proteins for a flattened bilayer (see Section 2.4.2.3).[47,59,63,68,75,77,132-134,141,142,152,161] The presence of adventitious detergent or lipids in the mesophase may also play a key role in facilitating this phase change (see Section 2.4.2.2).[32,47,63,66,68,72,79,80,86,155,160]

The clustering of membrane proteins in locally lamellar regions is energetically favored because it relieves strain associated with interactions between the membrane protein and the highly curved bilayer of the cubic phase, in addition to the energies associated with crystal nucleation.[53,59] Thus while high curvature is conducive for protein nucleation in that it drives membrane proteins together in locally lamellar regions, these locally lamellar regions must increase in size in order to accommodate Type I crystals. The lamellar phase is also thought to serve as a conduit for protein diffusion, connecting the growing crystal to the bulk cubic phase.[26,32,47,50,54,55,63,67,68] The hypothesis for the lamellar conduit is supported both by the growth of Type I crystals and by freeze-fracture electron crystallography, atomic force microscopy (AFM), and microdiffraction analysis of the mesophase around a growing crystal.[32,47,53,55]

2.4 The Role of Lipid Phase Behavior in *In Meso* Membrane Protein Crystallization

The *in meso* crystallization of membrane proteins has tremendous potential to enhance the rate of structure determination since it avoids many of the key issues that currently plague crystallization efforts.

The amphiphilic nature of membrane proteins that is crucial to their role in the transduction of energy/information across cell membranes also makes them difficult to treat in solution. Solubilization of membrane proteins can be accomplished using detergents,[12,13,16,18-20,31,35-37,39,41] but the resulting detergent micelles around the hydrophobic part of the membrane proteins are often unable to maintain the necessary level of lateral pressure on the protein to maintain its functional conformation.[6,7,12,14,31,35-37,40,43,44] Furthermore, the spherical nature of micelles hampers the formation of protein-protein contacts needed to form a crystal.[19,31,39,54,94] As explained in Section 2.2, the *in meso* strategy overcomes these issues by embedding the membrane proteins in a cubic phase comprised of a complex network of curved lipid bilayers. The subsequent formation of a locally lamellar phase drives embedded membrane proteins together, hopefully leading to crystal nucleation and growth (Figure 2.4).[47,53,55,59]

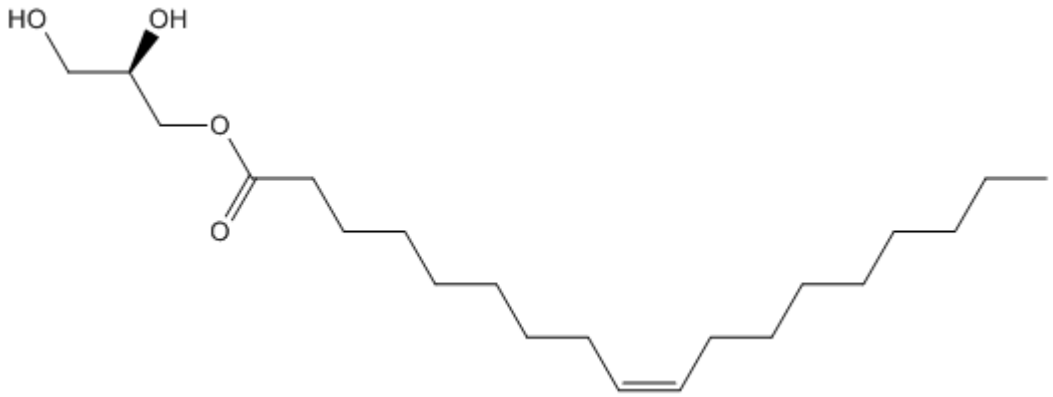

Figure 2.6. The structure of the 18-carbon monoacylglycerol monoolein (1-monooleoyl-*rac*-glycerol, 9.9 MAG). A glycerol head-group is attached to an 18-carbon chain with a single unsaturated C-C bond located halfway up the chain in the cis conformation.

Successful *in meso* crystallization has been reported for a variety of membrane proteins, but most commonly using the 18-carbon MAG known as monoolein (Figure 2.6).[7,13,32,45,50,51,53,54,57,61,64,66,72,73,79,80,82,84,85,92,129,130,134,135,159,162-171] Monoolein exhibits rich phase behavior, comprised of several cubic phases (Ia3d and Pn3m) that will transition into lamellar phases (Lc and Lα) upon lowering the water content and/or lowering the temperature (Figure 2.7).[27,157,172] Depending on the temperature and water content it is possible to obtain coexisting phases, such as Lα+Ia3d, or a fully hydrated phase in the presence of excess water, such as Pn3m+water. Interestingly, the phase behavior of these MAG/water systems shows significant metastability, particularly with respect to changes in temperature (Figure 2.7b).[26,27,32,42,47,49,68-70,77,131,132,137,152,157,172-174] This metastability represents a kinetic trapping of a non-equilibrium state upon cooling of the system.

While the vast majority of *in meso* crystallization experiments have been performed using monoolein, consideration of only a single lipid imposes a serious limit on the accessible phase space for *in meso* crystallization of membrane proteins. A library of many lipids and/or lipid mixtures suitable for *in meso* crystallization needs to be developed to expand the range of accessible temperatures and mesophase properties such as bilayer thickness, curvature, and water channel dimension in order to capitalize on the

promise of this method.[32,66,67,69,70,157] Additionally, recent studies have begun to elucidate the importance of native lipids from the source organism in maintaining the function and stability of membrane proteins.[79,80,86,92,160]

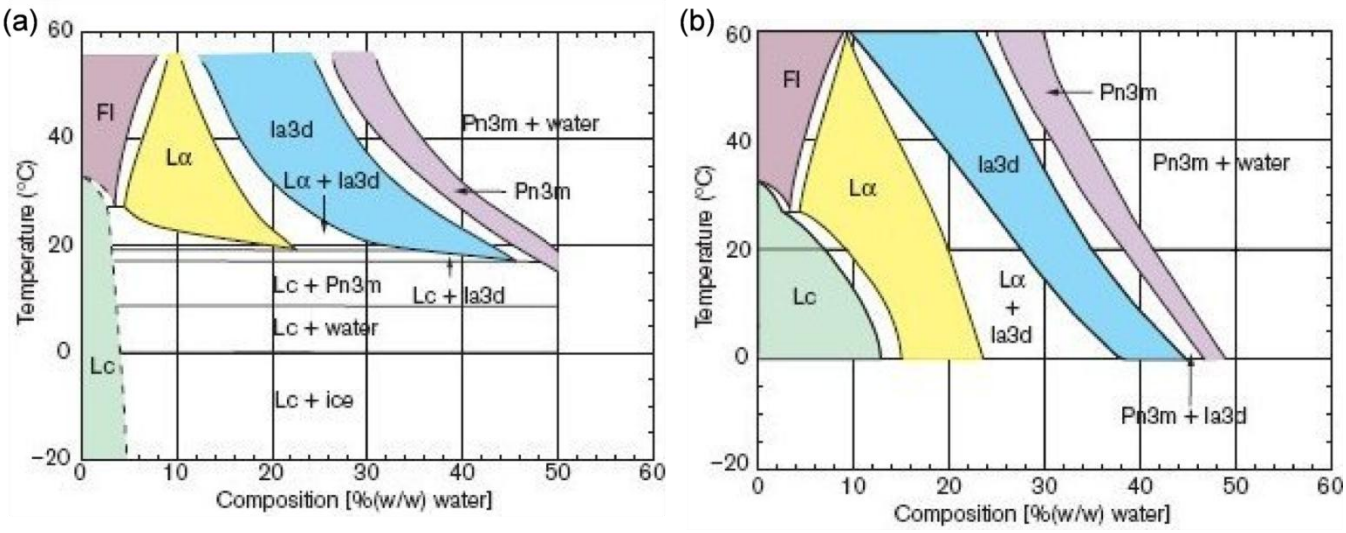

Figure 2.7. Temperature/composition phase diagram for the monoolein/water system. **(a)** Equilibrium phase diagram. **(b)** Metastable phase diagram. Legend: Lamellar phases start with an "L;" Cubic phases contain a "3." A more detailed nomenclature legend for the different phases can be found in Figure 2.3. (Figure adapted from Caffrey, 2000).[27]

2.4.1 The Phase Behavior of MAG/Water Systems

To increase the number of lipids available for *in meso* crystallization of membrane proteins, Caffrey and coworkers have systematically explored the phase behavior of various MAGs.[32,67,69,70,157] MAGs have a simple molecular structure of a glycerol-based head-group and a single unsaturated bond in their hydrophobic alkyl chain (Figure 2.6). They exhibit phase behavior that can access the full range of temperature and concentration induced mesophases while remaining within biologically relevant constraints such as temperature and water content.[26] An examination of the behavior of a variety of MAG/water systems has demonstrated that decreasing chain length results in a decreased thickness of the lipid bilayer and an increase in the diameter of the aqueous channel.[32] Additionally, the chain length and position of the single unsaturated bond can be easily shifted to further alter the phase behavior.

The MAG homologs are classified using a so-called N-T matrix.[67,69,70] The lipid is assigned a coordinate in N-T space defined by the length of the carbon chain on either side of the olefinic bond. The region between the double bond and the glycerol head-group is referred to as the neck (N) while the region extending from the double bond to the terminal methyl group is the tail (T). For the commonly used 18-carbon monoolein, the N-T matrix designation is 9.9 MAG, describing a monoacylglycerol with 9 carbons in the neck region and 9 carbons in the tail region. Other lipids that have been reported on include the 18-carbon lipid monovaccenin (11.7 MAG),[83] the 16-carbon lipids monopalmitolein (9.7 MAG)[7] and 7.9 MAG,[70] and the 14-carbon lipid 7.7 MAG.[32,67]

Determination of the phase diagram for a MAG is highly labor intensive, involving preparation of all individual compositions, followed by transfer into X-ray capillaries and analysis. To determine the phase diagram for an individual MAG, mesophase samples of specific concentrations are prepared using the coupled syringe mixer (Figure 2.5a).[154] The phase identity of each sample is then analyzed by a variety of techniques including small angle X-ray diffraction and differential scanning calorimetry.[69,70,157,172,173] X-ray analysis provides direct insight into the dimensions of the mesophases: for example, a fully hydrated cubic Pn3m phase of monoolein and water has a bilayer thickness of 32Å and water channels with a diameter of 40Å.[67] Temperature-controlled sample holders are also limited in the number of samples which can be mounted at one time. The metastable character of the various mesophases requires long incubation times in excess of 3 hours at each temperature increment to minimize these effects.[42,67,69,70,152,157,172] Actual diffraction data collection takes between 15 minutes to 24 hours using a 'bench-top' X-ray source[69,150,157] or less than a minute when a synchrotron source is used.[152,173]

The temperature dependence of the microstructure of various lipidic mesophases has proven to be a critical factor for crystallization of membrane proteins. While monoolein (9.9 MAG) has been used preferentially for *in meso* crystallization trials thus far, it is unable to accommodate a cubic phase at lower temperatures such as 4°C without relying on metastable phase behavior (Figure 2.7b).[26,27,32,49,68,77,132] While it is possible to perform crystallization at lower temperatures,[70,76] these metastable phases cannot be counted on for reproducible results in crystallization experiments lasting many hours.[26,27,32,68,70,77,157] Instead, Caffrey and coworkers utilized rational design based off of the phase behavior for various MAGs for which the phase diagrams are known to identify 7.9 MAG as a potential candidate for low temperature *in meso* membrane protein crystallization.[32,70] Following synthesis, characterization of the phase behavior for 7.9 MAG/water systems showed mesophases which are not only stable at much lower temperatures than those of monoolein, but which matched the predicted behavior from rational design very closely. Successful *in meso* crystallization of the membrane protein bacteriorhodopsin was performed in 7.9 MAG at 6°C. This demonstration of a rationally designed alternative lipid suitable for *in meso* crystallization exemplifies the potential for dramatic success in crystallizing membrane proteins that are only stable at lower temperatures.

Stability and crystallizability can also be affected by the thickness and curvature of the lipid bilayer within the mesophase. The mesophase must be able to accommodate the membrane protein, but the curvature should also provide a sufficient driving force for crystallization to occur without preventing the protein from diffusing.[59,77,136] Combining the ideas of mesophase curvature and thickness, Caffrey and coworkers proposed the use of a shorter-chained lipid in order to decrease the "degree of comfort" experienced by the protein in the mesophase and increase the driving force for crystallization.[32,67] Their hypothesis was that the standard 16 or 18-carbon MAGs used previously formed membranes that accommodated membrane proteins to the point where the driving force favoring protein-protein interactions and the formation of stable nuclei was not significant. A 14-carbon MAG was chosen with the

idea of 14-carbons being a short enough chain to better facilitate crystallization, but not so short as to prevent reconstitution of the protein into the membranes of the mesophase.

In an attempt at rational design,[32,70] existing phase behavior information for longer chain MAGs was extrapolated to determine the optimum location for the single unsaturated C-C bond in the carbon chain.[67] The 14-carbon 7.7 MAG was chosen to have the desired overall chain length and the ability to form a cubic phase at room temperature. This shorter chain length resulted in both a thinner membrane and a lower degree of curvature for the cubic mesophases used for *in meso* crystallization as compared to the standard monoolein mesophases (Figure 2.8).[67] In crystallization trials using the membrane protein bacteriorhodopsin, the difference in lipid composition both required different crystallization conditions and resulted in a different crystallographic space group. It is also particularly interesting to note that in trials using the smaller 7.7 MAG the size of the resultant crystals was significantly larger than that for monoolein (maximum dimension of 200 μm vs. 80 μm) and were of better visual quality. This corresponds directly with their hypothesis of improving the driving force for crystallization via a smaller chain lipid. 7.7 MAG was also used to crystallize BtuB, a colorless *E. coli* outer membrane cobalamin transporter, which represents the first β-barrel membrane protein to be crystallized by the *in meso* method.[32,67]

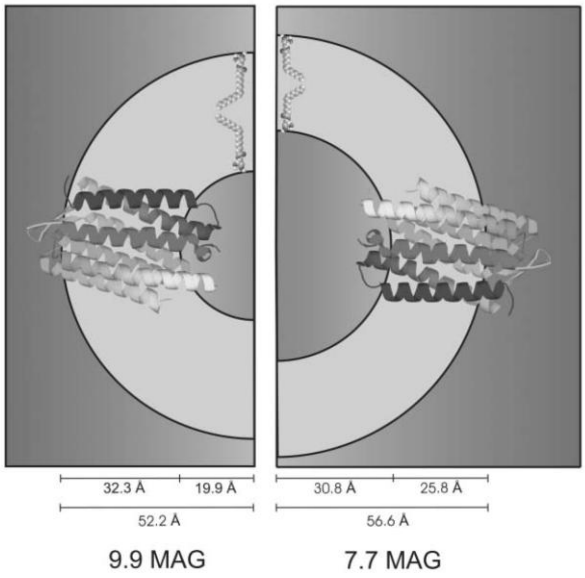

Figure 2.8. Cartoon representation of bacteriorhodopsin (PDB ID: 1C3W) in the highly curved cubic lipidic phase of fully hydrated 9.9 MAG (monoolein) and 7.7 MAG at 40°C. (Figure adapted from Misquitta, 2004).[67]

2.4.2 The Effect of Additives on the Phase Behavior of MAG/Water Systems

The reported successes for *in meso* crystallization have all hinged on prior characterization of the phase behavior of the various water/lipid systems; such as lattice parameters and structural data from X-ray diffraction studies as a function of both temperature and composition (i.e. water content).[172,173] While rational design of MAG/water systems has demonstrated powerful predictive abilities, it will remain necessary to experimentally characterize the phase behavior of various lipid mesophases. In addition to

understanding the phase behavior of binary MAG/water mixtures, it is important to consider the effects of a variety of additives which might be present during an *in meso* crystallization trial, in addition to the membrane protein itself. These contaminating agents can include detergents and native lipids carrying through from protein purification or intentionally added, precipitants, and other biologically relevant molecules and cofactors and may have a significant effect on both the observed phase behavior and the crystallization trial itself.[11,32,47,62,63,66,68,77,79,86,91,132-134,141-144,146,147,149-152,155,156,174-177]

As will be discussed in more detail in Section 2.3, the *in meso* crystallization method requires the formation of a bicontinuous cubic phase to create a "fluid" environment through which the reconstituted membrane proteins can diffuse.[32,47,49,53,55,132,136] One of the first concerns in a crystallization trial is the tendency of the various components of the crystallization screen such as salts and precipitating agents to destabilize the cubic phase.[32,132] A detailed examination of the effects of two commonly used sparse matrix screens, Hampton Screen and Hampton Screen 2, was made.[132] Based on the binary monoolein/water phase diagram, samples were prepared at a ratio of monoolein to aqueous phase to produce both fully hydrated and water-stressed cubic phases using the precipitant solution both at full strength and at a 50% dilution. The diluted precipitant was tested because in traditional crystallization methods the precipitant solution is typically diluted in a 1:1 ratio with the protein solution, and so the precipitant solutions as supplied by the manufacturer might simply be too strong. A variety of observations were made including the tendency of salts to decrease the lattice parameter, thus increasing the curvature of the cubic phase, and a phase change from cubic Pn3m to cubic Ia3d followed by a decrease in the lattice parameter due to the water withdrawing effects of higher molecular weight polyethylene glycols (PEGs). However, the overall level of hydration in the mesophase remained a key factor in determining the phase behavior. Based on the results of this study a new crystallization screen designed to be compatible with *in meso* crystallization, the Cubic Screen, was developed by Emerald Biosystems.[178] While an examination of the effects of a sparse matrix screen provided direct insight into the design of crystallization trials, the complex mixture of chemicals present in a screening solution make isolating the effects of individual classes of chemicals difficult. A variety of additive-specific studies have been performed, but the breadth of information in the literature is no doubt limited by the sample and labor-intensive nature of the experiments.

2.4.2.1 The Effect of Salts on the Phase Behavior of MAG/Water Systems

An examination of the effect of salts on the phase behavior of MAG/water mesophases is particularly interesting in the context of protein crystallization. Salts are commonly used in crystallization experiments and have also been well studied with respect to their interaction with proteins. The Hofmeister or lyotropic series was generated based on the efficiency of ions in precipitating proteins.[133,142,161,179-184] The series for anions and cations are expressed as follows, though the position of polyvalent ions may vary with pH. Also, the effect of anions is typically much stronger than that of cations.

Anions: $SO_4^{2-} > HPO_4^{2-} > CH_3CO_2^- > citrate^{3-} > tartrate^{2-} > F^- > Cl^- > Br^- > NO_3^- > I^- > ClO_4^- > SCN^-$

Cations: $Ca^{2+} > Li^{+} > Na^{+} > K^{+} > NH_4^{+} > Mg^{2+}$

For the anionic series, species to the left of Cl^- are referred to as kosmotropes and are strongly hydrated ions that structure the water around them and have a stabilizing effect on proteins. Kosmotropes also display salting-out effects on proteins where the solubility of the protein decreases with increasing salt concentration. The species to the right of Cl^- are termed chaotropes and destabilize the structure of water and folded proteins. Chaotropes typically result in salting-in behavior where protein solubility increases with increasing salt concentration.[181]

An examination of the effects of a series of sodium salts on the phase behavior of MAG/water systems with roughly 30% w/w lipid demonstrated that changes in the energetics of phase transitions due to the presence of salt are consistent with the anionic Hofmeister series.[133,142,161] This observation corresponds to the stabilization of one phase over another. Chaotropic solutes (NaSCN) were found to increase the lattice constant of the cubic phase while kosmotropes (NaBr, NaCl, and Na_2SO_4) decreased the lattice constant. These trends were explained by the effect of the various ions on the amount of interfacial water present at the bilayer surface. Because kosmotropes stabilize the structure of bulk water, they tend to be excluded from interfacial regions and therefore reduce the amount of interfacial water present. A decreased amount of interfacial water would then be expected to cause a corresponding decrease in the interfacial area present, resulting in changes in curvature and/or preferential stabilization of one phase over another (Figure 2.9). For example, the decreased lattice constant observed for the kosmotropic salts corresponds to an increase in curvature and a decrease in the interfacial area present, agreeing with this hypothesis. Similar trends have been observed in the phase behavior of phospholipids and glycolipids as well as nonionic surfactant systems.[133]

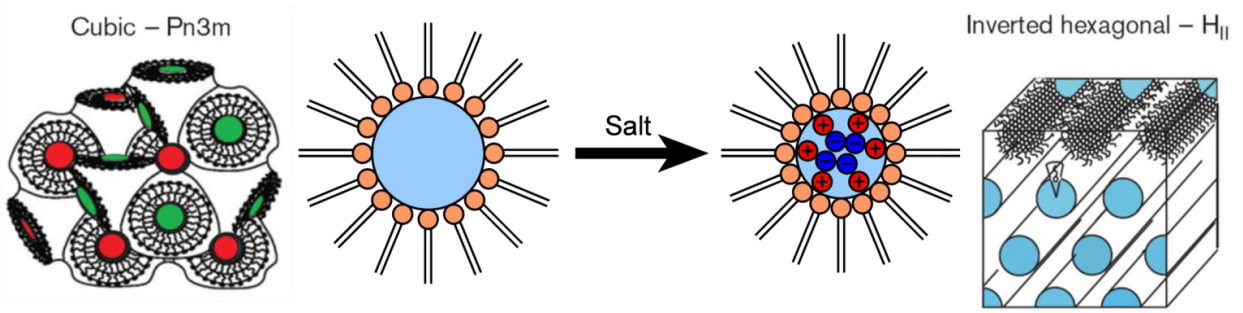

Figure 2.9. Depiction of the effects of a kosmotropic salt on the curvature of a cubic phase. Addition of the salt results in a decrease of the interfacial area between the lipidic phase and the aqueous channel, shrinking the size of this channel and increasing the curvature. Increases in the curvature of this interface beyond the capacity of the cubic phase result in a change to an inverted hexagonal phase. (Portions of the figure adapted from Caffrey, 2003).[26]

Separate studies utilizing fully hydrated cubic phases also demonstrated that increasing concentrations of salt consistently decreased the lattice parameter of the cubic phase, thus increasing the curvature.[141,152] A trend of decreasing lattice parameter with increasing temperature was also observed.[152] These trends were again consistent with the Hofmeister series for both anions and cations (Figure 2.10). At constant pH and cation (ammonium), sulfate anions resulted in a more significant

decrease in the lattice parameter of the cubic phase than did phosphate anions. With constant anion (phosphate) the combination of the sodium and potassium anions resulted in a more significant decrease in the lattice parameter than did ammonium. As before, the decrease in lattice parameter is associated with an increase in curvature and a concomitant decrease in the interfacial area.

A variety of other studies have commented on the effects of salt in the literature, though the effect of salts were not studied explicitly. From an examination of the effects of detergents on the cubic phase of monoolein it was demonstrated that the presence of ammonium sulfate results in a significant decrease in the lattice parameter of cubic phase, even in the presence of 10% mol/mol octyl glucoside. In direct agreement with the anionic Hofmeister series, the presence of equivalent levels of sodium and potassium phosphate resulted in a much smaller decrease in the lattice parameter of the cubic phase than did ammonium sulfate.[68]

From the study focused on the effects of the Hampton Crystallization Screens on the cubic phase, trends in the effect of salts on the lattice parameter of the cubic phase were also observed. Although cationic and pH effects were neglected, the ability of salts to shrink the lattice parameter of the cubic phase was reported in the order of citrate ≈ sulfate > tartrate > phosphate > formate > acetate > chloride.[132] While some of the ordering here reflects the Hofmeister series, such as the relative positioning of sulfate, phosphate, and chloride, many of the other ions are seemingly out of place. It is possible that the overall difference in behavior observed between the various studies is a result of variations in both the different MAG/aqueous phase compositions and the solution pH used for the trials. However, more extensive testing is needed to investigate this.

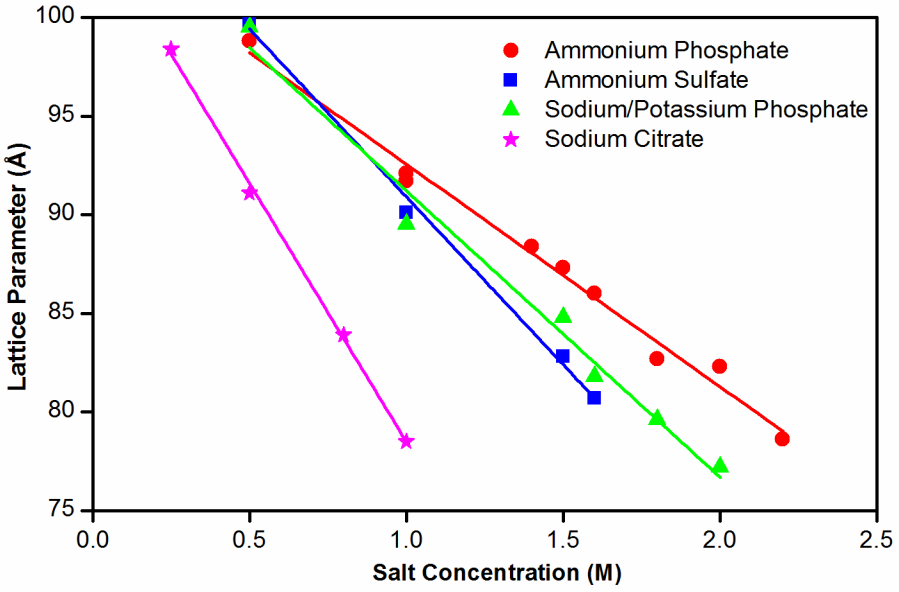

Figure 2.10. Plot of the lattice parameter of the fully hydrated cubic Pn3m phase of monoolein in the presence of salts of varying concentrations at pH 6.5. Trends consistent with the Hofmeister series are observed. In the presence of the ammonium cation, sulfate anions showed a larger decrease in the lattice parameter of the cubic phase than did phosphate ions. In the presence of phosphate anions sodium and potassium showed a more significant effect on lattice parameter than did ammonium. (Data replotted from Vargas, 2004).[141]

2.4.2.2 The Effect of Amphiphiles on the Phase Behavior of MAG/Water Systems

In addition to the salts and precipitants which are added during the course of a crystallization trial, it is also critical to understand the effects of detergents, lipids, and other amphiphiles which can be incorporated into the cubic phase during the reconstitution of the membrane protein. Naturally occurring lipids and detergents in particular may have a significant impact on the phase behavior of the MAG/aqueous solution mesophase because of the differences in the preferred curvature of these amphiphiles as compared to the curvature adopted by the mesophase (Figure 2.11).[42,47,91,134]

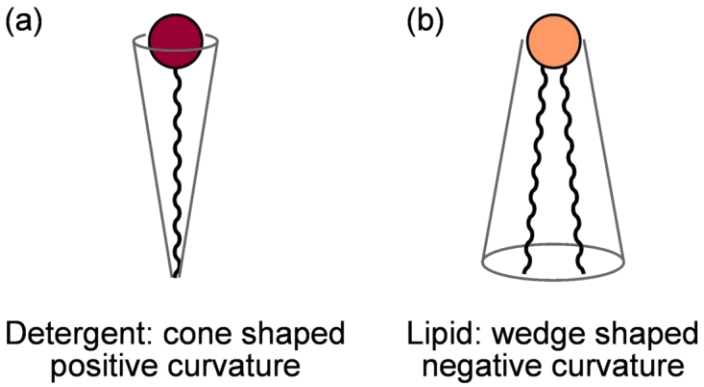

Figure 2.11. Schematic depiction of the geometric shape and resultant curvature for typical detergents and lipids. **(a)** Detergents typically have a single aliphatic tail, resulting in a cone shape and the preference for areas of positive curvature, such as micelles. **(b)** Naturally occurring lipids often have two aliphatic tails, imparting a cylindrical or wedge shape to the molecule which prefers areas of negative or flat curvature.

A variety of studies have investigated the effects of common crystallization detergents on the stability of the cubic phase. The cubic phase itself can be characterized as an infinitely periodic minimal surface (IPMS) with negative Gaussian curvature and zero mean curvature.[37,42,53,59,66,91,133,134,144-147,150-152,157,175,185] However, detergents preferentially self assemble into structures with positive curvature.[37,42,47,134] Therefore it is reasonable to expect that with increasing loading, detergents will eventually destabilize the cubic phase in favor of a structure with less negative curvature.

An examination of the alkyl glucoside family of detergents in a monoolein mesophase showed a tendency for the detergent to destabilize the Pn3m phase in favor of cubic Ia3d and lamellar Lα phases.[32,42,68,134,140] Increasing detergent concentration at constant temperature resulted in a slight increasing of the lattice parameter of the cubic phases while increases in temperature at constant detergent loading resulted in a decrease in the lattice parameter. Similar results were observed for a series of maltosides, alkyl fos-cholines, lauryldimethylamine-oxide (LDAO), sodium dodecyl sulfate (SDS), heptyl thioglucoside, and Cymal.[32,63,68,77,155] Whereas the effects of salts and dissolved precipitants must be coupled with interactions between water and the polar head-groups of the MAGs, amphiphilic molecules like detergents can interact with both the apolar aliphatic and polar head-groups and aqueous channel aspects of the mesophase. It is interesting to consider the effects of these two contributions separately.

The polar detergent head-group is expected to interact with both the glycerol head-groups of the MAG and also the water within the aqueous channel. The effects of these head-groups can be simulated by considering the effects of dissolved sugars on the cubic phase. The addition of a variety of dissolved sugars, including glucose and maltose, resulted in a decrease in the lattice parameter of the cubic phase.[91,142,155,175] These sugars were also observed to stabilize the Pn3m cubic phase to very low values of lattice parameter without undergoing a phase transition.[175] This can be explained as a water withdrawing effect where dissolved sugar molecules order the water around them, thus sequestering it away from the lipid head-groups. This behavior is that of a kosmotropic agent from the Hofmeister series and a similar ordering based on the strength of the interaction can be made, with the number of monosaccharide rings present in the sugar molecule (shown in parenthesis below) having a significant impact on the level of interaction observed with the cubic phase:[155,175]

Saccharides: maltotriose (3) > trehalose (2) > maltose (2) > sucrose (2) > glucose (1)

With respect to the effects of detergent head-groups, the larger disaccharide maltoside head-group resulted in a more significant decrease in lattice parameter and a larger degree of destabilization than did the monosaccharide glucoside head-group.[42,155,175]

The tendency for a detergent to destabilize the cubic phase can be related to the length of its aliphatic tail.[42,68] In the study of the alkyl glucoside family of detergents the shorter-chain detergents (i.e. hexyl glucoside) facilitated a phase change from the cubic Pn3m to the cubic Ia3d and lamellar Lα phases at lower concentrations than did the longer-chain detergents (i.e. decyl glucoside). This trend can be observed by the shifting of the phase boundaries as a function of detergent chain length (Figure 2.12). In this sense the geometric argument associated with the shape of the detergent molecule agrees with experimental observations. For a given head-group, the cone shape of shorter-chain detergents will tend to impart a stronger need for positive curvature and thus a stronger destabilizing effect on the negatively curved cubic phase than would longer-chain detergents. Based on the opposing nature of the interactions between the head-group and the aliphatic tail of the detergent, the tail effects appear to dominate the observed changes in phase behavior.

Having understood the effects of the various components separately, it is interesting to return to the context of a crystallization experiment and understand the balance between the effects of the various precipitants and amphiphiles. For instance, the addition of detergent has been shown to increase the lattice parameter and destabilize the cubic phase in favor of lamellar phases,[32,68,155] while the addition of salt has been shown to decrease the lattice parameter of the cubic phase with eventual destabilization in favor of the inverted hexagonal phase.[132,133,141,142] These opposing effects can be used to stabilize a cubic phase using increasing salt concentration in the presence of increasing detergent concentration.[32,68] For instance, the cubic Pn3m phase of monoolein could be stabilized up to a detergent concentration of 1.18 M octyl glucoside by using 2 M sodium/potassium phosphate at pH 5.6 and 20°C. This is a tremendous stabilization compared to a transition above 40 mM octyl glucoside in the absence of salt.[68]

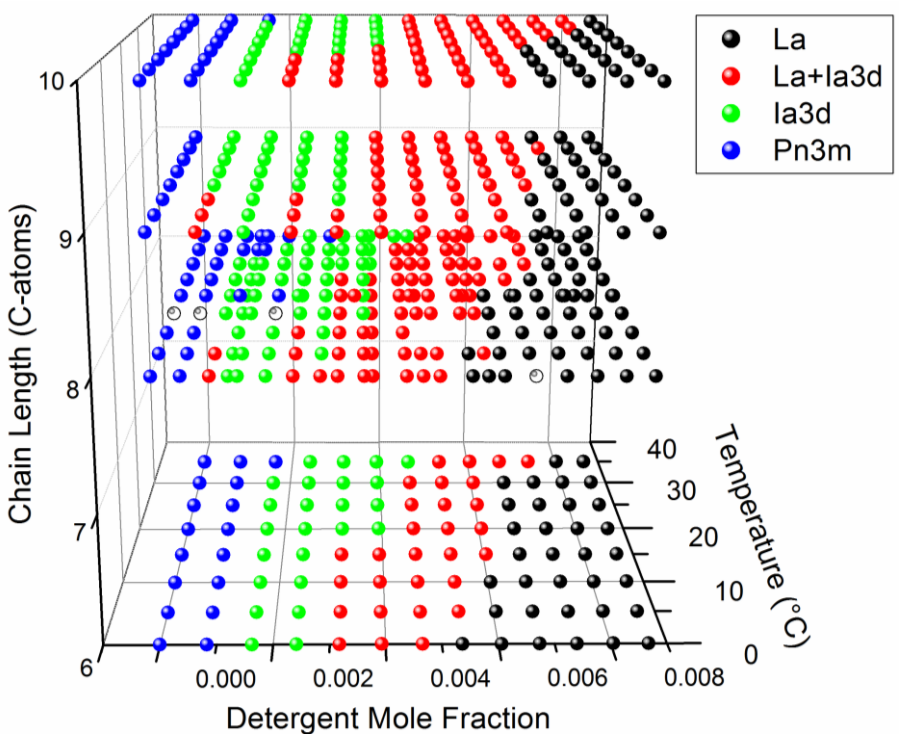

Figure 2.12. Plot of the metastable phase behavior of four monoolein/water/alkyl glucoside systems as a function of detergent mole fraction, temperature, and detergent chain-length. Samples were prepared using a 60% w/w monoolein, 40% w/w detergent solution for hexyl, octyl, nonyl, and decyl glucosides. A shift in the location of the phase boundaries to increasing detergent concentration is seen with increasing chain length. (Data replotted from Misquitta, 2003).[68]

While membrane protein crystallization is most commonly associated with detergents, lipids and other amphiphiles may be present in the crystallization mixture, either adventitiously despite purification procedures, or intentionally to stabilize the protein in its natural conformation.[37,66,72,79,80,86,160] For instance, the detergent-free *in meso* crystallization of bacteriorhodopsin has been performed via the direct reconstitution of naturally occurring purple membranes into a monoolein mesophase.[72] Purple membrane is composed of phosphatidylglycerol (PG), phosphatidylglycerophosphate (PGP-Me), phosphatidylglycerosulfate (PGPS), and squalene, all of which can promote the formation of a lamellar phase over the cubic phase that is desired for *in meso* crystallization.[24,134] Phosphatidylcholine (PC) is also a common component of cellular membranes and causes a decrease in the curvature of cubic phases in favor of the formation of low curvature lamellae.[32,47,66] Phosphatidylethanolamine (PE), on the other hand, increases the curvature of cubic phases in favor of the formation of inverse hexagonal phases.[32,66] Anionic lipids such as phosphatidylserine (PS) and cardiolipin resulted in the formation of a cubic Im3m phase, followed by a lamellar Lα on continued loading.[32,66] Cholesterol is also a naturally occurring component of many membranes and has been proven necessary for the crystallization of several human G-protein coupled receptors.[32,79,80,86,160] While cholesterol occurs naturally in a lamellar phase, the cubic Pn3m phase was capable of accommodating relatively large amounts of the steroid through an increase in the lattice parameter before triggering a conversion to the cubic Im3m phase.[66] In

each of these cases the geometric shape and charge of the additive molecule can be used to rationalize the observed changes in phase behavior.[66]

In addition to adventitious or stabilizing lipids, it is also possible to intentionally dope MAG/water mesophases with lipids in order to tailor the geometric properties of the mesophase.[32] The anionic lipid distearoylphosphatidylglycerol (DSPG) can be used to decrease the curvature of the cubic phase, thereby increasing the dimensions of the aqueous channels to better facilitate membrane protein reconstitution and diffusion.[134,145,151] This modification to the traditional monoolein preparation of the *in meso* crystallization method resulted in crystals of bacteriorhodopsin growing faster, more readily, and to a larger final size. However, diffraction analysis on the crystals was not performed, so no comparison of crystal quality can be made. Also, the use of a mixture of the commonly used 1-monoolein with its isomer, 2-monoolein, has been suggested for fine-tuning of the cubic phase lattice parameter while holding the chemistry of the MAG/water interface constant.[66]

As in the case of detergents, the effects of lipid and salt additives can be balanced in order to stabilize a particular phase.[32,146] For instance, the addition of the charged lipid dioleoylphosphatidic acid (DOPA) to a fully hydrated monoolein-based cubic phase caused an increase in lattice parameter that resulted in a transition from the cubic Pn3m to the cubic Im3m and finally to the lamellar Lα phases. However, the addition of NaCl stabilized the cubic Pn3m phase over a much broader range of DOPA loading.[146] These observations were rationalized based on a charge density argument where significant electrostatic interactions at the membrane surface from the DOPA stabilize the less highly curved Im3m and Lα phases whereas charge screening from the addition of salt to the solution enables the recovery of the cubic Pn3m phases.

2.4.2.3 The Effect of Membrane Proteins on the Phase Behavior of MAG/Water Systems

In addition to all of the various precipitants, additives, and other chemicals that can be present in an *in meso* crystallization trial the effect of the reconstituted membrane protein should also be considered. The lipid bilayers that form cellular membranes are only a few nanometers thick and because local curvature is on the order of a few tens of nanometers the cellular membrane can be approximated as a flat bilayer for a majority of cases.[186] Membrane proteins are thus well adapted to a flat bilayer environment.[24] The incorporation of a membrane protein into a highly curved cubic phase results in a hydrophobic mismatch between the length and shape of the membrane-spanning portion of the protein and the hydrophobic region of the lipid bilayer.[59,63,75,77,134] This mismatch is energetically unfavorable and can result in distortion of the bilayer to cover up exposed hydrophobic patches on the membrane protein (Figure 2.13).[53] This distortion can be thought of as a locally flattened region in the saddle of the highly curved cubic phase, creating an energetic driving force for membrane proteins to cluster together in flattened regions of the membrane and stabilizing the formation of a lamellar phase.[53,59,134] This preference of the reconstituted membrane protein for the lamellar phase is a key aspect of the proposed mechanism whereby *in meso* crystallization occurs.

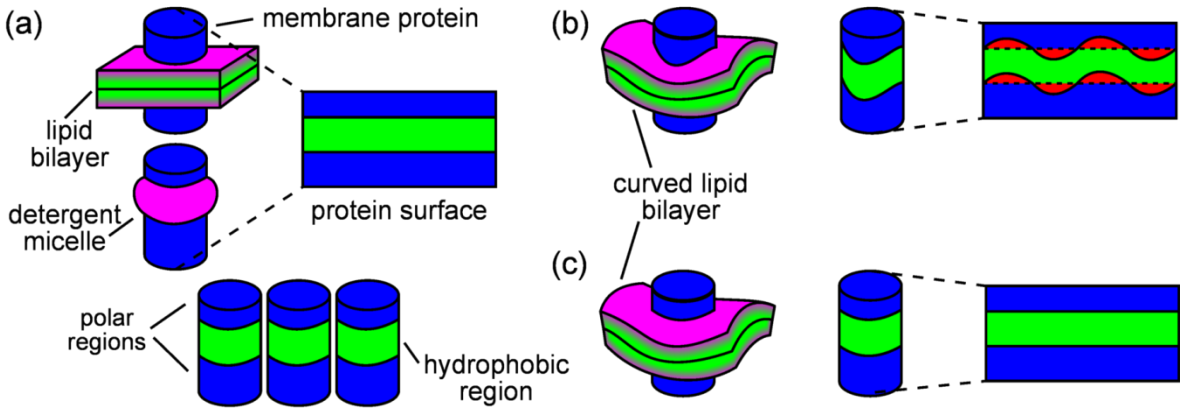

Figure 2.13. Hydrophobic matching of the protein-membrane interface in bilayers of varying curvature. Membrane proteins are shown as cylinders with their hydrophobic portions highlighted in green and their polar portions colored in blue. Lipid bilayers are shown as planar structures with purple polar surfaces and a green embedded hydrophobic region. A solubilizing detergent micelle is shown as a purple torus around the protein. For each structure a rolled out depiction of the membrane protein surface is shown. Overlap of the hydrophobic areas of the membrane protein and lipid bilayer are shown in green. Areas of hydrophobic mismatch are indicated in red. **(a)** A membrane protein interacting with a planar lipid bilayer (top), a detergent micelle (middle), and neighboring protein molecules (bottom). No hydrophobic mismatch is observed in these cases. **(b)** A membrane protein interacting with a negatively curved bilayer such as the bicontinuous cubic phase. The saddle shape of the membrane results in significant hydrophobic mismatch. **(c)** Relief of the hydrophobic mismatch in a highly curved bilayer can be achieved by local distortion of the membrane. (Figure adapted from Nollert *et al.*, 2001).[53]

2.5 Key Challenges

In summary, the *in meso* method for crystallizing membrane proteins has tremendous potential to enhance the rate of current structure determination efforts. This method has been demonstrated to be successful for a wide range of membrane protein types.[7,32,45,50,51,54,64,79,80,83,84,130,159] However, a number of remaining challenges associated with this method could be overcome by novel approaches.

One of the foremost challenges associated with both the *in meso* method and the characterization and development of new mesophase systems is the scale at which samples can be prepared. Methods have been developed which allow for sample dispensing at sub-nanoliter volumes, although it is still necessary to prepare a minimum of ~10 µL of mesophase due to challenges associated with the mixing of a viscid and an inviscid solution to form a highly viscous and non-Newtonian mesophase. Variations in the lipid composition of a crystallization mesophase is one potentially powerful variable that could be investigated during *in meso* crystallization screening experiments, in addition to more traditional variables. However, the introduction of such a variable would require intensive sample preparation and relatively large volumes of both protein and lipid. Similar difficulties are encountered during the characterization of lipidic phase behavior. Transitioning from syringe-based mesophase preparation methods to a microfluidic approach would enable not only an increase in the number of samples while using less material, but would also allow for a significant decrease in the actual preparative scale of an individual sample.

While the viscosity of the mesophases used with the *in meso* method has been a challenge for traditional methods of sample preparation,[32,74,138,139] these difficulties have presented a significant barrier

for the translation of the *in meso* method to the microscale. Chapter 3 develops a series of design rules for overcoming the limitations of highly viscous fluids at the microscale and Chapter 4 applies these results for the development of a microfluidic platform for *in meso* membrane protein crystallization.

In transitioning to microscale platforms for *in meso* crystallization and lipidic phase behavior studies, the benefits of scale and sample handling cannot be fully accessed without the ability to perform *in situ* analysis on the resultant samples. However, the traditional materials used for many microfluidic platforms are incompatible with X-ray analysis, and thus new materials and fabrication methods must be identified and optimized. Chapter 5 presents the development of a microfluidic platform for *in situ* X-ray analysis. This efficacy of this platform is then validated using both traditional monochromatic (Chapter 5) and Laue (Chapter 6) crystallographic techniques for protein structure determination. In Chapter 7 this device architecture is applied to microfluidic studies of lipid phase behavior and the effects of additives. Finally, Chapter 8 summarizes the results described in this dissertation and directions for further research are discussed.

2.6 References

(1) Baker, M. *Nat Methods* **2010**, *7*, 429.

(2) Wallin, E.; von Heijne, G. *Protein Sci* **1998**, *7*, 1029.

(3) Willis, M. S.; Koth, C. M. In *Methods in Molecular Biology: Structural Proteomics - High Throughput Methods*; Kobe, B., Guss, M., Huber, T., Eds.; Humana Press: Totowa, NJ, 2008; Vol. 426, p 277.

(4) Michel, H. *Trends Biochem Sci* **1983**, *8*, 56.

(5) Quick, M.; Javitch, J. A. *P Natl Acad Sci USA* **2007**, *104*, 3603.

(6) Trubetskoy, V. S.; Burke, T. J. *Am Lab* **2005**, *37*, 19.

(7) Landau, E. M.; Rosenbusch, J. P. *P Natl Acad Sci USA* **1996**, *93*, 14532.

(8) Pecina, P.; Houstkova, H.; Hansikova, H.; Zeman, J.; Houstek, J. *Physiol Res* **2004**, *53*, S213.

(9) Arinaminpathy, Y.; Khurana, E.; Engelman, D. M.; Gerstein, M. B. *Drug Discovery Today* **2009**, *14*, 1130.

(10) Overington, J. P.; Al-Lazikani, B.; Hopkins, A. L. *Nat Rev Drug Discov* **2006**, *5*, 993.

(11) Kulkarni, C. V. 2010; Vol. 12, p 237.

(12) Koszelak-Rosenblum, M.; Krol, A.; Mozumdar, N.; Wunsch, K.; Ferin, A.; Cook, E.; Veatch, C. K.; Nagel, R.; Luft, J. R.; DeTitta, G. T.; Malkowski, M. G. *Protein Sci* **2009**, *18*, 1828.

(13) Nollert, P.; Navarro, J.; Landau, E. M. *Method Enzymol* **2002**, *343*, 183.

(14) Hanson, D. K.; Mielke, D. L.; Laible, P. D. In *Current Topics in Membranes, Volume 63*; Volume 63 ed.; DeLucas, L., Ed.; Academic Press: 2009, p 51.

(15) Tanabe, M.; Iverson, T. M. In *Current Topics in Membranes, Volume 63*; Volume 63 ed.; DeLucas, L., Ed.; Academic Press: 2009, p 229.

(16) Ostermeier, C.; Michel, H. *Current Opinion in Structural Biology* **1997**, *7*, 697.

(17) Geertsma, E. R.; Groeneveld, M.; Slotboom, D. J.; Poolman, B. *P Natl Acad Sci USA* **2008**, *105*, 5722.

(18) Newby, Z. E. R.; O'Connell, J. D.; Gruswitz, F.; Hays, F. A.; Harries, W. E. C.; Harwood, I. M.; Ho, J. D.; Lee, J. K.; Savage, D. F.; Miercke, L. J. W.; Stroud, R. M. **2009**, *4*, 619.

(19) Hunte, C.; Michel, H. *Current Opinion in Structural Biology* **2002**, *12*, 503.

(20) Landau, E. M. In *Methods and Results in Crystallization of Membrane Proteins*; Iwata, S., Ed. 2003, p 37.
(21) Zhou, H.-X. *The Journal of Physical Chemistry B* **2009**, *113*, 7995.
(22) Phillips, R.; Ursell, T.; Wiggins, P.; Sens, P. **2009**, *459*, 379.
(23) Ramadurai, S.; Holt, A.; Krasnikov, V.; van den Bogaart, G.; Killian, J. A.; Poolman, B. *J Am Chem Soc* **2009**, *131*, 12650.
(24) Rhinow, D.; Hampp, N. *The Journal of Physical Chemistry B* **2010**, *114*, 549.
(25) Lou, H.; Beis, K.; Naismith, J. H. In *Current Topics in Membranes, Volume 63*; Volume 63 ed.; DeLucas, L., Ed.; Academic Press: 2009, p 269.
(26) Caffrey, M. *Journal of Structural Biology* **2003**, *142*, 108.
(27) Caffrey, M. *Current Opinion in Structural Biology* **2000**, *10*, 486.
(28) Liu, W.; Caffrey, M. *Biochemistry-Us* **2006**, *45*, 11713.
(29) Eriks, L. R.; Mayor, J. A.; Kaplan, R. S. *Anal Biochem* **2003**, *323*, 234.
(30) Zhang, J.; Wang, S.-C.; Lee, C. T. *The Journal of Physical Chemistry B* **2009**, *113*, 8569.
(31) Seddon, A. A.; Curnow, P.; Booth, P. J. *Bba-Biomembranes* **2004**, *1666*, 105.
(32) Caffrey, M. *Ann Rev Biophys* **2009**, *38*, 29.
(33) Navarro, A.; Wu, H.-S.; Wang, S. S. *Separation and Purification Technology* **2009**, *68*, 129.
(34) Chae, P. S.; Laible, P. D.; Gellman, S. H. *Mol. BioSyst. Y1 - 2010/// 2010*.
(35) le Maire, M.; Champeil, P.; Moller, J. V. *Bba-Biomembranes* **2000**, *1508*, 86.
(36) Iacovache, I.; Biasini, M.; Kowal, J.; Kukulski, W.; Chami, M.; van der Goot, F. G.; Engel, A.; Rémigy, H.-W. *Journal of Structural Biology*, *In Press, Corrected Proof*.
(37) Nollert, P. *Prog Biophys Mol Bio* **2005**, *88*, 339.
(38) Yoshikawa, S.; Shinzawaitoh, K.; Ueda, H.; Tsukihara, T.; Fukumoto, Y.; Kubota, T.; Kawamoto, M.; Fukuyama, K.; Matsubara, H. *J Cryst Growth* **1992**, *122*, 298.
(39) Garavito, R. M.; Picot, D. *Methods* **1990**, *1*, 57.
(40) Rummel, G.; Hardmeyer, A.; Widmer, C.; Chiu, M. L.; Nollert, P.; Locher, K. P.; Pedruzzi, I.; Landau, E. M.; Rosenbusch, J. P. *Journal of Structural Biology* **1998**, *121*, 82.
(41) Ostermeier, C.; Iwata, S.; Ludwig, B.; Michel, H. *Nat Struct Biol* **1995**, *2*, 842.
(42) Persson, G.; Edlund, H.; Lindblom, G. *European Journal of Biochemistry* **2003**, *270*, 56.
(43) Johansson, L. C.; Wöhri, A. B.; Katona, G.; Engström, S.; Neutze, R. *Current Opinion in Structural Biology* **2009**, *19*, 372.
(44) Knowles, T. J.; Finka, R.; Smith, C.; Lin, Y.-P.; Dafforn, T.; Overduin, M. *J Am Chem Soc* **2009**, *131*, 7484.
(45) Pebay-Peyroula, E.; Rummel, G.; Rosenbusch, J. P.; Landau, E. M. *Science* **1997**, *277*, 1676.
(46) Nollert, P. *Methods* **2004**, *34*, 348.
(47) Caffrey, M. *Cryst Growth Des* **2008**, *8*, 4244.
(48) Caffrey, M.; Lyons, J.; Smyth, T.; Hart, D. J. In *Current Topics in Membranes, Volume 63*; Volume 63 ed.; DeLucas, L., Ed.; Academic Press: 2009, p 83.
(49) Caffrey, M.; Cherezov, V. **2009**, *4*, 706.
(50) Cherezov, V.; Yamashita, E.; Liu, W.; Zhalnina, M.; Cramer, W. A.; Caffrey, M. *J Mol Biol* **2006**, *364*, 716.
(51) Cherezov, V.; Liu, W.; Derrick, J. P.; Luan, B.; Aksimentiev, A.; Katritch, V.; Caffrey, M. *Proteins: Structure, Function, and Bioinformatics* **2008**, *71*, 24.
(52) Li, L.; Fu, Q.; Kors, C.; Stewart, L.; Nollert, P.; Laible, P.; Ismagilov, R. *Microfluid Nanofluid* **2009**, *8*, 789.
(53) Nollert, P.; Qiu, H.; Caffrey, M.; Rosenbusch, J. P.; Landau, E. M. *Febs Lett* **2001**, *504*, 179.
(54) Cherezov, V.; Clogston, J.; Papiz, M. Z.; Caffrey, M. *J Mol Biol* **2006**, *357*, 1605.

(55) Cherezov, V.; Caffrey, M. *Faraday Discussions* **2007**, *136*, 195.

(56) Cherezov, V.; Caffrey, M. *J Appl Crystallogr* **2006**, *39*, 604.

(57) Chiu, M. L.; Nollert, P.; Loewen, M. C.; Belrhali, H.; Pebay-Peyroula, E.; Rosenbusch, J. P.; Landau, E. M. *Acta Crystallogr D* **2000**, *56*, 781.

(58) Efremov, R.; Shiryaeva, G.; Bueldt, G.; Islamov, A.; Kuklin, A.; Yaguzhinsky, L.; Fragneto-Cusani, G.; Gordeliy, V. *Journal of Crystal Growth: Proceedings of the 14th International Conference on Crystal Growth and the 12th International Conference on Vapor Growth and Epitaxy* **2005**, *275*, e1453.

(59) Grabe, M.; Neu, J.; Oster, G.; Nollert, P. *Biophys J* **2003**, *84*, 854.

(60) Nollert, P. In *Methods and Results in Crystallization of Membrane Proteins*; Iwata, S., Ed. 2003, p 57.

(61) Kolbe, M.; Besir, H.; Essen, L. O.; Oesterhelt, D. *Science* **2000**, *288*, 1390.

(62) Kors, C. A.; Wallace, E.; Davies, D. R.; Li, L.; Laible, P. D.; Nollert, P. *Acta Crystallographica Section D* **2009**, *65*, 1062.

(63) Liu, W.; Caffrey, M. *Journal of Structural Biology* **2005**, *150*, 23.

(64) Luecke, H.; Schobert, B.; Lanyi, J. K.; Spudich, E. N.; Spudich, J. L. *Science* **2001**, *293*, 1499.

(65) Lunde, C. S.; Rouhani, S.; Facciotti, M. T.; Glaeser, R. M. *Journal of Structural Biology* **2006**, *154*, 223.

(66) Cherezov, V.; Clogston, J.; Misquitta, Y.; Abdel-Gawad, W.; Caffrey, M. *Biophys J* **2002**, *83*, 3393.

(67) Misquitta, L. V.; Misquitta, Y.; Cherezov, V.; Slattery, O.; Mohan, J. M.; Hart, D.; Zhalnina, M.; Cramer, W. A.; Caffrey, M. *Structure* **2004**, *12*, 2113.

(68) Misquitta, Y.; Caffrey, M. *Biophys J* **2003**, *85*, 3084.

(69) Misquitta, Y.; Caffrey, M. *Biophys J* **2001**, *81*, 1047.

(70) Misquitta, Y.; Cherezov, V.; Havas, F.; Patterson, S.; Mohan, J. M.; Wells, A. J.; Hart, D. J.; Caffrey, M. *Journal of Structural Biology* **2004**, *148*, 169.

(71) Peddi, A.; Muthusubramaniam, L.; Zheng, Y. F.; Cherezov, V.; Misquitta, Y.; Caffrey, M. *IEEE Transactions on Automation Science and Engineering* **2007**, *4*, 129.

(72) Nollert, P.; Royant, A.; Pebay-Peyroula, E.; Landau, E. M. *Febs Lett* **1999**, *457*, 205.

(73) Paas, Y.; Cartaud, J.; Recouvreur, M.; Grailhe, R.; Dufresne, V.; Pebay-Peyroula, E.; Landau, E. M.; Changeux, J. P. *P Natl Acad Sci USA* **2003**, *100*, 11309.

(74) Perry, S. L.; Roberts, G. W.; Tice, J. D.; Gennis, R. B.; Kenis, P. J. A. *Cryst Growth Des* **2009**, *9*, 2566.

(75) Qutub, Y.; Reviakine, I.; Maxwell, C.; Navarro, J.; Landau, E. M.; Vekilov, P. G. *J Mol Biol* **2004**, *343*, 1243.

(76) Rouhani, S.; Facciotti, M. T.; Woodcock, G.; Cheung, V.; Cunningham, C.; Nguyen, D.; Rad, B.; Lunde, C. S.; Glaeser, R. M. *Biopolymers* **2002**, *66*, 300.

(77) Sennoga, C.; Heron, A.; Seddon, J. M.; Templer, R. H.; Hankamer, B. *Acta Crystallogr D* **2003**, *59*, 239.

(78) Pebay-Peyroula, E.; Rosenbusch, J. P. *Current Opinion in Structural Biology* **2001**, *11*, 427.

(79) Cherezov, V.; Rosenbaum, D. M.; Hanson, M. A.; Rasmussen, S. G. F.; Thian, F. S.; Kobilka, T. S.; Choi, H. J.; Kuhn, P.; Weis, W. I.; Kobilka, B. K.; Stevens, R. C. *Science* **2007**, *318*, 1258.

(80) Jaakola, V. P.; Griffith, M. T.; Hanson, M. A.; Cherezov, V.; Chien, E. Y. T.; Lane, J. R.; IJzerman, A. P.; Stevens, R. C. *Science* **2008**, *322*, 1211.

(81) Rosenbaum, D. M.; Cherezov, V.; Hanson, M. A.; Rasmussen, S. G. F.; Thian, F. S.; Kobilka, T. S.; Choi, H. J.; Yao, X. J.; Weis, W. I.; Stevens, R. C.; Kobilka, B. K. *Science* **2007**, *318*, 1266.

(82) Lanyi, J. K.; Schobert, B. *Biochemistry-Us* **2004**, *43*, 3.

(83) Gordeliy, V. I.; Labahn, J.; Moukhametzianov, R.; Efremov, R.; Granzin, J.; Schlesinger, R.; Buldt, G.; Savopol, T.; Scheidig, A. J.; Klare, J. P.; Engelhard, M. *Nature* **2002**, *419*, 484.

(84) Katona, G.; Andreasson, U.; Landau, E. M.; Andreasson, L.-E.; Neutze, R. *J Mol Biol* **2003**, *331*, 681.

(85) Deisenhofer, J.; Epp, O.; Sinning, I.; Michel, H. *J Mol Biol* **1995**, *246*, 429.

(86) Hunte, C.; Richers, S. *Current Opinion in Structural Biology* **2008**, *18*, 406.

(87) Wöhri, A. B.; Johansson, L. C.; Wadsten-Hindrichsen, P.; Wahlgren, W. Y.; Fischer, G.; Horsefield, R.; Katona, G.; Nyblom, M.; Öberg, F.; Young, G.; Cogdell, R. J.; Fraser, N. J.; Engström, S.; Neutze, R. *Structure* **2008**, *16*, 1003.

(88) Porcar, L.; Hamilton, W. A.; Butler, P. D. *Langmuir* **2003**, *19*, 10779.

(89) Wadsten, P.; Wo?hri, A. B.; Snijder, A.; Katona, G.; Gardiner, A. T.; Cogdell, R. J.; Neutze, R.; Engström, S. *J Mol Biol* **2006**, *364*, 44.

(90) Gabrielsen, M.; Gardiner, A. T.; Fromme, P.; Cogdell, R. J. In *Current Topics in Membranes, Volume 63*; Volume 63 ed.; DeLucas, L., Ed.; Academic Press: 2009, p 127.

(91) Engström, S.; Alfons, K.; Rasmusson, M.; Ljusberg-Wahren, H. *Progress in Colloid and Polymer Science* **1998**, *108*, 93.

(92) Wacker, D.; Fenalti, G.; Brown, M. A.; Katritch, V.; Abagyan, R.; Cherezov, V.; Stevens, R. C. *J Am Chem Soc* **2010**, *132*, 11443.

(93) Rosenbusch, J. P. *Journal of Structural Biology* **1990**, *104*, 134.

(94) Li, L.; Nachtergaele, S.; Seddon, A. M.; Tereshko, V.; Ponomarenko, N.; Ismagilov, R. F. *J Am Chem Soc* **2008**, *130*, 14324.

(95) Fritzsch, G. In *Photosynthesis: Molecular Biology of Energy Capture*; Volume 297 ed.; McIntosh, L., Ed.; Academic Press: 1998, p 57.

(96) Faham, S.; Ujwal, R.; Abramson, J.; Bowie, J. U. In *Current Topics in Membranes, Volume 63*; Volume 63 ed.; DeLucas, L., Ed.; Academic Press: 2009, p 109.

(97) Michel, H. *Embo J* **1982**, *1*, 1267.

(98) Hubalek, F.; Binda, C.; Li, M.; Mattevi, A.; Edmondson, D. E. *Acta Crystallogr D* **2003**, *59*, 1874.

(99) Li, L.; Mustafi, D.; Fu, Q.; Tereshko, V.; Chen, D. L. L.; Tice, J. D.; Ismagilov, R. F. *P Natl Acad Sci USA* **2006**, *103*, 19243.

(100) Ostermeier, C.; Harrenga, A.; Ermler, U.; Michel, H. *P Natl Acad Sci USA* **1997**, *94*, 10547.

(101) Caffrey, M. *Current Opinion in Structural Biology* **2002**, *12*, 471.

(102) Newstead, S.; Ferrandon, S.; Iwata, S. *Protein Sci* **2008**, *17*, 466.

(103) Abramson, J.; Riistama, S.; Larsson, G.; Jasaitis, A.; Svensson-Ek, M.; Laakkonen, L.; Puustinen, A.; Iwata, S.; Wikstrom, M. *Nat Struct Biol* **2000**, *7*, 910.

(104) Aoyama, H.; Muramoto, K.; Shinzawa-Itoh, K.; Hirata, K.; Yamashita, E.; Tsukihara, T.; Ogura, T.; Yoshikawa, S. *P Natl Acad Sci USA* **2009**, *106*, 2165.

(105) Fei, M. J.; Yamashita, E.; Inoue, N.; Yao, M.; Yamaguchi, H.; Tsukihara, T.; Shinzawa-Ito, K.; Nakashima, R.; Yoshikawa, S. *Acta Crystallogr D* **2000**, *56*, 529.

(106) Hunsicker-Wang, L. M.; Pacoma, R. L.; Chen, Y.; Fee, J. A.; Stout, C. D. *Acta Crystallogr D* **2005**, *61*, 340.

(107) Iwata, S.; Ostermeier, C.; Ludwig, B.; Michel, H. *Nature* **1995**, *376*, 660.

(108) Tsukihara, T.; Aoyama, H.; Yamashita, E.; Tomizaki, T.; Yamaguchi, H.; ShinzawaItoh, K.; Nakashima, R.; Yaono, R.; Yoshikawa, S. *Science* **1996**, *272*, 1136.

(109) Tsukihara, T.; Aoyama, H.; Yamashita, E.; Tomizaki, T.; Yamaguchi, H.; Shinzawaitoh, K.; Nakashima, R.; Yaono, R.; Yoshikawa, S. *Science* **1995**, *269*, 1069.

(110) Harrenga, A.; Michel, H. *J Biol Chem* **1999**, *274*, 33296.

(111) Svensson-Ek, M.; Abramson, J.; Larsson, G.; Tornroth, S.; Brzezinski, P.; Iwata, S. *J Mol Biol* **2002**, *321*, 329.

(112) Qin, L.; Hiser, C.; Mulichak, A.; Garavito, R. M.; Ferguson-Miller, S. *P Natl Acad Sci USA* **2006**, *103*, 16117.

(113) Qin, L.; Liu, J.; Mills, D. A.; Proshlyakov, D. A.; Hiser, C.; Ferguson-Miller, S. *Biochemistry-Us* **2009**, *48*, 5121.

(114) Qin, L.; Mills, D. A.; Buhrow, L.; Hiser, C.; Ferguson-Miller, S. *Biochemistry-Us* **2008**, *47*, 9931.

(115) Soulimane, T.; Buse, G.; Bourenkov, G. P.; Bartunik, H. D.; Huber, R.; Than, M. E. *Embo J* **2000**, *19*, 1766.

(116) Liu, B.; Luna, V. M.; Chen, Y.; Stout, C. D.; Fee, J. A. *Acta Crystallographica Section F: Structural Biology and Crystallization Communications* **2007**, *63*, 1029.

(117) Luna, V. M.; Chen, Y.; Fee, J. A.; Stout, C. D. *Biochemistry-Us* **2008**, *47*, 4657.

(118) Inaba, K.; Murakami, S.; Suzuki, M.; Nakagawa, A.; Yamashita, E.; Okada, K.; Ito, K. *Cell* **2006**, *127*, 789.

(119) Allen, J. P. *Proteins* **1994**, *20*, 283.

(120) Chang, C. H.; Schiffer, M.; Tiede, D.; Smith, U.; Norris, J. *J Mol Biol* **1985**, *186*, 201.

(121) Deisenhofer, J.; Epp, O.; Miki, K.; Huber, R.; Michel, H. *Nature* **1985**, *318*, 618.

(122) Stowell, M. H. B.; McPhillips, T. M.; Rees, D. C.; Soltis, S. M.; Abresch, E.; Feher, G. *Science* **1997**, *276*, 812.

(123) RCSB Protein Data Bank. http://www.rcsb.org/ (July 11, 2010).

(124) Raman, P.; Cherezov, V.; Caffrey, M. *Cellular and Molecular Life Sciences (CMLS)* **2006**, *63*, 36.

(125) Membrane Proteins of Known 3D Structure. http://blanco.biomol.uci.edu/Membrane_Proteins_xtal.html (July 11, 2010).

(126) Buschmann, S.; Warkentin, E.; Xie, H.; Langer, J. D.; Ermler, U.; Michel, H. *Science* **2010**, *329*, 327.

(127) Faham, S.; Boulting, G. L.; Massey, E. A.; Yohannan, S.; Yang, D.; Bowie, J. U. *Protein Sci* **2005**, *14*, 836.

(128) Faham, S.; Bowie, J. U. *J Mol Biol* **2002**, *316*, 1.

(129) Rasmussen, S. G. F.; Choi, H. J.; Rosenbaum, D. M.; Kobilka, T. S.; Thian, F. S.; Edwards, P. C.; Burghammer, M.; Ratnala, V. R. P.; Sanishvili, R.; Fischetti, R. F.; Schertler, G. F. X.; Weis, W. I.; Kobilka, B. K. *Nature* **2007**, *450*, 383.

(130) Höfer, N.; Aragão, D.; Caffrey, M. *Biophys J* **2010**, *99*, L23.

(131) Caffrey, M.; Cheng, A. *Current Opinion in Structural Biology* **1995**, *5*, 548.

(132) Cherezov, V.; Fersi, H.; Caffrey, M. *Biophys J* **2001**, *81*, 225.

(133) Takahashi, H.; Matsuo, A.; Hatta, I. *Phys Chem Chem Phys* **2002**, *4*, 2365.

(134) Sparr, E.; Wadsten, P.; Kocherbitov, V.; Engstrom, S. *Bba-Biomembranes* **2004**, *1665*, 156.

(135) Borshchevskiy, V.; Efremov, R.; Moiseeva, E.; Buldt, G.; Gordeliy, V. *Acta Crystallographica Section D* **2010**, *66*, 26.

(136) Cherezov, V.; Liu, J.; Griffith, M.; Hanson, M. A.; Stevens, R. C. *Cryst Growth Des* **2008**, *8*, 4307.

(137) Liu, W.; Hanson, M. A.; Stevens, R. C.; Cherezov, V. *Biophys J* **2010**, *98*, 1539.

(138) Bonacucina, G.; Palmieri, G. F.; Craig, D. Q. M. *J Pharm Sci-Us* **2005**, *94*, 2452.

(139) Mezzenga, R.; Meyer, C.; Servais, C.; Romoscanu, A. I.; Sagalowicz, L.; Hayward, R. C. *Langmuir* **2005**, *21*, 3322.

(140) Persson, G.; Edlund, H.; Amenitsch, H.; Laggner, P.; Lindblom, G. *Langmuir* **2003**, *19*, 5813.

(141) Vargas, R.; Mateu, L.; Romero, A. *Chem Phys Lipids* **2004**, *127*, 103.

(142) Takahashi, H.; Matsuo, A.; Hatta, I. *Mol Cryst Liq Cryst* **2000**, *347*, 475.

(143) Awad, T. S.; Okamoto, Y.; Masum, S. M.; Yamazaki, M. *Langmuir* **2005**, *21*, 11556.

(144) Caboi, F.; Nylander, T.; Razumas, V.; Talaikyte, Z.; Monduzzi, M.; Larsson, K. *Langmuir* **1997**, *13*, 5476.

(145) Engblom, J.; Miezis, Y.; Nylander, T.; Razumas, V.; Larsson, K. In *Surface and Colloid Science*; Springer: Berlin / Heidelberg, 2000; Vol. 116, p 9.

(146) Li, S. J.; Yamashita, Y.; Yamazaki, M. *Biophys J* **2001**, *81*, 983.
(147) Masum, S. M.; Li, S. J.; Awad, T. S.; Yamazaki, M. *Langmuir* **2005**, *21*, 5290.
(148) Murgia, S.; Lampis, S.; Angius, R.; Berti, D.; Monduzzi, M. *The Journal of Physical Chemistry B* **2009**, *113*, 9205.
(149) Okamoto, Y.; Masum, S. M.; Miyazawa, H.; Yamazaki, M. *Langmuir* **2008**, *24*, 3400.
(150) Razumas, V.; Larsson, K.; Miezis, Y.; Nylander, T. *J Phys Chem-Us* **1996**, *100*, 11766.
(151) Razumas, V.; Talaikyte, Z.; Barauskas, J.; Larsson, K.; Miezis, Y.; Nylander, T. *Chem Phys Lipids* **1996**, *84*, 123.
(152) Caffrey, M. *Biochemistry-Us* **1987**, *26*, 6349.
(153) Cherezov, V.; Caffrey, M. *J Appl Crystallogr* **2005**, *38*, 398.
(154) Cheng, A. H.; Hummel, B.; Qiu, H.; Caffrey, M. *Chem Phys Lipids* **1998**, *95*, 11.
(155) Ai, X.; Caffrey, M. *Biophys J* **2000**, *79*, 394.
(156) Boyle-Roden, E.; Hoefer, N.; Dey, K. K.; Grandinetti, P. J.; Caffrey, M. *J Magn Reson* **2007**, *189*, 13.
(157) Qiu, H.; Caffrey, M. *Biomaterials* **2000**, *21*, 223.
(158) Cherezov, V.; Peddi, A.; Muthusubramaniam, L.; Zheng, Y. F.; Caffrey, M. *Acta Crystallogr D* **2004**, *60*, 1795.
(159) Luecke, H.; Schobert, B.; Richter, H. T.; Cartailler, J. P.; Lanyi, J. K. *J Mol Biol* **1999**, *291*, 899.
(160) Hanson, M. A.; Stevens, R. C. *Structure* **2009**, *17*, 8.
(161) Hofmeister, F. *Arch. Exptl. Pathol. Pharmakol.* **1888**, *24*, 247.
(162) Luecke, H.; Richter, H. T.; Lanyi, J. K. *Science* **1998**, *280*, 1934.
(163) Belrhali, H.; Nollert, P.; Royant, A.; Menzel, C.; Rosenbusch, J. P.; Landau, E. M.; Pebay-Peyroula, E. *Structure* **1999**, *7*, 909.
(164) Edman, K.; Nollert, P.; Royant, A.; Belrhali, H.; Pebay-Peyroula, E.; Hajdu, J.; Neutze, R.; Landau, E. M. *Nature* **1999**, *401*, 822.
(165) Luecke, H.; Schobert, B.; Richter, H. T.; Cartailler, J. P.; Lanyi, J. K. *Science* **1999**, *286*, 255.
(166) Luecke, H.; Schobert, B.; Cartailler, J. P.; Richter, H. T.; Rosengarth, A.; Needleman, R.; Lanyi, J. K. *J Mol Biol* **2000**, *300*, 1237.
(167) Rouhani, S.; Cartailler, J. P.; Facciotti, M. T.; Walian, P.; Needleman, R.; Lanyi, J. K.; Glaeser, R. M.; Luecke, H. *J Mol Biol* **2001**, *313*, 615.
(168) Schobert, B.; Cupp-Vickery, J.; Hornak, V.; Smith, S. O.; Lanyi, J. K. *J Mol Biol* **2002**, *321*, 715.
(169) Facciotti, M. T.; Cheung, V. S.; Nguyen, D.; Rouhani, S.; Glaeser, R. M. *Biophys J* **2003**, *85*, 451.
(170) Facciotti, M. T.; Cheung, V. S.; Lunde, C. S.; Rouhani, S.; Baliga, N. S.; Glaeser, R. M. *Biochemistry-Us* **2004**, *43*, 4934.
(171) Reshetnyak, A.; Borshchevskiy, V.; Klare, J.; Moiseeva, E.; Engelhardt, M.; Buldt, G.; Gordeliy, V. *Journal of Surface Investigation: X-ray, Synchrotron and Neutron Techniques* **2008**, *2*, 894.
(172) Briggs, J.; Chung, H.; Caffrey, M. *J Phys Ii* **1996**, *6*, 723.
(173) Briggs, J.; Caffrey, M. *Biophys J* **1994**, *66*, 573.
(174) Yaghmur, A.; Kriechbaum, M.; Amenitsch, H.; Steinhart, M.; Laggner, P.; Rappolt, M. *Langmuir* **2010**, *26*, 1177.
(175) Saturni, L.; Rustichelli, F.; Di Gregorio, G. M.; Cordone, L.; Mariani, P. *Phys Rev E* **2001**, *6404*.
(176) Bitan-Cherbakovsky, L.; Yuli-Amar, I.; Aserin, A.; Garti, N. *Langmuir* **2009**.
(177) Clogston, J.; Caffrey, M. *J Control Release* **2005**, *107*, 97.
(178) Emerald BioSystems Inc. http://www.emeraldbiosystems.com (July 2, 2010).
(179) Carbonnaux, C.; Rieskautt, M.; Ducruix, A. *Protein Sci* **1995**, *4*, 2123.
(180) Lorber, B.; Delucas, L. J.; Bishop, J. B. *J Cryst Growth* **1991**, *110*, 103.
(181) Zhang, Y.; Cremer, P. S. *Curr Opin Chem Biol* **2006**, *10*, 658.

(182) Ducruix, A. F.; Ries-Kautt, M. M. *Methods* **1990**, *1*, 25.
(183) Ries-Kautt, M. M.; Ducruix, A. F. *J Biol Chem* **1989**, *264*, 745.
(184) Forsythe, E. L.; Pusey, M. L. *J Cryst Growth* **1996**, *168*, 112.
(185) Efrat, R.; Abramov, Z.; Aserin, A.; Garti, N. *The Journal of Physical Chemistry B* **2010**, *114*, 10709.
(186) Parthasarathy, R.; Groves, J. T. *Soft Matter* **2007**, *3*, 24.

Chapter 3

Overcoming the Challenge of Pumping Viscous Fluids at the Microscale*

Abstract

The use of fluids that are significantly more viscous than water in microfluidics has been limited due to their high resistance to flow in microscale channels. This chapter reports a theoretical treatment for flow of highly viscous fluids in deforming microfluidic channels, particularly with respect to transient effects, and discusses the implications of these effects on the design of appropriate microfluidic devices for highly viscous fluids. Theory describing flow in a deforming channel is coupled with design equations, both for steady-state flows and for the transient periods associated with the initial deformation and final relaxation of a channel. The results of this analysis allow for the description of these systems and also an assessment of the significance of different parameters on various deformation and/or transient effects. To exemplify their utility, these design rules were applied to two applications: (i) pumping highly viscous fluids for a nanoliter scale mixing application and (ii) precise metering of fluids in microfluidics.

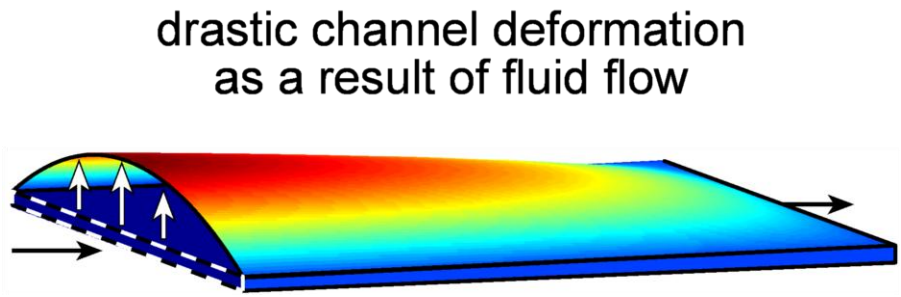

* Part of this work has been published: S.L. Perry, J.J.L. Higdon, and P.J.A. Kenis, *Design Rules for Pumping and Metering of Highly Viscous Fluids*, Lab on a Chip 2010 Vol. 10(22), 3112-3124.

3.1 Introduction

Microfluidic approaches have been demonstrated for a wide variety of applications ranging from virus detection[1] and protein crystallization[2] to distillation[3] and fuel cells.[4] The idea of a "lab on a chip," capable of performing ever more complex chemical and/or biological processes, has been realized in numerous examples through the integration of multiple unit operations such as mixing, reaction, separation, and detection on a single chip. Soft lithography continues to spur the development of microfluidic technology by providing a fast and easy method for the rapid prototyping of highly complex networks of channels with integrated pneumatic valves and peristaltic pumps.[5] The elastomer polydimethylsiloxane (PDMS) has been used in particular for this purpose because of its ability to replicate features down to sub-micrometer length scales, such as photolithographically defined channel networks, and the ease by which the resulting molded layers can be assembled into fully functional microfluidic chips.[6] Additional advantages of PDMS over other materials include its optical transparency and its elasticity. The bulk properties of PDMS are equivalent to an incompressible rubber-like elastic material, with a Young's modulus *E* typically in the range of 0.5 to 4 MPa and a Poisson ratio of $\sigma = 0.5$.[7,8] The pneumatic valves and peristaltic pumps that are now being used in many microfluidic devices would not be possible without the high level of deformability of PDMS.[9-11] A number of models for these pneumatic valves and pumps have been reported to describe and predict their operation.[12-14]

To date microfluidic applications have been mostly limited to systems where the fluid viscosities are similar to that of water because of the challenges associated with pumping highly viscous and/or non-Newtonian flows. In fact, the pressures that would be required to drive highly viscous fluids (*i.e.*, ~10^5x more viscous than water) through a typical microfluidic channel can be extreme, to the point of exceeding the ability of most pumping systems used for microfluidics, and/or the capacity of the materials to sustain such high pressures.[15-17] Thus, strategies that overcome these challenges are needed to enable the pumping of viscous fluids. In designing a microfluidic device for use with highly viscous fluids the single most important consideration is the viscous resistance to flow. Microfluidic devices are typically operated under conditions of low Reynolds number flow. Steady-state operation at low Reynolds number requires $\rho uh/\eta << 1$ while for unsteady flow we have the additional requirement that $\rho\omega h/\eta << 1$, where ρ is the fluid density, u is the linear flow velocity, h is the channel height, is the η fluid viscosity, and ω is the frequency of oscillation. For the laminar flows encountered in microfluidic devices, resistance to flow scales linearly with viscosity and the length of a channel and with the inverse square of the cross-sectional area of a channel.[18] Thus for a specified maximum pressure, flow resistance can be decreased by decreasing the length over which the fluid is flowing, and especially by enlarging the cross-sectional area of the channel. While these geometric modifications can be used to facilitate flow of viscous fluids, the pressures required for flow in a given microfluidic configuration may cause the microfluidic channels to deform, particularly if elastomeric materials such as PDMS are used. Channel deformation occurs if the applied pressure exceeds the stiffness of the material. Channel geometry will vary as a function of pressure, which in turn varies as a function of position along the channel. Deformation will be larger at the inlet of the channel

where the pressure is highest, and will decrease towards the outlet. Previous studies have discussed the effects of channel deformation in microfluidic configurations, but these studies were limited to externally driven, steady-state flow.[7,19,20] Channel deformation has also been useful experimentally. Hardy *et al*. developed a microfluidic analog for the study of blood vessels by exploiting the deformability of microchannels in PDMS.[19] Channel deformation as a result of viscous fluid flow in non-rigid channels also introduces a variety of transient phenomena that may have a profound effect on the operations performed on-chip, such as the precise metering of fluids which is required in many microfluidic applications. For these and several other on-chip operations, transients as a result of viscous fluid flow must be taken into account, yet mathematical descriptions to estimate these transients are presently not available.

This chapter develops relevant theory for the flow of highly viscous fluids in deforming microfluidic channels, particularly with respect to transient effects, and discusses potential implications on the design of appropriate microfluidic devices for such highly viscous fluids. A simple model for a pneumatic valve will be introduced to characterize the efficiency whereby an applied valve actuation pressure is translated into a driving force for fluid flow, and scaling relationships between valve actuation and flow effects will be identified to aid the design of microfluidic chips for viscous flows (Section 3.2.1). Next the effects of channel deformation on viscous flows will be considered. After a steady-state analysis similar to prior work (Section 3.2.2.1),[7,19,20] relevant theory will be derived for the fully transient problem (Section 3.2.2.2). The results of the theoretical analysis will then be applied to (i) the challenges of pumping and precise metering of viscous fluids despite channel deformation effects, and (ii) the design of a microfluidic device for the mixing of highly viscous and non-Newtonian fluids.

3.2 Theory

3.2.1 The Effect of Valve Membrane Actuation on Pressure-Driven Flow in a Rigid Channel

The use of integrated microfluidic pneumatic pumps, comprised of three peristaltic valves in series,[2,9,11] has become increasingly common, particularly in highly complex microfluidic networks. This kind of on-chip method to drive fluid flow is desirable because it enables complex fluid routing while providing better precision and flexibility than external pressure sources. In a multilayer microfluidic device, a valve can be defined by an area where a microfluidic feature from one layer overlaps with that of a second layer, either above or below. A thin membrane of elastomeric material separates these two layers and deflects upon the application of pressure to the valve layer, translating an externally applied pressure to an internally applied pressure via deflection of the membrane and eventually sealing off flow in the fluid layer (Figure 3.1a). An on-chip pump can be created by placing three or more of these valves in series and actuating them in a sequence to create a peristaltic pumping action (Figure 3.1b).[9]

A linearized model, valid for small deflection of a thin membrane was used to understand the effects of various design parameters on the operation of these valves and the resultant downstream pressure on the fluid.[21] More accurate predictions may be obtained using detailed non-linear analyses,[12-14] however,

the linear model captures the essential scaling needed for the initial design of microfluidic valves. For the case of a circular membrane, the pressure drop associated with this deflection is described by

$$P_{appl} - P_{in} = \frac{16Ea^3 z}{3(1-\sigma^2)s^4} \tag{3-1}$$

where the Young's modulus E and Poisson's ratio σ characterize the deformability of the valve material, and the valve membrane is of radius s, thickness a, and experiences an applied pressure P_{appl} (Figure 3.1d). Deflection of the membrane is taken to be in the z-direction and is characteristic of the amount of deflection of the center of the membrane. Full actuation of the valve is defined when $z = h_v$, the height of the valve chamber. Within the valve chamber, the assumption is made that the only pressure losses are those due to deflection of the membrane, resulting in a pressure in the valve chamber of P_{in}.

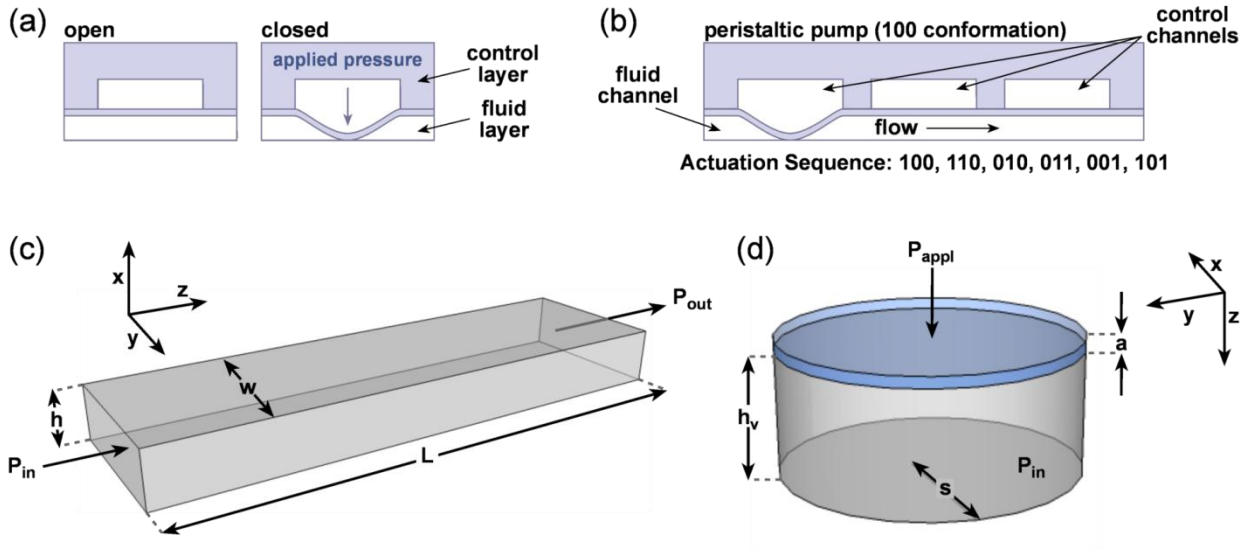

Figure 3.1. **(a)** Depiction of the actuation of a push-down type pneumatic valve. **(b)** Depiction of a 3-phase peristaltic pump where a set of three pneumatic valves are actuated in sequence to drive fluid flow. The (100) actuation phase is shown. **(c)** Schematic depiction of a microfluidic channel of length L, width w, and height h. Inlet pressure is P_{in}, pressure at outlet is P_{out}. **(d)** Depiction of a theoretical pneumatic valve with circular membrane (highlighted in blue) of radius s and thickness a to be deflected a height h_v. Applied pressure is P_{appl}, pressure inside of the valve is P_{in}.

Eq. (3-1) can be used to consider the pressure driving force available for pumping after valve actuation, assuming a pressure difference across the valve of $\Delta P = P_{appl} - P_{in}$. Eq. (3-1) can be normalized by the applied pressure P_{appl} and a parameter α can be defined that describes the pressure losses associated with the actuation, or stiffness, of the valve.

$$\alpha = \frac{P_{appl} - P_{in}}{P_{appl}} = \frac{16Ea^3 h_v}{3P_{appl}(1-\sigma^2)s^4} \tag{3-2}$$

From Eq. (3-2) it follows that the term α approaches zero when the pressure losses due to the valve are small. The case where actuation of a pneumatic valve has a negligible effect on the pressures associated with fluid flow can be defined in the limit of ($\alpha \to 0$). This limit can be approached physically

by modifying the stiffness (E/P_{appl}) and/or the geometry (a^3h_v/s^4) of the valve. When the ratio of E/P_{appl} is small, the applied pressure is able to easily overcome the resistance of the valve material to deformation. The thickness of the valve membrane a along with the extent of deflection h_v can be modified along with the radius of the valve s in order to minimize the geometric term a^3h_v/s^4.

A method to determine P_{in}, the pressure available for pumping at the inlet of a microfluidic channel, has now been established, whether it is directly applied by an external source or determined using Eq. (3-1). Fluid flow in a long microfluidic channel of length L, width w, and height h (Figure 3.1c) can now be considered. Typically microfluidic channels have a low aspect ratio such that $w >> h$, and the channel can be treated effectively as an infinite slit. Furthermore, the small dimensions of these channels lead to a small Reynolds number and thus laminar flow. The driving pressure P_{in} is dissipated over the length of the channel to an outlet pressure of P_{out}. The z-axis is taken to be in the direction of flow along the length of the channel.

The hydrodynamics of viscous flow in an infinite slit of rigid geometry are well understood and an expression for the volumetric flowrate $\dot{V}$ can be easily derived in terms of the channel dimensions, pressure gradient dP/dz, and fluid viscosity η.[18]

$$\dot{V} = -\frac{h^3 w}{12\eta}\frac{dP}{dz} \tag{3-3}$$

For a channel of set dimensions, termed a 'rigid' channel, a linear pressure drop ($\Delta P/L$) is realized over the length of the channel with $\Delta P = P_{in} - P_{out}$. Note that since the pressure front is assumed to transfer instantaneously through an incompressible fluid, this result is valid for all times.

3.2.2 The Effect of Channel Deformation on Viscous Flow

In using elastomeric materials, deformation of the bulk material defining a channel is possible (Figure 3.2). Thus, rather than considering a thin membrane as in Section 3.2.1, the deformation of an infinite slab subject to an applied surface pressure will now be considered.

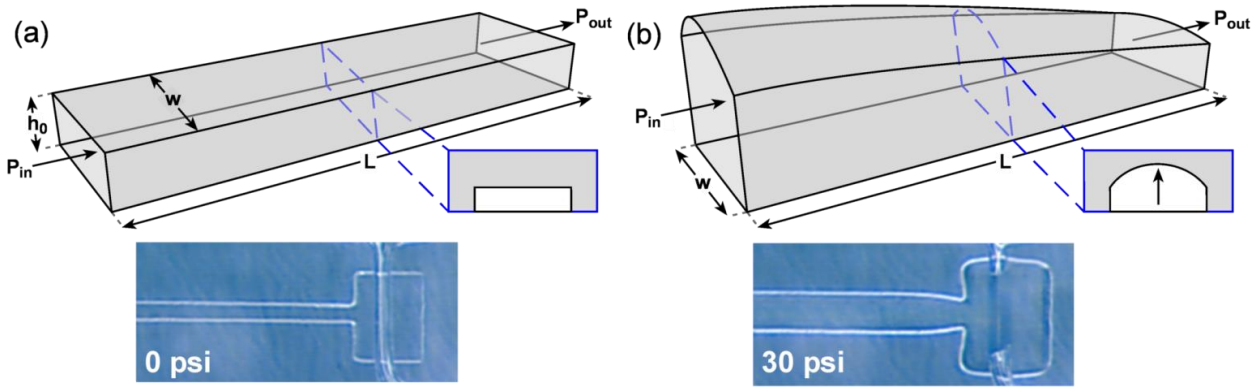

Figure 3.2. Schematic depiction and optical micrograph of **(a)** an undeformed PDMS microfluidic channel and **(b)** a highly deformed PDMS channel under the influence of 207 kPa (30 psi) applied pressure. Schematic depictions are not drawn to scale.

3.2.2.1 Steady-State Viscous Flow in a Deformed Channel

Deformation of the channel can be modeled as a distributed pressure over an infinite slab.[22] For a typical PDMS device on a stiff glass substrate, it is only necessary to consider deformation of the top wall of the microfluidic channel so long as the aspect ratio of the device does not approach unity (also a requirement for viscous flow in an infinite slit).[7,22] The maximum deformation of a slab can be written in terms of the ratio of pressure to Young's modulus P/E, a characteristic length which for a low aspect ratio channel is the width w, and a proportionality constant c which takes into consideration the geometry of the deforming area and is of order of magnitude ~ 1.[7,19,22] Thus,

$$\Delta h_{max} = \frac{cPw\left(1+\sigma\right)}{E} \tag{3-4}$$

Previous work has demonstrated that this deformation is parabolic across the width of a microfluidic channel.[7,19] Owing to the nonlinear dependence on the channel height h in Eq. (3-3), the change in $\dot{V}$ with variable h cannot be captured by using an average value for h. Nonetheless, it is convenient to compute $\langle\Delta h\rangle = 2/3\Delta h_{max}$, as has been done previously, [7,19] and thus an expression for an effective height $h(z)$ along the length of the channel as a function of $P(z)$ and the initial channel height h_0 can be written. Note that the relevant coefficient for the effective height may differ from 2/3 in practice.

$$h\left(z\right) = h_0\left(1+\frac{2cP\left(z\right)w\left(1+\sigma\right)}{3Eh_0}\right) \tag{3-5}$$

Substituting this function for the channel height into our expression for volumetric flowrate from Eq. (3-3), the following expression for the volumetric flowrate in a deformed channel as a function of the pressure drop along the length of the channel is generated.

$$\dot{V} = -\frac{h_0^3 w}{12\eta}\left(1+\frac{2cPw\left(1+\sigma\right)}{3Eh_0}\right)^3\frac{\partial P}{\partial z} \tag{3-6}$$

At steady-state the volumetric flowrate is constant, and Eq. (3-6) can be integrated over the length of the channel assuming an inlet pressure of P_{in} and letting P_{out} = 0. Combining the integrated form of Eq. (3-6) with Eq. (3-3) and defining a non-dimensional parameter β, which characterizes the tendency of a channel to deform, an analytical form of the steady-state volumetric flowrate for a deformed channel can be obtained in terms of the volumetric flowrate for a rigid channel and a correction term that depends on β. The rigid solution can be obtained by setting β = 0.

$$\dot{V}_{ssdef} = \dot{V}_{rigid}\left(1+\frac{3\beta}{2}+\beta^2+\frac{\beta^3}{4}\right) \tag{3-7}$$

where

$$\beta = \frac{2cP_{in}w(1+\sigma)}{3Eh_0} = \frac{2\Delta h_{max}}{h_0} \tag{3-8}$$

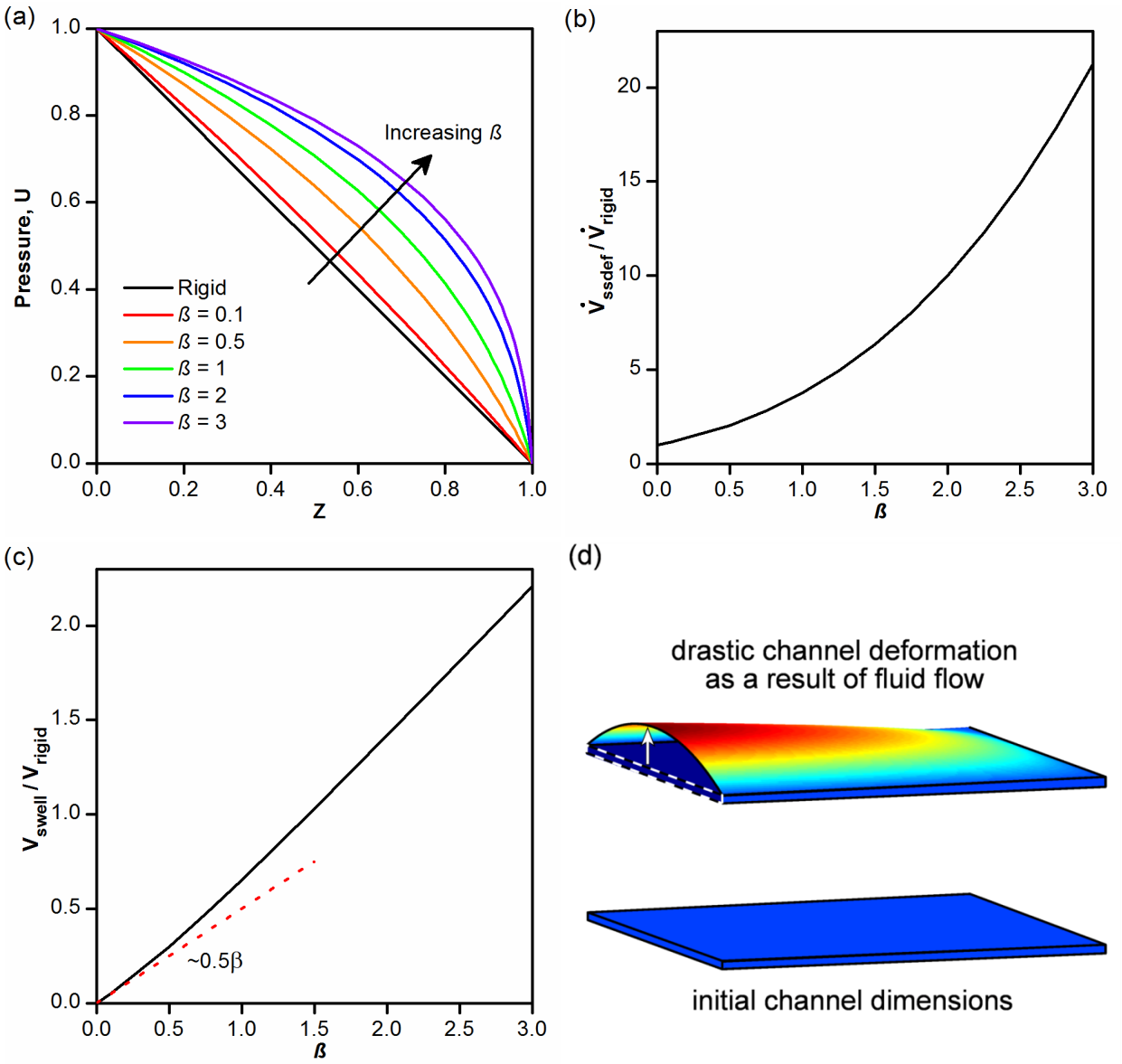

Figure 3.3. **(a)** Steady-state pressure profiles for different values of β along the microfluidic channel. Pressures in the deformed channels are larger than the linear rigid case at all points in the channel. **(b)** Steady-state volumetric flowrate normalized by the flowrate in a rigid channel as a function of the deformation parameter β. **(c)** The change in the channel volume normalized by the rigid channel volume as a function of β. In the limit of small β this curve can be approximated as 0.5β, as shown. **(d)** Depiction of the effects of steady-state channel deformation based on the results of the MATLAB simulation. Image is drawn to scale with h_0 = 10 µm.

β describes the tendency of the material to deform given the ratio P_{in}/E. The larger the applied pressure compared to the Young's modulus, the larger the deformation. For the purposes of the analyses presented here – particularly given the approximation of flow in an infinite slit – an examination of deformation behavior over only the range of $\beta < 3$ will be made. This threshold for analysis was

established based on the aspect ratio of the deformed device such that the assumption of an infinite slit is still valid. For example, if a channel of width w = 100 μm and initial height h_0 = 10 μm is considered, the initial aspect ratio is 0.1, indicating an order of magnitude difference between the two dimensions. However, for the case of β = 3, channel deformation results in an average channel height of h = 40 μm and an aspect ratio of 0.4, indicating that the height and width of the channel are of nearly the same order of magnitude.

To obtain an expression for $P(z)$ Eq. (3-6) is integrated and substituted into Eq. (3-7):

$$P(z) = \frac{P_{in}}{\beta}\left\{\left[\frac{z}{L}\left[1-(1+\beta)^4\right]+(1+\beta)^4\right]^{\frac{1}{4}}-1\right\} \tag{3-9}$$

Owing to the deformation of the channel, a 4th root decay of pressure along the channel length is observed, rather than the linear dependence seen in the rigid case (Figure 3.3a). In the limit of small β, Eq. (3-9) reduces to the rigid limit described by Eq. (3-3).

Combining the expressions for channel height in Eq. (3-5), and pressure in Eq. (3-9), integration over the length of the channel allows for determination of the change in volume V_{swell} due to the deformation.

$$V_{swell} = V_{rigid}\left[\frac{4}{5}\left(\frac{1-(1+\beta)^5}{1-(1+\beta)^4}\right)-1\right] \tag{3-10}$$

Having developed the mathematics behind steady-state flow in a deformed channel, the physical meaning behind some of these results can be considered. As described by Eq. (3-9), and shown in Figure 3.3a, the pressure profile along the length of the channel is nonlinear, which corresponds to the channel deformation. At the beginning of the channel where the large applied pressure results in a large deformation (Figure 3.3d), relatively small pressure losses occur resulting in pressure gradients that are lower than for the purely rigid case. However, near the end of the channel where deformations are small (Figure 3.3d), much steeper pressure gradients are observed. Both channel deformation and steeper pressure gradients combine to enhance the volumetric flowrate. At steady-state, the most significant result of channel deformation is the 3rd order polynomial dependence of the volumetric flowrate on β described by Eq. (3-7) and plotted in Figure 3.3b. While for small deformations this effect can be neglected, a dramatic increase in flowrates is seen at larger deformations. For example, at a value of β = 1, typical for many microfluidic systems, the volumetric flowrate resulting from the deformed channel is 375% higher than the corresponding flowrate expected for a rigid channel. (See Appendix A.1 for calculated values of β as a function of various microfluidic device geometries). An additional effect of channel deformation is an increase in the total volume of the channel. While the precise dependence of the swell volume with respect to deformation given in Eq. (3-10) is complicated, one can approximate the relationship depicted in Figure 3.3c as $V_{swell}/V_{rigid} \sim 0.5\beta$ from a Taylor series expansion for small β. The effect of the swell volume should have little impact on steady-state operation of a device but can become

significant when considering unsteady effects where the channel volume changes with time, causing the inlet and outlet volumetric flowrates to be unequal.

3.2.2.2 Unsteady Viscous Flow in a Deforming Channel

To examine unsteady viscous flow, a mass balance relating changes in h to $\dot{V}$ is used.

$$\frac{\partial h}{\partial t} = -\frac{1}{w}\frac{\partial \dot{V}}{dz} \tag{3-11}$$

Assuming that h changes slowly with z, we can combine Eq. (3-11) with the expression for volumetric flowrate, Eq. (3-6) and write an equation for the channel pressure P as a function of z and t.

$$\frac{\partial P}{\partial t} = \frac{\partial}{\partial z}\left[\frac{Eh_0^3}{8c\eta w(1+\sigma)}\left(1+\frac{2cPw(1+\sigma)}{3Eh_0}\right)^3\frac{\partial P}{\partial z}\right] \tag{3-12}$$

The initial condition is $P = 0$ at $t = 0$, and boundary conditions are $P = P_{in}$ at $z = 0$; $P = 0$ at $z = L$.

The expression is non-dimensionalized using the core variables: applied pressure P_{in}, the channel length L, and the fluid viscosity η. These variables are chosen because they are physical parameters which can be easily controlled and which define resultant quantities in our system such as volumetric flowrate. The non-dimensional forms of the variables are:

$$U = \frac{P}{P_{in}} \qquad Z = \frac{z}{L} \qquad \tau = \frac{tP_{in}}{\eta} \tag{3-13}$$

Applying this non-dimensionalization and the definition for β from Eq. (3-8), the following partial differential equation is obtained:

$$\frac{\partial U}{\partial \tau} = \frac{\partial}{\partial Z}\left[\gamma(1+\beta U)^3\frac{\partial U}{\partial Z}\right] \tag{3-14}$$

The non-dimensionalized initial condition is $U = 0$ at $\tau = 0$, the boundary conditions are $U = 1$ at $Z = 0$ and $U = 0$ at $Z = 1$, and γ is defined as:

$$\gamma = \frac{1}{12\beta}\left(\frac{h_0}{L}\right)^2 \tag{3-15}$$

The form of Eq. (3-14) is analogous to that of a diffusion equation with a variable diffusivity of $\gamma(1+\beta U)^3$. Because γ is related to this variable diffusivity it can be used to define a dimensionless diffusive time τ^*.

$$\tau^* = \gamma\tau = \frac{\gamma P_{in} t}{\eta} \tag{3-16}$$

With this definition the following modified partial differential equation results:

$$\frac{\partial U}{\partial \tau^*} = \frac{\partial}{\partial Z}\left[\left(1+\beta U\right)^3 \frac{\partial U}{\partial Z}\right] \tag{3-17}$$

The modified non-dimensionalized initial condition is U = 0 at τ^* = 0, and the boundary conditions are U = 1 at Z = 0 and U = 0 at Z = 1.

The boundary value problem defined by Eq. (3-17) with associated initial and boundary conditions was solved numerically in MATLAB (Mathworks Inc., version 7.6.0.324).[23] A variable grid mesh was used to capture the increasingly steep behavior of the function near the outlet at Z = 1. Details of the variable mesh can be found in Appendix A.3. At long times the solution is observed to approach the steady-state values predicted from the analytical solutions. Results are shown below for β = 1, which is typical for a PDMS channel (Figure 3.4). A copy of the code used can be found in Appendix A.6.

As mentioned previously, the form of the boundary value problem is the same as nonlinear diffusion in a channel. It is intuitive to think of a large slug of concentration entering the channel and then slowly diffusing along its length. In an analogous fashion, the pressure profile within the channel develops first as a sharp impulse at the entrance of the channel and then spreads down the length of the channel as deformation occurs and steady-state is reached (Figure 3.4a). From Eq. (3-5) the channel height scales directly with pressure. Deformation or “inflation” of the channel due to the applied pressures thus matches the changes in pressure profile.

The initial impulse of pressure also translates to the initial generation of steep pressure gradients. These steep gradients allow for rapid filling at the start of the deforming channel. However, the pressure gradients take time to propagate down the length of the channel, resulting in a lag between the start of flow at the inlet and the observation of flow at the outlet. This lag time can be more clearly observed by examining a plot of normalized volumetric flowrate at the outlet as a function of time (Figure 3.4c).

A similar analysis can be used to examine the case where a deformed channel is allowed to relax in the absence of an inlet pressure. In this instance the pressure driving force for flow comes from the deformed channel as it relaxes. Referring again to the diffusion analogy, the steady-state concentration (or in this case pressure) profile slowly decays to zero as material diffuses to the outlet (Figure 3.4b). However, the driving force for this diffusion decreases with time as the concentration profile levels out in the channel. Translating this analogy to pressure and fluid flow, an initially high flowrate at the outlet is observed that asymptotically approaches zero as the pressure gradients in the channel become negligible (Figure 3.4c).

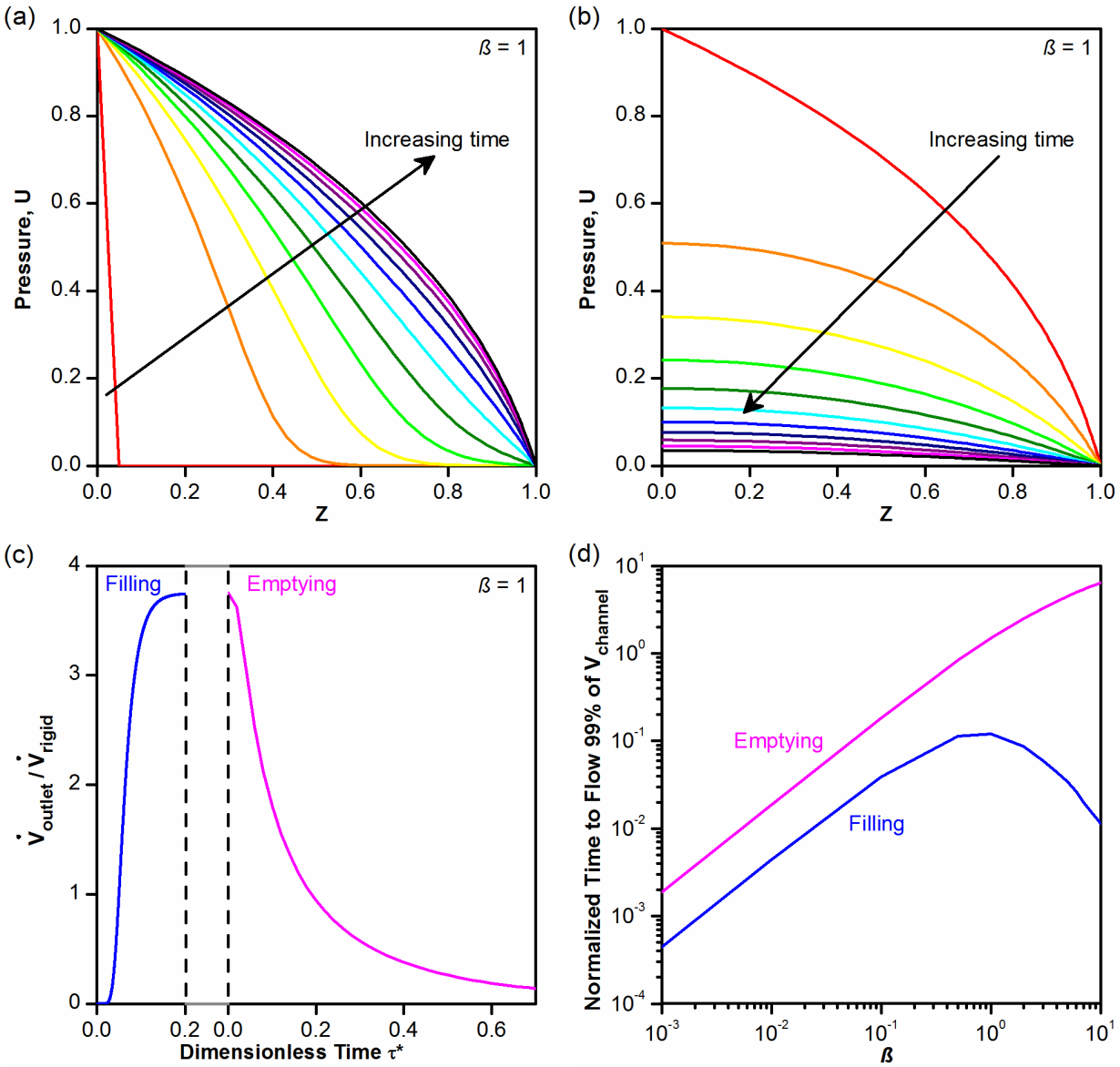

Figure 3.4. Results from the MATLAB simulation of the fully transient problem of pressure-driven viscous flow in a deforming channel using parameters that are typical for flow in a PDMS channel giving a value of $\beta = 1$. Here the channel is deforming to reach a steady-state profile over time. Dimensionless pressure over the length of the channel Z **(a)** at intervals from $\tau^* = 0$ to $\tau^* = 0.1$ for the filling case, and **(b)** over intervals from $\tau^* = 0$ to $\tau^* = 1.0$ for the emptying case. **(c)** Volumetric flowrate at the outlet normalized by the flowrate for a rigid channel as a function of time for both filling and emptying. **(d)** Time to fill or empty 99% of the channel volume for the transient filling and emptying cases, respectively, as normalized to the rigid case.

The trends in the pressure driving force for flow are very different between the filling and emptying cases. For the filling case there is a constant inlet pressure that then propagates along the length of the channel. This results in a fairly rapid approach to steady-state. However, for the emptying case the pressure driving force decreases with time, asymptotically approaching zero. A comparison of the outlet volumetric flowrate curves for the two cases in Figure 3.4c shows that the time to reach steady-state is significantly longer for the emptying case.

Variations in the rate at which a deforming channel approaches steady-state varies with β can also be examined (Figure 3.4d). The time for filling is characterized as the swell volume divided by the volumetric flowrate. If the β dependence of this filling time is then analyzed the following result is obtained:

$$t_{fill} \sim \frac{V_{swell}}{\dot{V}} \sim \frac{\beta P}{\left(1+\beta P\right)^3} \tag{3-18}$$

In the limit of small β, the filling time scales linearly with β. This relationship is the result of roughly linear increases in the swell volume that dominates over negligible increases in the volumetric flowrate. However, in the limit of large β, the time scales as the inverse square of β as increases in the channel volume are balanced by the geometric increases in the volumetric flowrate.

While it is more difficult to extract trends for the emptying case, Figure 3.4c and Figure 3.4d clearly show that the time for the emptying case to reach steady-state is significantly longer than that of the filling case. Despite this difference, similar trends with β are observed.

3.3 Design Rules

In Section 3.2 a theoretical analysis of various aspects of the microfluidic system yielded key equations to describe flow in rigid and deforming channels as well as the ability to induce pressure-driven flow by the actuation of microfluidic pneumatic valves. Here these key equations will be analyzed to establish practical design rules for use in the design of microfluidic devices. First the effects of pneumatic valves on pressure-driven flow will be summarized (Section 3.3.1). The case of steady-state pumping in a channel will then be considered, including the possible effects of channel deformation (Section 3.3.2). Next metering applications will be considered, and three different strategies to achieve precise metering will be presented while accounting for both steady-state and transient channel deformation effects (Section 3.3.3). In Section 3.3.4 these design rules will be applied to cases in actual microfluidic applications.

Note that the expressions given here reflect only the scaling behavior of the various parameters. For applications where high precision is required, the values predicted here may not be sufficiently accurate. In those cases, the device should either be calibrated under actual operating conditions, or the theory should be modified to more accurately describe such cases.

3.3.1 Effective Pneumatic Valves for Pumping Viscous Fluids

This chapter is concerned with the idea of handling viscous fluids in a microfluidic device. Overcoming the resistance of highly viscous fluids typically necessitates a high pressure driving force. Therefore, it is important to minimize ancillary pressure losses associated with the transfer of pressure to the fluid, as with the actuation of a pneumatic valve.

In Eq. (3-2) the parameter α was established which describes pressure losses associated with stiffness during the actuation of the valve. This provides a design equation for the effective incorporation

of microfluidic pneumatic valves to drive fluid flow. In the limit of an ideal valve that actuates without pressure losses the parameter $\alpha \rightarrow 0$. In designing a valve for pumping, the parameters in Eq. (3-2) can be optimized corresponding to the geometry ($a^3 h_v / s^4$) and the relative stiffness of the valve (E/P_{appl}) to minimize the value of α.

Using typical physical constants for PDMS (E = 700 kPa, and σ = 0.5)[7,8] and typical valve configurations (α = 10 μm and h_v = 10 μm), the value of α is small (< 0.05) for valves sizes s > 100 μm at actuation pressures as low as 10 kPa (1.45 psi). Similar values for α can be obtained with smaller valves through the use of higher pressures.

The results presented here are similar to work done by Quake *et al.* concerning the design of a valve.[12] While the goal of their work was the creation of a valve that could be actuated successfully, here their ideas have been extended to design a valve with minimal pressure losses.

The simplest pumping scenario is the constant pressure case where steady-state can be reached and maintained. This can be achieved through the use of an external syringe pump or pressure source. However, on-chip pumping by a series of pneumatic valves is inherently a discrete process which can be characterized as a fluctuating pressure source. As shown in Figure 3.1b, a pneumatic pump can be created by arranging three or more valves in series, and actuating these valves in a peristaltic sequence (100, 110, 010, 011, 001, 101 where 1 refers to the actuation or closing of a valve and 0 refers to the opening of a particular valve in the series).[9] Thus, six sequential valve actuations must take place for a discrete unit of fluid to be pushed through the pump. For such a pump to maintain a pseudo-steady-state in a deformed channel, the timescale of the pumping cycles must be smaller than the timescale for relaxation of the deformed channel. However, the timescale for pumping must also be longer than the timescale for relaxation of the small segments of deforming channel between valves. Fortunately, the distance between pump valves is typically small and since the relaxation time scales with channel length, the relaxation time for these small channel segments is not significant.

While balancing pump design against deformation of the channel may need to be considered in extreme cases, the advantage of moving fluid within a peristaltic pump as opposed to down a long channel is the difference in length-scale. The distance between sequential valves in a pump can be made very short, allowing for a high driving force. Flow between valves can be further facilitated by considering the dimensions of the valves as compared to the fluid channel as per Eq. (3-3). Increasing the width or height of the valve allows for easier flow. In fact, if the design rules associated with Section 3.3.1 and Eq. (3-2) have been used to design an efficient valve, the thin membrane forming the “roof” of each of the valves, can be allowed to deflect upwards, providing an artificially larger chamber for the fluid to enter.

3.3.2 Steady-State Pumping in a Microfluidic Channel

Eq. (3-3) provides a design equation in which parameters such as the applied pressure, flowrate, and channel geometry can be optimized to facilitate flow of a fixed volume of a viscous fluid. Using an initial channel design and specifying a volumetric flowrate, an initial estimate of the applied pressure that would be needed to drive flow can be made and then the design and/or operation of the device can be adjusted to lower this pressure if the estimated pressure is not feasible.

However, while large applied pressures can be used to drive flow, such increases also affect the potential for channel deformation to occur. Thus the combined effects of changing a particular parameter first on the pressure using Eq. (3-3), and then the total effect of both the parameter and the pressure change on β using Eq. (3-8) were examined. As an example, consider the parameter h. The pressure scales as $1/h^3$ and β scales as $\Delta P/h$, thus the total effect is $\beta \sim 1/h^4$. The scaling of these parameters is given in Table 3.1.

Table 3.1 provides a 1st order estimate of the scaling relationships that various geometric, materials, and operational parameters have on the applied pressure necessary to drive flow and on the resultant deformation. For small deformations ($\beta << 1$), these scaling relationships constitute a rigorous quantitative estimate. For $\beta \sim 1$, these estimates may be refined to give quantitative predictions using Eq. (3-7), the full expression for volumetric flow in a deformed channel. It is interesting to note that for the same initial microfluidic geometry (identical w, h, and L) and fluid, a larger extent of channel deformation (i.e. lower E) will result in a higher steady-state volumetric flowrate for a given applied pressure. Thus while analysis of the resultant system is more complicated, the deformation itself could be beneficial.

Table 3.1. Scaling relationships for steady-state pumping of a fixed volume of a viscous fluid developed from Eqs. (3-3) and (3-8).

Parameter	Flow Effect	Deformation Effect
w	$\Delta P \sim 1/w$	$\beta \sim$ constant
h	$\Delta P \sim 1/h^3$	$\beta \sim 1/h^4$
L	$\Delta P \sim L$	$\beta \sim L$
t	$\Delta P \sim 1/t$	$\beta \sim 1/t$
E	No effect	$\beta \sim 1/E$

3.3.3 Precise Metering Operations

In many microfluidic applications it is necessary not only to pump fluids but to do so with precise control over the volumes metered. Pumping fluids in a rigid channel is simple because flow achieves steady-state instantaneously. Thus the simplest strategy to design a device for precise metering is to use the scaling relationships in Table 3.1 such that β is small and deformations can be neglected. If design of a microfluidic device such that channel deformation is negligible is not possible, it becomes necessary to carefully account for transient periods associated with the starting and stopping of flow. Here three strategies for precise metering in a deformed channel are presented which balance the speed of a single metering operation against simplicity of operation.

3.3.3.1 Steady-State Metering with a Shunt

For flow in a deforming channel, transient effects are associated only with the initial filling of the channel before steady-state is reached and the relaxation of the channel once the applied pressure is removed. While the behavior of these transient periods can be accounted for, the device design and operation can be modified to decouple these transient periods from the actual metering operation by establishing a shunt to which flow can be directed during these transient periods or between metering instances. In this manner, steady-state flow as predicted by Eq. (3-7) can be established in the channel, and then flow can be switched from the shunt to the desired outlet as needed (Figure 3.5).

This method can provide very fast metering but requires more complicated control over the various flow streams. Additionally, it is potentially wasteful with respect to the material shunted.

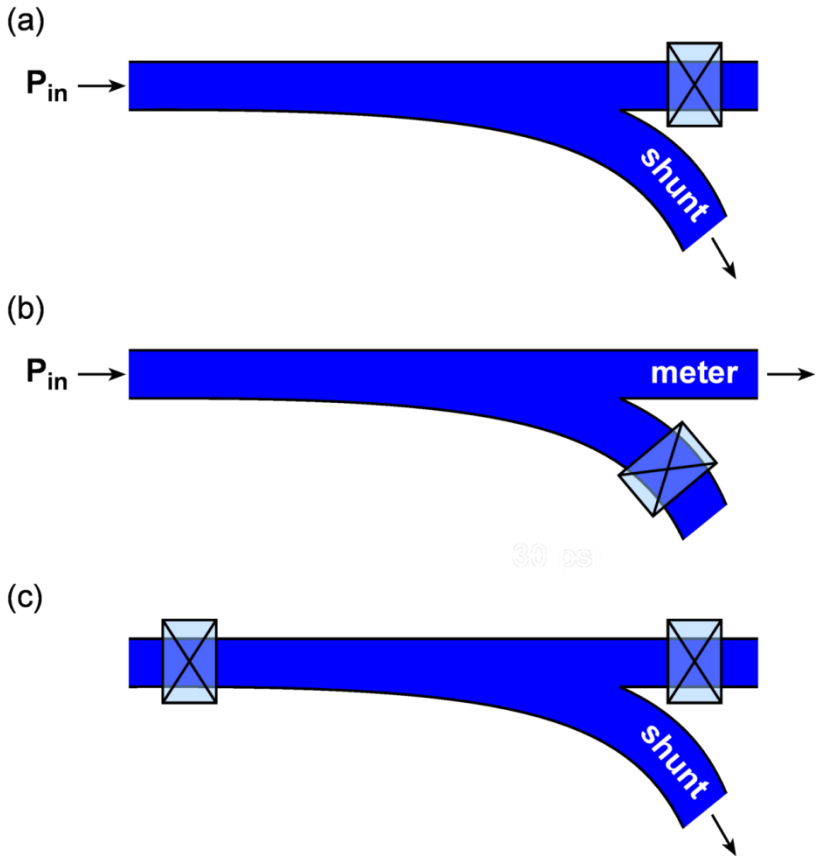

Figure 3.5. Depiction of a metering operation using a shunt in order to avoid concerns associated with the initial and final transients. **(a)** Flow is directed to the shunt during the period associated the initial deformation of the channel. **(b)** Once steady-state has been reached flow is switched from the shunt to the desired outlet. **(c)** Once metering is finished flow is returned to the shunt and the inlet to the channel is sealed, allowing the excess fluid present in the channel because of the deformation to drain out.

3.3.3.2 Metering with an Initial Transient (Half-Shunt)

To avoid the complications of switching between shunting and metering operations while maintaining steady-state, the initial transient behavior could instead be accounted for while using a shunt to avoid transient associated with channel relaxation. Beginning with a fully relaxed channel and the fluid at rest,

a lag is observed during metering between the start of pumping and the evolution of flow at the outlet which can be treated as a correction to the steady-state solution. Once the desired quantity of fluid has been metered the outlet of the channel can simply be sealed off to prevent excess fluid associated with the channel deformation from affecting the metering precision. The excess fluid present in the deformed channel can then be drained away as the channel returns to its rest state (Figure 3.6).

A correction can be defined in terms of a lag time or a lag volume which is the difference between the actual, or transient, curve and the volume of fluid which would be metered at steady-state (Figure 3.7a). This value can then be added as a constant correction term to the steady-state solution predicted by Eq. (3-7).

$$t_{lag}\left(V\right) = t\left(V\right) - t_{ss} \tag{3-19}$$

$$V_{lag}\left(t\right) = V_{ss} - V\left(t\right) \tag{3-20}$$

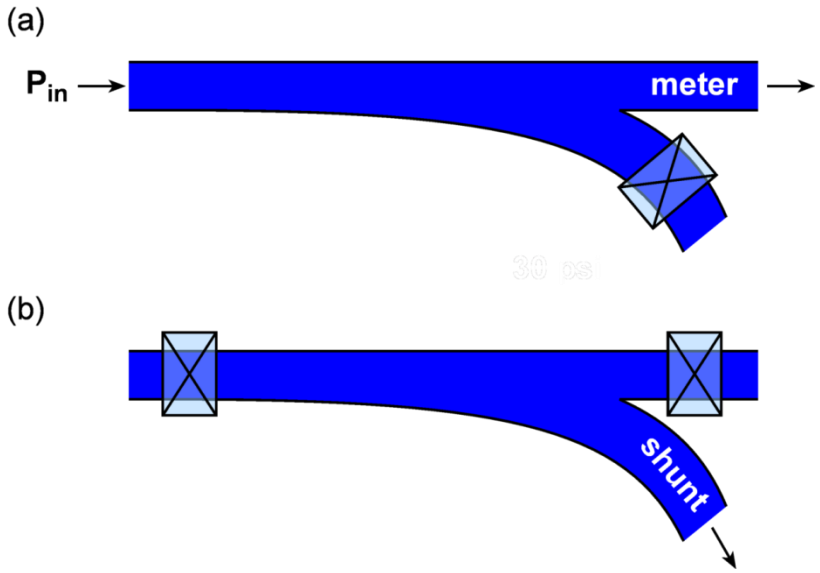

Figure 3.6. Depiction of a metering operation using a half-shunt to avoid concerns associated with the final transient. **(a)** Metering is performed during the initial deformation of the channel and on into steady-state operation, depending upon the volume of fluid to be metered. **(b)** Once metering is finished, flow is directed to the shunt and the inlet to the channel is sealed, allowing the excess fluid present in the channel because of the deformation to drain out.

While Figure 3.7a provides a graph of the lag volume for β = 1, developing a universal relationship for all values of β is more useful. Because the lag volume increases exponentially during the transient period before asymptotically leveling off at steady-state it is useful to normalize the lag volume to that of the steady-state value, V_{lagss}. The dependence of lag volume on time is more complicated. However, an effective time can be defined based on a 2nd order polynomial scaling for the dimensionless diffusive time.

$$\tau^*_{scale} = A\tau^{*2} + B\tau^* \tag{3-21}$$

$$\frac{V_{lag}}{V_{lagss}} = 1 - \exp\left(-k\tau^*_{scale}\right) \tag{3-22}$$

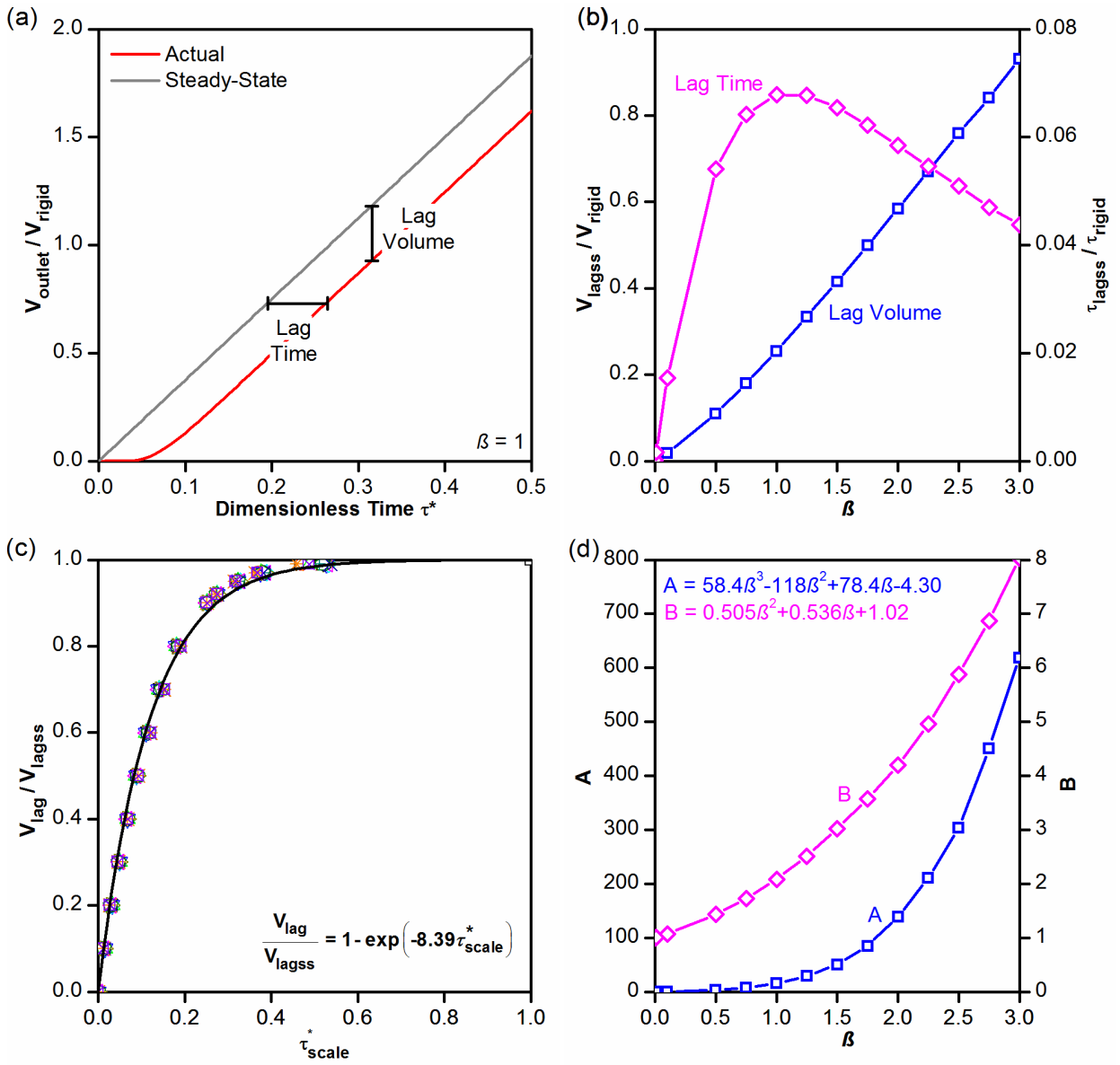

Figure 3.7. Results from the MATLAB simulation of the fully transient problem of pressure-driven viscous flow in a deforming channel. **(a)** The volume passing through the outlet normalized by the volume of a rigid channel as a function of time for the transient case and for hypothetical instantaneous steady-state flow. **(b)** The steady-state lag time normalized by the time to for flow in the rigid case to accomplish a total rigid channel volume and the steady-state lag volume normalized to the channel volume for metering as a function of β. **(c)** A plot of normalized lag volume vs. a scaled dimensionless time. The solid curve is an exponential fit to the data which is universal for all β. **(d)** A plot of the fit parameters A and B for reversing the normalization the universal lag volume curve as a function of β. Polynomial fits are shown.

The fit parameters A and B were obtained by matching values of the effective time for each value of β to the case of β = 0.001 when the lag volume parameter = 0.4 and 0.9. Additional details associated with this fitting are given in Appendix A.2. Plots of both A and B as a function of β are given in Figure 3.7d along with the associated polynomial fit of the curves. The R^2 values for each of these curves were

> 0.999. The resulting data was then fit to a simple exponential curve by least squares analysis with a value of k = 8.39 for the fitting constant. A plot of both the data and the resulting curve fit are given in Figure 3.7c.

Examining variations of the steady-state lag time and lag volume as a function of β (Figure 3.7b) is also useful. Similar to the trends observed in the swelled volume of the channel (Figure 3.3c), the steady-state lag volume increases in a nearly linear fashion as a function of β. This similarity is expected since the lag volume is directly related to the extra volume of fluid needed to fill the deformed channel. Actual values for the lag time and lag volume are calculated and discussed in Section 3.3.4.2 below.

The trends in the relationship of lag time vs. β are identical to those observed for the time to fill a channel vs. β from Eq. (3-18) and Figure 3.4d. At small deformations a nearly linear relationship between lag time and β exists because increases in the channel volume dominate over the relatively small increases in the volumetric flowrate. However, as deformation becomes more pronounced, the benefits of an increased volumetric flowrate are counteracted by increases in channel volume, resulting in an inverse square dependence of lag time with β.

As demonstrated in Figure 3.4c, the timescale for the transient period associated with filling a deforming channel is significantly shorter than the timescale associated with relaxation of the channel. Thus while the half-shunt metering strategy described here is slower than the fully steady-state shunt method (Section 3.3.3.1), it is faster than the fully transient strategy presented in Section 3.3.3.3 below.

3.3.3.3 Fully Transient Metering

The simplest method for precise metering is also the slowest and involves considering the fully transient problem. In this case the pressures associated with pumping will first cause the channel to deform. Thus the time associated with this initial transient can be estimated using the plots of lag volume (Figure 3.7). If the volume to be metered is such that the system reaches steady-state, Eq. (3-7) can be used as previously to determine the time needed for pumping. However, it is now necessary to also consider the time needed to fully relax the channel and thus empty out the desired volume of fluid. Figure 3.4d provides an estimate of the time needed for the channel to fully relax as a function of β.

In determining a metering protocol for this fully transient case, the previously described strategies can be used to determine the time for the desired volume of fluid minus that of the swell volume to reach the outlet. At this point the pumping must be shut off and the inlet of the channel sealed to prevent backflow.

3.3.4 Applications of the Design Rules

Thus far the physics behind various phenomena present in a microfluidic device have been described and associated design rules were developed. These design rules will now be applied to two examples in actual microfluidic applications: (i) a microfluidic device for mixing highly viscous fluids and (ii) the precise metering of fluid using a pneumatic on-chip pump over a range of fluid viscosities.

3.3.4.1 Creating a Mixer for Highly Viscous Fluids

Microfluidic applications involving highly viscous fluids have lagged behind their less viscous counterparts mostly due to the difficulty in flowing high viscosity fluids on the microscale. The simple scaling relationships that resulted from the work presented above (Table 3.1) enable the design of microfluidic devices capable of driving flow for fluids that are not only highly viscous but also non-Newtonian. These design rules were coupled with strategies for mixing to create a microfluidic mixer capable of operating with fluids of both differing and high viscosities.[2] Additional details on the design and operation of this mixer are given in Chapter 4.

The majority of microfluidic mixers, such as the ring mixer devised by the Quake group[11,24,25] or the herringbone mixer devised by Stroock and coworkers,[26,27] require driving flow over relatively long distances. These mixer designs have difficulty operating with higher viscosity fluids, especially when trying to mix fluids of significantly different viscosities. Thus instead of striving to establish complex flow patterns in a long channel, a mixing strategy that is compatible with the need to pump higher viscosity fluids was developed (Figure 3.8). Chapter 4 describes the operation and application of this device to mix a viscous lipid (monoolein) and an inviscid aqueous solution.[2] Here a description is given as to how the scaling relationships were used in its design. The viscous fluid mixer is composed of three microfluidic chambers connected by small microfluidic channels. In this two-layer PDMS device, isolation valves are located both over the inlet lines used to fill the device and over the channels connecting each of the three chambers. Large microfluidic injection valves are also located over each of the three large chambers containing the fluids to be mixed. These injection valves are used to pump fluid from one compartment to another while the various isolation valves on the connecting channels control the direction of fluid flow. Mixing is achieved by first driving flow in a linear fashion from the side chambers into the center chamber through all of the available injection lines. Two recirculating loops of flow are then created on the two halves of the device by using first one injection line for flow to the side chambers, then two lines to return to the center chamber, and then again a single line to refill the side chambers. These straight-line and recirculating flow patterns are repeated to drive fluid mixing in a tendril-whorl fashion.[28] This mixer was used to prepare self-assembling aqueous/lipid mesophases where the viscosity of the initial aqueous and lipid solutions differed by a factor of ~30 (2.45×10^{-2} Pa-s for the lipid phase versus 7.98×10^{-4} Pa-s for the aqueous phase). Furthermore, the resulting mixture had a viscosity ~10^5 times larger than that of water (~48.3 Pa-s at a shear rate of 71.4 s^{-1}) and displayed non-Newtonian fluid behavior. These mesophases are of interest particularly in structural biology applications, including membrane protein crystallization, (see Chapter 2).[29]

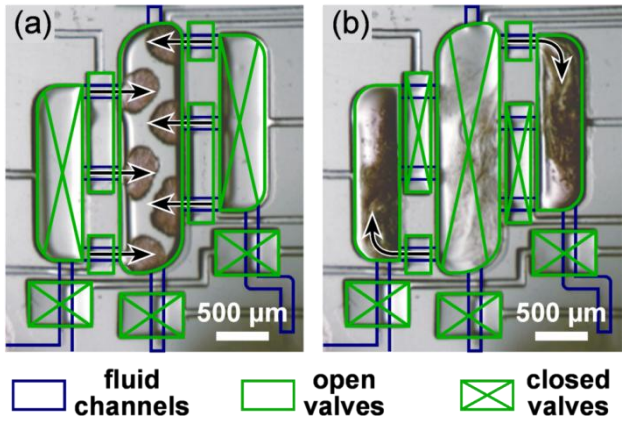

Figure 3.8. Optical micrograph of a microfluidic mixer designed to mix highly viscous fluids or fluids of vastly different viscosities. Pneumatic valves are outlined in green and are located as isolation valves over inlet lines leading into each of three larger chambers as well as over lines connecting the three chambers. Valves used to drive fluid flow are located over each of the three large chambers. **(a)** The injection of an aqueous solution from the side chambers into the center chamber containing a highly viscous lipid. **(b)** Injection of fluid from the center chamber to the side chambers through a single injection line. See Chapter 4 for more details on the mixing sequence.

In designing this microfluidic mixing device, the first challenge that needed to be overcome was pumping fluids with viscosities several orders of magnitude higher than water. This increased viscous resistance was countered by designing the geometry of the device based on the design rules in Table 3.1, such that operational parameters including the applied pressure to drive flow, could be optimized (i.e. minimized to attainable pressure levels). Instead of trying to pump a highly viscous fluid over a long distance in a narrow channel, the mixer was configured such that (i) the distance for flow L is short and (ii) the width w of the device is large. The use of large fluid chambers allow for minimization of the distance over which fluid was pumped in a narrow channel. These large chambers have the added benefit of ensuring, as per the scaling relationships associated with the parameter α in Eq. (3-2), that the pneumatic valves located over each chamber are able to efficiently drive flow without pressure losses. Including these chamber valves in our design provided two additional benefits: (i) Whereas the actual height of the fluid chambers in the device is a constant, the presence of an easily deflectable valve over each of the chambers allows each of the chambers to be effectively considered as having a much larger height than was initially designed. The design rules derived here (Table 3.1) show that the required pressure to drive viscous flow scales with the cube of the channel height, meaning that even small increases in height significantly decrease the pressure needed to drive fluid flow. (ii) The entire contents of each individual chamber are pumped with a single actuation, rather than by repeated pumping steps to move smaller portions of fluid around. (iii) Lastly, the device was operated relatively slowly such that adverse effects of the increased fluid viscosity which had not been overcome through device design could be compensated for by accepting a lower flowrate. The mesophase that is formed upon mixing in this study also displayed viscoelastic behavior. An additional benefit of the decreased flowrate was adequate compensation for the relaxation timescales associated with the fluid.

Based on the geometry of the device and the large applied pressures needed to drive flow, the calculated value of β ~ 2 indicates that deformation of the channels connecting the compartments will be significant. As discussed previously (Section 3.2.2), this kind of deformation decreases pressure losses along the length of a channel and can provide further benefits for moving highly viscous fluids between chambers. While deformation is only an issue for the short channels connecting the larger microfluidic chambers, the short length of these channels means that the lag time and volume will be relatively small compared to the total volume of fluid to be pumped. Additionally, relaxation of the extra volume in these channels is not a concern because microfluidic isolation valves over each of these channels are actuated as part of the mixing sequence and will expel fluid remaining in the channel.

3.3.4.2 Peristaltic Fluid Metering

The Case of a Rigid Channel

The ability to precisely meter out picoliter-scale (or smaller) quantities of fluids has been clearly demonstrated in microfluidic devices, usually by the peristaltic actuation of a series of pneumatic valves.[24] This method typically assumes that the volume of fluid displaced under the valve will be moved down the channel without losses due to channel deformation. For a given driving pressure ΔP, Eq. (3-3) gives the maximum flowrate through a channel based on the channel geometry and fluid viscosity. When using a peristaltic pump, an average volumetric flowrate can be calculated based on the volume displaced by a single cycle of the pump V_{valve} and the pumping frequency f.

$$\dot{V} = fV_{valve} \tag{3-23}$$

The pump should be capable of pumping at any flowrate up to the maximum flowrate specified by the channel geometry and fluid viscosity at which point the viscous resistance to flow will dominate over pumping rate. The maximum pumping rate associated with a given frequency can be calculated for a given system by combining Eqs. (3-3) and (3-23). In the interest of examining viscosity effects on pumping, a system parameter k_{system} can be defined which captures the geometric and operating parameters of the system as shown in Eq. (3-24).

$$f = \left(\frac{h^3 w \Delta P}{12 L V_{valve}} \right) \frac{1}{\eta} = \frac{k_{system}}{\eta} \tag{3-24}$$

Hansen and coworkers describe the exact problem resulting from a limiting pump speed in their work on a microfluidic formulator.[24] In this formulator they use a three valve peristaltic pump to precisely meter out small volumes (~80 pL) of fluid. While for aqueous solutions (η ~ 0.001 Pa-s) they are capable of successfully operating their pump at a very fast rate of 100 Hz, they observe a drop-off in metering accuracy for more viscous fluids (η ~ 0.4 Pa-s) even at a pump rate of 10 Hz. They determined that it was necessary to decrease the pump speed to 5 Hz in order to accurately meter out the more viscous fluid.

Using the analysis provided by Eq. (3-24) with the geometry of the microfluidic formulator used by Hansen and coworkers (h = 9 µm, w = 80 µm, L = 4712 µm, V_{valve} = 80 pL), and an estimated value for the pressure applied by the valve of ΔP = 207 kPa, one calculates a value of k_{system} = 2.7 Pa. From this value for k_{system}, the limiting pumping frequency was calculated as a function of viscosity, and plotted in Figure 3.9. The curve defined by Eq. (3-24) provides an upper bound on the range of pumping frequencies and viscosities for which accurate metering based on incremental increases in the volumetric flowrate can be accomplished, thus defining an "accurate metering window." Beyond this window the relation between the frequency and the volumetric flow rate is unclear, hampering accurate metering. Note that this analysis assumes that the channel or chamber into which the fluid is being pumped is rigid, thus transient effects can be ignored.

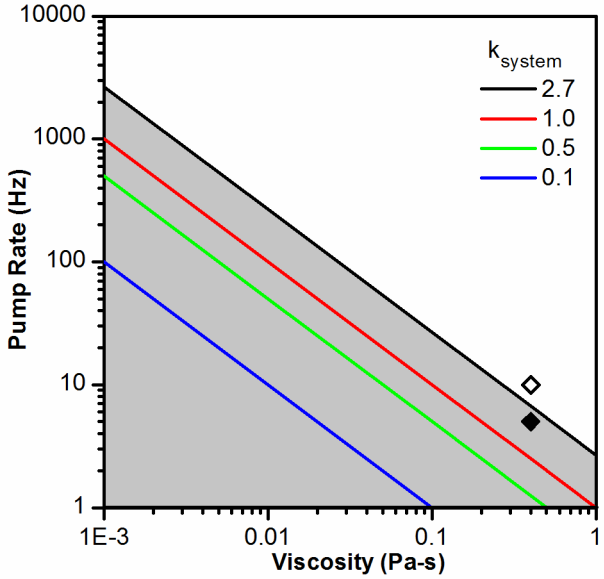

Figure 3.9. Pump rate curves for peristaltic metering systems characterized by different values of k_{system}. These curves indicate the upper bound of an "accurate metering window." The black curve represents the system described by Hansen *et al.* with k_{system} = 2.7 Pa.[24] The associated metering window is highlighted in grey. Two points are shown, corresponding to the limiting case of 10 Hz (◇) which could not accurately meter a fluid with a viscosity of 0.4 Pa-s, and 5 Hz (◆) which falls within the metering window.

In their work, Hansen and coworkers reported that metering of a viscous fluid (η ~ 0.4 Pa-s) could not be accomplished at a pumping rate of 10 Hz, whereas accurate metering could be done at a slower rate of 5 Hz. If these two points are examined graphically, it can be observed that the faster pumping rate of 10 Hz falls outside of the metering window (Figure 3.9, ◇) whereas adjusting the pumping rate to 5 Hz shifts the condition so that it falls within the accurate metering window (Figure 3.9, ◆). In other words, the simple approach to indicate what ranges of operational parameters for a given system will allow for precise metering that is reported here, based on Eq. (3-24), is able to accurately describe these experimentally observed data.

The Case of a Deforming Channel

The fluid metering described above assumes that the channel or chamber into which the fluid is being pumped is rigid and that transient effects do not need to be taken into account. To examine the extent to which the initial transient can affect metering, the metering example from Hansen and coworkers[24] can also be considered while taking channel deformation into account. The assumption that $\beta = 1$ and that the timescale for actuation of the peristaltic pump is much faster than the timescale for channel deformation are made such that the discrete nature of peristaltic pump actuation can be neglected. Given the value of β, the analysis regarding the effect of channel deformation on viscous flow provided in Section 3.2.2 allows for the determination of a variety of parameters for the system. For this metering example, the most important parameters are the steady-state volumetric flowrate, the lag time, and the lag volume. As was mentioned previously (Section 3.2.2.1), for a value of $\beta = 1$ the volumetric flowrate resulting from the deformed channel is 375% higher than the corresponding flowrate expected for a rigid channel. Thus if a limiting pumping rate analysis from Eq. (3-24) is performed, the deformation of the channel is observed to reduce the resistance to flow and thus allow for the system to operate at a faster steady-state pumping rate than in the limit of the rigid case. In fact, for the same viscous fluid ($\eta \sim 0.4$ Pa-s), a maximum pumping rate of 25 Hz is predicted, a 5x increase over that of the rigid case.

The lag time and lag volume are also very important when taking the initial transient of a metering operation into account. For a system with $\beta = 1$, Figure 3.7b can be used to read off normalized values for these two parameters with respect to a rigid system ($V_{lagss}/V_{rigid} = 0.254$ and $\tau_{lagss}/\tau_{rigid} = 0.0679$). While the values of these normalized parameters are applicable to any system, the actual dimensional values for the lag time and volume will depend on the system parameters involved in the normalization variables V_{rigid} and τ_{rigid}.

$$V_{rigid} = whL \tag{3-25}$$

$$\tau_{rigid} = \frac{V_{rigid}}{\dot{V}_{rigid}} = \frac{12\eta L^2}{h^2 \Delta P} \tag{3-26}$$

As can be seen in Eqs. (3-25) and (3-26), V_{rigid} scales linearly with the channel length L, whereas τ_{rigid} scales with the length squared. If two channels are considered where one is twice the length of the other and the lag behavior associated with the initial transient is analyzed, a significant difference between the two channels will be observed. The lag volume for the longer channel will be twice that of the shorter one while the lag time will be four times longer. A summary of these scaling relationships is given in Table 3.2.

The effects of this lag period can now be considered with respect to the metering example from Hansen and coworkers. For this system the accuracy of metering was taken to be equal to the volume pumped by a single cycle of the peristaltic pump, 80 pL. However, a lag volume of 0.863 nL was

determined, which corresponds to nearly 11 cycles of the pump. While the magnitude of this lag volume depends upon the channel geometry as shown in Table 3.2., it is important to note the potentially significant error in the volume of fluid metered that can result from channel deformation.

Table 3.2. Scaling relationships for the lag volume (V_{lag}) and lag time (t_{lag}) associated with the initial transient resulting from channel deformation. These results were developed from the definitions for V_{rigid} and τ_{rigid}.

Parameter	Lag Volume	Lag Time
w	$V_{lag} \sim w$	No effect
h	$V_{lag} \sim h$	$t_{lag} \sim 1/h^2$
L	$V_{lag} \sim L$	$t_{lag} \sim L^2$
ΔP	No effect	$t_{lag} \sim 1/\Delta P$
η	No effect	$t_{lag} \sim \eta$

3.4 Conclusions

In summary, key equations for the actuation of microfluidic pneumatic valves and pressure-driven viscous flow have been derived for both rigid and deforming microfluidic channels at steady-state and unsteady conditions. These mathematical expressions were then translated into a series of scaling relationships which can be used in the design, construction, and operation of microfluidic devices. Here the focus was on pumping and precise metering. These design rules were then applied to two specific tasks: (i) the design of a microfluidic device to mix highly viscous fluids and (ii) the precise metering of fluids over a range of viscosities using an on-chip pneumatic peristaltic pump.

The analysis performed here focused on Newtonian fluids to clearly lay out the various scaling relationships that exist. However, similar rules can also be developed for non-Newtonian fluids. The two most commonly considered types of non-Newtonian fluid behavior are shear thickening and shear thinning, related to how the fluid reacts to different shear stresses. At a single flow condition, a non-Newtonian fluid can be described by an apparent viscosity, which can be used with the design equations developed here. Additional non-Newtonian behaviors such as viscoelasticity are characterized most importantly by a characteristic timescale. In the case of a viscoelastic fluid, actions that occur faster than this characteristic timescale for relaxation cause the material to respond elastically rather than as a viscous fluid. Thus by operating a device at a timescale longer than this relaxation time the non-Newtonian behavior will be negligible and the equations derived here for steady and unsteady flow of viscous fluids in microfluidic channels will still apply.

The design rules in this work will aid the design of microfluidic systems that involve a significant challenge, such as the need to handle high fluid viscosities or the need to meter fluids precisely. Furthermore, the results in this work for the first time quantify the transient effects that deforming channels have on the performance of microfluidic systems. This analysis will enable the design of devices whereby transient deformation effects can be minimized to a level that is acceptable for the intended application or the transient effects can be accurately accounted for.

3.5 Acknowledgements

This work was funded by NIH (R01 GM086727) and a NIH Kirschstein Predoctoral Fellowship from the National Institute of Biomedical Imaging and Bioengineering (F31 EB008330). Professor Jonathan J.L. Higdon and Ashlee N. Ford were invaluable in their assistance with this work.

3.6 References

(1) Pal, R.; Yang, M.; Lin, R.; Johnson, B. N.; Srivastava, N.; Razzacki, S. Z.; Chomistek, K. J.; Heldsinger, D. C.; Haque, R. M.; Ugaz, V. M.; Thwar, P. K.; Chen, Z.; Alfano, K.; Yim, M. B.; Krishnan, M.; Fuller, A. O.; Larson, R. G.; Burke, D. T.; Burns, M. A. Lab Chip 2005, 5, 1024.

(2) Perry, S. L.; Roberts, G. W.; Tice, J. D.; Gennis, R. B.; Kenis, P. J. A. Cryst Growth Des 2009, 9, 2566.

(3) Wootton, R. C. R.; deMello, A. J. Chem Commun 2004, 266.

(4) Jayashree, R. S.; Gancs, L.; Choban, E. R.; Primak, A.; Natarajan, D.; Markoski, L. J.; Kenis, P. J. A. J Am Chem Soc 2005, 127, 16758.

(5) Xia, Y. N.; Whitesides, G. M. Angew Chem Int Edit 1998, 37, 551.

(6) Rogers, J. A.; Nuzzo, R. G. Materials Today 2005, 8, 50.

(7) Gervais, T.; El-Ali, J.; Gunther, A.; Jensen, K. F. Lab Chip 2006, 6, 500.

(8) Lötters, J. C.; Olthuis, W.; Veltink, P. H.; Bergveld, P. J Micromech Microeng 1997, 7, 145.

(9) Unger, M. A.; Chou, H. P.; Thorsen, T.; Scherer, A.; Quake, S. R. Science 2000, 288, 113.

(10) Schudel, B. R.; Choi, C. J.; Cunningham, B. T.; Kenis, P. J. A. Lab Chip 2009, 9, 1676.

(11) Chou, H. P.; Unger, M. A.; Quake, S. R. Biomedical Microdevices 2001, 3, 323.

(12) Studer, V.; Hang, G.; Pandolfi, A.; Ortiz, M.; Anderson, W. F.; Quake, S. R. J Appl Phys 2004, 95, 393.

(13) Kartalov, E. P.; Scherer, A.; Quake, S. R.; Taylor, C. R.; Anderson, W. F. J Appl Phys 2007, 101.

(14) Goulpeau, J.; Trouchet, D.; Ajdari, A.; Tabeling, P. J Appl Phys 2005, 98, 044914.

(15) Li, L.; Fu, Q.; Kors, C.; Stewart, L.; Nollert, P.; Laible, P.; Ismagilov, R. Microfluid Nanofluid 2009.

(16) McDonald, J. C.; Duffy, D. C.; Anderson, J. R.; Chiu, D. T.; Wu, H. K.; Schueller, O. J. A.; Whitesides, G. M. Electrophoresis 2000, 21, 27.

(17) Vlachopoulou, M. E.; Tserepi, A.; Pavli, P.; Argitis, P.; Sanopoulou, M.; Misiakos, K. J Micromech Microeng 2009, 19.

(18) Bird, R. B.; Stewart, W. E.; Lightfoot, E., N. Transport Phenomena; John Wiley & Sons: New York, 1960.

(19) Hardy, B. S.; Uechi, K.; Zhen, J.; Kavehpour, H. P. Lab Chip 2009, 9, 935.

(20) Holden, M. A.; Kumar, S.; Beskok, A.; Cremer, P. S. J Micromech Microeng 2003, 13, 412.

(21) Timoshenko, S. Strength of Materials: Part II Advanced Theory and Problems; 3rd ed.; D. Van Nostrand Company, Inc.: Princeton, NJ, 1955; Vol. 2.

(22) Love, A. E. H. A Treatise on the Mathematical Theory of Elasticity; 4th ed.; Cambridge University Press: Cambridge, 1934.

(23) 7.6.0.234 ed.; Mathworks Inc.: Natick, MA, 2008.

(24) Hansen, C. L.; Sommer, M. O. A.; Quake, S. R. P Natl Acad Sci USA 2004, 101, 14431.

(25) Squires, T. M.; Quake, S. R. Rev Mod Phys 2005, 77, 977.

(26) Stroock, A. D.; Dertinger, S. K. W.; Ajdari, A.; Mezic, I.; Stone, H. A.; Whitesides, G. M. Science 2002, 295, 647.

(27) Stroock, A. D.; Dertinger, S. K.; Whitesides, G. M.; Ajdari, A. Anal Chem 2002, 74, 5306.

(28) Ottino, J. M. Sci Am 1989, 260, 56.

(29) Caffrey, M. Ann Rev Biophys 2009, 38, 29.

Chapter 4

Design and Application of Microfluidic Platforms for *In Meso* Membrane Protein Crystallization[*†‡]

Abstract

This chapter describes a microfluidic method for the formation of aqueous/lipid mesophases to enable screening of suitable crystallization conditions of membrane proteins from a membrane-like phase in sub-20 nL volumes. This integrated microfluidic chip and the employed mixing strategy address the specific challenges associated with the mixing of fluids of highly different viscosities (here a factor of 30) as well as the non-Newtonian character of the resulting mesophases. The chip requires less than 20 nL of material per condition screened whereas typically on the order of 10 µL or more is needed for a batch preparation in the present screening methods. This approach was validated with the successful crystallization of the membrane protein bacteriorhodopsin.

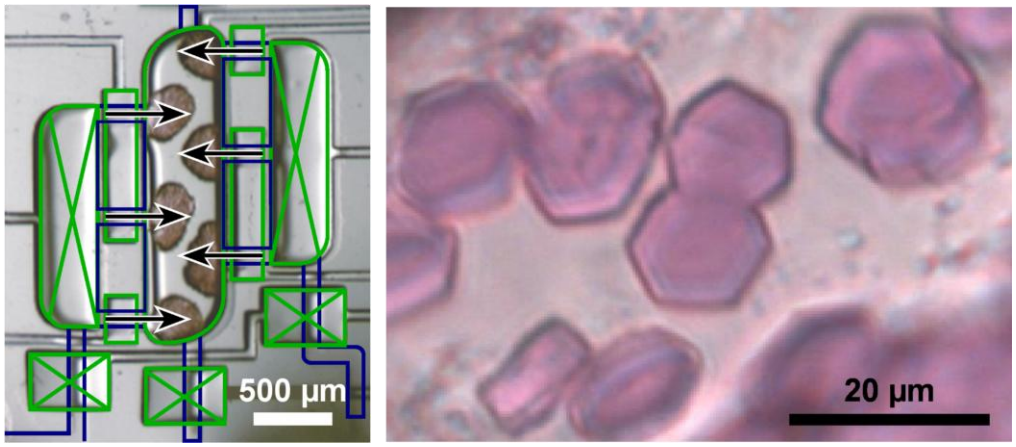

[*] Part of this work has been published: S.L. Perry, J.D. Tice, G.W. Roberts, and P.J.A. Kenis, *Microfluidic Generation of Lipidic Mesophases for Membrane Protein Crystallization*, Crystal Growth & Design 2009, Vol. 9(6), 2566-2569.

[†] Highlighted in: *Finding Crystallization Sweet Spots*, Chemical & Engineering News, Vol. 87(22), 22.

[‡] A patent application has been submitted pertaining to this work: *Microfluidic Device for Preparing Mixtures*, P.J.A. Kenis., J.D. Tice, S.L. Perry, and G.W. Roberts, US Patent Application US 2010/0022007 A1, filed July 2008.

4.1 Introduction

As was described in Chapters 1 and 2, membrane proteins are critical components of many fundamental biological processes, enabling cell signaling and material and energy transduction across cellular boundaries.[1-7] As such, their malfunction has been linked to numerous diseases and they are common targets for pharmacological treatments.[6-11] However, an understanding of the mechanisms whereby these proteins operate and attempts at rational drug design have been limited by difficulties in obtaining high resolution structural information.[12]

Two of the most significant bottlenecks for membrane protein structure determination are (i) obtaining sufficient quantities of high quality protein samples and (ii) growing high quality protein crystals.[2,13-39] These challenges are exacerbated for amphiphilic membrane proteins because of difficulties with over-expression[9,11,35,40-46] and stability once removed from their native membrane environment.[1,7,11,26,41,47-53] As a result of these difficulties, a tremendous disparity has developed between the number of known structures for membrane proteins (661 as of July 11, 2010) as compared to soluble, globular proteins (>66,000).[54,55]

In recent years, microfluidic technology has been successfully utilized for high throughput screening of crystallization conditions at the sub-nanoliter scale.[56,57] The small volumetric scale of microfluidics coupled with significant benefits related to fluid handling and control have the potential to enable the next generation of structural biology studies. However, crystallization of membrane proteins in microfluidic systems thus far has been limited to *in surfo* methods where detergents are used to solubilize membrane proteins[11,33,35,40,43,45-47,50-52,58-60] and crystallization is attempted as for soluble proteins.[5,11,47,48,56,58,61,62]

The *in meso* crystallization method, as described in Chapter 2, is an alternative to the *in surfo* method. It uses an artificial aqueous/lipid mesophase to maintain membrane proteins in a membrane-like environment.[1,25,26,33,40,43,46-48,60,63-106] This method exploits the complex phase behavior of aqueous/lipid systems (e.g. lamellar, bicontinuous cubic phases),[33,60,73,74,86,106-110] creating local variations in the curvature of the lipid bilayers to drive crystal nucleation and growth.[1,26,64,65,74,79,106,108] Despite its benefits, implementation of the *in meso* approach to crystallization on the microscale has been particularly difficult because of the challenges associated with mixing fluids of vastly different viscosities.[33,94,111,112] Thus far, the aqueous/lipid mesophases necessary for the *in meso* approach have been prepared either by centrifugation[52,60,64,110,113-127] or using coupled microsyringes.[33,60,67,83,86,88,108,127-132] Unfortunately the preparative scale of both of these methods requires the creation of relatively large amounts of mesophase (10-500 µL) due to the scale at which mixing can be performed.

While many microfluidic strategies for mixing have been reported,[20,133] they are limited to the mixing of fluids which have similar and have relatively low viscosities, such as two aqueous solutions. The viscosities of the solutions to be mixed here differ by a factor of ~30; 2.45×10^{-2} Pa-s for the monoolein lipid phase, versus 7.98×10^{-4} Pa-s for the aqueous phase. Furthermore, the resulting mesophase has a viscosity that is a factor of ~10^5 larger (~48.3 Pa-s at a shear rate of 71.4 s^{-1}, see Section 4.3.1) than the

viscosity of the aqueous phase. Moreover, the resulting mixture exhibits highly non-Newtonian behavior.[111,112] The highly viscous and non-Newtonian nature of the fluids render previously reported microfluidic mixing approaches ineffective.

As described in Chapter 3, the pressure required to move increasingly viscous fluids through a channel of set dimensions scales with viscosity. In microfluidic chips where flow is driven by the actuation of pneumatic valves, the maximum achievable pressure is limited by the actuation pressure supplied to the valves, which in turn limits the viscosity a fluid can have to be used in a given microfluidic network. To still be able to pump fluids of high viscosities, for example, the lipids used here, an adjustment of channel dimensions, specifically the reduction of channel length and/or enlargement of the cross-sectional area, was used to overcome pressure limitations, as per the design rules established in Chapter 3. Additionally, non-Newtonian fluid behavior, such as the viscoelastic properties of the lipidic mesophases created here, needs to be accounted for. For pneumatic pumping to be effective, the rate of individual valve actuation needs to be reduced to a timescale longer than the timescale of viscoelastic relaxation present in the fluid. Otherwise the fluid will deform and bounce back elastically as opposed to actual flow.

This chapter describes an integrated microfluidic chip (Figure 4.1) capable of mixing lipids with aqueous solutions to enable sub-microliter screening for crystallization conditions *in meso*.[94] The principles of chaotic mixing were employed via time-periodic flow in a tendril-whorl fashion to prepare homogeneous aqueous/lipid mesophases.[134] Each experiment consumes less than 20 nL of material with the potential to scale down further to the 0.1 nL level. This approach was validated by the successful *in meso* crystallization of the well-characterized membrane protein bacteriorhodopsin.[1,26,64,74,135]

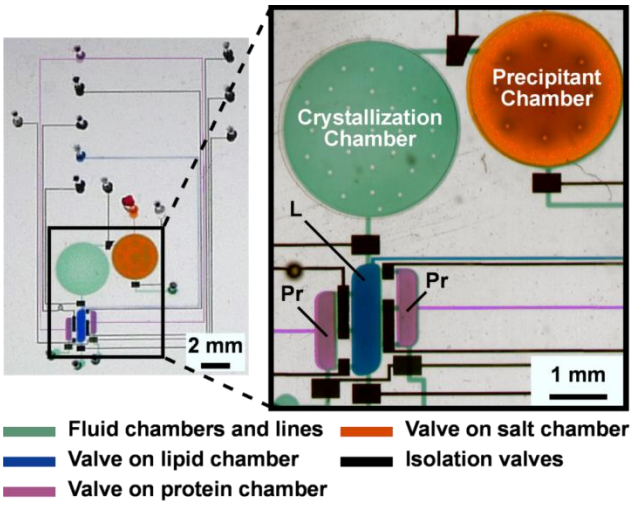

Figure 4.1. Optical micrograph of a microfluidic chip capable of mixing lipids (L) and aqueous protein (Pr) solutions by pneumatic actuation of the isolation valves (black) between the chambers and the injection valves (purple and blue) on top of the three large chambers (2-Pr, L). Crystallization occurs in a separate crystallization chamber where the mesophase is combined with a precipitant solution that is introduced from a separate circular chamber at the top. The fluidic layer is filled with a green solution and is partially covered by various valves (purple, blue, black, orange) in the control layer.

4.2 Materials and Methods

4.2.1 Device Fabrication and Operation

The microfluidic chip was fabricated out of polydimethylsiloxane (PDMS, General Electric RTV 650) bonded to a glass substrate using standard multi-layer soft lithographic procedures reported previously.[57,136] Briefly, the various control and fluid layers were designed using Macromedia Freehand MX (Macromedia Inc.). Based on this design, photolithography was used to fabricate replica masters using high resolution transparencies (5080 dpi, University of Illinois at Urbana-Champaign Printing Services) as masks. The positive-tone photoresist SPR 220 (Rohm and Haas Electronic Materials) was used to fabricate the master for the fluid layer with ~10 μm tall features. A reflow step at 120°C for 2 min was used to create rounded features in order to facilitate valving. The master for the control layer was fabricated using the negative-tone photoresist SU-8-25 (Microchem). The fabricated masters were then treated with (tridecafluoro-1,1,2,2-tetrahydrooctyl) trichlorosilane (Gelest, Inc.), a silanizing agent, to allow for easy release of PDMS subsequent replicas.

Fluid and control layers were fabricated via replica molding from these masters. Spin-coating was used to control the thickness of PDMS for the fluid layer. A spin rate of 2400 rpm was used to obtain a total PDMS film thickness of 40 μm, resulting in a valve membrane thickness of ~30 μm. A much thicker control layer (~5 mm) was fabricated in order to facilitate connections for fluid and valve lines. The fluid and control layers were prepared using PDMS with different ratios of monomer to cross-linking agent. The control layer was prepared using an excess of cross-linker (5:1 ratio) while the fluid layer was prepared with a 20:1 ratio, creating a deficiency in cross-linker. The two layers were partially cured for ~40 minutes at 65°C and then aligned and allowed to fully cure. The differences in cross-linking concentration facilitates bonding between the two layers creating a monolithic structure. Inlet holes were punched using a 27 AWG needle with a thin wire plunger. The finished PDMS device structure was then bonded to a glass substrate using an oxygen plasma treatment to create a chemical bond.

Fluids (protein and precipitant solutions and lipid) were supplied to the device using 30 AWG polytetrafluoroethylene (PTFE) tubing (Cole-Parmer Instrument Co.). Pneumatic connections for valves were made using 24 AWG PTFE tubing coupled with a thin metal tube. Pneumatic control for the various valve lines was accomplished using a computer-controlled bank of solenoid valves coupled to a nitrogen tank (Fluidigm Corp.). The 32 individual control lines are separated into two banks of 16, enabling the use of two different pressures. Typically, one bank is set at a lower pressure for driving fluid flow and the other is set to a higher pressure for actuation of isolation valves at a higher pressure.

4.2.2 Crystallization Experiments

Crystallization experiments were set up and visualized using a stereomicroscope (Leica, MZ12.5) with an attached digital camera. The camera was operated using Micrometrics SE software. For visualization of the various lipidic mesophases and protein crystals, images were taken with the use of

cross-polarizers. Incubation of crystallization experiments was performed in a dark box at room temperature.

4.2.3 Protein, Lipid, and Precipitant Solutions

The membrane protein bacteriorhodopsin was purified from isolated purple membranes from *Halobacterium salinarium* using standard procedures reported in the literature.[64,137] Briefly, a sample of purple membrane was removed from the freezer, thawed, resuspended in 10 mL of 150 mM KCl (Sigma) and then collected by centrifugation (15 min, 50,000 rpm, TLA 100.3 rotor, 4°C). The collected pellet is then resuspended in 6 mL of 25 mM NaH_2PO_4 (EMD Chemicals), pH 6.9. Solubilization of the bacteriorhodopsin was performed by the addition of 1 mL of 20% (w/v) β-octylglucoside (anagrade, Anatrace), sonication for 1 min, and then an overnight incubation in the dark at room temperature without stirring. Following incubation the pH of the solution is adjusted to 5.5 using 0.1M HCl (Fisher), and centrifugation for 45 min at 15°C at 50,000 rpm (TLA 100.3 rotor) is used to isolate the solubilized protein from the membrane fraction. The sample was then filtered through a 0.45 µm syringe filter (Fisher) and concentrated to < 2 mL with a Centriprep YM-50 filtration device (Millipore). The protein sample was then treated by size exclusion chromatography using a Superdex 200 10/300 GL (GE Healthcare) gel filtration column on an Äktabasic Fast Protein Liquid Chromatography (FPLC) instrument (Amersham Biosciences) with 1.2% β-octylglucoside in 25 mM NaH_2PO_4, pH 5.5 as the running buffer. All solutions used for gel chromatography were degassed and filtered (0.2 µm, Millipore) prior to use. Fractions were pooled based on the ratio of absorbance at 280 nm compared to 550 nm (A_{280}/A_{550} = 1.5 – 2.0). The purified sample was then concentrated with a Centriprep YM-50 filtration device to the desired concentration and filtered through a 0.1 µm (Ultrafree-MC, Millipore) spin filter. Protein concentration was determined by absorbance measurements at 550 nm using an extinction coefficient of 58,000 $M^{-1}cm^{-1}$.[88] SDS-PAGE analysis of samples taken throughout the purification procedure show a single protein band (Figure 4.2).

2.5M Sørenson phosphate buffer pH 5.5 was prepared from a mixture of 16.06g of dibasic $Na_2HPO_4 \cdot 7H_2O$ (EMD Chemicals) and 1.90g of monobasic KH_2PO_4 (Sigma) for 50 mL of solution. Prior to setting up a crystallization experiment, precipitant solutions were filtered through 0.22 µm (Steriflip, Millipore) filters.

Monoolein (1-monooleoyl-*rac*-glycerol, Fluka) was purchased and stored at -12°C. Small aliquots of lipid were used at a time in order to limit the potential for oxidation.[67] For a crystallization experiment a small aliquot of lipid was gently melted to facilitate loading into a microfluidic chip.

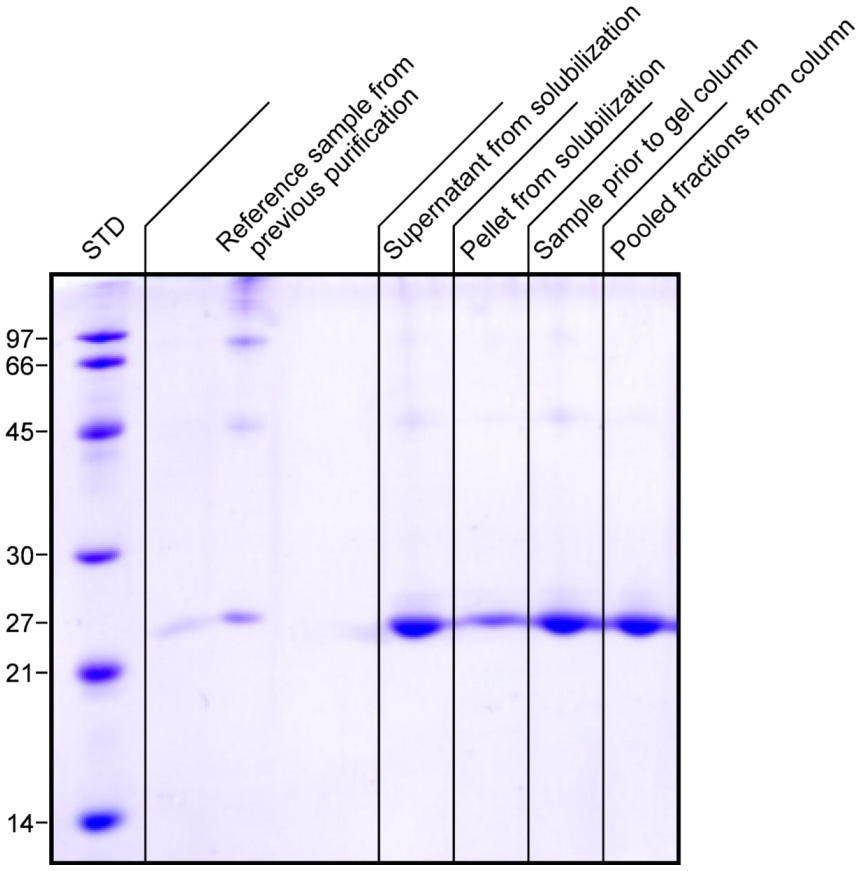

Figure 4.2. Image of an SDS-PAGE urea gel stained with Coomasie Blue used to investigate the quality of the bacteriorhodopsin throughout the purification process. From left to right a molecular weight standard (STD) is shown, followed by a reference sample from a previous purification. Additional aggregate peaks are seen in this sample because of long term storage and repeated freeze/thaw cycles. The subsequent columns on the gel show the purity of the sample after solubilization, and before and after size exclusion chromatography. In all of these columns a single peak is seen, corresponding to bacteriorhodopsin at a molecular weight of 26.8 kDa.

4.3. Results and Discussion

4.3.1 Design and Operation

The microfluidic chip shown in Figure 4.1 was designed to perform metering and mixing solutions followed by crystallization. Fluid flow in the bottom, fluid layer is controlled pneumatically. Isolation valves (black) over lines connecting the various chambers are used to control the direction of fluid flow while injection valves located over each fluid chamber (purple, blue, and orange) are used to drive the movement of material from one chamber into the next. The short length of the injection lines between fluid chambers as well as the larger size of the fluid chambers compared to the injection lines allow for the pumping of highly viscous and non-Newtonian fluids. Protein solution and lipid are introduced into the side (4.9 nL each) and center chambers (9.6 nL), respectively (Figure 4.4a), displacing air, which escapes by permeation through the PDMS. In the present configuration some additional volume is lost in the supply lines and inlets (~40%), however this design has not been optimized.

For protein crystallization it is necessary to screen a range of conditions. Thus a microfluidic array chip was created to facilitate higher throughput crystallization screening. In these devices a total of eight

individual mixing units with attached crystallization and precipitant chambers, as in Figure 4.1 are operated using a single set of pneumatic valve (Figure 4.3). Protein and lipid solutions are filled in through a single set of lines. However, separate inlets for precipitant solution were included to allow for testing of different crystallization conditions. This scaled-out configuration reduces the relative losses within the chip (18% loss for lipid and 30% loss for protein) as compared to a single crystallization unit and could be further optimized.

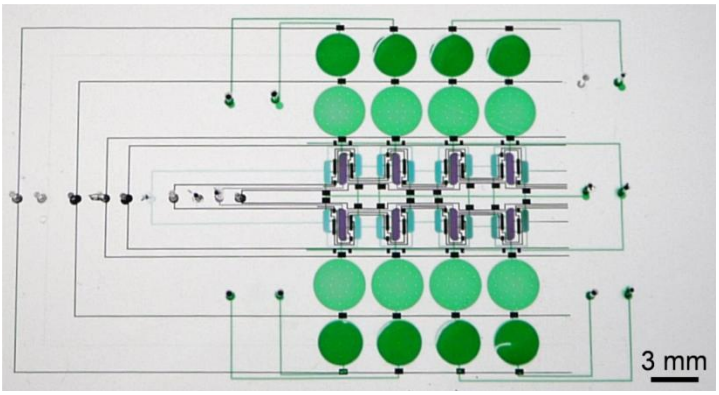

Figure 4.3. Optical micrograph of a scaled out 4x2 array of *in meso* crystallization devices. All eight devices are connected by a single set of inlets for protein and lipid and a single set of control valves. Isolation valves are shown in black. Injection valves on top of the three mixing chambers are shown in purple and blue. Separate inlets feed into the dark green precipitant chambers to allow for precipitant screening. Crystallization occurs in a separate crystallization chamber (light green) in which the mesophase is combined with a precipitant solution that is introduced from a separate circular chamber by the actuation of a pneumatic valve (dark green).

One important consideration in working at the microscale is whether the amount of material contained within the device is adequate to the task at hand. While bacteriorhodopsin has been crystallized *in meso* from sub-nanoliter boluses of mesophase,[76] it is interesting to investigate the number of crystals which could be reasonably expected to result from the amount of material present in a single lipid mixer. From the literature, conservative estimates for the dimensions of typical *in meso*-grown crystals of bacteriorhodopsin result in a single crystal volume of ~12.5 pL (50 x 50 x 5 µm).[1,64,138] Comparing this value with an estimate for the volume of a single protein molecule, as calculated from unit cell parameters ($a = b = 60.63$Å, $c = 108.16$Å and $\alpha = \beta = 90^{\circ}$, $\gamma = 120^{\circ}$)[135] gives on the order of 3×10^{10} protein molecules/crystal. Assuming a protein concentration on the order of 15 mg/mL, for the volume of protein used in a single crystallization trial roughly 3×10^{12} molecules of bacteriorhodopsin should be present, allowing for the formation of ~100 crystals per device.

Mixing in microfluidic devices is a significant challenge. In order to create chaotic mixing in a system dominated by laminar flow the fluids must be stretched and folded upon themselves until the thickness of the lamellae is such that diffusion dominates. For mixing of aqueous mixtures in a batch system, a microfluidic ring mixer has been reported previously that operates at high Péclet numbers such that a band of fluid is wrapped repeatedly around on itself.[139] Without invoking such symmetry arguments, another way to kinematically drive mixing is through the use of multiple mixing motions.[134] A simple back

and forth motion, as in the coupled syringe mixer used traditionally for preparing *in meso* crystallization samples,[33,67,83,86,88,108,127-132] is ineffective at small length scales because the fluid motion resulting from the first actuation will be identical to all subsequent repetitions. However, if the fluid is translated in one direction, and then a different motion, such as a rotation is included, mixing is improved. The addition of asymmetries to a system with respect to fluid flow or mixing times can give further improvements.

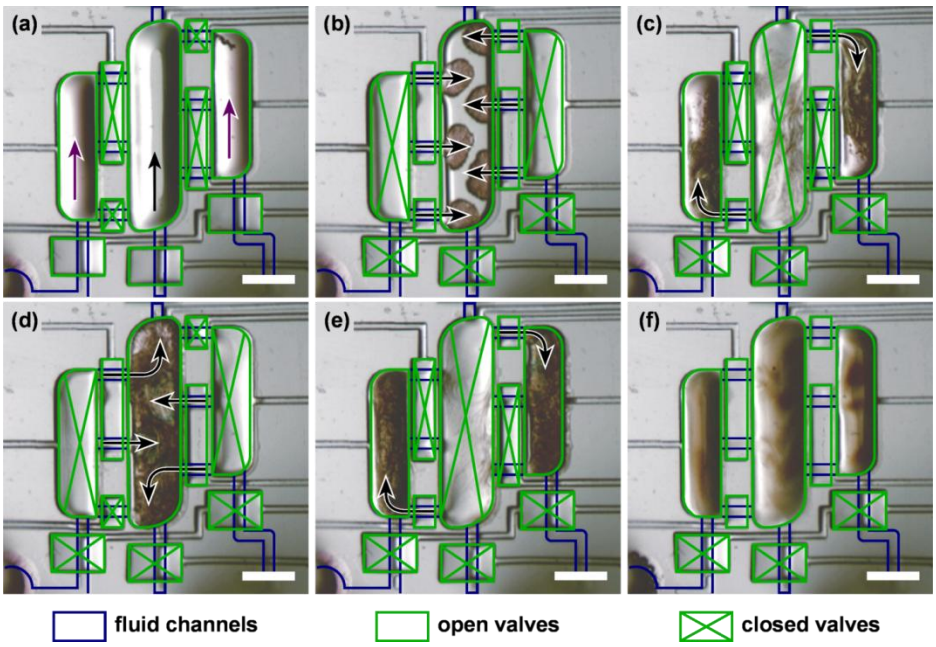

Figure 4.4. Optical micrographs of an aqueous 13.5 mg/mL bacteriorhodopsin solution (left and right chambers) being mixed with the lipid monoolein (center chamber) in a microfluidic chip. The blue lines delineate the edges of the fluidic channels. **(a)** Filling of chambers with protein solution and lipid through inlet channels (arrows); **(b)** straight-line injection of protein into the lipid-containing center chamber; **(c-e)** consecutive, chamber-to-chamber injection of the fluid mixture through different sets of inlets to create a net circulatory motion. The mixing cycle then repeats starting at **(b)**. **(f)** The slightly birefringent mixture (observed through partially crossed polarizers) after 1 min. of mixing. Scale bars: 500 µm.

The mixing chambers are designed to produce different types of fluid motion on two scales of operation. At the larger scale of fluid flow between chambers, flow proceeds alternately in a linear fashion from the side chambers to the center chamber through all of the available injection lines (Figure 4.4b), and then by two recirculating loops that utilize one injection line for flow directed into the side chambers and the remaining two lines to return to the center chamber (Figure 4.4c-e). These two motions are used to avoid issues associated with the reversibility of laminar flow. The asymmetric arrangement of the side chambers enables offset fluid injection into the center chamber. The rounded chambers also reduce dead volume (fluid not involved in mixing). Additionally, the injection lines between chambers only represent a short distance over which the pressure drop in the fluid is dissipated, thus avoiding further difficulties associated with moving highly viscous fluids over long distances. A complete mixing cycle is composed of a sequence of 12 different valve actuations (Figure 4.5).

The sequence of valve actuation for filling the chip is shown in Figure 4.5a-c. First protein solution and lipid are filled through inlet channels into their respective chambers (Figure 4.5a). The channels

connecting chambers are shut with microfluidic valves to prevent different liquids from coming into contact during the filling process. Once filling is complete, the inlet isolation valves over the inlet channels are actuated, isolating the reagents within the microfluidic chambers (Figure 4.5b). The isolation valves over the injection lines are then opened upon start of the computer-driven mixing program (Figure 4.5c).

The 12-step sequence of valve actuation for the mixing program is shown in Figure 4.5d-o. Cycles of this sequence are run with equal time spacing per step at speeds varying from 5 to 25 seconds per cycle. (1) Injection of fluid from the side chambers into the center chamber through all six injection lines by actuation of the pneumatic valve over the center chamber (Figure 4.5d). (2) The diagonally opposed isolation valves covering two injection lines each are closed (Figure 4.5e). (3) The valves over the side chambers are opened (Figure 4.5f). (4) The mixture is directed back into the side chambers through two of the six fluid channels by utilizing valves over the center chamber and a set of diagonal injection lines (Figure 4.5g). (5) The diagonal isolation valves covering two injection channels each are opened and the opposite set of isolation valves, covering only a single injection line each, are closed (Figure 4.5h). (6) The valve over the center chamber is opened (Figure 4.5i). (7) Actuation of the side chamber valves pushes the mixture is pushed into the center chamber through two injection lines on a side (Figure 4.5j). (8) The isolation valves over the single injection channels are opened and those over the double injection channels are closed (Figure 4.5k). (9) The valves over the side chambers are opened (Figure 4.5l). (10) The mixture is injected into the side chambers by actuation of the valve over the center chamber (Figure 4.5m). (11) The isolation valves over all of the injection lines are opened (Figure 4.5n). (12) The valve over the center chamber is opened. Figure 4.5o shows the state of the mixture after a single mixing cycle. A homogeneous mixture can be achieved after mixing for <1 min (Figure 4.5p), though the mixture tends to be slightly birefringent. This birefringence decreases with time, as shown in Figure 4.5q after 1 min of mixing.

Based on the rate of pumping achieved using this 12-step sequence and observations of the flow, the viscosity and shear rate of the mesophase during mixing can be estimated. The largest shear rates will be present in the injection lines, therefore the calculation will utilize this particular geometry, approximating the system as two-dimensional flow through a slit. Defining the system as in Figure 4.6, laminar fluid flow occurs in the x-direction. The height of the channel is defined with respect to y, with the coordinate axis centered in the channel. Thus the deformation rate of the fluid, or change in the angle α with time can be described in terms of the shear rate, where u is the fluid velocity along the channel.[140]

$$\frac{\partial \alpha}{\partial t} = \frac{\partial u}{\partial y} \tag{4-1}$$

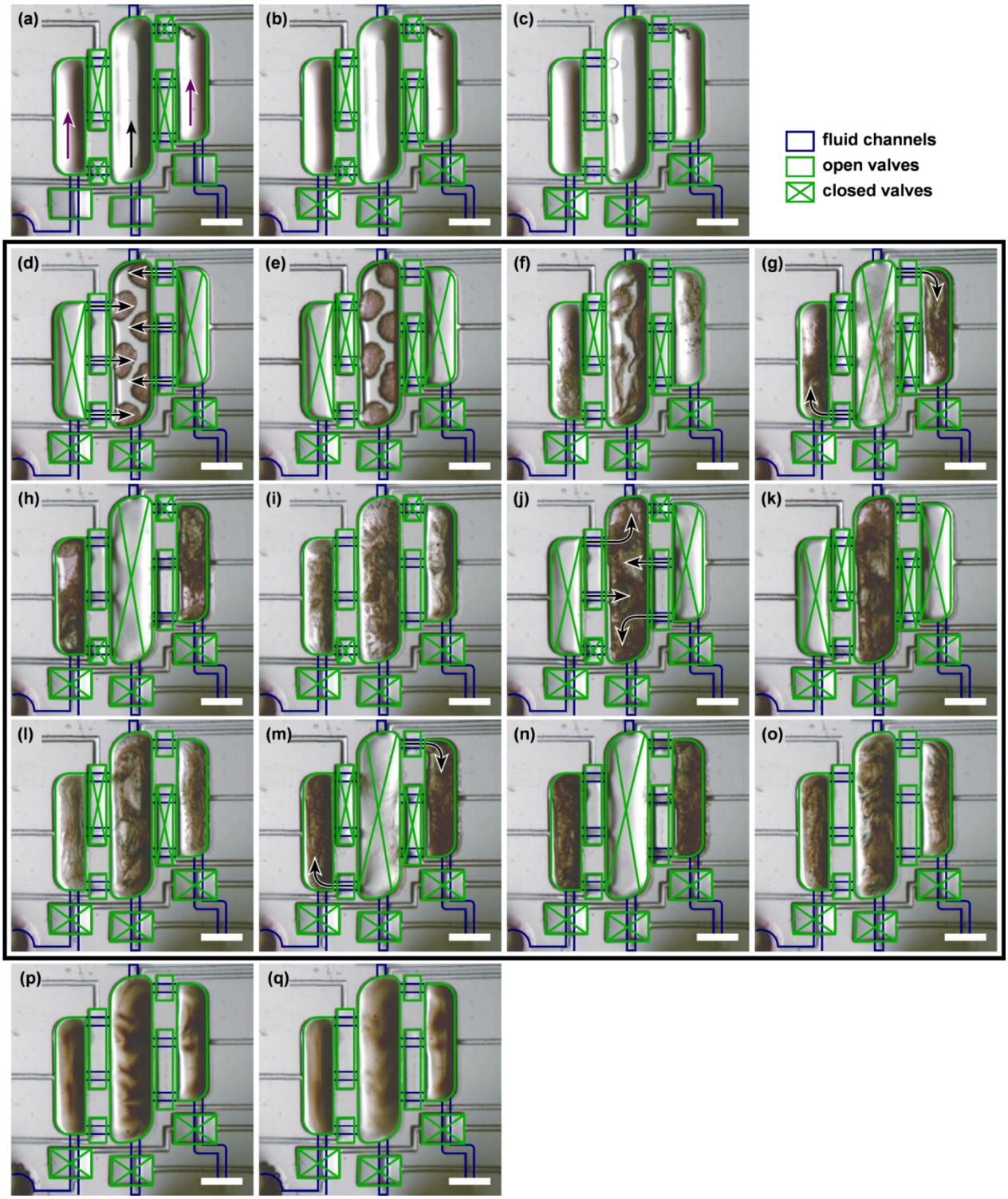

Figure 4.5. Schematic depiction of mixing device operation. Optical micrograph are of an aqueous solution of 13.5 mg/mL bacteriorhodopsin solution being mixed with the lipid monoolein on a microfluidic device acquired through a cross-polarizer. Blue lines delineate the edges of the channels which contained reagents, green lines delineate valves. **(a-c)** Protein solution and lipid loading sequence. **(d-o)** The step-by step mixing sequence. **(p)** The slightly birefringent mixture after <1 min of mixing. **(q)** The less birefringent mixture after 1 min of mixing. Scale bars: 500 µm.

An estimation of the fluid velocity in the channel can be made based on the length and height of the channel (δl = 300 μm, δy = 10 μm) and the time for valve actuation. For the 12-step mixing sequence actuated at a rate of 5 s/cycle a single step occurs in δt = 0.42 s. Although actuation of the valve is much faster than this, flow is observed during the entire period of actuation, providing a conservative estimate.

$$\frac{\partial u}{\partial y} = \frac{\delta l}{\delta t \delta y} \tag{4-2}$$

Thus the shear rate in the injection channels during mixing is estimated at 71.4 s^{-1}.

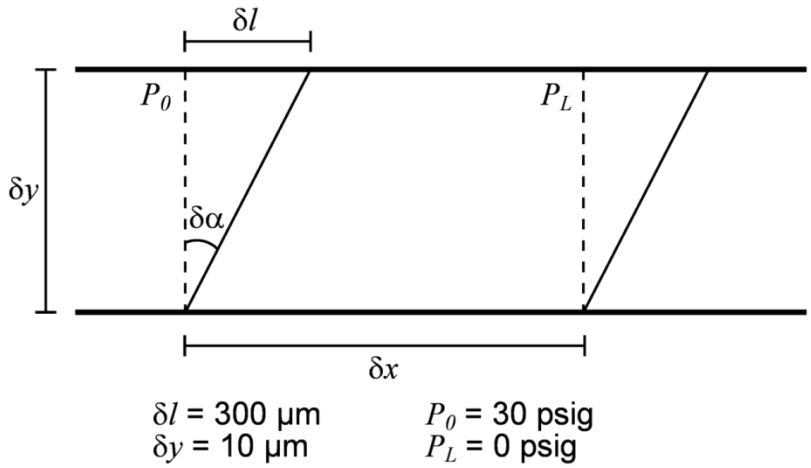

Figure 4.6. Schematic depiction of the geometry and parameters used in the estimation of shear rate and mesophase viscosity during mixing. Flow occurs in the x-direction and the channel height is defined with respect to y. The deformation of a fluid element at a particular height y can be described by the change in angle $\delta\alpha$, which translates to a deformation length δl at height δy. The inlet pressure P_0 is assumed to equal the 30 psig supplied by the pneumatic lines and this pressure is assumed to be spent at the out let of the channel P_L = 0 psig.[140]

Although lipidic mesophases have been clearly demonstrated to have non-Newtonian fluid properties,[111,112] as a simple estimate the viscosity (μ) of the mesophase fluid at the above shear rate (71.4s^{-1}) can be evaluated using the Newtonian fluid model.

$$\tau_{yx} = \mu \frac{\partial u}{\partial y} \tag{4-3}$$

The shear stress for fluid flow through a slit can be written as:[141]

$$\tau_{yx} = \left(\frac{P_0 - P_L}{L} \right) y \tag{4-4}$$

where L is the length of the channel in the x-direction and P_0 and P_L describe the inlet and outlet pressures respectively. Thus for the microfluidic geometries defined here the shear stress τ_{xy} = 3447 Pa. Using this model the viscosity of the mesophase is estimated to be 48.3 Pa-s during mixing. This value for the fluid viscosity is approximately 60,000x larger than that of water at 30°C and 2,000x larger than that for pure monoolein lipid at 30°C.

During mixing each point of injection leads to mixing by tendril-whorl type flow (Figure 4.7).[134] In this manner chaotic mixing is done by stretching and folding the two fluid components until the length-scale of the individual fluid lamellae is on the order of the diffusion length. Tendril-type flow occurs as the fluid stretches upon moving from one fluid chamber to another through a narrow injection channel (Figure 4.7c). Whorl-type flow occurs as fluid leaves the injection channel and enters a fluid chamber where it then folds around in an eddy-like fashion (Figure 4.7b). This whorl motion is further enhanced when fluid enters a chamber from multiple injection lines. Birefringence (or the lack thereof) was used to visualize the extent of mixing in the chip.[26,33,40,48,64,67,71,73-75,77,79,88,89,92,95,96,103,113,114,125,142-146] The aqueous/lipid mixture was observed to be homogeneous and mostly non-birefringent within 1-2 min. of mixing (Figure 4.4f and Figure 4.5q), indicating the formation of the desired cubic phase.

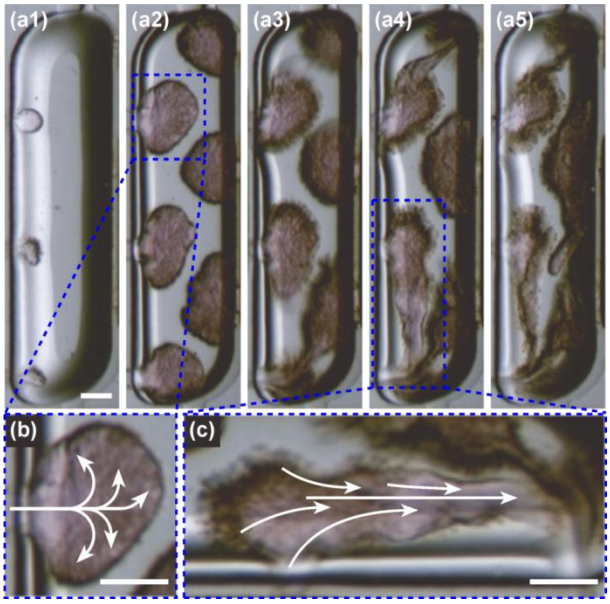

Figure 4.7. Optical micrographs of an aqueous 13.5 mg/mL bacteriorhodopsin solution being mixed with the lipid monoolein in the center chamber of a microfluidic chip. **(a1-a5)** Injection of protein solution into the lipid such that tendril-whorl flow occurs; **(b)** eddying (whorl) flow within the injected protein solution indicated by divergent arrows; **(c)** stretching (tendril) flow, indicated by convergent arrows, as the contents of the center chamber are pushed through a the narrow injection line. Scale bars: 150 µm.

4.3.2 Validation of the Platform Using Bacteriorhodopsin as a Model Protein

After mixing is complete, the mesophase is transferred to a crystallization chamber via actuation of the chamber valves. This is done in order to provide better control over the interaction of the mesophase and a precipitant solution. The movement of the mesophase itself is achieved by actuation of the chamber valves in the mixer to first concentrate material in the center chamber (Figure 4.8b), and then drive it out of the mixer and into the circular crystallization chamber of defined geometry upon opening of an isolation valve over the line connecting the two portions of the device (Figure 4.8c). A specific amount of a precipitant solution, e.g. 2.5 M Sørenson phosphate buffer, can then be injected from the precipitant chamber (Figure 4.8d).

The amount of a precipitant solution can be metered by dead filling of the precipitant chamber. One isolation valve is used to prevent the precipitant solution from leaking into the crystallization chamber until desired. A second isolation valve is used to seal the precipitant chamber inlet once filling is complete. With this inlet valve closed, the outlet valve connecting the chamber to the mixing chambers is opened and actuation of the valve over the precipitant chamber is used to drive in the precipitant solution (Figure 4.8d). This injection can be performed either before the mesophase is moved to the crystallization chamber or afterwards, as shown here. Injection of the precipitant prior to moving the bolus is preferred in order to avoid air bubbles, as shown in Figure 4.8d.

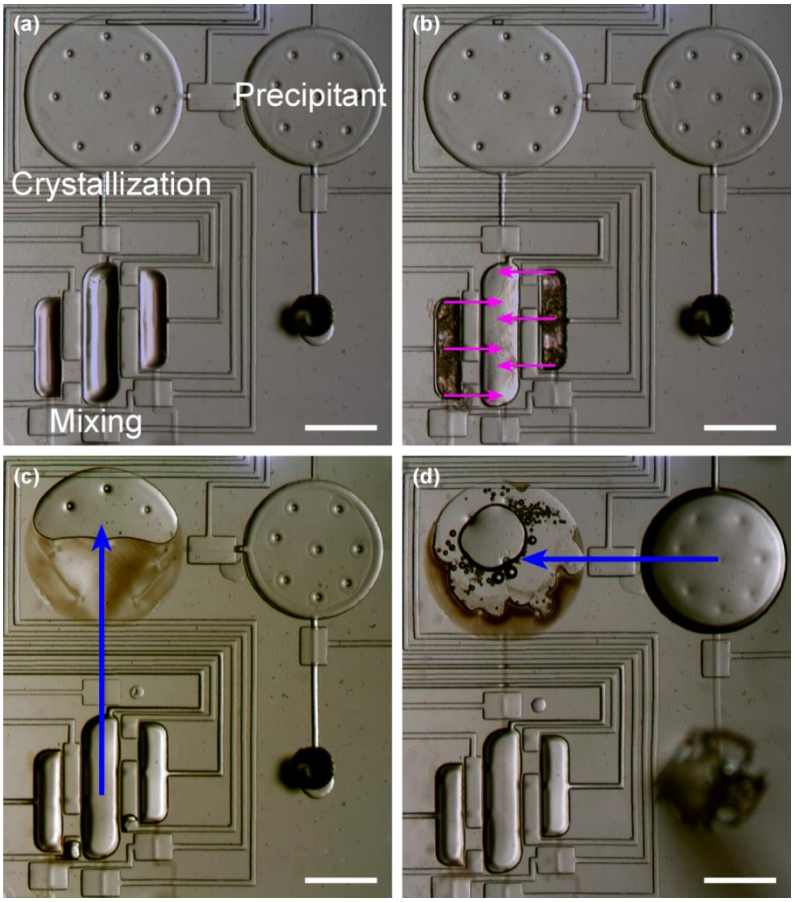

Figure 4.8. A series of optical micrographs under cross polarization depicting the preparation of an in-meso crystallization trial on chip using 13.5 mg/mL bacteriorhodopsin solution and monoolein. **(a)** The homogeneously mixed mesophase. **(b)** Valves over the side chambers are used to concentrate the mixture into the center chamber. **(c)** The valve over the center chamber is used to drive the mesophase trial into the crystallization chamber. **(d)** A precipitant solution of 2.5M Sørenson buffer, pH 5.5 is injected into the crystallization chamber from the precipitant chamber by actuation of a valve over the precipitant chamber. Scale bars: 1 mm.

Alternatively, a chip where a large well has been punched through the PDMS over the crystallization chamber can be used for crystallization trials to facilitate harvesting of crystals (Figure 4.9a). In this punched-hole chip the precipitant solution is pipetted directly into the well prior to preparation of the mesophase, and the well is sealed with Crystal Clear tape (Hampton Research) for the duration of the

crystallization experiment. The size of this precipitant reservoir is large enough that evaporative losses through the PDMS would be insignificant during the course of an experiment.

As a proof-of-concept, *in meso* crystallization of the membrane protein bacteriorhodopsin was performed using this chip. A precipitant solution of 2.5 M Sørenson phosphate buffer at pH 5.5 was pipetted into the precipitant reservoir and sealed. The lipid monoolein and a solution of bacteriorhodopsin (13.5 mg/mL solubilized in 25 mM NaH_2PO_4 with 1.2% w/v octyl *β*-D-glucopyranoside, pH 5.5) were then mixed into a homogeneous mesophase. The resulting bolus of mesophase was then moved from the mixing chambers to the crystallization chamber by actuation of valves (Figure 4.9a). Finally, the entire chip was sealed with Crystal Clear tape and stored in the dark at room temperature. Plate-like purple hexagonal crystals appeared within a few days (Figure 4.9b) and grew to a diameter of 20-50 µm, comparable with dimensions reported in the literature.[1,26]

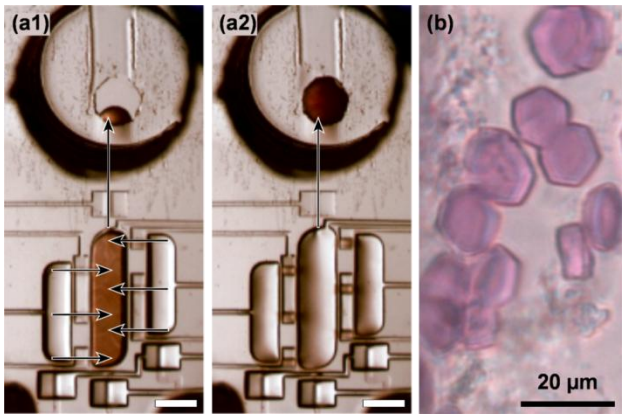

Figure 4.9. (a) Optical micrographs of a homogeneous mesophase of 13.5 mg/mL bacteriorhodopsin solution and monoolein being moved from the mixing chambers into the crystallization chamber in a punched-hole chip by actuation of the mixing chamber valves in a punched-hole chip. Scale bar: 500 µm. **(b)** Optical micrograph of the resulting bacteriorhodopsin crystals grown on-chip via the in meso method.

4.4. Conclusions

In conclusion, a microfluidic chip for the on-chip formation of lipidic mesophases for *in meso* crystallization at volumes sub-20 nL has been demonstrated. This achievement is particularly significant due to the challenges of not only mixing fluids of different viscosities, but also driving fluid flow of highly viscous materials on the microfluidic scale. The feasibility of *in meso* membrane protein crystallization was then validated using the membrane protein bacteriorhodopsin. Compared to the present *in meso* crystallization screening approaches, the operational scale and amenability for high throughput processing of the microfluidic approach introduced here allows for a 1000-fold decrease in the preparative scale at which the mixing necessary for mesophase formulation can be performed. This capability is particularly necessary to extend crystallization screening for the *in meso* technique to include multiple lipids and/or different lipid compositions. In addition to crystallization screening, the ability to set up a large number of trials will allow detailed study of the interactions between artificial mesophases, membrane proteins, and precipitating agents. Better understanding of these interactions will facilitate the

rational design of sparse matrix crystallization screens geared to determine suitable *in meso* crystallization conditions for membrane proteins of unknown structure.[1,108]

4.5 Acknowledgements

This work was funded through the NIH Roadmap for Medical Research (R21 GM075930-01) a NIH Kirschstein Predoctoral Fellowship (F31 EB008330) and a critical research initiative grant (Campus Research Board, UIUC). Thanks to Professor Steven Sligar and Dr. Tim Baybert, as well as Professor Chad Rienstra, Dr. Robert B. Gennis, and Dr. Deborah Berthold for the bacteriorhodopsin samples and assistance with purification, and Professor Jonathan J.L. Higdon for helpful discussions. Also, Griffin W. Roberts and Joshua D. Tice were invaluable in their efforts associated with the development of the microfluidic chips.

4.6 References

(1) Landau, E. M.; Rosenbusch, J. P. *P Natl Acad Sci USA* **1996**, *93*, 14532.
(2) Baker, M. *Nat Methods* **2010**, *7*, 429.
(3) Wallin, E.; von Heijne, G. *Protein Sci* **1998**, *7*, 1029.
(4) Willis, M. S.; Koth, C. M. In *Methods in Molecular Biology: Structural Proteomics - High Throughput Methods*; Kobe, B., Guss, M., Huber, T., Eds.; Humana Press: Totowa, NJ, 2008; Vol. 426, p 277.
(5) Michel, H. *Trends Biochem Sci* **1983**, *8*, 56.
(6) Quick, M.; Javitch, J. A. *P Natl Acad Sci USA* **2007**, *104*, 3603.
(7) Trubetskoy, V. S.; Burke, T. J. *Am Lab* **2005**, *37*, 19.
(8) Pecina, P.; Houstkova, H.; Hansikova, H.; Zeman, J.; Houstek, J. *Physiol Res* **2004**, *53*, S213.
(9) Arinaminpathy, Y.; Khurana, E.; Engelman, D. M.; Gerstein, M. B. *Drug Discovery Today* **2009**, *14*, 1130.
(10) Overington, J. P.; Al-Lazikani, B.; Hopkins, A. L. *Nat Rev Drug Discov* **2006**, *5*, 993.
(11) Koszelak-Rosenblum, M.; Krol, A.; Mozumdar, N.; Wunsch, K.; Ferin, A.; Cook, E.; Veatch, C. K.; Nagel, R.; Luft, J. R.; DeTitta, G. T.; Malkowski, M. G. *Protein Sci* **2009**, *18*, 1828.
(12) Dauter, Z.; Lamzin, V. S.; Wilson, K. S. *Current Opinion in Structural Biology* **1997**, *7*, 681.
(13) Collingsworth, P. D.; Bray, T. L.; Christopher, G. K. *J Cryst Growth* **2000**, *219*, 283.
(14) Durbin, S. D.; Feher, G. *Annu Rev Phys Chem* **1996**, *47*, 171.
(15) Talreja, S.; Kenis, P. J. A.; Zukoski, C. F. *Langmuir* **2007**, *23*, 4516.
(16) Talreja, S.; Kim, D. Y.; Mirarefi, A. Y.; Zukoski, C. F.; Kenis, P. J. A. *J Appl Crystallogr* **2005**, *38*, 988.
(17) Yoshizaki, I.; Nakamura, H.; Sato, T.; Igarashi, N.; Komatsu, H.; Yoda, S. *J Cryst Growth* **2002**, *237*, 295.
(18) Anderson, M. J.; Hansen, C. L.; Quake, S. R. *P Natl Acad Sci USA* **2006**, *103*, 16746.
(19) Hansen, C.; Quake, S. R. *Current Opinion in Structural Biology* **2003**, *13*, 538.
(20) Hansen, C. L.; Sommer, M. O. A.; Quake, S. R. *P Natl Acad Sci USA* **2004**, *101*, 14431.
(21) Lounaci, M.; Rigolet, P.; Abraham, C.; Le Berre, M.; Chen, Y. *Microelectron Eng* **2007**, *84*, 1758.
(22) Zheng, B.; Roach, L. S.; Ismagilov, R. F. *J Am Chem Soc* **2003**, *125*, 11170.
(23) Zhou, X.; Lau, L.; Lam, W. W. L.; Au, S. W. N.; Zheng, B. *Anal. Chem.* **2007**.
(24) Cherezov, V.; Caffrey, M. *J Appl Crystallogr* **2003**, *36*, 1372.

(25) Qutub, Y.; Reviakine, I.; Maxwell, C.; Navarro, J.; Landau, E. M.; Vekilov, P. G. *J Mol Biol* **2004**, *343*, 1243.

(26) Rummel, G.; Hardmeyer, A.; Widmer, C.; Chiu, M. L.; Nollert, P.; Locher, K. P.; Pedruzzi, I.; Landau, E. M.; Rosenbusch, J. P. *Journal of Structural Biology* **1998**, *121*, 82.

(27) Gavira, J. A.; Toh, D.; Lopez-Jaramillo, J.; Garcia-Ruiz, J. M.; Ng, J. D. *Acta Crystallogr D* **2002**, *58*, 1147.

(28) Ng, J. D.; Gavira, J. A.; Garcia-Ruiz, J. M. *Journal of Structural Biology* **2003**, *142*, 218.

(29) Stevens, R. C. *Current Opinion in Structural Biology* **2000**, *10*, 558.

(30) McPherson, A. In *Current Topics in Membranes, Volume 63*; Volume 63 ed.; DeLucas, L., Ed.; Academic Press: 2009, p 5.

(31) Gabrielsen, M.; Gardiner, A. T.; Fromme, P.; Cogdell, R. J. In *Current Topics in Membranes, Volume 63*; Volume 63 ed.; DeLucas, L., Ed.; Academic Press: 2009, p 127.

(32) Page, R. In *Methods in Molecular Biology: Structural Proteomics - High Throughput Methods*; Kobe, B., Guss, M., Huber, T., Eds.; Humana Press: Totowa, NJ, 2008; Vol. 426, p 345.

(33) Caffrey, M. *Ann Rev Biophys* **2009**, *38*, 29.

(34) Brostromer, E.; Nan, J.; Li, L.-F.; Su, X.-D. *Biochemical and Biophysical Research Communications* **2009**, *386*, 634.

(35) Newby, Z. E. R.; O'Connell, J. D.; Gruswitz, F.; Hays, F. A.; Harries, W. E. C.; Harwood, I. M.; Ho, J. D.; Lee, J. K.; Savage, D. F.; Miercke, L. J. W.; Stroud, R. M. **2009**, *4*, 619.

(36) Navarro, A.; Wu, H.-S.; Wang, S. S. *Separation and Purification Technology* **2009**, *68*, 129.

(37) Newman, J.; Fazio, V. J.; Lawson, B.; Peat, T. S. *Cryst Growth Des* **2010**, *10*, 2785.

(38) Li, G.; Chen, Q.; Li, J.; Hu, X.; Zhao, J. *Anal Chem* **2010**, *82*, 4362.

(39) Jia, Y.; Liu, X.-Y. *The Journal of Physical Chemistry B* **2006**, *110*, 6949.

(40) Nollert, P.; Navarro, J.; Landau, E. M. *Method Enzymol* **2002**, *343*, 183.

(41) Hanson, D. K.; Mielke, D. L.; Laible, P. D. In *Current Topics in Membranes, Volume 63*; Volume 63 ed.; DeLucas, L., Ed.; Academic Press: 2009, p 51.

(42) Tanabe, M.; Iverson, T. M. In *Current Topics in Membranes, Volume 63*; Volume 63 ed.; DeLucas, L., Ed.; Academic Press: 2009, p 229.

(43) Ostermeier, C.; Michel, H. *Current Opinion in Structural Biology* **1997**, *7*, 697.

(44) Geertsma, E. R.; Groeneveld, M.; Slotboom, D. J.; Poolman, B. *P Natl Acad Sci USA* **2008**, *105*, 5722.

(45) Hunte, C.; Michel, H. *Current Opinion in Structural Biology* **2002**, *12*, 503.

(46) Landau, E. M. In *Methods and Results in Crystallization of Membrane Proteins*; Iwata, S., Ed. 2003, p 37.

(47) Seddon, A. A.; Curnow, P.; Booth, P. J. *Bba-Biomembranes* **2004**, *1666*, 105.

(48) Johansson, L. C.; Wöhri, A. B.; Katona, G.; Engström, S.; Neutze, R. *Current Opinion in Structural Biology* **2009**, *19*, 372.

(49) Knowles, T. J.; Finka, R.; Smith, C.; Lin, Y.-P.; Dafforn, T.; Overduin, M. *J Am Chem Soc* **2009**, *131*, 7484.

(50) le Maire, M.; Champeil, P.; Moller, J. V. *Bba-Biomembranes* **2000**, *1508*, 86.

(51) Nollert, P. *Prog Biophys Mol Bio* **2005**, *88*, 339.

(52) Persson, G.; Edlund, H.; Lindblom, G. *European Journal of Biochemistry* **2003**, *270*, 56.

(53) Iacovache, I.; Biasini, M.; Kowal, J.; Kukulski, W.; Chami, M.; van der Goot, F. G.; Engel, A.; Rémigy, H.-W. *Journal of Structural Biology*, *In Press, Corrected Proof*.

(54) Membrane Proteins of Known 3D Structure. http://blanco.biomol.uci.edu/Membrane_Proteins_xtal.html (July 11, 2010).

(55) RCSB Protein Data Bank. http://www.rcsb.org/ (July 11, 2010).

(56) Li, L.; Mustafi, D.; Fu, Q.; Tereshko, V.; Chen, D. L. L.; Tice, J. D.; Ismagilov, R. F. *P Natl Acad Sci USA* **2006**, *103*, 19243.

(57) Hansen, C. L.; Skordalakes, E.; Berger, J. M.; Quake, S. R. *P Natl Acad Sci USA* **2002**, *99*, 16531.

(58) Garavito, R. M.; Picot, D. *Methods* **1990**, *1*, 57.

(59) Ostermeier, C.; Iwata, S.; Ludwig, B.; Michel, H. *Nat Struct Biol* **1995**, *2*, 842.

(60) Kulkarni, C. V. 2010; Vol. 12, p 237.

(61) Sommer, M. O. A.; Larsen, S. *J Synchrotron Radiat* **2005**, *12*, 779.

(62) Rosenbusch, J. P. *Journal of Structural Biology* **1990**, *104*, 134.

(63) Pebay-Peyroula, E.; Rummel, G.; Rosenbusch, J. P.; Landau, E. M. *Science* **1997**, *277*, 1676.

(64) Nollert, P. *Methods* **2004**, *34*, 348.

(65) Caffrey, M. *Cryst Growth Des* **2008**, *8*, 4244.

(66) Caffrey, M.; Lyons, J.; Smyth, T.; Hart, D. J. In *Current Topics in Membranes, Volume 63*; Volume 63 ed.; DeLucas, L., Ed.; Academic Press: 2009, p 83.

(67) Caffrey, M.; Cherezov, V. **2009**, *4*, 706.

(68) Cherezov, V.; Yamashita, E.; Liu, W.; Zhalnina, M.; Cramer, W. A.; Caffrey, M. *J Mol Biol* **2006**, *364*, 716.

(69) Cherezov, V.; Liu, W.; Derrick, J. P.; Luan, B.; Aksimentiev, A.; Katritch, V.; Caffrey, M. *Proteins: Structure, Function, and Bioinformatics* **2008**, *71*, 24.

(70) Li, L.; Fu, Q.; Kors, C.; Stewart, L.; Nollert, P.; Laible, P.; Ismagilov, R. *Microfluid Nanofluid* **2009**, *8*, 789.

(71) Nollert, P.; Qiu, H.; Caffrey, M.; Rosenbusch, J. P.; Landau, E. M. *Febs Lett* **2001**, *504*, 179.

(72) Cherezov, V.; Clogston, J.; Papiz, M. Z.; Caffrey, M. *J Mol Biol* **2006**, *357*, 1605.

(73) Caffrey, M. *Current Opinion in Structural Biology* **2000**, *10*, 486.

(74) Caffrey, M. *Journal of Structural Biology* **2003**, *142*, 108.

(75) Cherezov, V.; Caffrey, M. *Faraday Discussions* **2007**, *136*, 195.

(76) Cherezov, V.; Caffrey, M. *J Appl Crystallogr* **2006**, *39*, 604.

(77) Chiu, M. L.; Nollert, P.; Loewen, M. C.; Belrhali, H.; Pebay-Peyroula, E.; Rosenbusch, J. P.; Landau, E. M. *Acta Crystallogr D* **2000**, *56*, 781.

(78) Efremov, R.; Shiryaeva, G.; Bueldt, G.; Islamov, A.; Kuklin, A.; Yaguzhinsky, L.; Fragneto-Cusani, G.; Gordeliy, V. *Journal of Crystal Growth: Proceedings of the 14th International Conference on Crystal Growth and the 12th International Conference on Vapor Growth and Epitaxy* **2005**, *275*, e1453.

(79) Grabe, M.; Neu, J.; Oster, G.; Nollert, P. *Biophys J* **2003**, *84*, 854.

(80) Nollert, P. In *Methods and Results in Crystallization of Membrane Proteins*; Iwata, S., Ed. 2003, p 57.

(81) Kolbe, M.; Besir, H.; Essen, L. O.; Oesterhelt, D. *Science* **2000**, *288*, 1390.

(82) Kors, C. A.; Wallace, E.; Davies, D. R.; Li, L.; Laible, P. D.; Nollert, P. *Acta Crystallographica Section D* **2009**, *65*, 1062.

(83) Liu, W.; Caffrey, M. *Journal of Structural Biology* **2005**, *150*, 23.

(84) Luecke, H.; Schobert, B.; Lanyi, J. K.; Spudich, E. N.; Spudich, J. L. *Science* **2001**, *293*, 1499.

(85) Lunde, C. S.; Rouhani, S.; Facciotti, M. T.; Glaeser, R. M. *Journal of Structural Biology* **2006**, *154*, 223.

(86) Cherezov, V.; Clogston, J.; Misquitta, Y.; Abdel-Gawad, W.; Caffrey, M. *Biophys J* **2002**, *83*, 3393.

(87) Misquitta, L. V.; Misquitta, Y.; Cherezov, V.; Slattery, O.; Mohan, J. M.; Hart, D.; Zhalnina, M.; Cramer, W. A.; Caffrey, M. *Structure* **2004**, *12*, 2113.

(88) Misquitta, Y.; Caffrey, M. *Biophys J* **2003**, *85*, 3084.

(89) Misquitta, Y.; Caffrey, M. *Biophys J* **2001**, *81*, 1047.

(90) Misquitta, Y.; Cherezov, V.; Havas, F.; Patterson, S.; Mohan, J. M.; Wells, A. J.; Hart, D. J.; Caffrey, M. *Journal of Structural Biology* **2004**, *148*, 169.

(91) Peddi, A.; Muthusubramaniam, L.; Zheng, Y. F.; Cherezov, V.; Misquitta, Y.; Caffrey, M. *IEEE Transactions on Automation Science and Engineering* **2007**, *4*, 129.

(92) Nollert, P.; Royant, A.; Pebay-Peyroula, E.; Landau, E. M. *Febs Lett* **1999**, *457*, 205.

(93) Paas, Y.; Cartaud, J.; Recouvreur, M.; Grailhe, R.; Dufresne, V.; Pebay-Peyroula, E.; Landau, E. M.; Changeux, J. P. *P Natl Acad Sci USA* **2003**, *100*, 11309.

(94) Perry, S. L.; Roberts, G. W.; Tice, J. D.; Gennis, R. B.; Kenis, P. J. A. *Cryst Growth Des* **2009**, *9*, 2566.

(95) Rouhani, S.; Facciotti, M. T.; Woodcock, G.; Cheung, V.; Cunningham, C.; Nguyen, D.; Rad, B.; Lunde, C. S.; Glaeser, R. M. *Biopolymers* **2002**, *66*, 300.

(96) Sennoga, C.; Heron, A.; Seddon, J. M.; Templer, R. H.; Hankamer, B. *Acta Crystallogr D* **2003**, *59*, 239.

(97) Pebay-Peyroula, E.; Rosenbusch, J. P. *Current Opinion in Structural Biology* **2001**, *11*, 427.

(98) Cherezov, V.; Rosenbaum, D. M.; Hanson, M. A.; Rasmussen, S. G. F.; Thian, F. S.; Kobilka, T. S.; Choi, H. J.; Kuhn, P.; Weis, W. I.; Kobilka, B. K.; Stevens, R. C. *Science* **2007**, *318*, 1258.

(99) Jaakola, V. P.; Griffith, M. T.; Hanson, M. A.; Cherezov, V.; Chien, E. Y. T.; Lane, J. R.; IJzerman, A. P.; Stevens, R. C. *Science* **2008**, *322*, 1211.

(100) Rosenbaum, D. M.; Cherezov, V.; Hanson, M. A.; Rasmussen, S. G. F.; Thian, F. S.; Kobilka, T. S.; Choi, H. J.; Yao, X. J.; Weis, W. I.; Stevens, R. C.; Kobilka, B. K. *Science* **2007**, *318*, 1266.

(101) Lanyi, J. K.; Schobert, B. *Biochemistry-Us* **2004**, *43*, 3.

(102) Gordeliy, V. I.; Labahn, J.; Moukhametzianov, R.; Efremov, R.; Granzin, J.; Schlesinger, R.; Buldt, G.; Savopol, T.; Scheidig, A. J.; Klare, J. P.; Engelhard, M. *Nature* **2002**, *419*, 484.

(103) Katona, G.; Andreasson, U.; Landau, E. M.; Andreasson, L.-E.; Neutze, R. *J Mol Biol* **2003**, *331*, 681.

(104) Deisenhofer, J.; Epp, O.; Sinning, I.; Michel, H. *J Mol Biol* **1995**, *246*, 429.

(105) Hunte, C.; Richers, S. *Current Opinion in Structural Biology* **2008**, *18*, 406.

(106) Höfer, N.; Aragão, D.; Caffrey, M. *Biophys J* **2010**, *99*, L23.

(107) Briggs, J.; Chung, H.; Caffrey, M. *J Phys Ii* **1996**, *6*, 723.

(108) Cherezov, V.; Fersi, H.; Caffrey, M. *Biophys J* **2001**, *81*, 225.

(109) Caffrey, M.; Cheng, A. *Current Opinion in Structural Biology* **1995**, *5*, 548.

(110) Takahashi, H.; Matsuo, A.; Hatta, I. *Phys Chem Chem Phys* **2002**, *4*, 2365.

(111) Bonacucina, G.; Palmieri, G. F.; Craig, D. Q. M. *J Pharm Sci-Us* **2005**, *94*, 2452.

(112) Mezzenga, R.; Meyer, C.; Servais, C.; Romoscanu, A. I.; Sagalowicz, L.; Hayward, R. C. *Langmuir* **2005**, *21*, 3322.

(113) Persson, G.; Edlund, H.; Amenitsch, H.; Laggner, P.; Lindblom, G. *Langmuir* **2003**, *19*, 5813.

(114) Sparr, E.; Wadsten, P.; Kocherbitov, V.; Engstrom, S. *Bba-Biomembranes* **2004**, *1665*, 156.

(115) Vargas, R.; Mateu, L.; Romero, A. *Chem Phys Lipids* **2004**, *127*, 103.

(116) Takahashi, H.; Matsuo, A.; Hatta, I. *Mol Cryst Liq Cryst* **2000**, *347*, 475.

(117) Awad, T. S.; Okamoto, Y.; Masum, S. M.; Yamazaki, M. *Langmuir* **2005**, *21*, 11556.

(118) Caboi, F.; Nylander, T.; Razumas, V.; Talaikyte, Z.; Monduzzi, M.; Larsson, K. *Langmuir* **1997**, *13*, 5476.

(119) Engblom, J.; Miezis, Y.; Nylander, T.; Razumas, V.; Larsson, K. In *Surface and Colloid Science*; Springer: Berlin / Heidelberg, 2000; Vol. 116, p 9.

(120) Engström, S.; Alfons, K.; Rasmusson, M.; Ljusberg-Wahren, H. *Progress in Colloid and Polymer Science* **1998**, *108*, 93.

(121) Li, S. J.; Yamashita, Y.; Yamazaki, M. *Biophys J* **2001**, *81*, 983.

(122) Masum, S. M.; Li, S. J.; Awad, T. S.; Yamazaki, M. *Langmuir* **2005**, *21*, 5290.
(123) Murgia, S.; Lampis, S.; Angius, R.; Berti, D.; Monduzzi, M. *The Journal of Physical Chemistry B* **2009**, *113*, 9205.
(124) Okamoto, Y.; Masum, S. M.; Miyazawa, H.; Yamazaki, M. *Langmuir* **2008**, *24*, 3400.
(125) Razumas, V.; Larsson, K.; Miezis, Y.; Nylander, T. *J Phys Chem-Us* **1996**, *100*, 11766.
(126) Razumas, V.; Talaikyte, Z.; Barauskas, J.; Larsson, K.; Miezis, Y.; Nylander, T. *Chem Phys Lipids* **1996**, *84*, 123.
(127) Caffrey, M. *Biochemistry-Us* **1987**, *26*, 6349.
(128) Cheng, A. H.; Hummel, B.; Qiu, H.; Caffrey, M. *Chem Phys Lipids* **1998**, *95*, 11.
(129) Cherezov, V.; Caffrey, M. *J Appl Crystallogr* **2005**, *38*, 398.
(130) Ai, X.; Caffrey, M. *Biophys J* **2000**, *79*, 394.
(131) Boyle-Roden, E.; Hoefer, N.; Dey, K. K.; Grandinetti, P. J.; Caffrey, M. *J Magn Reson* **2007**, *189*, 13.
(132) Qiu, H.; Caffrey, M. *Biomaterials* **2000**, *21*, 223.
(133) Stroock, A. D.; Dertinger, S. K. W.; Ajdari, A.; Mezic, I.; Stone, H. A.; Whitesides, G. M. *Science* **2002**, *295*, 647.
(134) Ottino, J. M. *The kinematics of mixing: stretching, chaos, and transport*; Cambridge University Press, 1989.
(135) Luecke, H.; Schobert, B.; Richter, H. T.; Cartailler, J. P.; Lanyi, J. K. *J Mol Biol* **1999**, *291*, 899.
(136) Unger, M. A.; Chou, H. P.; Thorsen, T.; Scherer, A.; Quake, S. R. *Science* **2000**, *288*, 113.
(137) *Archaea, A Laboratory Manual - Halophiles*; DasSarma, S.; Fleischmann, E. M., Eds.; Cold Spring Harbor Laboratory Press, 1995.
(138) Belrhali, H.; Nollert, P.; Royant, A.; Menzel, C.; Rosenbusch, J. P.; Landau, E. M.; Pebay-Peyroula, E. *Structure* **1999**, *7*, 909.
(139) Squires, T. M.; Quake, S. R. *Rev Mod Phys* **2005**, *77*, 977.
(140) Fox, R. W.; McDonald, A. T.; Pritchard, P. J. *Introduction to Fluid Mechanics*; John Wiley & Sons, 2004.
(141) Bird, R. B.; Stewart, W. E.; Lightfoot, E., N. *Transport Phenomena*; John Wiley & Sons: New York, 1960.
(142) Liu, W.; Hanson, M. A.; Stevens, R. C.; Cherezov, V. *Biophys J* **2010**, *98*, 1539.
(143) Wadsten, P.; Wo?hri, A. B.; Snijder, A.; Katona, G.; Gardiner, A. T.; Cogdell, R. J.; Neutze, R.; Engström, S. *J Mol Biol* **2006**, *364*, 44.
(144) Wöhri, A. B.; Johansson, L. C.; Wadsten-Hindrichsen, P.; Wahlgren, W. Y.; Fischer, G.; Horsefield, R.; Katona, G.; Nyblom, M.; Öberg, F.; Young, G.; Cogdell, R. J.; Fraser, N. J.; Engström, S.; Neutze, R. *Structure* **2008**, *16*, 1003.
(145) Kissick, D. J.; Gualtieri, E. J.; Simpson, G. J.; Cherezov, V. *Anal Chem* **2009**, *82*, 491.
(146) Porcar, L.; Hamilton, W. A.; Butler, P. D. *Langmuir* **2003**, *19*, 10779.

Chapter 5

Design and Application of Microfluidic Platforms for *In Situ* Protein Crystallography*

Abstract

Recent efforts associated with the Protein Structure Initiative by the National Institutes of Health (NIH) have dramatically eased the bottlenecks associated with protein expression, purification, and crystallization for structural analysis. While strategies exist for dealing with each of these challenges in a high throughput fashion, crystal harvesting and mounting for X-ray analysis is still largely a manual process. During mounting there is significant potential for damaging fragile protein crystals, both from physical and environmental shock. Microfluidic strategies for protein crystallization have been limited in their application for a variety of reasons including (i) difficulties in harvesting crystals from a chip and/or (ii) the need to translate results obtained on chip to a larger scale. Here an X-ray transparent device architecture is described which allows for *in situ* X-ray analysis of protein crystals while maintaining the advanced fluid handling capabilities of multilayer microfluidics. The design uses a traditional thin polydimethylsiloxane (PDMS) fluid layer to enable the actuation of pneumatic valves. Thin films of cyclic olefin copolymer (COC) are used both for the device substrate and as a patterned control layer. This structure takes advantage of the low X-ray scattering cross-section of organic polymers such as COC while minimizing the path-length of the more strongly scattering silicon-based PDMS. These COC-based chips have also been shown to have significantly lower evaporative losses than traditional PDMS chips. This device architecture has been applied to microfluidic platforms for the microbatch crystallization of soluble proteins. *In situ* crystal quality screening and full structure determination have been demonstrated, both at room temperature and under cryogenic conditions. This approach was validated by crystallization and analysis of the soluble proteins lysozyme, thaumatin, and ribonuclease A and will be extended to microfluidic platforms for *in meso* membrane protein crystallization.

* Part of this work will be published: S.L. Perry, S. Guha, A.S. Pawate, V. Argawal, S. Nair, and P.J.A. Kenis, *X-ray Compatible Microfluidic Crystallization Platforms for In Situ Protein Crystallography*, (in preparation).

5.1 Introduction

While the success of structural biology efforts has been limited by bottlenecks associated with protein expression,[1-10] purification,[10-12] and crystallization,[12-37] the development of high throughput strategies utilizing robotics[29,38-42] and/or microfluidics[19,21-23,27,28,30,36,43-86] have helped to overcome these challenges. Automated methods also exist for the screening and collection of X-ray diffraction data from crystals.[42,87] Despite this level of automation, the harvesting and mounting of crystals for X-ray analysis remains the only fully manual step in the structural biology pipeline.[19,28,39,79,88]

Harvesting and mounting can be particularly challenging for crystals that are very small and/or fragile. Historically the size of crystals which could be analyzed was well within the realm of mounting. However, developments in synchrotron and beamline technologies continue to decrease the size of crystal which can be analyzed, opening up the potential for studying recalcitrant protein targets which only form tiny crystals.[26,29,87,89] Also, protein crystals typically have a very large solvent content and are susceptible to dehydration and environmental shock, in addition to physical damage, during handling.[9,52,90-106] The large surface area-to-volume ratio of small crystals has the potential to make dehydration and environmental effects an even more significant challenge. The ability to grow crystals within the confines of a microfluidic chip and then perform *in situ* crystallographic analysis would side-step these challenges. Furthermore, removal of physical handling has the potential to enable structural biology studies of difficult proteins by facilitating the analysis of higher quality crystals by avoiding the potential for damage.[18,44,46,47,49,51,52,59,70,107,108] In terms of microfluidic platforms for protein crystallization, *in situ* analysis would further enable the utility of these technologies by eliminating the challenge of harvesting crystals from a chip.

This chapter discusses first some of the material considerations associated with *in situ* X-ray diffraction studies (Section 5.3.1), followed by strategies for adapting current microfluidic crystallization platforms to X-ray transparent materials (Sections 5.2.1 and 5.3.2). The efficacy of these crystallization platforms for *in situ* analysis is then validated using first simple chips for the crystallization of the soluble proteins lysozyme, thaumatin, and ribonuclease A (Section 5.3.3). This chip technology was then extended to array chips for the screening and optimization of crystallization conditions for lysozyme (Section 5.3.4). Development efforts of this X-ray transparent device architecture are also extended to the microfluidic platforms for the *in meso* membrane protein crystallization[85] from Chapter 4 and is discussed in Section 5.3.5.

5.2 Materials and Methods

5.2.1 Device Fabrication

Microfluidic chips were fabricated out of a thin polydimethylsiloxane (PDMS, General Electric RTV 650) fluid layer bonded to both a molded cyclic olefin copolymer (COC, 2-4 mil, 5013 and 6013, from TOPAS Advanced Polymers Inc.) control layer and a flat COC substrate. Molding of the PDMS fluid layer was done using standard soft lithographic procedures reported previously.[82,109] Briefly, the various control

and fluid layers were designed using Macromedia Freehand MX (Macromedia Inc.). From the original design, the mask for the fluid layer was increased by 1.7% in order to ensure alignment of the layers. Based on this design, photolithography was used to fabricate replica masters for both the control and fluid layers as well as a separate master for inlet holes using high resolution transparencies (5080 dpi, University of Illinois at Urbana-Champaign Printing Services) as masks. The masters for the control and inlet hole layers were fabricated using the negative-tone photoresist SU-8-25 (Microchem). The masters for the fluid layers were fabricated using SU-8-25 or SU-8-2050 for 25 and 50 µm tall features, respectively. The fabricated masters were then treated with (tridecafluoro-1,1,2,2-tetrahydrooctyl) trichlorosilane (Gelest, Inc.), a silanizing agent, to allow for easy release of PDMS replicas.

Fluid, control, and inlet hole layers were fabricated via replica molding from these masters. Spin-coating was used to control the thickness of PDMS for the fluid layer. The PDMS used for the fluid layer for simple well and array chip devices was prepared using a ratio of 15:1 (monomer to cross-linker) while the fluid layer for *in meso* crystallization devices used 20:1 PDMS. Spin rates of 1750 and 1150 rpm were used to obtain a total PDMS film thickness of 45 and 70 µm respectively, resulting in a valve membrane thickness of ~20 µm. A much thicker layer of 10:1 (monomer to cross-linker) PDMS (~5 mm) was fabricated to facilitate the integration of robust connections for fluid and valve lines. All PDMS layers were cured at 75°C on a level hot plate. Inlet connections through the thick PDMS layer were punched using a 27 AWG needle with a thin wire plunger.

10:1 PDMS was also used to fabricate an inverse master of the control layer with the silicon master mounted on top of a stack of wafers in order to create a thick mold (Figure 5.1a). High temperature epoxy resin (Conapoxy FR 1080, 83:100 hardener:epoxy, by mass) was mixed using a Thinky planetary centrifugal mixer (Thinky USA Inc.) for 15 min at 2000 rpm with rotation and then degassed for 12 min at 2200 rpm. The epoxy mixture was then poured into the PDMS master and cured on a level hot plate at 120°C for 4 hours to yield a robust epoxy master for use in hot embossing COC.[78,110,111] In the first 30 min of curing occasionally bubbles needed to be removed from the surface of the PDMS master with a pipette tip.

Control layers were replicated via hot embossing (Carver hot press, model 3851-0) of COC films against an epoxy master (Figure 5.1b).[78,110,111] Two PDMS slabs were used to cushion and help provide firm contact between the epoxy master, the COC film, and a glass backing slide. Hot pressing was done at 350°F, 50°F higher than the glass transition temperature (T_g) of the material, at a negligible applied pressure. For best results the molded layers were removed from the epoxy master at 250°F, 50°F below T_g. Flat substrates were also prepared by hot embossing between two glass slides in order to remove surface texture created during initial fabrication of the COC sheets. Inlets for the COC control layer and PDMS fluid layer were drilled using a 750 µm drill bit. The device was protected from dirt and damage during this process by a protective layer of Scotch Tape (3M).

The COC control layer was chemically bonded to the thin PDMS fluid layer. Simple well devices were bonded using an oxygen plasma treatment while subsequent devices utilized cross-linking between an epoxy-terminated silane on the surface of the control layer and an amine-terminated silane on the surface of the fluid layer.[112] An 1 minute oxygen plasma treatment was used to activate the PDMS and COC surfaces for the formation of a silane bond. The COC control layer was immersed in a 1% v/v solution of 3-glycidoxypropyltrimethoxysilane (GPTMS, Sigma Aldrich) and the PDMS fluid layer was immersed in a 1% v/v solution of 3-aminopropyltrimethoxysilane (APTMS, Sigma Aldrich) for 20 minutes. After rinsing with DI water and blowing dry with nitrogen the two layers were aligned and brought into contact (Figure 5.1b). A strong bond forms almost immediately and the structure was allowed to cure for 1 hour at room temperature.[112] For simple array chips utilizing actuate-to-open valves[113,114] it was not necessary to bond the device to the COC substrate or to the PDMS inlet layer. However, for devices utilizing actuate-to-close valves[109] or positive pressure to drive in fluid, as in a gradient mixer, it was necessary to bond the PDMS fluid layer to the COC substrate and the PDMS layer defining the inlet holes to the COC control layer.

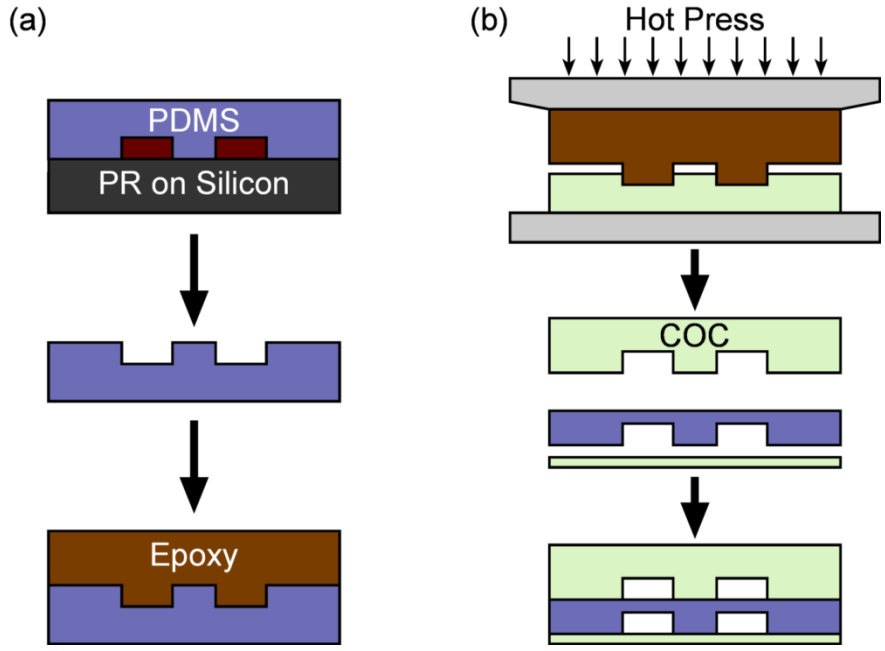

Figure 5.1. Schematic depiction of the procedure for fabricating a hybrid COC/PDMS/COC X-ray transparent microfluidic device. **(a)** Replica molding is used to create first a PDMS inverse master from a silicon master. A second replica molding step is then used to create a robust epoxy master from the inverse PDMS mold. **(b)** Hot embossing using the epoxy replica as the master is then used to mold features into sheets of COC. The molded COC sheet is then aligned and bonded to a traditional PDMS fluid layer. The resultant device is then bonded to a thin COC substrate.

5.2.2 Protein and Precipitant Solutions

Hen egg white lysozyme (Sigma) was dissolved in 50 mM sodium acetate (Sigma-Aldrich) at pH 4.6 with 20% (w/v) glycerol (Fisher Scientific) at a concentration of ~100 mg/mL. Lysozyme concentrations were determined by UV absorbance measurements (Lambda 650 UV-Vis spectrophotometer, Perkin Elmer) at 280 nm using an extinction coefficient of 2.64 mL/(mg-cm).[115] For proof-of-concept

crystallography experiments precipitant solutions of 1M and 2M NaCl (Aldrich) in 50 mM sodium acetate, pH 4.6 with 20% (w/v) glycerol were prepared. For screening experiments Crystal Screen chemicals were used directly (Hampton Research).

Thaumatin from *Thaumatococcus daniellii* (Sigma) was dissolved in 100 mM NaH_2PO_4 (EMD Chemicals) at pH 6.5 at a concentration of 82 mg/mL. The protein concentration was determined by UV absorbance measurements at 280 nm using an extinction coefficient of 1.25 mL/(mg-cm).[116] A precipitant solution of 30% (w/v) Na/K tartrate (Malinckrodt) and 20% w/v glycerol in 100 mM NaH_2PO_4 pH 7.0 was used.[72]

Ribonculease A (R-5500, Sigma) from bovine pancreas was dissolved in 100 mM sodium acetate at pH 4.5 at a concentration of 229 mg/mL. The protein concentration was determined by UV absorbance measurements at 280 nm using an extinction coefficient of 0.70 mL/(mg-cm).[117] A precipitant solution of saturated NaCl in 100 mM sodium acetate at pH 4.5 was used.[118]

Prior to setting up a crystallization experiment, protein solutions were filtered through 0.1 µm (Ultrafree-MC, Millipore) filters. Precipitant solutions were filtered through 0.22 µm (Steriflip, Millipore) filters.

5.2.3 Crystallization Experiments

Crystallization experiments were set up and visualized using either a stereomicroscope (Leica, MZ12.5) with an attached digital camera (Leica, DFC295) operated using Leica Application Suite software or a computer controlled imaging system comprised of an optical microscope (Leica Z16 APO) equipped with an auto-zoom lens (Leica 10447176), a digital camera (Leica DFC280), and a motorized x-y stage (Semprex KL66) controlled by Image Pro Plus (Media Cybernetics). For visualization of protein crystals, images were occasionally taken with the use of cross-polarizers.

For proof-of-concept large well and array chip crystallization experiments, actuate-to-open valving and fluid filling was achieved by the application of vacuum from a small vacuum pump (Gast) connected to the device through a plastic gas manifold (Cole-Parmer Instrument Co.) and 24 AWG PTFE tubing coupled with a thin metal tube to a small block of PDMS aligned over the inlets for the various control lines. Fluids (protein and precipitant solutions) were supplied to the device by pipetting 1 – 2 µL of solution onto the inlet hole. Vacuum within the chip due to actuation of valves and the air permeability of PDMS then served to pull fluid into the chambers. Protein and precipitant solutions were mixed for large well experiments prior to loading into the microfluidic device. For array chip experiments the protein and precipitant solutions were loaded separately and allowed to combine on-chip (Section 5.3.4).

For testing of devices for *in meso* crystallization, the device was operated as described in Chapter 4. Fluids were supplied to the device using 30 AWG polytetrafluoroethylene (PTFE) tubing (Cole-Parmer Instrument Co.). Pneumatic connections for valves were made using 24 AWG PTFE tubing coupled with a thin metal tube. Pneumatic control for the various valve lines was accomplished using a computer-

controlled bank of solenoid valves coupled to a nitrogen tank (Fluidigm Corp.). The 32 individual control lines are separated into two banks of 16, enabling the use of two different pressures. Typically, one bank is set at a lower pressure for driving fluid flow and the other is set to a higher pressure for actuation of isolation valves at a higher pressure.

Traditional microbatch-under-oil crystallization trials were set up combining 2 µL each of protein and precipitant solutions in a Greiner wellplate (Hampton Research).

Proof-of-concept crystallization trials of lysozyme in traditional wellplates as well as simple large well devices and array chips were incubated at 4°C. Incubation of screening experiments for lysozyme as well as crystallization trials for thaumatin and ribonuclease A were performed in a dark box at room temperature.

5.2.4 X-ray Diffraction Experiments

The majority of experiments were carried out at the 21-ID beamlines at the Advanced Photon Source at Argonne National Laboratory with the assistance of the Life Sciences Collaborative Access Team (LS-CAT).[119] Beamlines 21-ID-F and 21-ID-G operate at a fixed wavelength (λ = 0.979 Å or 12.7 keV). All 21-ID stations utilize MD-2 diffractometers (EMBL, with LS-CAT developed extensions) with on-axis sample viewing and automatic sample alignment. 21-ID-F utilizes a MarMosaic 225 detector while 21-ID-G utilizes a MAR 200 CCD detector. Samples were mounted on a standard magnetic goniometer mount (Hampton Research) with an attached metal tube into which a slit was cut and set-screw was used for securing samples (Figure 5.2b - inset). Data collection was performed either at room temperature or under cryogenic conditions. Flash-cooling of samples was achieved by direct immersion into liquid nitrogen. Various sample-to-detector distances were used based on the quality of the crystal present. Typical data collection was done using a 1° oscillation with a 1 s exposure.

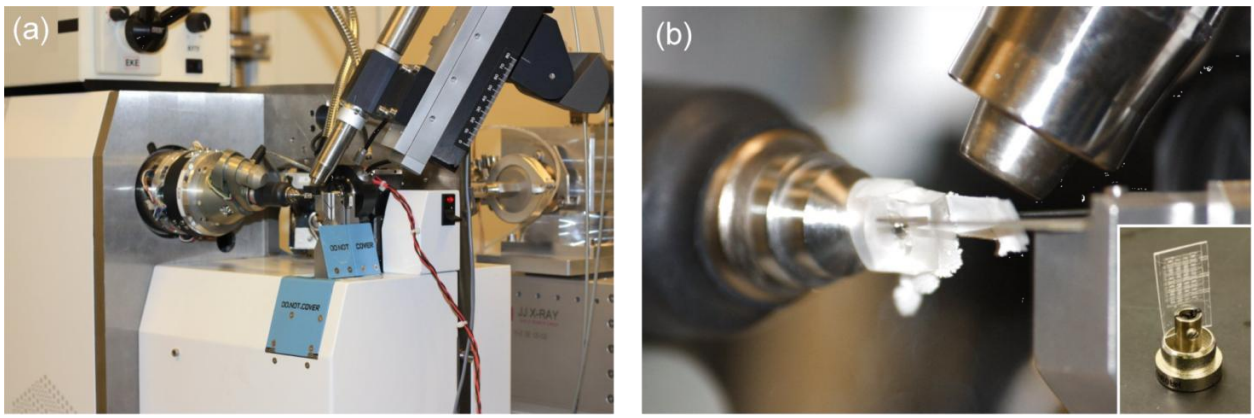

Figure 5.2. Photographs of **(a)** the macromolecular crystallography setup at 21-ID-F and **(b)** a single well microfluidic chip for protein crystallography mounted for *in situ* data collection. The inset shows a 24-well array device attached to a magnetic goniometer mount.

Bench-top diffraction experiments were performed at the George L. Clark X-ray Facility at the University of Illinois using a Bruker General Area Diffraction Detector System (GADDS) equipped with a

four circle diffractometer and HiStar multiwire area detector. A rotating anode generator (Bruker M18XHF22) operating at 40kV and 60mA was used with a graphite monochromator supplying a Cu Kα radiation beam (λ = 1.54 Å or 8.048 keV). The sample to detector distance is ~18 cm. Data collection was done in a coupled mode where $2\omega = 2\theta$ such that multiple frames could be collected over a wider range of 2θ. Typically two such frames were collected, spanning the range of 2θ from 0° to 40° (up to 2.3 Å resolution).

5.2.5 Analysis of X-ray Diffraction Data

Analysis of X-ray diffraction data collected at the synchrotron was performed using HKL2000 software for indexing, refinement, integration, and scaling. (HKL Research Inc.).[120] The resolution range of the data was established based on the resolution shell at which I/σ fell below 3.0 provided that R_{sym} was also less than 0.50. Diffraction data collected at the University of Illinois was analyzed using the GADDS software (version 4.1.08, Bruker AXS) and Topas 3 (Bruker AXS). Subsequent processing of crystallography datasets was done using the CCP4 suite of programs.[121-123] MTZ files were generated using Scalepack2mtz. Molecular replacement[124] for lysozyme was done in Phaser using PDB structure 193L as a model.[125] Model refinement and solvent building were performed using Refmac5 and aRP-Solvent, respectively. Electron density maps were displayed using COOT.[126]

5.3 Results and Discussion

5.3.1 Characterization of Device Materials

In designing an X-ray transparent microfluidic device for use in protein crystallography three main considerations with respect to the interaction between materials and X-rays must be taken into account: (i) attenuation and (ii) scattering of X-rays passing through device materials, and (iii) the strength of the diffraction resulting from a crystal. Attenuation results from the absorption of photons into the material, thereby decreasing the intensity of both the incident X-ray beam and the resultant signal. Scattering is an elastic redirection of photons based on the internal structure of the material and can affect the signal-to-noise. The strength of the diffraction signal from a crystal is related to not only the degree of order within the crystal, but also the packing density and size of the crystal.[12,127-130]

Attenuation can be calculated for a particular energy based on the exponential decay in intensity of a narrow beam of monochromatic photons from an incident intensity I_0 as it passes through a material of thickness x with a linear attenuation coefficient of the material μ.[131,132]

$$I = I_0 \exp(-\mu x) \tag{5-1}$$

Attenuation coefficients have been well studied and documented for elemental materials.[131] For a compound containing multiple elements, a linear attenuation coefficient can be calculated based on the sum of the contribution to attenuation from each of the individual elements i, weighted based on their mass fraction w_i.

$$\mu = \sum \mu_i w_i \tag{5-2}$$

Table 5.1 lists the atomic mass fractional compositions of various materials commonly used in microfluidic device manufacture and Figure 5.3a shows calculated values for the linear attenuation coefficient for SiO_2, PDMS, and COC as a function of photon energy. As can be seen, the attenuation coefficient varies significantly as a function of photon energy. Soft X-rays (lower energy) attenuate much more strongly than do harder X-rays (higher energy), thus the energy of X-rays used for an experiment can have a significant effect on the signal observed from a device.

Table 5.1. Atomic mass fraction, density, and a calculated value for the linear attenuation coefficient μ at 1Å (12.4 keV) for various materials used in microfluidic devices. SiO_2 = quartz,[133] PDMS = polydimethylsiloxane ($Si_{61}O_{60}C_{124}H_{368}$),[132] COC = cyclic olefin copolymer (C_9H_{14}),[111] PMMA = polymethylmethacrylate (C_5H_8O),[132] PI = polyimide ($C_{22}H_{10}N_2O_5$).[134]

Element	SiO_2	PDMS	COC	PMMA	PI
H	--	0.08100	0.11546	0.09586	0.02636
C	--	0.32882	0.88454	0.71394	0.69118
N	--	--	--	--	0.07328
O	0.53257	0.21194	--	0.19020	0.20918
Si	0.46743	0.37824	--	--	--
Density (g/cm^3)	2.65	0.92	1.02	0.94	1.42
μ at 1Å (cm^{-1})	9.330	7.334	1.131	1.472	1.618

Using values for the attenuation coefficient for X-rays with a wavelength of 1Å (12.4 keV), the transmission factor I/I_0 can then be calculated as a function of material thickness. A plot of I/I_0 is shown in Figure 5.3b for PDMS and COC. Because crystallography experiments commonly involve sample rotation, variations in path length as a function of the incident angle also need to be taken into account (Figure 5.3c).

Several interesting observations can be made from the data presented in Table 5.1 and Figure 5.3. PDMS and PMMA have very similar densities; however the linear attenuation coefficient for PDMS is significantly higher. This difference arises from the silicon content in PDMS. Heavier atoms present a larger cross-section for interacting with photons and will thus cause a larger degree of attenuation. The density of a material also plays a role in the degree of attenuation observed, with higher density materials increasing the number of atoms which can interact with a photon for a given path length, though this effect is less significant than elemental composition.

Knowing the attenuation coefficient for various materials, an expression for the attenuation through a series of different films *j* can be calculated based on Eq. (5-1).

$$I = I_0 \exp\left(-\sum \mu_j x_j\right) \tag{5-3}$$

A typical device used here will have an X-ray path length of 145 µm of COC and 20 µm of PDMS (50 µm COC substrate, 20 µm PDMS membrane, 75 µm COC control layer). Figure 5.3d shows a plot of transmission factor I/I_0 as a function of photon energy for this device geometry.

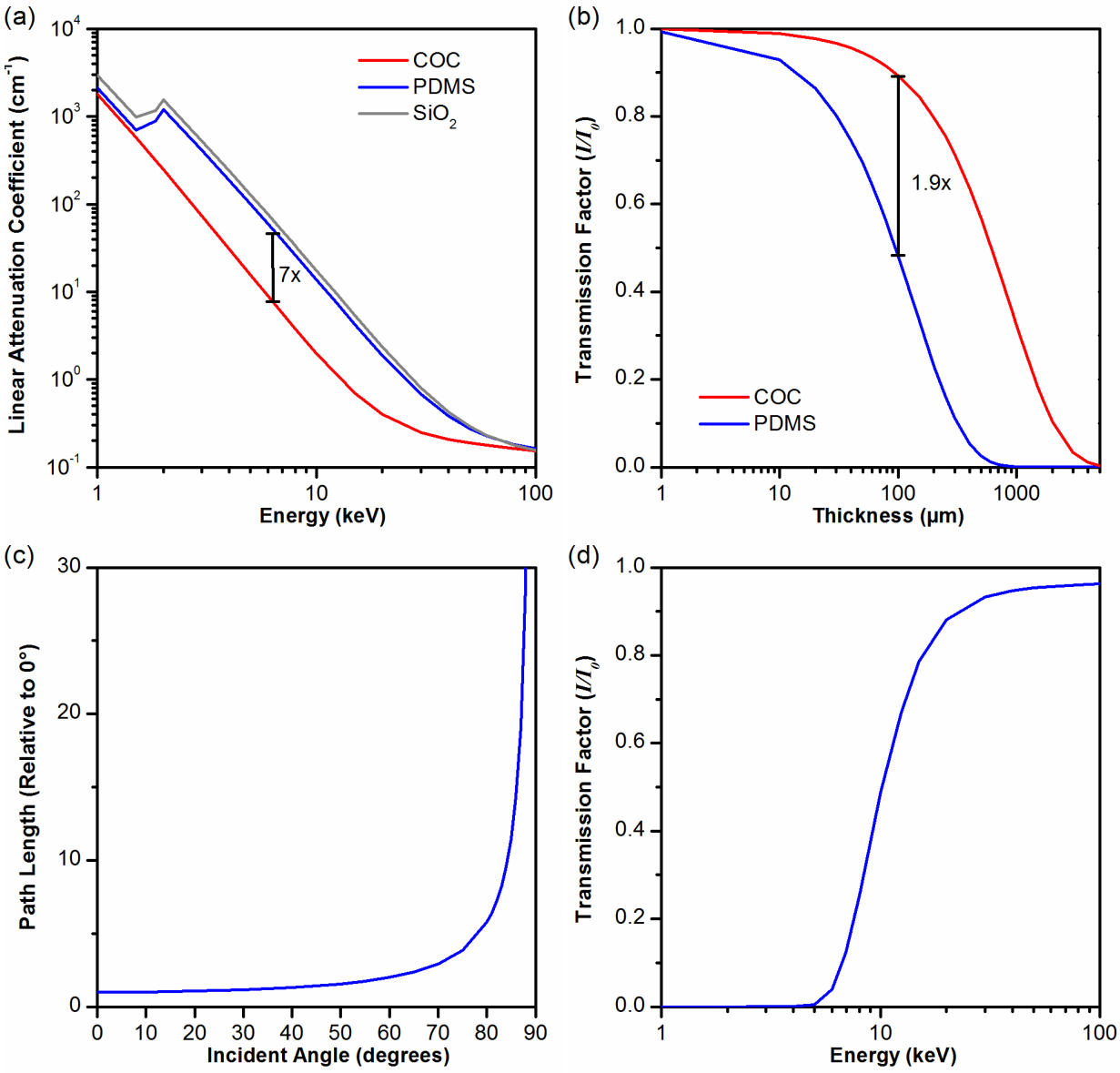

Figure 5.3. **(a)** Linear attenuation coefficient for PDMS, COC, and SiO_2 (quartz) as a function of photon energy. **(b)** Transmission factor I/I_0 as a function of film thickness for PDMS and COC. The transmission factor was calculated at a photon energy of 12.4 keV, or a wavelength of 1Å. **(c)** The relative path length through a material as a function of incident angle. Values for the path length have been normalized relative to the path length at 0° (normal incidence). **(d)** Transmission factor I/I_0 as a function of photon energy for a typical device architecture (50 µm COC substrate, 20 µm PDMS membrane, 175 µm COC control layer).

In addition to attenuation, background scatter from the device materials can also increase. Scattering is a result of the internal structure of a material. Thus the characteristic length-scale of this internal geometry defines the location of a scatter ring. An analysis of both PDMS and COC shows that these materials produce a characteristic scattering pattern (Figure 5.4). Scatter from both PDMS and COC

occurs at relatively low angles of q-spacing or areas of low resolution diffraction; q ≈ 0.161 Å^{-1} (7.5 Å) for PDMS and q ≈ 0.232 Å^{-1} (5.2 Å) for COC. A comparison of the scatter from different thicknesses of COC shows that a roughly linear relationship exists between scattering intensity and sample thickness.

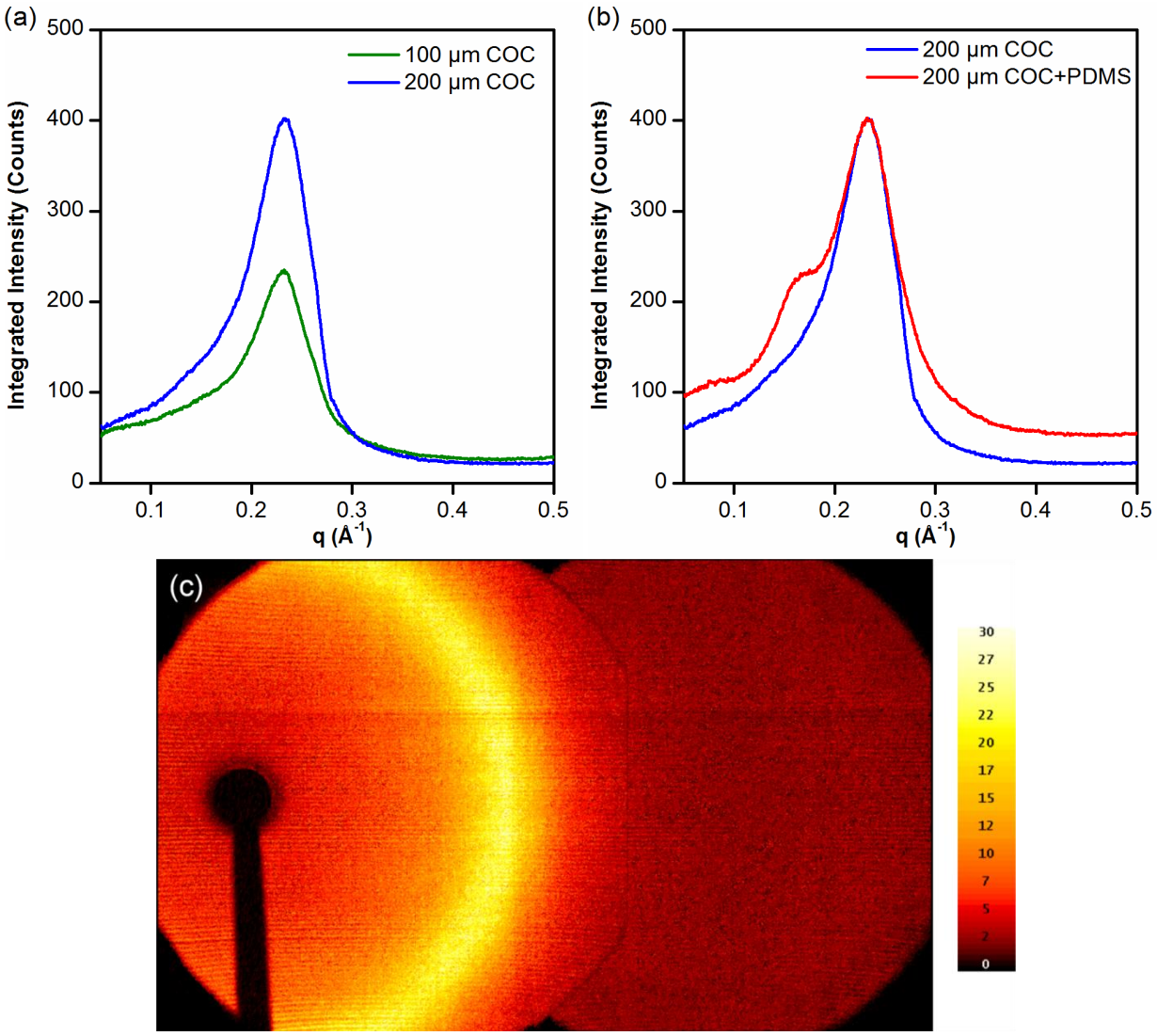

Figure 5.4. Diffractograms showing the background scattering contribution of **(a)** varying thicknesses of COC sheets (6013, Topas) and **(b)** COC sheets with and without the presence of a thin PDMS membrane (< 30 µm). Scattering from COC occurs around q ≈ 0.232 Å^{-1} (5.2 Å). Scattering from PDMS occurs around q ≈ 0.161 Å^{-1} (7.5 Å). ($q = 4\pi\sin\theta/\lambda$ where 2θ is the scattering angle, λ is the X-ray wavelength). **(c)** A compiled image from the two frames of taken of the scattering from a 100 µm COC device.

5.3.2 Device Fabrication and Characterization

While the use of hot embossing with COC has been reported previously for microfluidic devices, the majority of structures reported on have been relatively simple, single layer devices.[78,110] Consequently, it was necessary to determine design and fabrication parameters for the assembly of a multilayer microfluidic device composed of both PDMS and COC and confirm the quality of pattern transfer and sealing between dense microfluidic structures.

Scanning electron microscopy (Hitachi S-4800 High Resolution SEM) was used to visualize the quality of pattern transfer between an SU-8-25 on silicon master, the resulting inverse PDMS master, the epoxy master for hot embossing, and the final COC structure (Figure 5.5). As can be seen, the pattern transfer between replica molding steps is very good, as is the quality of the embossed COC film. Features with a minimum spacing of 50 µm were easily resolved. Testing of the minimum resolution achievable by this method was beyond the scope of this work.

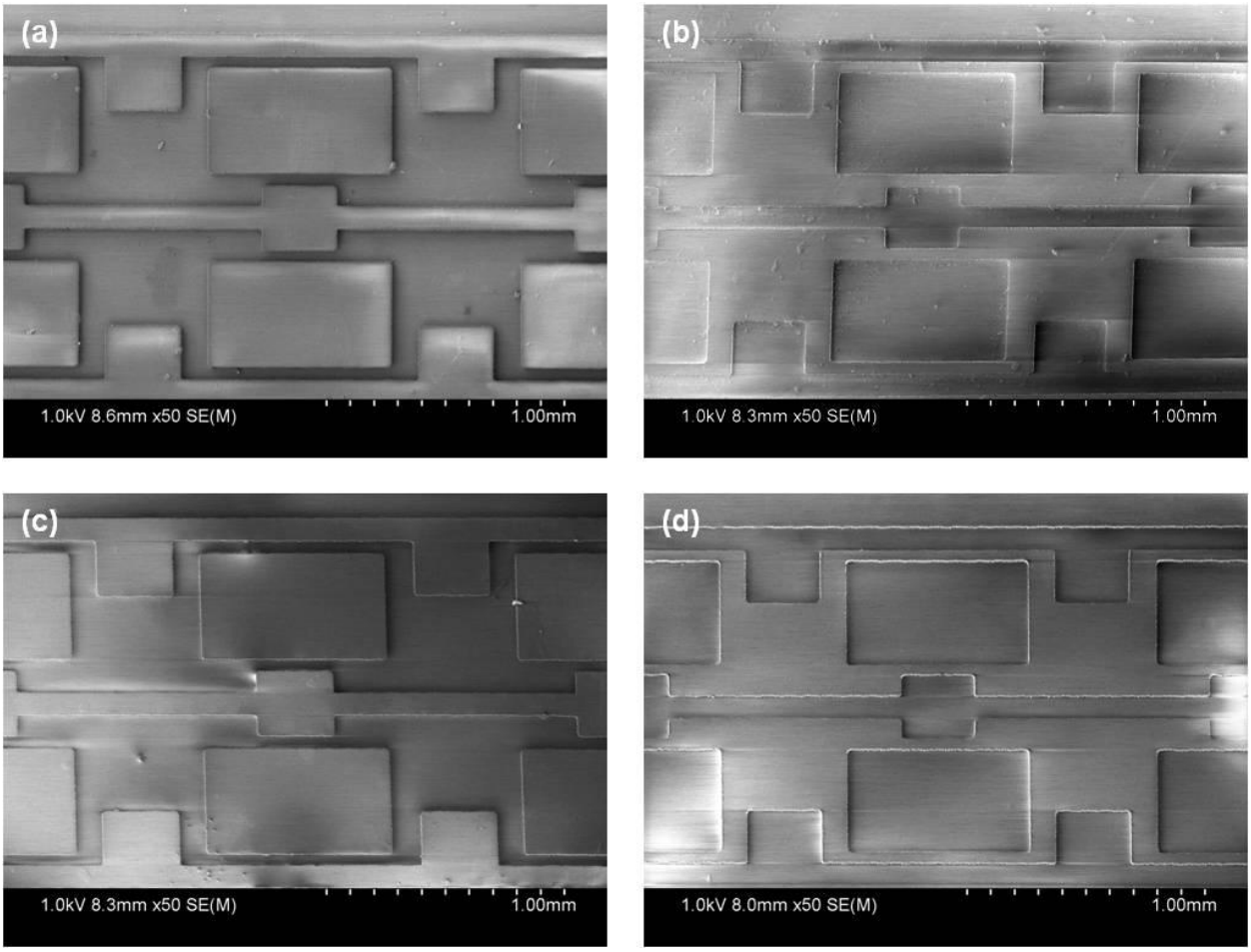

Figure 5.5. SEM images of the various stages of fabrication of the control layer for an array chip. **(a)** The SU-8-25 on silicon master. **(b)** The PDMS inverse master, molded from the silicon master in **(a)**. **(c)** The epoxy master replicated from the PDMS master in **(b)**, used for hot embossing. **(d)** The final COC control layer formed via hot embossing from the epoxy master in **(c)**.

An additional design parameter necessary for the fabrication of multilayer microfluidic devices is the relative scaling factor to be used between device features on the various layers. In traditional PDMS devices it is common to scale the uppermost device layer in order to account for relaxation of the features upon removal from the mold.[82] In the case of aligning an embossed COC control layer over a PDMS fluid layer it proved necessary to increase the scale of the fluid layer by 1.7% to match the dimensions of the hot pressed COC layer. Additionally, the epoxy masters were observed to expand slowly over time. Thus masters were remade after 20 cycles through the hot press.

Adhesion between the various layers of the device is also a key requirement, not only for fabrication, but also for device operation. In particular, the use of actuate-to-close valves requires the seal between layers to withstand significant pressures. During initial testing the chemical bond resulting from a simple plasma treatment between PDMS and COC proved to be inadequate to withstand even mild pressures. However, the chemical bond resulting from an APTMS/GPTMS treatment (Section 5.2.1) was tested and able to withstand pressures of at least 30 psi.

Evaporative losses and solvent absorption have been particularly challenging for PDMS-based microfluidic devices. For crystallization trials which may need to incubate for days or weeks it is vital to minimize or control solvent evaporation from a device. While a variety of strategies to overcome this limitation have been developed, including diffusion barriers and environmental control, it is desirable to avoid this issue. The hybrid device structure used here to facilitate X-ray transparency is also advantageous for minimizing evaporative losses from a microfluidic device. COC has very low water absorption and can serve as an effective barrier against evaporation.[111] Additionally, minimizing the thickness of the PDMS fluid layer helps to limit water losses into this film. Sealing of device inlets can be achieved using Crystal Clear tape. The evaporation rate of water from these hybrid PDMS/COC devices was examined via automated data acquisition and image analysis using Image J (NIH). Unsurprisingly, the rate of evaporation was found to correlate strongly with the quality of device fabrication. In particular these experiments demonstrated the need to planarize the substrate COC sheets via hot pressing in order to avoid leakage. For high quality devices a negligible rate of evaporation was observed over a 24 hour period, and crystallization trials were observed to be stable over at least 5 days.

A variety of device structures were fabricated and tested during the development of these hybrid COC/PDMS X-ray transparent microfluidic devices. The simplest proof-of-concept structures were comprised of a single large well covered by a matching control layer (Section 5.3.3). The control layer in this device was used only to supply vacuum pressure to the fluidic chamber for loading, no valve structures were present. These devices were used to confirm that the device materials were amenable to both on-chip protein crystallization, and *in situ* X-ray analysis at both room temperature and cryogenic conditions. The final device structures tested were highly integrated array chips for screening crystallization conditions of soluble or detergent solubilized proteins (Section 5.3.4), and microfluidic chips for *in meso* membrane protein crystallization[85] from Chapter 4 (Section 5.3.5). These two types of devices utilized actuate-to-open and actuate-to-close valves, respectively. The use of both types of valves allowed for the testing of complex device integration separately from the requirement of a firmly bonded device.

5.3.3 Validation of Device Architecture with Single Microfluidic Well Configuration: Crystallization of Soluble Proteins

The simple device architecture shown in (Figure 5.6a) was utilized for proof-of-concept experiments. In developing fabrication procedures for PDMS/COC devices, the use of simple device structures allowed for validation of particular aspects of the fabrication procedure while avoiding complications related to

complex microfluidic valving. The soluble proteins lysozyme, thaumatin, and ribonuclease A were crystallized in a batch fashion in these simple devices (Figure 5.6b-d).

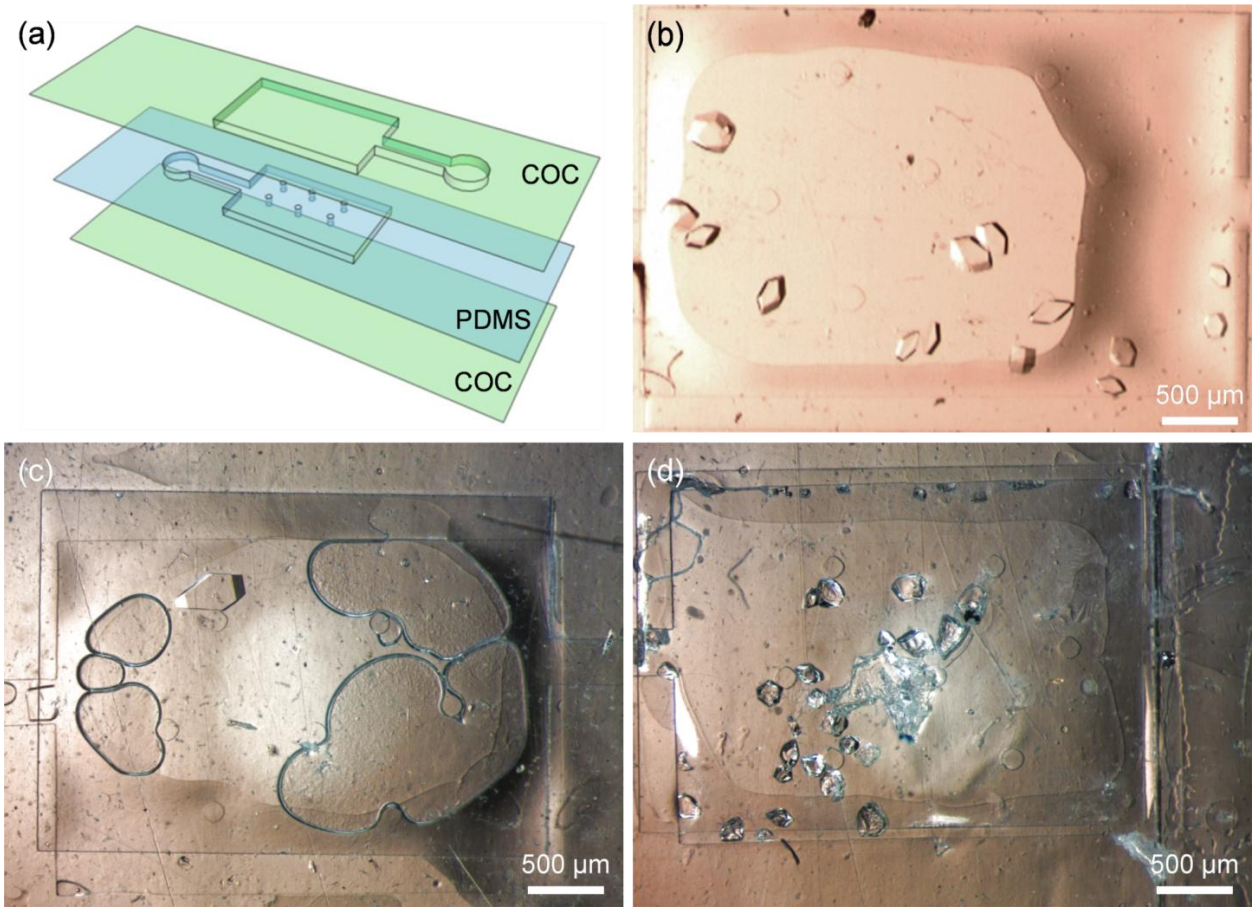

Figure 5.6. **(a)** Schematic depiction of a simple large well device. A large rectangular well with support posts is molded in PDMS (blue) and aligned with a matching COC control layer and substrate (green). The entire assembly is then attached to a COC substrate. Optical micrographs of **(b)** lysozyme, **(c)** thaumatin, and **(d)** ribonuclease A crystals grown on chip.

A second advantage of this particular geometry is that the resultant device is small enough to be used for cryogenic data collection. The two concerns for cryocooling are (i) the ability of the material to transfer heat at a fast enough rate to ensure vitrification of the sample, and (ii) the need to maintain the sample within a cryostream during data collection. While a larger array of individual devices was fabricated as a single chip for ease in handling, the individual wells were cut out using a rotary cutting blade (Olfa), mounted onto a modified magnetic cap, and cryocooled in liquid nitrogen. No difficulties in cryocooling were observed, though the planar geometry of a microfluidic chip is not ideal for use with the traditional cryostream used to maintain the sample temperature during data collection. Figure 5.2 shows a photograph of a sample mounted for data collection at 21-ID-F at the Advanced Photon Source at Argonne National Laboratory.

In situ cryogenic X-ray diffraction data was collected on various crystals of lysozyme, thaumatin, and ribonuclease A (Figure 5.7). A diffuse scatter ring from the device materials was observed, as described

in Section 5.3.2, however, the presence of this increased background did not significantly interfere with data processing. Unfortunately, optical alignment of crystals at oblique angles proved difficult. As a result, the alignment of the crystal within the X-ray beam was often lost during the collection of data over large rotational angles, as is needed for a complete dataset. In Section 5.3.4 potential strategies to overcome this challenge will be discussed.

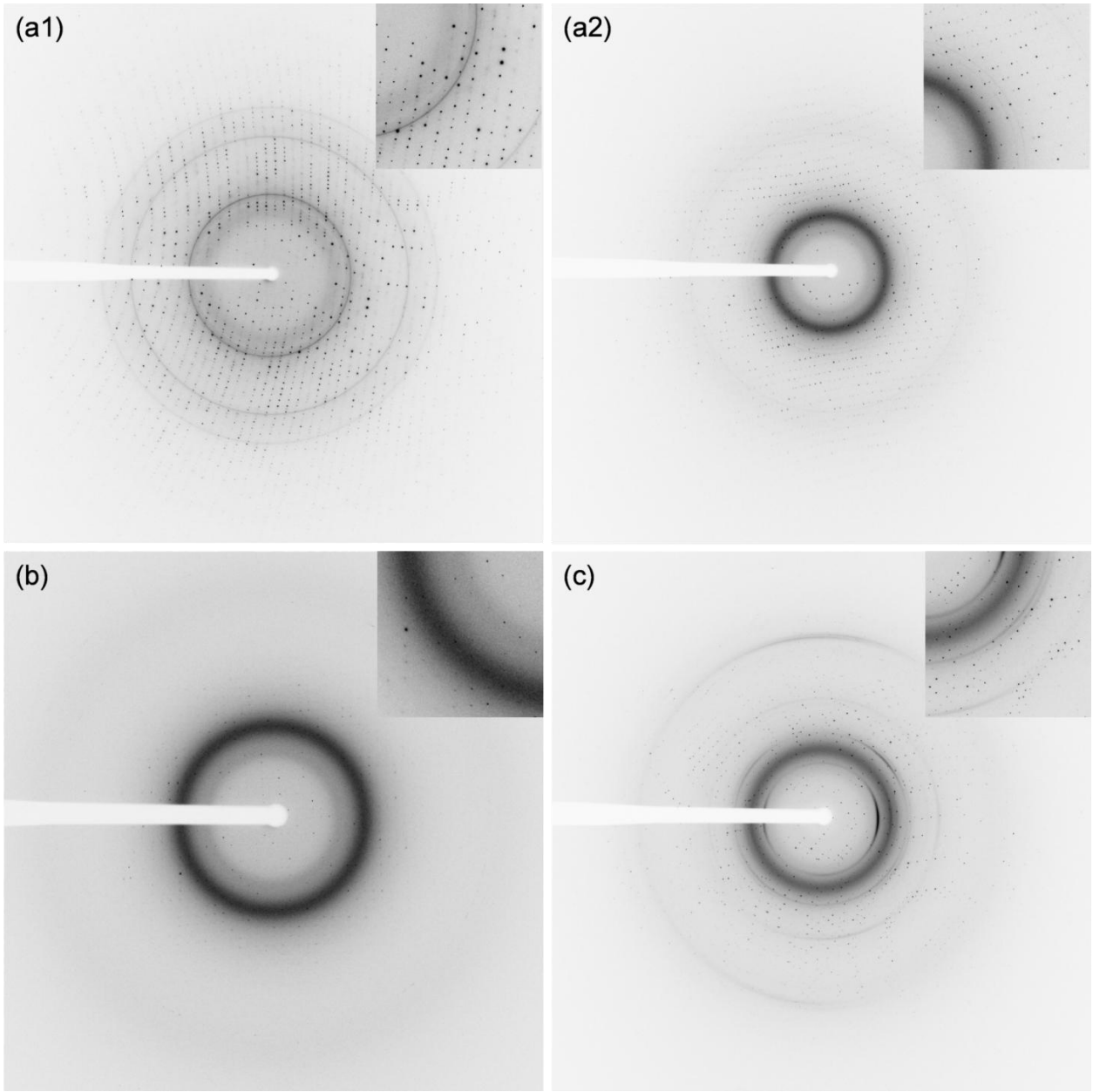

Figure 5.7. Diffraction data collected under cryogenic conditions. **(a1)** Diffraction data from a lysozyme crystal grown using the traditional microbatch method and mounted on a standard crystal mount. **(a2)** Data from a lysozyme crystal grown in a large well device and analyzed *in situ*. Sample to detector distance was 100 mm. *In situ* data from a crystal of **(b)** thaumatin and **(c)** ribonuclease A. Sample to detector distance was 150 mm. Insets provide a closer view of spot quality.

The diffraction data in Figure 5.7 shows clearly defined diffractions spots. Though the resolution to which crystals of each protein diffracted varied, individual spots are circular, indicating the high quality and low mosaicity of the crystals. The data collected on the various crystals could be easily indexed for analysis despite background scatter from the device.

The quality of the diffraction data obtained for lysozyme grown and mounted via traditional methods (Figure 5.7a1) can be compared with data collected from a microfluidic device (Figure 5.7a2). Table 5.2 provides a comparison of two such crystals. Although the absolute value of the resolution obtained for the traditionally grown crystal is higher than for crystals grown in devices, the statistical measures of crystal quality such as R_{sym}, I/σ, and completeness are comparable.

Linear R-factor (R_{sym}) provides a measure of the average discrepancy of a particular observation based on an average value of redundant observations. Typical values for R_{sym} are 0.08 – 0.15 for all hkls and 0.25 – 0.50 for the highest resolution shell.[135] For an excellent crystal R_{sym} for all hkls can be as low as 0.05, but if the value exceeds 0.2-0.3 the data is becoming too inaccurate to be useful.[136,137] As can be seen, the values for R_{sym} for both of the crystals are well within this acceptable range.

Table 5.2. Crystallographic data statistics from the analysis of two lysozyme crystals under cryogenic conditions, one grown and mounted using traditional methods and the other grown and analyzed *in situ* in a microfluidic device. Reported values are for all hkls. Values shown in parenthesis represent the value for the highest resolution shell.

Parameter	Traditional	Microfluidic
Resolution	50 – 1.25 Å	50 – 1.5 Å
R_{sym}	0.058 (0.338)	0.077 (0.410)
Mosaicity	0.21° – 0.33°	0.33° – 0.61°
Redundancy	7.4 (5.8)	8.4 (5.9)
Completeness	99.1% (98.5%)	98.0% (92.3%)
I/σ	33.8 (3.7)	25.4 (3.0)
Frames of Data	100	112

The completeness of a dataset to a particular resolution is defined as the number of unique reflections measured, compared to the total number of unique reflections. It is desirable to have a completeness for all hkls >95%. Experimentally, the completeness of the dataset is a function of the amount of data taken. Depending upon the symmetry of the crystal and the diffraction experiment it can be necessary to take as much as 360° of data. However, for a higher symmetry crystal such as tetragonal lysozyme, 90° is often sufficient.[137]

Mosaic spread, or mosaicity is a measure of the disorder within a crystal.[138] The mosaicity in good quality protein crystals can be expected to fall within the range of 0.2° – 0.5°, thus the mosaic spread of the crystals reported in Table 5.2 are reasonable.[139] Although it would have been expected that crystals grown on-chip would have a lower mosaicity than ones harvested manually, it is possible that increases in mosaicity for the crystals grown on-chip are the result of delamination of the layers of the device during

mounting due to inadequate bonding. This challenge was overcome in subsequent generations of the PDMS/COC device through the use of APTMS/GPTMS bonding and additional data collected in more advanced devices will be discussed in Section 5.3.4.

The term I/σ describes the signal-to-noise ratio of the observed diffraction spots. This metric is particularly important when comparing data collected on-chip with data from a traditionally mounted crystal because it accounts for the potential effects of signal attenuation and background scatter from the device and is key in determining the resolution limit of a dataset. A more detailed discussion of signal-to-noise and attenuation effects will be presented in Section 5.3.4 and associated Figure 5.12.

5.3.4 X-ray Transparent Microfluidic Array Chips for the Crystallization of Soluble Proteins

Although the simple large wells described in Section 5.3.3 were adequate for initial proof-of-concept experiments, the ability of microfluidics to control and route very small volumes of liquid is a major strength. To this end, the fabrication and testing of microfluidic valves using the PDMS/COC X-ray transparent device architecture was necessary.

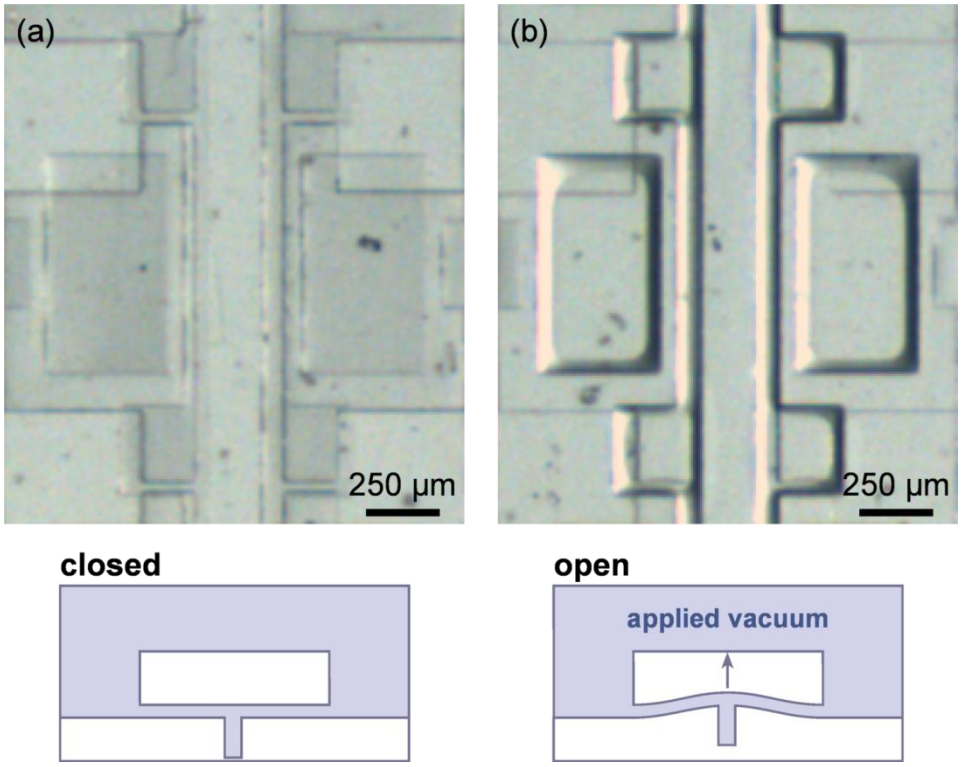

Figure 5.8. Optical micrographs and schematic depictions of an actuate-to-open valve[113,114] used in an array chip. The valve is shown **(a)** closed, in the relaxed position, and **(b)** open. Deflection of the PDMS valve membrane and subsequent filling of the device with fluid can be seen.

The X-ray transparent device architecture used here was chosen specifically to allow for microfluidic valving. The thin PDMS membrane present in the device results in significantly higher signal attenuation than would an equivalent thickness of COC. However, the flexibility of PDMS is critical for the actuation of valves. Two types of valve structures are common in microfluidics; (i) actuate-to-open[113,114] and (ii)

actuate-to-close.[109] Between these two, actuate-to-open valves are an easy next step to validate fabrication procedures because they can be tested without relying on a strong seal between the various layers of the device. Actuate-to-close valves will be discussed in Section 5.3.5 with respect to the microfluidic platform for *in meso* crystallization.

Actuate-to-open valves utilize vacuum pressure in order to deflect a thin PDMS membrane, thereby bridging a gap in a fluid line (Figure 5.8). Because of their method of actuation it is common for the fluid layer of a device containing actuate-to-open valves to be only reversibly sealed to the substrate by means of van der Waals forces. Additionally, the permeability of PDMS to air allows for the use of these vacuum actuated valves to not only permit fluid flow, but also to drive flow. Because actuate-to-open valves can be located directly over fluidic lines and compartments they enable high density arrays and have been utilized previously for combinatorial screening applications.[113] Testing demonstrated that the functionality of these valves was not affected by a transition to the PDMS/COC architecture used here. They are fully capable, not only of actuating but also of drawing fluid into a device (Figure 5.8b). Evaporation rate experiments, as discussed in Section 5.3.2 have shown that this valve structure is stable against evaporative losses over the course of days to weeks. Here their use has been adapted for use in microfluidic array chips designed to screen for and optimize crystallization conditions.

Microfluidic screening chips were designed for the screening of various protein/precipitant combinations for batch crystallization. A 24-well chip allows for the testing of six different precipitant solutions in quadruplicate (Figure 5.9). In this chip an individual crystallization trial is composed of two half-wells. Fluid control is achieved by three separate actuate-to-open valve lines. As shown in Figure 5.9b, the actuation of one valve is used to fill in first protein solution into a half-well, while the actuation of a second valve loads various precipitant solutions into the other half-well (Figure 5.9c). These two microfluidic compartments are then put into fluidic contact by the actuation of a third valve such that diffusion can take place (Figure 5.9d). The volume of an individual half-well varies as a function of channel height, Table 5.3 summarizes these values. The design of this chip was also expanded to a 96-well format (12 conditions replicated 8 times) and a 96-well format where the ratio of protein-to-precipitate is varied along each of the columns (Figure 5.10).

Table 5.3. Half-well volume for a standard microfluidic array chip with a 1:1 volume ratio of protein-to-precipitant as a function of fluid layer channel height.

Channel Height (μm)	Half-Well Volume (nL)
10	5.9
25	14.7
50	29.4
100	58.8
150	88.2

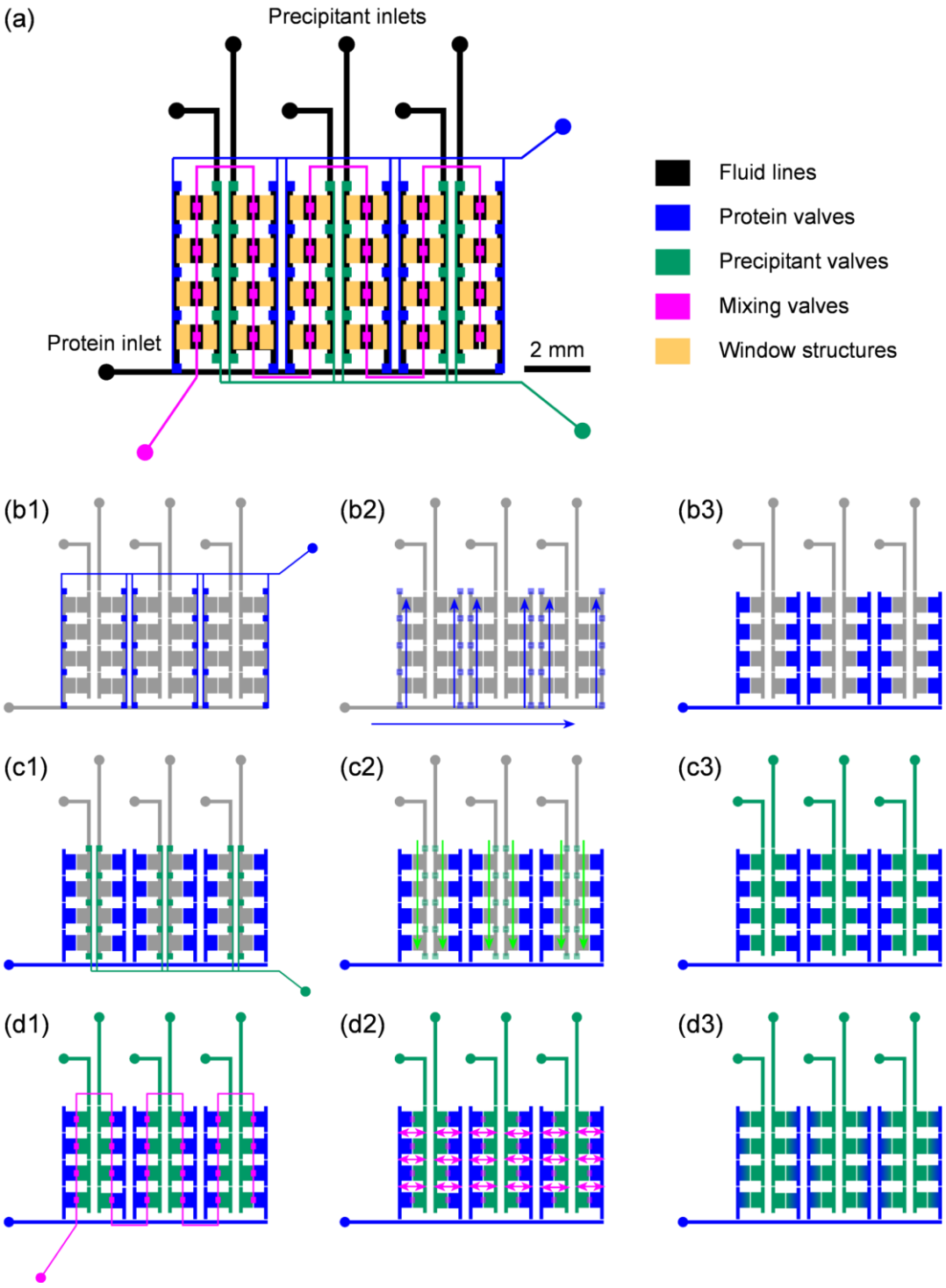

Figure 5.9. Schematic depiction of the design and operation of a 24-well microfluidic array chip for the crystallization of soluble or detergent solubilized proteins. **(a)** The complete device. Protein and precipitant inlets are indicated. The fluid layer is shown in black while the various features of the control layer have been identified based on function. Valves for the loading of protein are shown in blue, precipitant valves in green, and the valves to connect chambers and allow for diffusion between the protein and precipitant chambers are pink. Yellow window structures are shown in yellow. These structures are present in the control layer, but serve only to decrease the thickness of material present in the path of the X-ray beam. **(b-d)** Depiction of device operation. **(b)** Blue valves are actuated to fill in protein solution. **(c)** Green valves actuate to fill in precipitant solutions. **(d)** Pink valves actuate to connect the protein and precipitant chambers, allowing for diffusion over time.

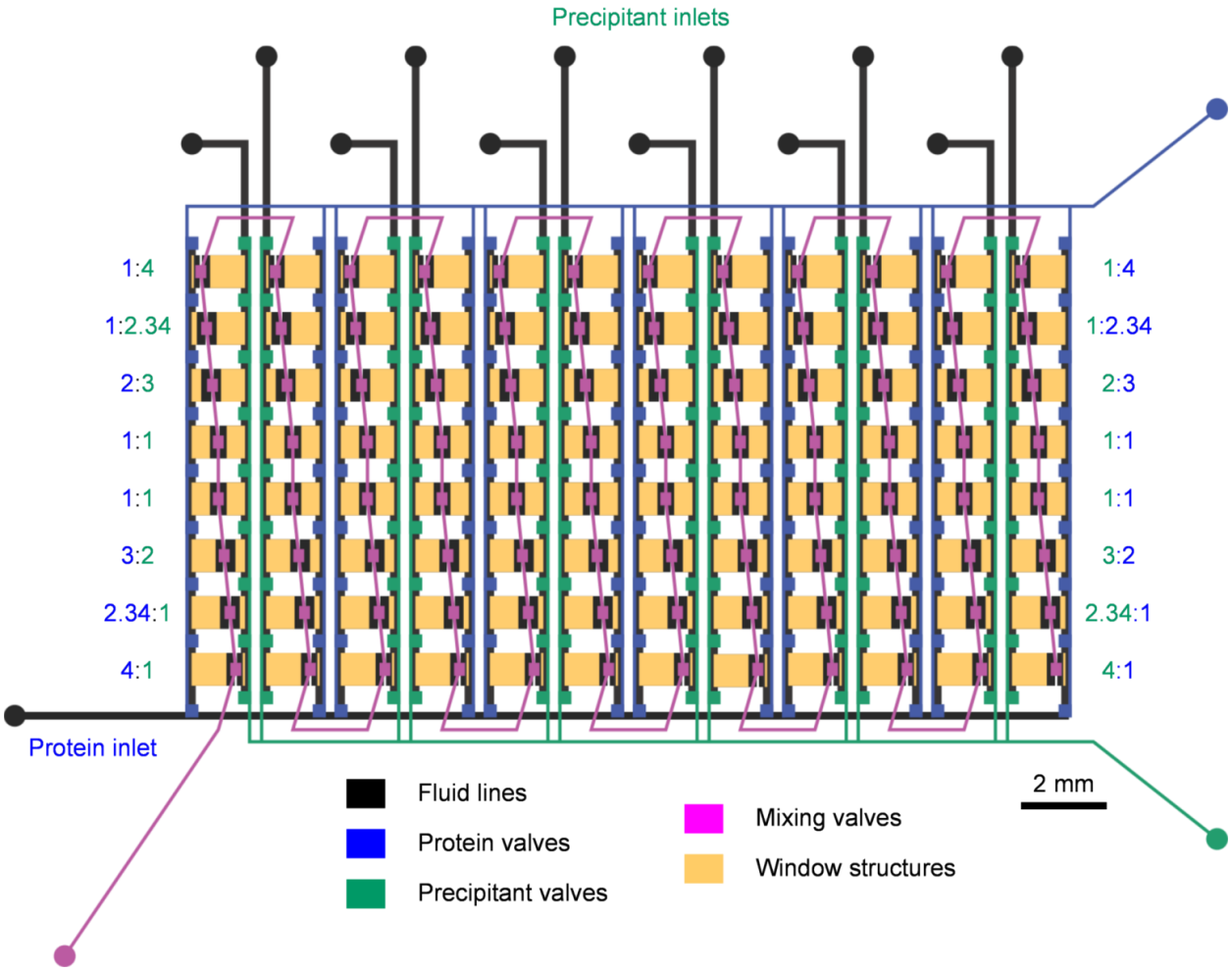

Figure 5.10. Schematic depiction of the design and operation of a 96-well microfluidic array chip with variable protein-to-precipitant ratios per screened condition for the crystallization of soluble or detergent solubilized proteins. Protein and precipitant inlets are indicated and the volumetric ratio of protein to precipitant is indicated where blue corresponds to the volume of protein and green to the volume of precipitant. The fluid layer is shown in black while the various features of the control layer have been identified based on function. Valves for the loading of protein are shown in blue, precipitant valves in green, and the valves to connect chambers and allow for diffusion between the protein and precipitant chambers are pink. Yellow window structures are shown in yellow. These structures are present in the control layer, but serve only to decrease the thickness of material present in the path of the X-ray beam.

The various microfluidic array chips were validated for crystallization screening experiments by testing a 100 mg/mL solution of lysozyme in 50 mM sodium acetate pH 4.6 with 20% glycerol against the 50 condition Crystal Screen kit (Hampton Research) at room temperature. After one week crystals were observed in 32 out of the 50 conditions in the array chips as compared to only 26 hits in the microbatch wellplate. Of the various hits observed between the traditional wellplate and our microfluidic chips, 21 of the conditions produced crystals on both platforms while 5 conditions yielded crystals uniquely in the microbatch wellplates and 11 hits were observed uniquely in the microfluidic array chips. The variability between these results can be explained both in terms of differences in the mixing of protein and precipitant solutions, slow concentration of solutions in the microfluidic chips over time, and the stochastic nature and variability of crystallization trials.[140] However, the performance of the microfluidic array chips

appears to equal if not exceed that of traditional crystallization screening methods, while requiring significantly smaller total volumes of protein.

Table 5.4. Summary of the crystallization results of a microfluidic batch screen of 100 mg/mL lysozyme in 50 mM sodium acetate pH 4.6 with 20% glycerol against the 50 condition Hampton Crystal Screen at room temperature. Conditions #16 and 18 shaded in grey resulted in crystalline material that was not protein in nature. Condition #25 shaded in pink could not be identified as either protein or salt because the crystal could not be located in the device during X-ray analysis. Conditions #30, 33, 34, and 40 shaded in blue were subjected to detailed crystal quality analysis and data collection at room temperature (Table 5.5).

Reagent #	Crystallization Solution
6	0.2 M Magnesium chloride hexahydrate, 0.1 M TRIS hydrochloride pH 8.5, 30% w/v Polyethylene glycol 4,000
7	0.1 M Sodium cacodylate trihydrate pH 6.5, 1.4 M Sodium acetate trihydrate
8	0.2 M Sodium citrate tribasic dihydrate, 0.1 M Sodium cacodylate trihydrate pH 6.5, 30% v/v 2-Propanol
9	0.2 M Ammonium acetate, 0.1 M Sodium citrate tribasic dihydrate pH 5.6, 30% w/v Polyethylene glycol 4,000
10	0.2 M Ammonium acetate, 0.1 M Sodium acetate trihydrate pH 4.6, 30% w/v Polyethylene glycol 4,000
11	0.1 M Sodium citrate tribasic dihydrate pH 5.6, 1.0 M Ammonium phosphate monobasic
12	0.2 M Magnesium chloride hexahydrate, 0.1 M HEPES sodium pH 7.5, 30% v/v 2-Propanol
15	0.2 M Ammonium sulfate, 0.1 M Sodium cacodylate trihydrate pH 6.5, 30% w/v Polyethylene glycol 8,000
16	0.1 M HEPES sodium pH 7.5, 1.5 M Lithium sulfate monohydrate
17	0.2 M Lithium sulfate monohydrate, 0.1 M TRIS hydrochloride pH 8.5, 30% w/v Polyethylene glycol 4,000
18	0.2 M Magnesium acetate tetrahydrate, 0.1 M Sodium cacodylate trihydrate pH 6.5, 20% w/v Polyethylene glycol 8,000
19	0.2 M Ammonium acetate, 0.1 M TRIS hydrochloride pH 8.5, 30% v/v 2-Propanol
20	0.2 M Ammonium sulfate, 0.1 M Sodium acetate trihydrate pH 4.6, 25% w/v Polyethylene glycol 4,000
21	0.2 M Magnesium acetate tetrahydrate, 0.1 M Sodium cacodylate trihydrate pH 6.5, 30% v/v (+/-)-2-Methyl-2,4-pentanediol
22	0.2 M Sodium acetate trihydrate, 0.1 M TRIS hydrochloride pH 8.5, 30% w/v Polyethylene glycol 4,000
23	0.2 M Magnesium chloride hexahydrate, 0.1 M HEPES sodium pH 7.5, 30% v/v Polyethylene glycol 400
25	0.1 M Imidazole pH 6.5, 1.0 M Sodium acetate trihydrate
27	0.2 M Sodium citrate tribasic dihydrate, 0.1 M HEPES sodium pH 7.5, 20% v/v 2-Propanol
28	0.2 M Sodium acetate trihydrate, 0.1 M Sodium cacodylate trihydrate pH 6.5, 30% w/v Polyethylene glycol 8,000
29	0.1 M HEPES sodium pH 7.5, 0.8 M Potassium sodium tartrate tetrahydrate
30	0.2 M Ammonium sulfate, 30% w/v Polyethylene glycol 8,000
31	0.2 M Ammonium sulfate, 30% w/v Polyethylene glycol 4,000
32	2.0 M Ammonium sulfate
33	4.0 M Sodium formate
34	0.1 M Sodium acetate trihydrate pH 4.6, 2.0 M Sodium formate
35	0.1 M HEPES sodium pH 7.5, 0.8 M Sodium phosphate monobasic monohydrate, 0.8 M Potassium phosphate monobasic
36	0.1 M TRIS hydrochloride pH 8.5, 8% w/v Polyethylene glycol 8,000
37	0.1 M Sodium acetate trihydrate pH 4.6, 8% w/v Polyethylene glycol 4,000
38	0.1 M HEPES sodium pH 7.5, 1.4 M Sodium citrate tribasic dihydrate
39	0.1 M HEPES sodium pH 7.5, 2% v/v Polyethylene glycol 400, 2.0 M Ammonium sulfate
40	0.1 M Sodium citrate tribasic dihydrate pH 5.6, 20% v/v 2-Propanol, 20% w/v Polyethylene glycol 4,000
41	0.1 M HEPES sodium pH 7.5, 10% v/v 2-Propanol, 20% w/v Polyethylene glycol 4,000
42	0.05 M Potassium phosphate monobasic, 20% w/v Polyethylene glycol 8,000
43	30% w/v Polyethylene glycol 1,500
44	0.2 M Magnesium formate dihydrate
45	0.2 M Zinc acetate dihydrate, 0.1 M Sodium cacodylate trihydrate pH 6.5, 18% w/v Polyethylene glycol 8,000
46	0.2 M Calcium acetate hydrate, 0.1 M Sodium cacodylate trihydrate pH 6.5 , 18% w/v Polyethylene glycol 8,000
47	0.1 M Sodium acetate trihydrate pH 4.6, 2.0 M Ammonium sulfate
48	0.1 M TRIS hydrochloride pH 8.5, 2.0 M Ammonium phosphate monobasic

Subsequent *in situ* analysis of crystal quality at room temperature allowed for distinguishing between protein and salt crystals, and provided information on the quality of the initial crystal hits. In addition to crystal quality screening, it was possible to collect complete or nearly complete high quality room temperature datasets for crystals grown in four. Such information would have been significantly more difficult to obtain without *in situ* analysis capabilities. Table 5.4 provides a summary of these crystal forming conditions while Table 5.5 summarizes the *in situ* crystallographic data obtained.

Two distinctive features of the diffraction data obtained for several of the screened conditions were the high quality of the data as described by R_{sym} and the low levels of mosaicity. As described previously, typical values for R_{sym} are 0.08 – 0.15 for all hkls and 0.25 – 0.50 for the highest resolution shell.[135] As can be seen from the data in Table 5.5, the value of R_{sym} over all hkls for all four of the crystals screened indicates the excellent quality of the crystals. In terms of mosaicity, while good quality protein crystals could be expected to have a mosaicity in the range of 0.2° – 0.5°,[139] the mosaic spread of several the crystals reported in Table 5.5 is significantly lower than this range.

Table 5.5. Crystallographic data statistics from the analysis of lysozyme crystals obtained via crystallization screening using Hampton Crystal Screen. Data was collected *in situ* at room temperature. Reported values are for all hkls. Values shown in parenthesis represent the value for the highest resolution shell. All crystals indexed as $P4_32_12$ tetragonal.

Parameter	Crystal Screen Reagent #			
	30	**33**	**34**	**40**
Resolution	50 – 1.75 Å	50 – 1.70 Å	50 – 1.60 Å	50 – 1.55 Å
R_{sym}	0.075 (0.300)	0.050 (0.365)	0.044 (0.302)	0.041 (0.281)
Mosaicity	0.08° – 0.27°	0.20° – 0.50°	0.15° – 0.20°	0.04° – 0.18°
Redundancy	4.3 (2.7)	6.2 (5.3)	5.3 (4.4)	5.7 (3.5)
Completeness	91.9% (77.3%)	97.5% (96.5%)	97.3% (93.4%)	99.4% (95.2%)
I/σ	21.2 (3.2)	37.0 (4.0)	34.7 (4.5)	32.7 (4.2)
Frames of Data	60	79	68	78

While the size of the array chips used in these screening experiments was not conducive for complete rotation for data collection, the symmetry of the lysozyme crystals obtained (tetragonal $P4_32_12$) was such that a complete dataset could be obtained within the limitations of the experimental setup (-60° to +60° from normal).[120,137] However, it is unreasonable to only apply *in situ* crystallographic analysis to protein crystals of high symmetry which bypasses limitations associated with chip rotation. An alternative strategy to enable data collection for any crystal is to collect a single shot, or a small wedge of diffraction data from a number of crystals and then merge the various datasets. This strategy has been used repeatedly in the literature for very small and/or fragile crystals that suffer from excessive radiation damage,[104,141-143] and is relatively common in Laue methods,[144-146] as will be described in Chapter 6.

To test the strategy of combining data taken from multiple crystals, a 24-well chip was used to grow lysozyme crystals at a single condition (120 mg/mL solution of lysozyme in 50 mM sodium acetate pH 4.6

with 20% glycerol combined with 1M NaCl (Aldrich) in 50 mM sodium acetate, pH 4.6 with 20% (w/v) glycerol). The array chip was filled as shown in Figure 5.9 and allowed to incubate. An optical micrograph of the resultant crystals is shown in Figure 5.11. For each of the various crystals in this chip 10° of data was collected (-5° to +5° from normal). Data from various crystals was then merged to obtain a complete dataset. Note that this data collection strategy requires that crystals be randomly oriented. Plate-like or other crystals with significant aspect ratios may tend to adopt a limited number of conformations due to the geometry of the microfluidic device.

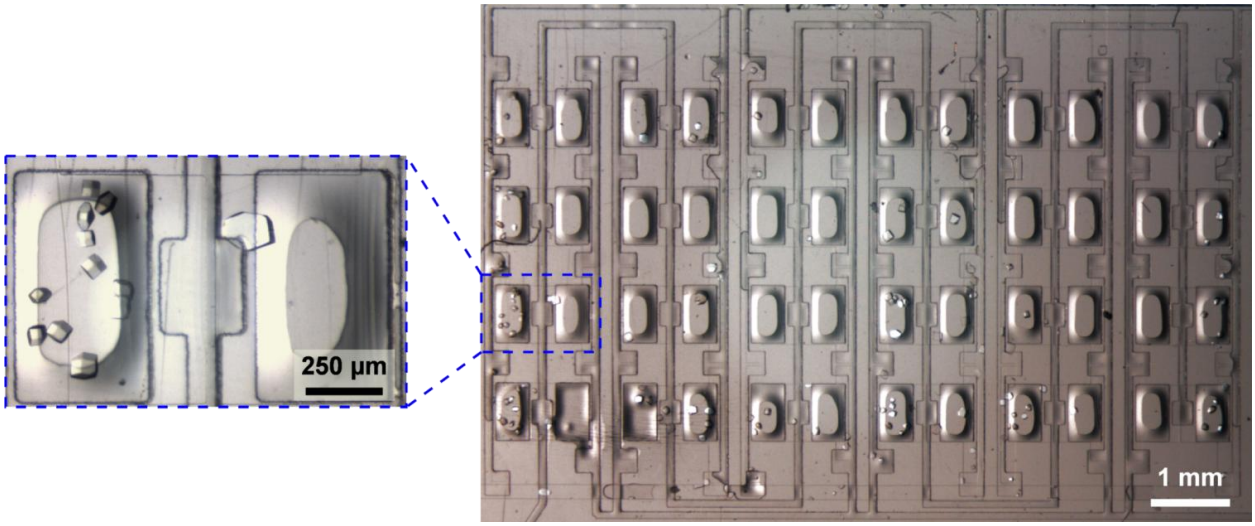

Figure 5.11. Optical micrograph of lysozyme crystals grown in a 24-well X-ray transparent PDMS/COC microfluidic array device. The inset shows a closer view of the crystals in a single well.

To provide a direct comparison of the quality of data that could be obtained by merging data collected on-chip at room temperature as compared to on-chip cryogenic data, a small section of a 24-well device containing was also cut out and used for the collection of a single crystal cryogenic dataset. This data was collected in addition to the data discussed in Section 5.3.3 in order to eliminate any variability associated with the difference in device design and crystallization kinetics. Table 5.6 provides a summary of dataset statistics, including R-values from model building for (i) a single crystal using traditional cryogenic methods, (ii) a single crystal using cryogenic on-chip data collection from a 24-well chip, and (iii) data merged from multiple crystals taken at room temperature.

As can be seen from the data in Table 5.6, high quality data was obtained in each case. Although the room temperature data does not extend to as high a resolution as in the cryogenic trials, this limitation results more from the sample-to-detector distance than from the quality of the crystals themselves. The data obtained for the room temperature crystals was analyzed to the edge of the detector and based on the value for I/σ in the highest resolution shell, the analysis could have been extended to higher resolution were the data present.

Table 5.6. Crystallographic data statistics from the analysis of lysozyme crystals; (i) the "traditional" sample was grown and mounted using traditional methods utilizing cryogenic data collection, (ii) cryogenic *in situ* analysis of a "single crystal" from a 24-well device, and (iii) the merging of small datasets from "multiple crystals" analyzed *in situ* at room temperature. Reported values are for all hkls. Values shown in parenthesis represent the value for the highest resolution shell except in the case of R (R_{free}) statistics from model building and for the Ramachandran plot statistics where the number in parenthesis indicates the number of residues in a given region.

Parameter	Traditional (cryogenic)	Microfluidic	
		Single Crystal (cryogenic)	Multiple Crystals (room temperature)
Data Collection			
Resolution	50 – 1.25 Å	50 – 1.35 Å	50 – 1.55 Å
R_{sym}	0.058 (0.338)	0.078 (0.488)	0.064 (0.362)
Mosaicity	0.21° – 0.33°	0.27° – 0.41°	0.03° – 0.08°
Redundancy	7.4 (5.8)	7.6 (6.0)	22.9 (5.7)
Completeness	99.1% (98.5%)	95.9% (98.8%)	98.1% (83.4%)
I/σ	33.8 (3.7)	25.8 (3.4)	51.4 (3.9)
Frames of Data	100	98	363
Refinement			
R (R_{free})	0.187 (0.230)	0.169 (0.194)	0.164 (0.227)
Ramachandran Plot			
Most Favored	95.28% (121)	97.64% (124)	96.06% (122)
In Allowed Regions	4.72% (6)	2.36% (3)	3.94% (5)
Disallowed	0.00% (0)	0.00% (0)	0.00% (0)

The area where the room temperature data excelled far above that of either cryogenic dataset is in terms of crystal mosaicity. The observed mosaic spread of the crystals was nearly an order of magnitude smaller than that of the cryogenic samples. Additionally, this small range of mosaicity was consistent for nearly all of the crystals grown in the 24-well chip. This consistency validates the reproducibility of well-to-well crystallization, in particular, demonstrating fine control of fluid transport and thus crystallization kinetics. While for the crystals analyzed here the range of mosaicity observed across all samples is acceptable, the potential for improving crystal quality could be particularly significant for crystals of membrane proteins which suffer from particularly weak crystal contacts.

As described in Section 5.3.3, I/σ describes the signal-to-noise ratio of the observed diffraction spots. A comparison I/σ as a function of resolution allows for a determination of the impact of signal attenuation and background scatter resulting from device materials as compared to traditional crystal mounting methods. As can be seen in Figure 5.12, a comparison of the two cryogenic datasets (square symbols) shows that *in-situ* analysis results in lower signal-to-noise than its traditionally mounted counterpart. This trend could be due in part to differences in crystal size, however, scaling of the values of I/σ for the traditional cryogenic sample based on the signal attenuation expected from the device materials (dashed line) results in good agreement with the signal-to-noise levels obtained on-chip. Interestingly, the data obtained on-chip at room temperature (triangles) shows values for I/σ at low resolution that are equivalent

to those obtained via traditional cryogenic methods. This observation begs the question as to whether the diffraction signal from the crystals is adversely affected by cryocooling. However, an in depth study of these effects is beyond the scope of the current investigation.

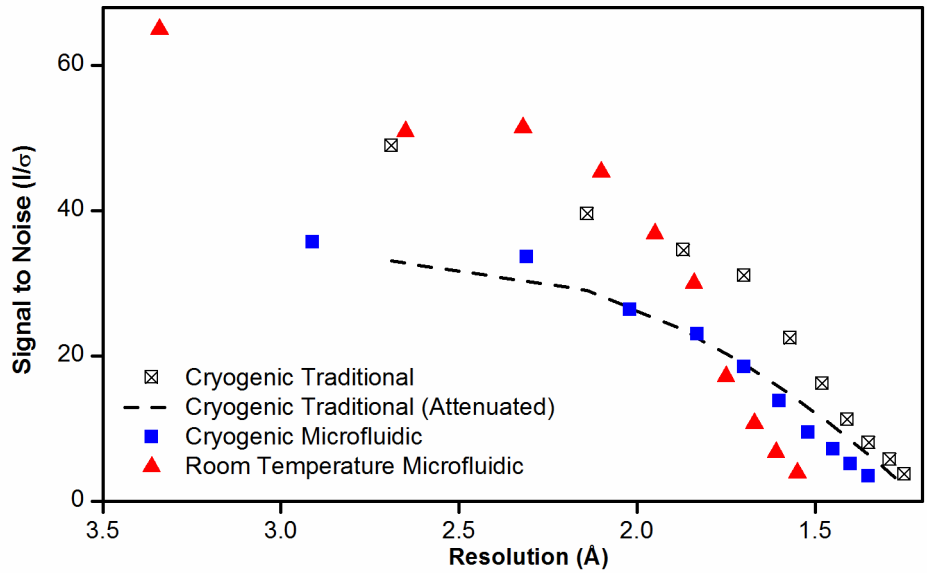

Figure 5.12. A plot comparing the signal-to-noise observed (I/σ) as a function of resolution for diffraction data collected using both traditional and on-chip methods. Square symbols denote data obtained under cryogenic conditions, using either a traditional mount or on-chip. The dashed line denotes the signal-to-noise for a traditionally mounted crystal as scaled by the attenuation factor expected for the material present in a microfludic device.

An additional figure of merit included in this analysis are the values for R and R_{free}. These R-factors are a measure of how well the refined structure agrees with the observed electron density maps. The free R-factor (R_{free}) provides a metric for cross-validating the quality of the structural model by comparing it with a small test set of "free" reflections which were not used in the refinement of the model.[138,139] Generally speaking, for a structure determination made with data to 2.0 Å resolution, the final R-factor would be expected to be ~20%, with R_{free} a few percent higher.[139] As can be seen from the data presented in Table 5.6, for all of the data collection strategies, the data extended beyond 2.0 Å and resulted in R-factors < 20%. It is interesting to note that both R and R_{free} are lower for data collected on-chip compared to data obtained via traditional cryogenic methods. Additionally, a larger fraction of residues in the structures obtained from on-chip data collection fall within the most favored zones for structural conformations on a Ramachandran plot.

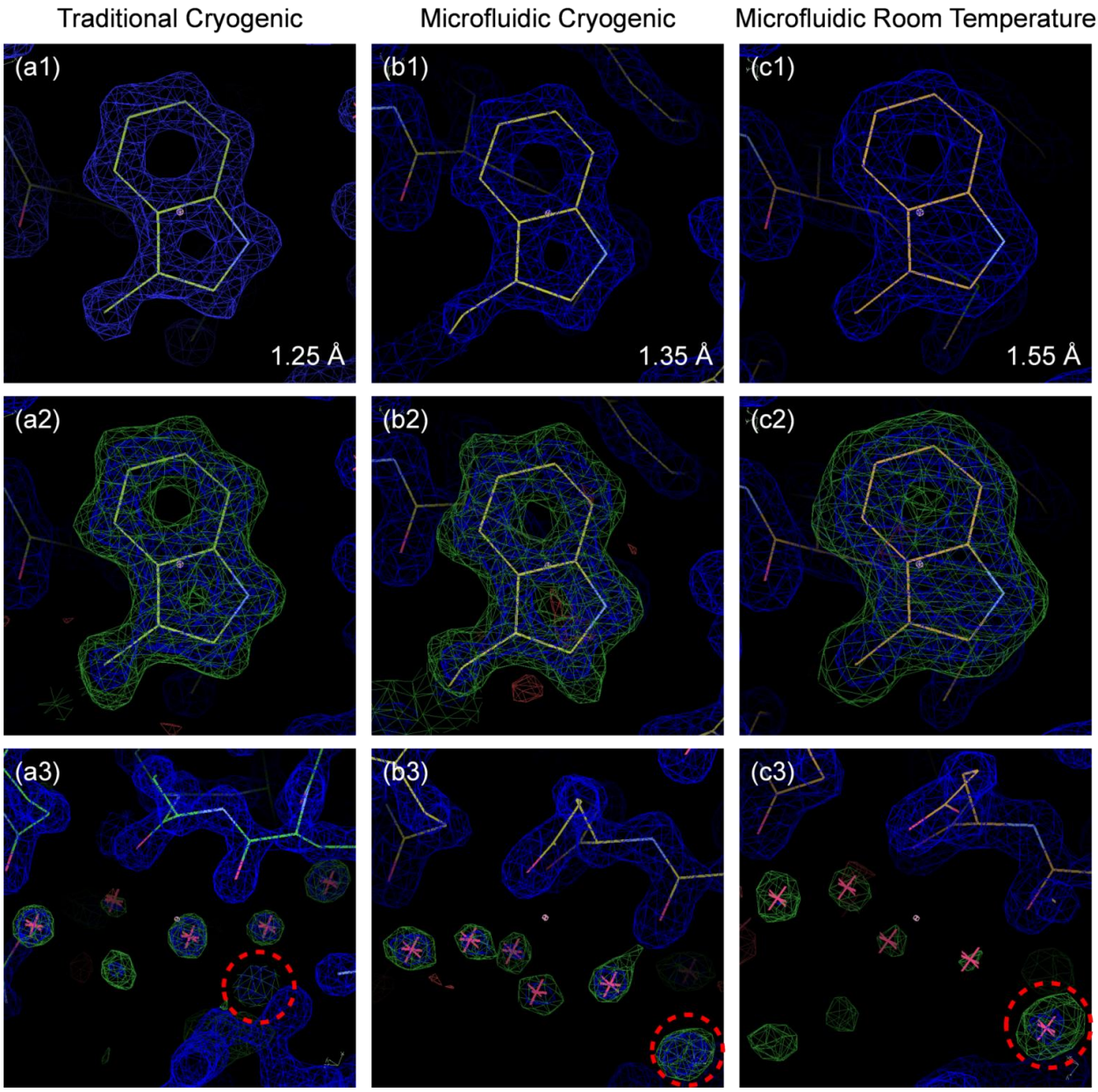

Figure 5.13. Electron density maps displaying various aspects of the structure of hen egg white lysozyme for **(a)** 1.25 Å data obtained using traditional single crystal cryogenic data collection, **(b)** 1.35 Å data from a single crystal data collected under cryogenic conditions from a 24-well microfluidic chip, and **(c)** 1.55 Å data obtained by merging data from many crystals grown on-chip and analyzed at room temperature. **(1)** The calculated structure for Trp111 at a sigma level of 2.0. **(2-3)** Maps showing the difference between the calculated and observed structures for **(2)** Trp111 and **(3)** water molecules located near Glu35. A "solvent" molecule visible at high sigma levels, suggesting the presence of a metal atom is highlighted. The calculated map (blue) is displayed at a sigma level of 2.0, while the difference map (green) is displayed at a sigma level of 3.0.

Examination of the resultant electron density maps provides a clear picture of the quality of structural data that can be obtained by these various data collection strategies (Figure 5.13). The high resolution data obtained allows for clear visualization of the structure of amino acid side-chains. As an example, the double-ring structure of the side-chain from tryptophan Trp111 can be clearly seen in all three cases (Figure 5.13a-c1), though the exact structure becomes clearer with the higher resolution data obtained

using the traditional cryogenic method (Figure 5.13a1). The validity of this structure within the final map can be verified by examining a Fourier difference map with Trp111 missing (Figure 5.13a-c2). A similar process can be performed to validate the location of water molecules within the structure (Figure 5.13a-c3). The agreement between the calculated (blue) and observed (green) maps clearly validates the location of these molecules within the structure. Additionally, analysis of the solvent difference map at high sigma levels can be used to identify metal atoms present in the structure. The "solvent" molecule highlighted in the lower right corner of Figure 5.13a-c3 is one such example of a heavier atom which could potentially be identified via this method, though the actual identity of the atom is beyond the scope of the analysis performed here.

Table 5.7. Crystallographic data statistics from the analysis of lysozyme crystals; (i) the "traditional" sample was grown and mounted using traditional methods utilizing cryogenic data collection, (ii) cryogenic *in situ* analysis of a "single crystal" from a large well device, and (iii) the merging of small datasets from "multiple crystals" analyzed *in situ* at room temperature. Reported values are for all hkls. Values shown in parenthesis represent the value for the highest resolution shell except in the case of R (R_{free}) statistics from model building and for the Ramachandran plot statistics where the number in parenthesis indicates the number of residues in a given region. The data for the cryogenic samples is the same as in Table 5.6, but was re-analyzed over the resolution range of 50 – 1.55Å to enable direct comparison with the room temperature data.

Parameter	Traditional (cryogenic)	Microfluidic	
		Single Crystal (cryogenic)	Multiple Crystals (room temperature)
Data Collection			
Resolution	50 – 1.55 Å	50 – 1.55 Å	50 – 1.55 Å
R_{sym}	0.052 (0.102)	0.072 (0.217)	0.064 (0.362)
Mosaicity	0.21° – 0.34°	0.27° – 0.45°	0.03° – 0.08°
Redundancy	7.7 (7.7)	7.9 (7.8)	22.9 (5.7)
Completeness	99.7% (100%)	94.7% (98.1%)	98.1% (83.4%)
I/σ	42.3 (19.4)	30.3 (10.0)	51.4 (3.9)
Frames of Data	100	98	363
Refinement			
R (R_{free})	0.173 (0.276)	0.162 (0.212)	0.164 (0.227)
Ramachandran Plot			
Most Favored	96.06% (122)	96.06% (122)	96.06% (122)
In Allowed Regions	3.94% (5)	3.94% (5)	3.94% (5)
Disallowed	0.00% (0)	0.00% (0)	0.00% (0)

In order to better compare equivalent statistics between the data collected by the various methods, the data originally presented in Table 5.6 was reanalyzed to a 1.55 Å cutoff in order to match the resolution obtained for the data merged from many crystals (Table 5.7). By comparing the statistics resulting from an equivalent resolution range it can be easily seen that relatively complete, high quality datasets were obtained in all cases. However, the mosaicity of the data resulting from the merging of data from multiple crystals is much lower than that for the cryogenically mounted samples. This decrease in mosaicity was observed despite the potential for increased radiation damage and can be attributed to

both the lack of physical handling as well as the absence of cryocooling which is known to increase crystal mosaicity.[147,148] A comparison of the resultant electron density maps is shown in Figure 5.14.

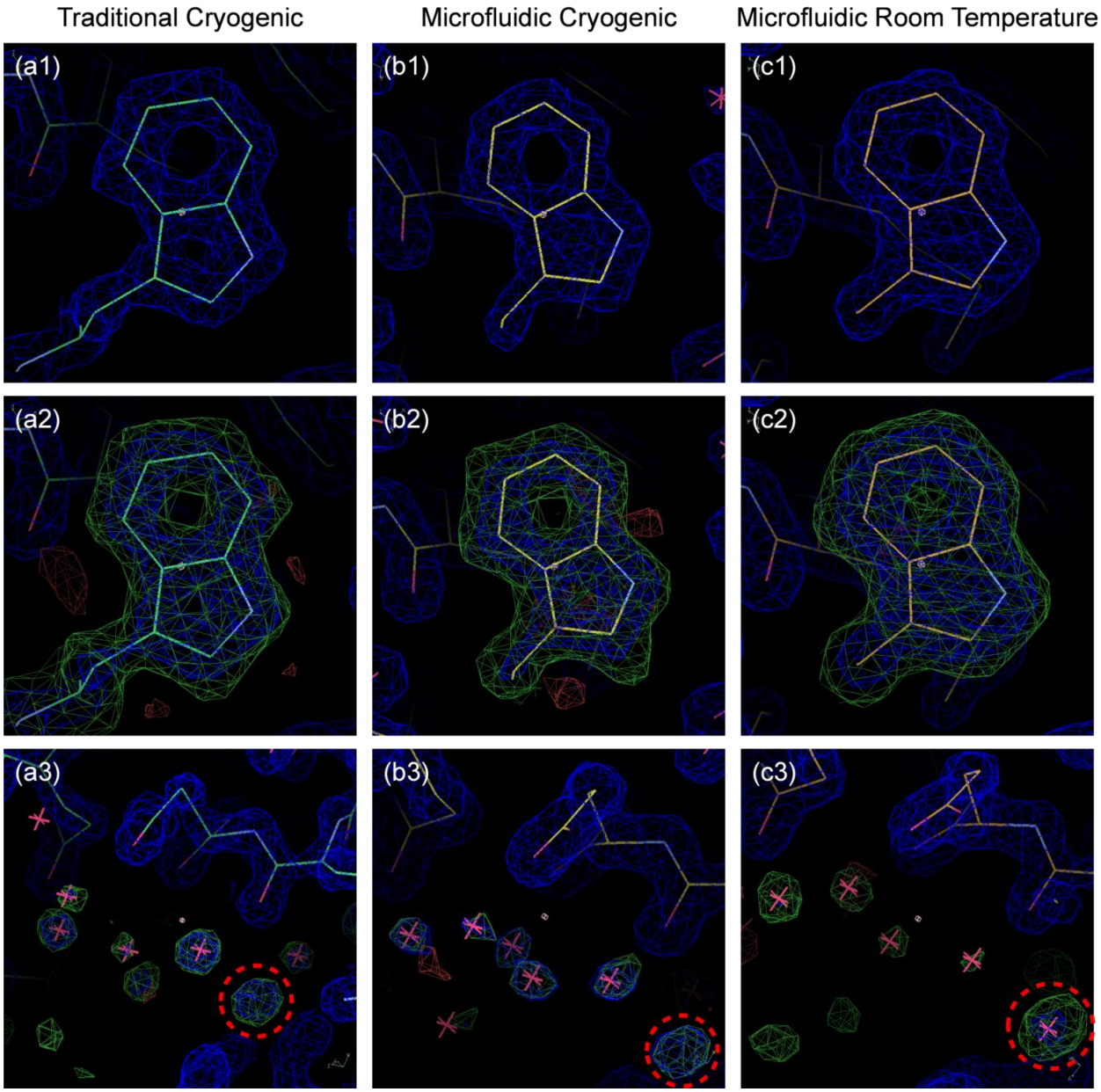

Figure 5.14. Electron density maps displaying various aspects of the structure of hen egg white lysozyme taken to 1.55 Å for **(a)** data obtained using traditional single crystal cryogenic data collection, **(b)** data from a single crystal data collected under cryogenic conditions from a 24-well microfluidic chip, and **(c)** data obtained by merging data from many crystals grown on-chip and analyzed at room temperature. **(1)** The calculated structure for Trp111 at a sigma level of 2.0. **(2-3)** Maps showing the difference between the calculated and observed structures for **(2)** Trp111 and **(3)** water molecules located near Glu35. A "solvent" molecule visible at high sigma levels, suggesting the presence of a metal atom is highlighted. The calculated map (blue) is displayed at a sigma level of 2.0, while the difference map (green) is displayed at a sigma level of 3.0.

5.3.5 X-ray Transparent Devices for the *In Meso* Crystallization and Study of Membrane Proteins

While the actuate-to-open valve configuration used in the array chips in Section 5.3.4 is amenable to use with soluble proteins and detergent solubilized membrane proteins, the microfluidic platform for *in*

meso membrane protein crystallization described in Chapter 4 relies on actuate-to-close valves to drive the flow of the highly viscous mesophase.[85,109] In order to achieve this level of valving it was necessary to extend the fabrication procedures described previously to include a strong irreversible seal between the thin PDMS fluid layer and COC substrate as before, as well as the COC control layer and a larger block of PDMS for the creation of inlet connections.

Previous attempts at using an oxygen plasma treatment to seal layers, as in traditional PDMS-based microfluidics resulted in an inadequate seal between layers. However, the use of the APTMS/GPTMS bonding strategy produced a high quality seal.[112] Initial testing demonstrated that APTMS/GPTMS treatment was not only able to seal densely packed features, but also was able to withstand applied pressures of at least 30 psi. Figure 5.15 shows the actuation of a single isolation valve in an *in meso* crystallization device without cross-talk between valves spaced only 50 µm apart.

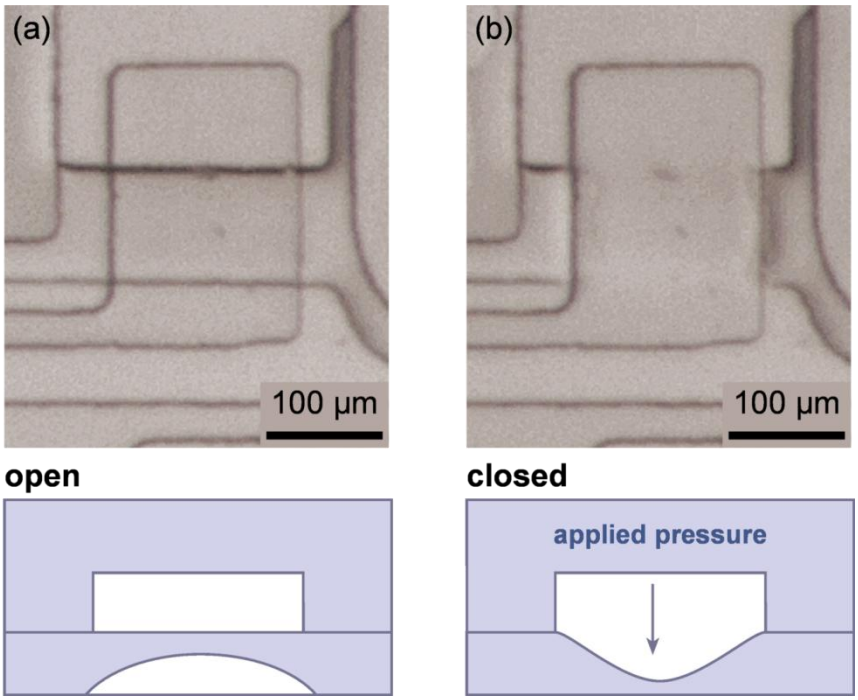

Figure 5.15. Optical micrographs and schematic depictions of an actuate-to-close,[109] push down microfluidic isolation valve used in an *in meso* crystallization device comprised of a PDMS fluid layer sandwiched between a COC substrate and control layer with a larger PDMS inlet layer providing pneumatic connections. The valve is shown in the **(a)** open, relaxed position, and in the **(b)** closed, actuated position. Deflection of the PDMS valve membrane can be seen inside the channel.

Validation of this PDMS/COC hybrid device architecture for *in meso* membrane protein crystallization is ongoing. However, the functionality of the device has already been demonstrated. Additionally, the decreased solvent loss from a PDMS/COC device as compared to a traditional PDMS device should be beneficial with respect to sample dehydration and incubation over extended periods of time.

5.4 Conclusions

In summary, an X-ray transparent device architecture composed of a thin PDMS fluid layer coupled with a thin COC control layer and substrate has been validated for use in protein crystallization trials and for *in situ* crystallographic analysis. This device architecture overcomes not only challenges associated with X-ray transparency, but also minimizes evaporative losses and allows for the incubation of crystallization trials for a longer period of time than would be possible with standard PDMS microfluidic devices.

These PDMS/COC microfluidic devices have been demonstrated for X-ray data collection at both room temperature and under cryogenic conditions. While the planar geometry of these chips may create rotational limitations in some experimental setups, strategies have been presented for not only the acquisition of a few frames of data for crystal quality screening, but also for the collection of complete datasets for protein structure determination. The application of this kind of crystallization and analysis platform has tremendous potential to enable structural biology studies of recalcitrant proteins where crystal size and/or fragility might otherwise hamper crystallographic analysis.

By coupling the advantages of microfluidic fluid handling with the ability to perform *in situ* diffraction analysis, the crystallization platforms demonstrated here circumvent difficulties associated with the manual harvesting of crystals, thus enabling reproducible analysis of high quality crystals. Additionally, the fluid handling capabilities of microfluidics allow for consistent well-to-well crystallization kinetics, thus facilitating the growth of a large number of crystals with minimal crystal-to-crystal variations in quality. Overcoming these challenges is particularly important for the analysis of protein crystals which may only form tiny crystals or which may be highly susceptible to radiation damage, thus necessitating the analysis of a large number of crystals in order to obtain a complete dataset. The platforms demonstrated here can be applied to not only soluble proteins, but also membrane proteins grown either *in surfo* or *in meso*. The ability to efficiently perform room temperature diffraction studies over a large number of crystals has the potential to shift the paradigm of protein structure determination from cryocrystallographic analysis of a single crystal to data collection of a large number of crystals at biologically relevant temperatures.

Having validated this approach for static protein structure determination, the fluid handling and *in situ* analysis capabilities of these microfluidic platforms could enable a wide range of truly exciting studies. For instance, real-time microfluidic fluid control could enable dynamic studies of the evolution of a protein structure as a function of various stimuli such as ligands, pH or environmental concentration changes as well as temperature changes. These capabilities could be particularly powerful when coupled with the fast data collection methods using polychromatic X-rays as will be discussed in Chapter 6.

5.5 Acknowledgements

This work was funded by NIH (R01 GM086727) and a NIH Kirschstein Predoctoral Fellowship from the National Institute of Biomedical Imaging and Bioengineering (F31 EB008330). Use of the Advanced

Photon Source was supported by the U. S. Department of Energy, Office of Science, Office of Basic Energy Sciences, under Contract No. DE-AC02-06CH11357. Use of the LS-CAT Sector 21 was supported by the Michigan Economic Development Corporation and the Michigan Technology Tri-Corridor for the support of this research program (Grant 085P1000817). Use of the National Synchrotron Light Source, Brookhaven National Laboratory, was supported by the U.S. Department of Energy, Office of Science, Office of Basic Energy Sciences, under Contract No. DE-AC02-98CH10886.

The collaborative efforts of Dr. Howard Robinson, Dr. Alexei Soares, and Dr. Jean Jakoncic at the National Synchrotron Light Source at Brookhaven National Laboratory and the Life Sciences Collaborative Access Team (LS-CAT) at the Advanced Photon Source at Argonne National Laboratory, Dr. Joseph Brunzelle in particular, made this work possible. Assistance provided by Dr. Howard Robinson, Dr. Alexei Soares, and Dr. Jean Jakoncic from the National Synchrotron Light Source at Brookhaven National Laboratory also helped to enable this project. Some materials characterization was performed at the George L. Clark X-ray Facility at the University of Illinois with the assistance of Dr. Danielle Gray. Also, Sudipto Guha was invaluable in his assistance with the development and testing of X-ray transparent microfluidic chips. Dr. Satish Nair, Vinayak Argawal, and Dr. Tiik Luk were also tremendously helpful with their assistance in data analysis.

5.6 References

(1) Nollert, P.; Navarro, J.; Landau, E. M. *Method Enzymol* **2002**, *343*, 183.

(2) Hanson, D. K.; Mielke, D. L.; Laible, P. D. In *Current Topics in Membranes, Volume 63*; Volume 63 ed.; DeLucas, L., Ed.; Academic Press: 2009, p 51.

(3) Tanabe, M.; Iverson, T. M. In *Current Topics in Membranes, Volume 63*; Volume 63 ed.; DeLucas, L., Ed.; Academic Press: 2009, p 229.

(4) Ostermeier, C.; Michel, H. *Current Opinion in Structural Biology* **1997**, *7*, 697.

(5) Arinaminpathy, Y.; Khurana, E.; Engelman, D. M.; Gerstein, M. B. *Drug Discovery Today* **2009**, *14*, 1130.

(6) Geertsma, E. R.; Groeneveld, M.; Slotboom, D. J.; Poolman, B. *P Natl Acad Sci USA* **2008**, *105*, 5722.

(7) Newby, Z. E. R.; O'Connell, J. D.; Gruswitz, F.; Hays, F. A.; Harries, W. E. C.; Harwood, I. M.; Ho, J. D.; Lee, J. K.; Savage, D. F.; Miercke, L. J. W.; Stroud, R. M. **2009**, *4*, 619.

(8) Koszelak-Rosenblum, M.; Krol, A.; Mozumdar, N.; Wunsch, K.; Ferin, A.; Cook, E.; Veatch, C. K.; Nagel, R.; Luft, J. R.; DeTitta, G. T.; Malkowski, M. G. *Protein Sci* **2009**, *18*, 1828.

(9) Hunte, C.; Michel, H. *Current Opinion in Structural Biology* **2002**, *12*, 503.

(10) Landau, E. M. In *Methods and Results in Crystallization of Membrane Proteins*; Iwata, S., Ed. 2003, p 37.

(11) Michel, H. *Trends Biochem Sci* **1983**, *8*, 56.

(12) Caffrey, M. *Ann Rev Biophys* **2009**, *38*, 29.

(13) Collingsworth, P. D.; Bray, T. L.; Christopher, G. K. *J Cryst Growth* **2000**, *219*, 283.

(14) Durbin, S. D.; Feher, G. *Annu Rev Phys Chem* **1996**, *47*, 171.

(15) Talreja, S.; Kenis, P. J. A.; Zukoski, C. F. *Langmuir* **2007**, *23*, 4516.

(16) Talreja, S.; Kim, D. Y.; Mirarefi, A. Y.; Zukoski, C. F.; Kenis, P. J. A. *J Appl Crystallogr* **2005**, *38*, 988.

(17) Yoshizaki, I.; Nakamura, H.; Sato, T.; Igarashi, N.; Komatsu, H.; Yoda, S. *J Cryst Growth* **2002**, *237*, 295.
(18) Anderson, M. J.; Hansen, C. L.; Quake, S. R. *P Natl Acad Sci USA* **2006**, *103*, 16746.
(19) Hansen, C.; Quake, S. R. *Current Opinion in Structural Biology* **2003**, *13*, 538.
(20) Hansen, C. L.; Sommer, M. O. A.; Quake, S. R. *P Natl Acad Sci USA* **2004**, *101*, 14431.
(21) Lounaci, M.; Rigolet, P.; Abraham, C.; Le Berre, M.; Chen, Y. *Microelectron Eng* **2007**, *84*, 1758.
(22) Zheng, B.; Roach, L. S.; Ismagilov, R. F. *J Am Chem Soc* **2003**, *125*, 11170.
(23) Zhou, X.; Lau, L.; Lam, W. W. L.; Au, S. W. N.; Zheng, B. *Anal. Chem.* **2007**.
(24) Cherezov, V.; Caffrey, M. *J Appl Crystallogr* **2003**, *36*, 1372.
(25) Qutub, Y.; Reviakine, I.; Maxwell, C.; Navarro, J.; Landau, E. M.; Vekilov, P. G. *J Mol Biol* **2004**, *343*, 1243.
(26) Rummel, G.; Hardmeyer, A.; Widmer, C.; Chiu, M. L.; Nollert, P.; Locher, K. P.; Pedruzzi, I.; Landau, E. M.; Rosenbusch, J. P. *Journal of Structural Biology* **1998**, *121*, 82.
(27) Gavira, J. A.; Toh, D.; Lopez-Jaramillo, J.; Garcia-Ruiz, J. M.; Ng, J. D. *Acta Crystallogr D* **2002**, *58*, 1147.
(28) Ng, J. D.; Gavira, J. A.; Garcia-Ruiz, J. M. *Journal of Structural Biology* **2003**, *142*, 218.
(29) Stevens, R. C. *Current Opinion in Structural Biology* **2000**, *10*, 558.
(30) Li, L.; Ismagilov, R. F. *Ann Rev Biophys* **2010**.
(31) McPherson, A. In *Current Topics in Membranes, Volume 63*; Volume 63 ed.; DeLucas, L., Ed.; Academic Press: 2009, p 5.
(32) Gabrielsen, M.; Gardiner, A. T.; Fromme, P.; Cogdell, R. J. In *Current Topics in Membranes, Volume 63*; Volume 63 ed.; DeLucas, L., Ed.; Academic Press: 2009, p 127.
(33) Page, R. In *Methods in Molecular Biology: Structural Proteomics - High Throughput Methods*; Kobe, B., Guss, M., Huber, T., Eds.; Humana Press: Totowa, NJ, 2008; Vol. 426, p 345.
(34) Dauter, Z.; Lamzin, V. S.; Wilson, K. S. *Current Opinion in Structural Biology* **1997**, *7*, 681.
(35) Newman, J.; Fazio, V. J.; Lawson, B.; Peat, T. S. *Cryst Growth Des* **2010**, *10*, 2785.
(36) Li, G.; Chen, Q.; Li, J.; Hu, X.; Zhao, J. *Anal Chem* **2010**, *82*, 4362.
(37) Jia, Y.; Liu, X.-Y. *The Journal of Physical Chemistry B* **2006**, *110*, 6949.
(38) Service, R. *Science* **2005**, *307*, 1554.
(39) Cherezov, V.; Peddi, A.; Muthusubramaniam, L.; Zheng, Y. F.; Caffrey, M. *Acta Crystallogr D* **2004**, *60*, 1795.
(40) Iacovache, I.; Biasini, M.; Kowal, J.; Kukulski, W.; Chami, M.; van der Goot, F. G.; Engel, A.; Rémigy, H.-W. *Journal of Structural Biology*, *In Press, Corrected Proof*.
(41) Chayen, N. E.; Stewart, P. D. S.; Maeder, D. L.; Blow, D. M. *J Appl Crystallogr* **1990**, *23*, 297.
(42) Fogg, M. J.; Wilkinson, A. J. *Biochemical Society Transactions* **2008**, *036*, 771.
(43) Li, L.; Du, W.; Ismagilov, R. F. *J Am Chem Soc* **2009**.
(44) Zheng, B.; Tice, J. D.; Ismagilov, R. F. *Adv Mater* **2004**, *16*, 1365.
(45) Zheng, B.; Tice, J. D.; Ismagilov, R. F. *Anal Chem* **2004**, *76*, 4977.
(46) Zheng, B.; Tice, J. D.; Roach, L. S.; Ismagilov, R. F. *Angew Chem Int Edit* **2004**, *43*, 2508.
(47) Zheng, B.; Gerdts, C. J.; Ismagilov, R. F. *Current Opinion in Structural Biology* **2005**, *15*, 548.
(48) Zheng, B.; Ismagilov, R. F. *Angew Chem Int Edit* **2005**, *44*, 2520.
(49) Yadav, M. K.; Gerdts, C. J.; Sanishvili, R.; Smith, W. W.; Roach, L. S.; Ismagilov, R. F.; Kuhn, P.; Stevens, R. C. *J Appl Crystallogr* **2005**, *38*, 900.
(50) Chen, D. L.; Gerdts, C. J.; Ismagilov, R. F. *J Am Chem Soc* **2005**, *127*, 9672.
(51) Chen, D. L. L.; Ismagilov, R. F. *Curr Opin Chem Biol* **2006**, *10*, 226.
(52) Gerdts, C. J.; Tereshko, V.; Yadav, M. K.; Dementieva, I.; Collart, F.; Joachimiak, A.; Stevens, R. C.; Kuhn, P.; Kossiakoff, A.; Ismagilov, R. F. *Angew Chem Int Edit* **2006**, *45*, 8156.

(53) Li, L.; Mustafi, D.; Fu, Q.; Tereshko, V.; Chen, D. L. L.; Tice, J. D.; Ismagilov, R. F. *P Natl Acad Sci USA* **2006**, *103*, 19243.

(54) Song, H.; Chen, D. L.; Ismagilov, R. F. *Angew Chem Int Edit* **2006**, *45*, 7336.

(55) Chen, D. L. L.; Li, L.; Reyes, S.; Adamson, D. N.; Ismagilov, R. F. *Langmuir* **2007**, *23*, 2255.

(56) Laval, P.; Salmon, J. B.; Joanicot, M. *J Cryst Growth* **2007**, *303*, 622.

(57) Dombrowski, R. D.; Litster, J. D.; Wagner, N. J.; He, Y. *Chem Eng Sci* **2007**, *62*, 4802.

(58) Maki, S.; Murai, R.; Yoshikawa, H. Y.; Kitatani, T.; Nakata, S.; Kawahara, H.; Hasenaka, H.; Kobayashi, A.; Okada, S.; Sugiyama, S.; Adachi, H.; Matsumura, H.; Takano, K.; Murakami, S.; Inoue, T.; Sasaki, T.; Mori, Y. *J Synchrotron Radiat* **2008**, *15*, 269.

(59) Gerdts, C. J.; Elliott, M.; Lovell, S.; Mixon, M. B.; Napuli, A. J.; Staker, B. L.; Nollert, P.; Stewart, L. *Acta Crystallographica Section D* **2008**, *64*, 1116.

(60) Salmon, J.-B.; Leng, J. *Comptes Rendus Chimie* **2009**, *12*, 258.

(61) Kreutz, J. E.; Li, L.; Roach, L. S.; Hatakeyama, T.; Ismagilov, R. F. *J Am Chem Soc* **2009**, *131*, 6042.

(62) Du, W.; Li, L.; Nichols, K. P.; Ismagilov, R. F. *Lab Chip* **2009**, *9*, 2286.

(63) Pang, Y.; Liu, J.; Li, H.; Lin, J. *Science in China Series B: Chemistry* **2009**, *52*, 1014.

(64) Luft, J. R.; Rak, D. M.; DeTitta, G. T. *J Cryst Growth* **1999**, *196*, 450.

(65) Steinert, C. P.; Mueller-Dieckmann, J.; Weiss, M.; Roessle, M.; Zengerle, R.; Koltay, P. In *Future Generation Communication and Networking* 2007, p 561.

(66) Lounaci, M.; Rigolet, P.; Casquillas, G. V.; Huang, H. W.; Chen, Y. *Microelectron Eng* **2006**, *83*, 1673.

(67) Korczynska, J.; Hu, T. C.; Smith, D. K.; Jenkins, J.; Lewis, R.; Edwards, T.; Brzozowski, A. M. *Acta Crystallogr D* **2007**, *63*, 1009.

(68) Shim, J. U.; Cristobal, G.; Link, D. R.; Thorsen, T.; Fraden, S. *Cryst Growth Des* **2007**, *7*, 2192.

(69) Shim, J. U.; Cristobal, G.; Link, D. R.; Thorsen, T.; Jia, Y.; Piattelli, K.; Fraden, S. *J Am Chem Soc* **2007**, *129*, 8825.

(70) Hansen, C. L.; Classen, S.; Berger, J. M.; Quake, S. R. *J Am Chem Soc* **2006**, *128*, 3142.

(71) Lau, B. T. C.; Baitz, C. A.; Dong, X. P.; Hansen, C. L. *J Am Chem Soc* **2007**, *129*, 454.

(72) Lopez-Jaramillo, F. J.; Garcia-Ruiz, J. M.; Gavira, J. A.; Otalora, F. *J Appl Crystallogr* **2001**, *34*, 365.

(73) Garcia-Ruiz, J. M.; Otalora, F.; Novella, M. L.; Gavira, J. A.; Sauter, C.; Vidal, O. *J Cryst Growth* **2001**, *232*, 149.

(74) Garcia-Ruiz, J. M.; Gonzalez-Ramirez, L. A.; Gavira, J. A.; Otalora, F. *Acta Crystallogr D* **2002**, *58*, 1638.

(75) Bolanos-Garcia, V. M. *J Cryst Growth* **2003**, *253*, 517.

(76) Ng, J. D.; Clark, P. J.; Stevens, R. C.; Kuhn, P. *Acta Crystallographica Section D* **2008**, *64*, 189.

(77) Ng, J. D.; Garcia-Ruiz, J. M.; Gavira-Gallardo, J. A.; Wells, M.; Jenkins, G. US, 2006.

(78) Dhouib, K.; Malek, C. K.; Pfleging, W.; Gauthier-Manuel, B.; Duffait, R.; Thuillier, G.; Ferrigno, R.; Jacquamet, L.; Ohana, J.; Ferrer, J.-L.; Theobald-Dietrich, A.; Giege, R.; Lorber, B.; Sauter, C. *Lab Chip* **2009**, *9*, 1412.

(79) Sugahara, M.; Kageyama, Y.; Kunishima, N. *J Appl Crystallogr* **2009**, *42*, 129.

(80) Sauter, C.; Otalora, F.; Gavira, J. A.; Vidal, O.; Giege, R.; Garcia-Ruiz, J. M. *Acta Crystallogr D* **2001**, *57*, 1119.

(81) Sauter, C.; Dhouib, K.; Lorber, B. *Crystal Growth and Design* **2007**, *7*, 2247.

(82) Hansen, C. L.; Skordalakes, E.; Berger, J. M.; Quake, S. R. *P Natl Acad Sci USA* **2002**, *99*, 16531.

(83) Kothe, M.; Kohls, D.; Low, S.; Coli, R.; Cheng, A. C.; Jacques, S. L.; Johnson, T. L.; Lewis, C.; Loh, C.; Nonomiya, J.; Sheils, A. L.; Verdries, K. A.; Wynn, T. A.; Kuhn, C.; Ding, Y. H. *Biochemistry-Us* **2007**, *46*, 5960.

(84) Sugahara, M.; Asada, Y.; Morikawa, Y.; Kageyama, Y.; Kunishima, N. *Acta Crystallogr D* **2008**, *64*, 686.

(85) Perry, S. L.; Roberts, G. W.; Tice, J. D.; Gennis, R. B.; Kenis, P. J. A. *Cryst Growth Des* **2009**, *9*, 2566.

(86) Li, L.; Fu, Q.; Kors, C.; Stewart, L.; Nollert, P.; Laible, P.; Ismagilov, R. *Microfluid Nanofluid* **2009**, *8*, 789.

(87) Cherezov, V.; Hanson, M. A.; Griffith, M. T.; Hilgart, M. C.; Sanishvili, R.; Nagarajan, V.; Stepanov, S.; Fischetti, R. F.; Kuhn, P.; Stevens, R. C. *Journal of The Royal Society Interface* **2009**, *6*, S587.

(88) van der Woerd, M.; Ferree, D.; Pusey, M. *Journal of Structural Biology* **2003**, *142*, 180.

(89) Cusack, S.; Belrhali, H.; Bram, A.; Burghammer, M.; Perrakis, A.; Riekel, C. *Nat Struct Biol* **1998**, *5*, 634.

(90) Matthews, B. W. *J Mol Biol* **1968**, *33*, 491.

(91) McPherson, A. *Crystallization of Biological Macromolecules*; CSHL Press, 1999.

(92) Garman, E. F.; Schneider, T. R. *J Appl Crystallogr* **1997**, *30*, 211.

(93) Asherie, N.; Jakoncic, J.; Ginsberg, C.; Greenbaum, A.; Stojanoff, V.; Hrnjez, B. J.; Blass, S.; Berger, J. *Cryst Growth Des* **2009**.

(94) Pentelute, B. L.; Gates, Z. P.; Tereshko, V.; Dashnau, J. L.; Vanderkooi, J. M.; Kossiakoff, A. A.; Kent, S. B. H. *J Am Chem Soc* **2008**, *130*, 9695.

(95) Cherezov, V.; Yamashita, E.; Liu, W.; Zhalnina, M.; Cramer, W. A.; Caffrey, M. *J Mol Biol* **2006**, *364*, 716.

(96) Cherezov, V.; Clogston, J.; Papiz, M. Z.; Caffrey, M. *J Mol Biol* **2006**, *357*, 1605.

(97) Li, L.; Nachtergaele, S.; Seddon, A. M.; Tereshko, V.; Ponomarenko, N.; Ismagilov, R. F. *J Am Chem Soc* **2008**, *130*, 14324.

(98) Feher, G.; Kam, Z. *Methods in Enzymology* **1985**, *114*, 77.

(99) Abramson, J.; Riistama, S.; Larsson, G.; Jasaitis, A.; Svensson-Ek, M.; Laakkonen, L.; Puustinen, A.; Iwata, S.; Wikstrom, M. *Nat Struct Biol* **2000**, *7*, 910.

(100) Fei, M. J.; Yamashita, E.; Inoue, N.; Yao, M.; Yamaguchi, H.; Tsukihara, T.; Shinzawa-Ito, K.; Nakashima, R.; Yoshikawa, S. *Acta Crystallogr D* **2000**, *56*, 529.

(101) Liu, B.; Chen, Y.; Doukov, T.; Soltis, S. M.; Stout, C. D.; Fee, J. A. *Biochemistry-Us* **2009**, *48*, 820.

(102) Ostermeier, C.; Harrenga, A.; Ermler, U.; Michel, H. *P Natl Acad Sci USA* **1997**, *94*, 10547.

(103) Tsukihara, T.; Aoyama, H.; Yamashita, E.; Tomizaki, T.; Yamaguchi, H.; Shinzawaitoh, K.; Nakashima, R.; Yaono, R.; Yoshikawa, S. *Science* **1995**, *269*, 1069.

(104) Jaakola, V. P.; Griffith, M. T.; Hanson, M. A.; Cherezov, V.; Chien, E. Y. T.; Lane, J. R.; IJzerman, A. P.; Stevens, R. C. *Science* **2008**, *322*, 1211.

(105) Lorber, B.; Witz, J. *Cryst Growth Des* **2008**, *8*, 1522.

(106) Urbani, A.; Gemeinhardt, S.; Warne, A.; Saraste, M. *Febs Lett* **2001**, *508*, 29.

(107) Anderson, M. J.; DeLaBarre, B.; Raghunathan, A.; Palsson, B. O.; Brunger, A. T.; Quake, S. R. *Biochemistry-Us* **2007**, *46*, 5722.

(108) Gerdts, C.; Nollert, P. In *Current Topics in Membranes, Volume 63*; Volume 63 ed.; DeLucas, L., Ed.; Academic Press: 2009, p 179.

(109) Unger, M. A.; Chou, H. P.; Thorsen, T.; Scherer, A.; Quake, S. R. *Science* **2000**, *288*, 113.

(110) Mehta, G.; Lee, J.; Cha, W.; Tung, Y. C.; Linderman, J. J.; Takayama, S. *Anal Chem* **2009**, *81*, 3714.

(111) Nunes, P. S.; Ohlsson, P. D.; Ordeig, O.; Kutter, J. P. *Microfluid Nanofluid* **2010**, *9*, 145.

(112) Tang, L.; Lee, N. Y. *Lab Chip* **2010**, *10*, 1274.
(113) Schudel, B. R.; Choi, C. J.; Cunningham, B. T.; Kenis, P. J. A. *Lab Chip* **2009**, *9*, 1676.
(114) Grover, W. H.; Skelley, A. M.; Liu, C. N.; Lagally, E. T.; Mathies, R. A. *Sensor Actuat B-Chem* **2003**, *89*, 315.
(115) Sophianopoulos, A. J.; Holcomb, D. N.; Vanholde, K. E.; Rhodes, C. K. *J Biol Chem* **1962**, *237*, 1107.
(116) Charron, C.; Giege, R.; Lorber, B. *Acta Crystallogr D* **2004**, *60*, 83.
(117) Tessier, P. M.; Johnson, H. R.; Pazhianur, R.; Berger, B. W.; Prentice, J. L.; Bahnson, B. J.; Sandler, S. I.; Lenhoff, A. M. *Proteins* **2003**, *50*, 303.
(118) Talreja, S.; Perry, S. L.; Guha, S.; Bhamidi, V.; Zukoski, C. F.; Kenis, P. J. A. *The Journal of Physical Chemistry B* **2010**, *114*, 4432.
(119) Life Sciences Collaborative Access Team (LS-CAT). http://ls-cat.org/
(120) Otwinowski, Z.; Minor, W. *Macromolecular Crystallography, Pt A* **1997**, *276*, 307.
(121) *Acta Crystallogr D* **1994**, *50*, 760.
(122) Langer, G.; Cohen, S. X.; Lamzin, V. S.; Perrakis, A. *Nat Protoc* **2008**, *3*, 1171.
(123) Murshudov, G. N.; Vagin, A. A.; Dodson, E. J. *Acta Crystallogr D* **1997**, *53*, 240.
(124) Evans, P.; McCoy, A. *Acta Crystallographica Section D* **2008**, *64*, 1.
(125) Vaney, M. C.; Maignan, S.; Ries-Kautt, M.; Ducruix, A. *Acta Crystallographica Section D* **1996**, *52*, 505.
(126) Emsley, P.; Cowtan, K. *Acta Crystallographica Section D* **2004**, *60*, 2126.
(127) Caffrey, M. *Cryst Growth Des* **2008**, *8*, 4244.
(128) Cherezov, V.; Liu, J.; Griffith, M.; Hanson, M. A.; Stevens, R. C. *Cryst Growth Des* **2008**, *8*, 4307.
(129) Liu, W.; Hanson, M. A.; Stevens, R. C.; Cherezov, V. *Biophys J* **2010**, *98*, 1539.
(130) Sennoga, C.; Heron, A.; Seddon, J. M.; Templer, R. H.; Hankamer, B. *Acta Crystallogr D* **2003**, *59*, 239.
(131) Hubbell, J. H.; Seltzer, S. M. *NIST Physical Reference Data* **1996**.
(132) Greaves, E. D.; Manz, A. *Lab Chip* **2005**, *5*, 382.
(133) *CRC Handbook of Chemistry and Physics*; 76th ed.; CRC Press: New York, 1996.
(134) Ratta, V. PhD, Virginia Polytechnic Institute, 1999.
(135) Nair, S. Class Notes MCB 446 - Crystallographic Symmetry: A Primer.
(136) Blow, D. *Outline of Crystallography for Biologists*; Oxford University Press: Oxford, 2007.
(137) Dauter, Z. In *Methods in Enzymology*; Charles W. Carter, Jr., Ed.; Academic Press: 1997; Vol. Volume 276, p 326.
(138) Rhodes, G. *Crystallography Made Crystal Clear - A Guide for Users of Macromolecular Models*; 3rd ed.; Elsevier: Amsterdam, 2006.
(139) Drenth, J. *Principles of Protein X-ray Crystallography*; 3rd ed.; Springer: New York, 2007.
(140) Newman, J.; Xu, J.; Willis, M. C. *Acta Crystallographica Section D* **2007**, *63*, 826.
(141) Cherezov, V.; Rosenbaum, D. M.; Hanson, M. A.; Rasmussen, S. G. F.; Thian, F. S.; Kobilka, T. S.; Choi, H. J.; Kuhn, P.; Weis, W. I.; Kobilka, B. K.; Stevens, R. C. *Science* **2007**, *318*, 1258.
(142) Wacker, D.; Fenalti, G.; Brown, M. A.; Katritch, V.; Abagyan, R.; Cherezov, V.; Stevens, R. C. *J Am Chem Soc* **2010**, *132*, 11443.
(143) McPherson, A. *J Appl Crystallogr* **2000**, *33*, 397.
(144) Baxter, R. H. G.; Ponomarenko, N.; Å rajer, V.; Pahl, R.; Moffat, K.; Norris, J. R. *P Natl Acad Sci USA* **2004**, *101*, 5982.
(145) Cornaby, S.; Szebenyi, D. M. E.; Smilgies, D.-M.; Schuller, D. J.; Gillilan, R.; Hao, Q.; Bilderback, D. H. *Acta Crystallographica Section D* **2010**, *66*, 2.

(146) Ren, Z.; Bourgeois, D.; Helliwell, J. R.; Moffat, K.; Srajer, V.; Stoddard, B. L. *J Synchrotron Radiat* **1999**, *6*, 891.
(147) Alcorn, T.; Juers, D. H. *Acta Crystallographica Section D* **2010**, *66*, 366.
(148) Juers, D. H.; Matthews, B. W. *Q Rev Biophys* **2004**, *37*, 105.

Chapter 6

Microfluidic Platforms for *In Situ* Laue Crystallography*

Abstract

The X-ray transparent device architecture developed in Chapter 5 was applied to the polychromatic, or Laue diffraction method. The microfluidic device structure used in this work is comprised of a thin polydimethylsiloxane (PDMS) fluid layer (middle) bonded to a thin cyclic olefin copolymer (COC) control layer (top) and a COC substrate (bottom) to form pneumatic valve structures. The effects of sample and device geometry were investigated using the soluble protein lysozyme as a model system. In collaboration with the BioCARS team at the Advanced Photon Source at Argonne National Laboratory, an automated "single-shot" method was developed for obtaining a complete dataset from many crystals grown on-chip to minimize the effects of radiation damage to the crystal on the resultant data. Data from 66 individual crystals was merged into a single dataset. A comparison of similar datasets collected using monochromatic vs. polychromatic radiation demonstrated that this "single-shot" microfluidic method for data collection can be used to collect high quality data, overcoming many of the challenges typically associated with Laue data collection.

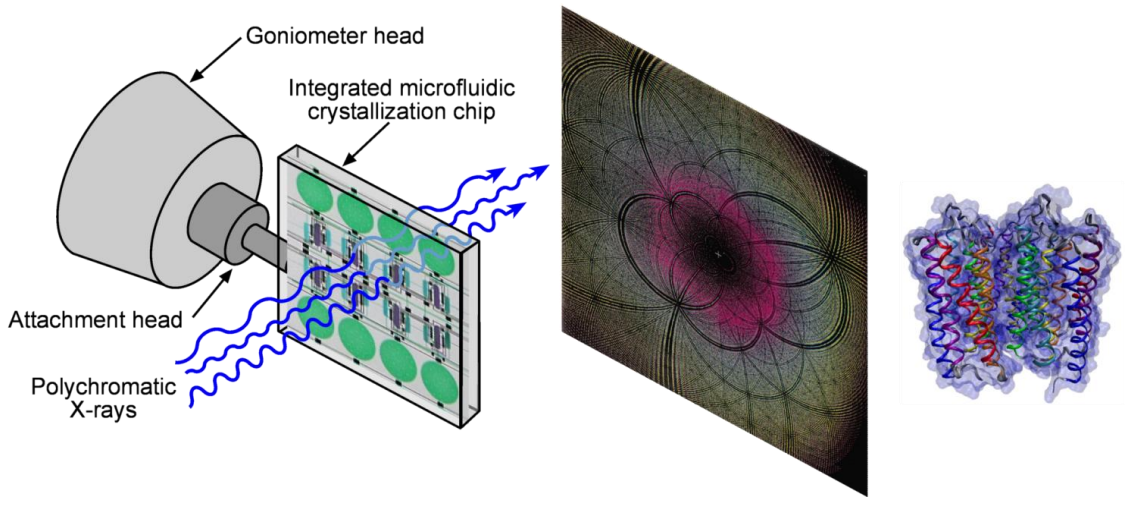

* Part of this work will be published: S.L. Perry, S. Guha, Z. Ren, and P.J.A. Kenis, *Automated Methods for In Situ Laue Crystallography Using Microfluidic Platforms for Protein Crystallization* (in preparation).

6.1 Introduction

While efforts in microfluidics for protein crystallization have advanced dramatically in the past ten years,[1-53] the idea of coupling microfluidic technology with advanced crystallographic techniques for *in situ* analysis is an area where significant advances can still be made. Thus far efforts have focused mainly on simple devices where monochromatic X-rays can be used to interrogate the sample.[2,4,5,13-15,17,19-21,26,27,31,40,42-45,47,52] In Chapter 5 a hybrid microfluidic device architecture was introduced which enabled *in situ* X-ray analysis of protein crystals grown on chip. While monochromatic X-ray diffraction is used for a majority of structural biology studies, polychromatic X-ray diffraction, termed Laue diffraction,[54] has various benefits over its more traditional counterpart. The most significant benefit of Laue diffraction is the speed at which data collection can be performed.[54] This faster rate of data collection is the result of using a range of X-ray wavelengths to interrogate the sample, resulting in an increased number of observed diffraction spots per image, thereby decreasing the number of frames of data which must be taken to form a complete dataset. This increased rate of data acquisition has enabled the use of Laue crystallography for a variety of experiments where monochromatic diffraction has been limited, including (i) the analysis of crystals which are not amenable to flash-freezing, (ii) room temperature structural studies when the lifetime of the crystal is too short for traditional data collection, and (iii) time resolved kinetic studies of structural changes.

Although performing data acquisition at room temperature is not an inherent requirement for Laue crystallography, it is not uncommon for experiments to be performed at ambient conditions either because the sample is not amenable to cryocooling, or because the experiment of interest involves determining the structure at near physiological conditions.[54] Cryocooling is typically used for monochromatic experiments because it decreases molecular motion, thereby potentially improving the obtainable resolution, and also decreasing the extent of radiation damage.[54-57] However, the stresses associated with cryocooling can also perturb the crystal structure,[56,57] increasing the mosaicity which can have a detrimental effect on the quality of Laue data that can be collected.

In terms of the speed of data collection at a synchrotron, in typical monochromatic experiments, frames of data are acquired using X-ray exposure times on the order of seconds. However, for Laue methods the exposure time is three to four orders of magnitude shorter.[58] The exposure time is measured in terms of the number of packets of radiation which the sample experiences. In a synchrotron, packets of electrons circulate around the ring at high speed in different bunch conformations depending upon the operational mode of the synchrotron. As each bunch passes the beamline a short dose of radiation is given off. The radiation exposure of the sample is thus given in terms of the number of these bunches and, in total, is on the order of microseconds or less.[58]

The use of such short exposure times and the increased density of data collection per frame have enabled time resolved structural studies at sub-nanosecond time resolution.[58] In these studies it is necessary to synchronize and trigger a uniform structural change for a majority of the molecules in the

crystal and then match the X-ray exposure time to the timescale of the resultant structural changes. Photolysis is a common method for initiating such a structural change because the pulse of light can be easily timed with data collection and is able to penetrate the entire crystal. However, chemical triggers can also be used.[54,58-60] Thus Laue crystallography provides a very elegant platform for performing extremely meaningful kinetic experiments that directly probe changes that occur during protein function.

While Laue crystallography possesses several advantages over monochromatic data collection, it also suffers from several significant limitations in terms of (i) radiation damage, (ii) sensitivity to crystal quality and background scatter, and (iii) the need for more intensive data analysis. The use of polychromatic radiation results in a more intense X-ray beam than for monochromatic experiments. Therefore while there is a tradeoff in terms of exposure time, radiation damage from exposure to the polychromatic beam can be significant, particularly at room temperature. Various data collection strategies have been developed to help overcome this limitation. Also, combining data collected from multiple crystals is common.[54,59,61]

The sensitivity of Laue crystallography to crystal quality, and in particular mosaicity is the result of spot elongation. During data analysis it is necessary to identify the exact location of the various diffraction spots observed. However, with an elongated or streaky spot identification of the spot location is much more difficult. This problem can be further compounded by high levels of background scatter which decrease the signal-to-noise ratio for weak spots. These limitations have typically restricted Laue data collection to crystals of relatively high quality and provided both a challenge and an opportunity for microfluidic crystallization platforms.

In addition to the identification of diffraction spots, data analysis for polychromatic diffraction in general is more difficult than for monochromatic diffraction. In indexing the various diffraction spots, both the indices of each spot as well as the wavelength of radiation responsible for its appearance must be determined. The intensity of the various spots must then be normalized with respect to the intensity of the incident radiation spectrum. Additionally, methods do not currently exist for *ab initio* structure determination using Laue diffraction, thus a Laue experiment must always be coupled with a monochromatic experiment in order to obtain phase information.

In this chapter the X-ray transparent microfluidic platforms described in Chapter 5 will be used to perform Laue crystallography. The efficacy of these platforms for *in situ* Laue analysis is first validated using a simple chip design (Section 6.3.1). 96-well crystallization array chips for the growth of a large number of crystals are then coupled with an automated process for collecting single-shot data which can be merged to generate a complete dataset (Section 6.3.2). A comparison between merged datasets acquired using monochromatic and polychromatic diffraction is then presented.

6.2 Materials and Methods

6.2.1 Device Fabrication and Operation

The simple large well chips and 96-well array chips used here were fabricated and filled as described in Chapter 5. Briefly, microfluidic chips were fabricated by bonding a thin polydimethylsiloxane (PDMS, General Electric RTV 650) fluid layer with either 25 µm or 50 µm features covered with a membrane thickness of ~20 µm. This fluid layer was chemically bonded to a molded cyclic olefin copolymer (COC, 2-4 mil, 5013 and 6013, from TOPAS Advanced Polymers Inc.) control layer and a flat COC substrate.

6.2.2 Protein and Precipitant Solutions

Hen egg white lysozyme (Sigma) was dissolved in 50 mM sodium acetate (Sigma-Aldrich) at pH 4.6 with 20% (w/v) glycerol (Fisher Scientific) at a concentration of either 88 mg/mL for simple large well experiments or 120 mg/mL for 96-well array chip experiments. Lysozyme concentrations were determined by UV absorbance measurements (Lambda 650 UV-Vis spectrophotometer, Perkin Elmer) at 280 nm using an extinction coefficient of 2.64 mL/(mg-cm).[62] For proof-of-concept Laue crystallography experiments precipitant solutions of 1M NaCl (Aldrich) in 50 mM sodium acetate, pH 4.6 with 20% (w/v) glycerol were prepared. Prior to setting up a crystallization experiment, protein solutions were filtered through 0.1 µm (Ultrafree-MC, Millipore) filters. Precipitant solutions were filtered through 0.22 µm (Steriflip, Millipore) filters.

6.2.3 Crystallization Experiments

Crystallization experiments were set up and visualized using either a stereomicroscope (Leica, MZ12.5) with an attached digital camera (Leica, DFC295) operated using Leica Application Suite software or a computer controlled imaging system comprised of an optical microscope (Leica Z16 APO) equipped with an auto-zoom lens (Leica 10447176), a digital camera (Leica DFC280), and a motorized x-y stage (Semprex KL66) controlled by Image Pro Plus (Media Cybernetics). For visualization of protein crystals, images were occasionally taken with the use of cross-polarizers.

For simple large well and array chip crystallization experiments, actuate-to-open valving and fluid filling was achieved by the application of vacuum from a small vacuum pump (Gast) connected to the device through a plastic gas manifold (Cole-Parmer Instrument Co.) and 24 AWG PTFE tubing coupled with a thin metal tube. Fluids (protein and precipitant solutions) were supplied to the device by pipetting 1 – 5 µL of solution onto the inlet hole. Vacuum within the chip from actuation of valves then pulled fluid into the chambers. After filling, the inlet holes for both the fluid and control layers were sealed with Crystal Clear tape (Hampton Research). Incubation of crystallization experiments was performed at 4°C.

6.2.4 X-ray Diffraction Experiments

Diffraction experiments were carried out at beamline 14-ID-B (Figure 6.1a) at the Advanced Photon Source at Argonne National Laboratories with the assistance of the BioCARS team.[63] Beamline 14-ID-B is an insertion device station with two in-line undulators (U27 and U23) that can operate over a wide energy range of 7 keV to 20 keV (1.77 Å to 0.62 Å) and can provide both a monochromatic and

polychromatic X-ray beams. Most data was collected with both undulators set to a peak energy of 12 keV (1.03 Å). Experiments were also performed with the energies of the undulators offset by 2 keV (U27 at 11.8 keV (1.05 Å), U23 at 13.8 keV (0.898 Å), thereby increasing the polychromatic range of the exposure and increasing the density of diffraction data obtained per image. A MARCCD-165 detector was used, with optical visualization provided by off-axis cameras.

Proof-of-concept large well devices were mounted on a standard magnetic goniometer mount with an attached metal tube into which a slit was cut and a set-screw was used for securing samples. X-ray exposures of 1 or 10 pulses of 11 electron bunches each were used. A sample-to-detector distance of 100 mm, 120 mm, or 150 mm was used depending on the strength of the diffraction signal observed. Collection of a complete dataset from a single crystal was attempted. 90° of data was collected using either a single pass method in steps of 8°, or in a gap filling mode in steps of 6°. All data collection was performed at room temperature.

For experiments using the 96-well array, chips were mounted in a plastic frame attached to an automated x-y-z translational stage (Eastern Air Devices) (Figure 6.1b). An automated python script coupled with two off-axis viewing cameras was used to identify and mark the location of individual crystals within the array chip (Figure 6.1c). Once identified, single-shot data collection on each crystal occurred in an automated fashion. X-ray exposures of 10 pulses of 11 electron bunches were used. A sample-to-detector distance of 110 mm was used. All data collection was performed at room temperature.

6.2.5 Analysis of X-ray Diffraction Data

Analysis of Laue X-ray diffraction data was performed using Precognition analysis software for indexing, geometric refinement, integration, and scaling (Renz Research Inc.).[64] Subsequent processing of crystallography datasets was done using the CCP4 suite of programs.[65-67] MTZ files were generated using Scalepack2mtz. Molecular replacement[68] for lysozyme was done in Phaser using PDB structure 193L as a model.[69] Model refinement and solvent building were performed using Refmac5 and aRP-Solvent, respectively. Electron density maps were displayed using COOT.[70]

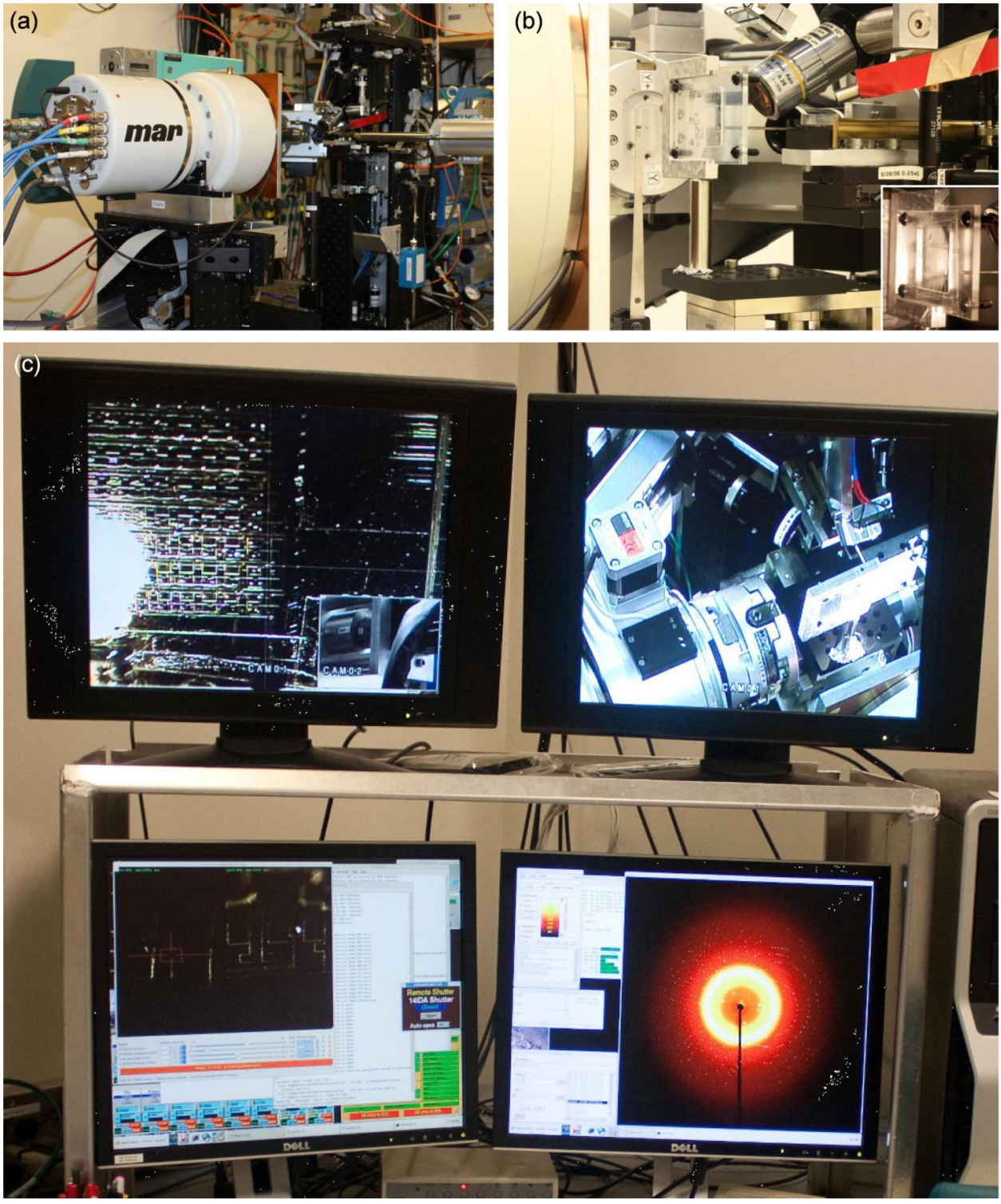

Figure 6.1. Photographs of **(a)** the Laue crystallography experimental setup at the 14-ID-B beamline at the Advanced Photon Source at Argonne National Laboratory and **(b)** a 96-well microfluidic array chip mounted for *in situ* data collection. The inset shows the device mounted in a plastic frame. **(c)** The control computers used for sample alignment and data collection. General sample position is shown on the top right. A lower magnification camera is used for gross positioning of the chip (top left). Finer control and crystal marking is performed using a split-screen view from two higher magnification cameras (lower left). Detector readout is seen on the lower right.

6.3 Results and Discussion

6.3.1 Proof-of-Concept On-Chip Laue Diffraction Experiments

A simple microfluidic well structure was used for proof-of-concept experiments to demonstrate on-chip Laue diffraction, as in Chapter 5, Section 5.3.3 (Figure 6.2a). The size of lysozyme crystals grown in these devices (Figure 6.2b) was limited by the height of the microfluidic chamber, resulting in a maximum path length through the crystal of ~25 µm. This path length is relatively small in comparison to the ~100 µm path length of the beam through the device materials for devices fabricated from 2 mil 5013 COC or the ~200 µm path length for devices fabricated from 4 mil 6013 COC (total thickness includes ~ 20 µm of PDMS). While the difference in these path lengths was not significant for monochromatic diffraction studies, it was important to validate this platform for use with Laue methods due to the increased sensitivity of this method to background scatter.

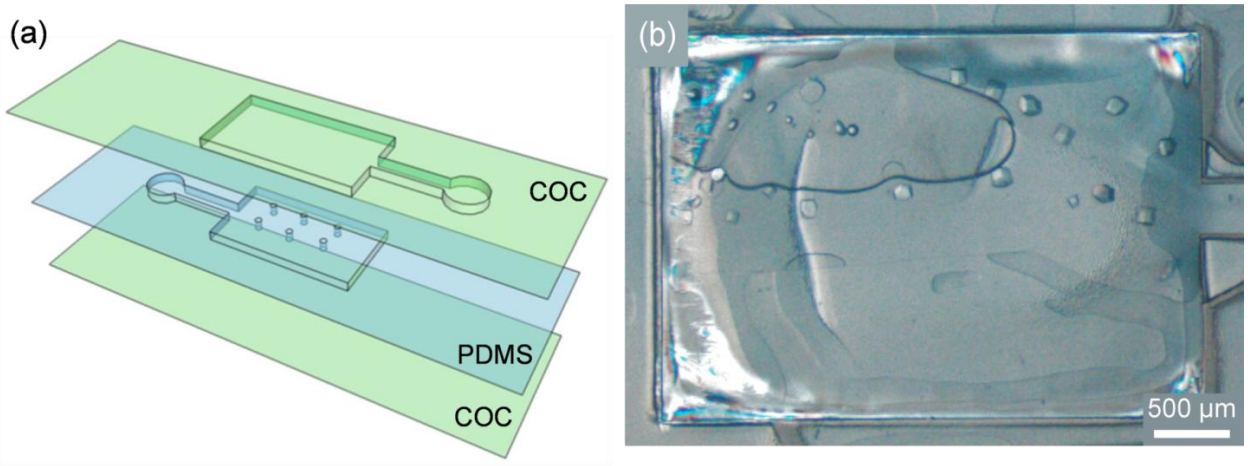

Figure 6.2. **(a)** Schematic depiction of a simple large well device. A large rectangular well with support posts is molded in PDMS (blue) and aligned with a matching COC control layer and substrate (green). The entire assembly is then attached to a COC substrate. **(b)** Optical micrographs of lysozyme crystals grown on chip.

In screening various crystals grown in these simple well structures, the significance of background scatter and crystal mosaicity were observed. In Figure 6.3a the effect of high crystal mosaicity can be clearly seen by the radial streaking of diffraction spots. Figure 6.3b-c show the diffraction patterns resulting from crystals with a much lower mosaicity. Similarly, the increased background scatter resulting from data collection through a thicker device limited the resolution to which spots could be clearly observed.

The effects of radiation damage from exposure to the polychromatic X-ray beam were observed during the course of data collection, both in terms of the quality of the diffraction image, and on the crystal itself. In Figure 6.3d optical micrographs clearly show damage to the crystal as a result of exposure to the beam. Radiation damage resulted in an increase in mosaicity as a function of exposure. Thus during the course of data collection on a single crystal the observed spots in the diffraction image changed from nearly circular to elongated streaks.

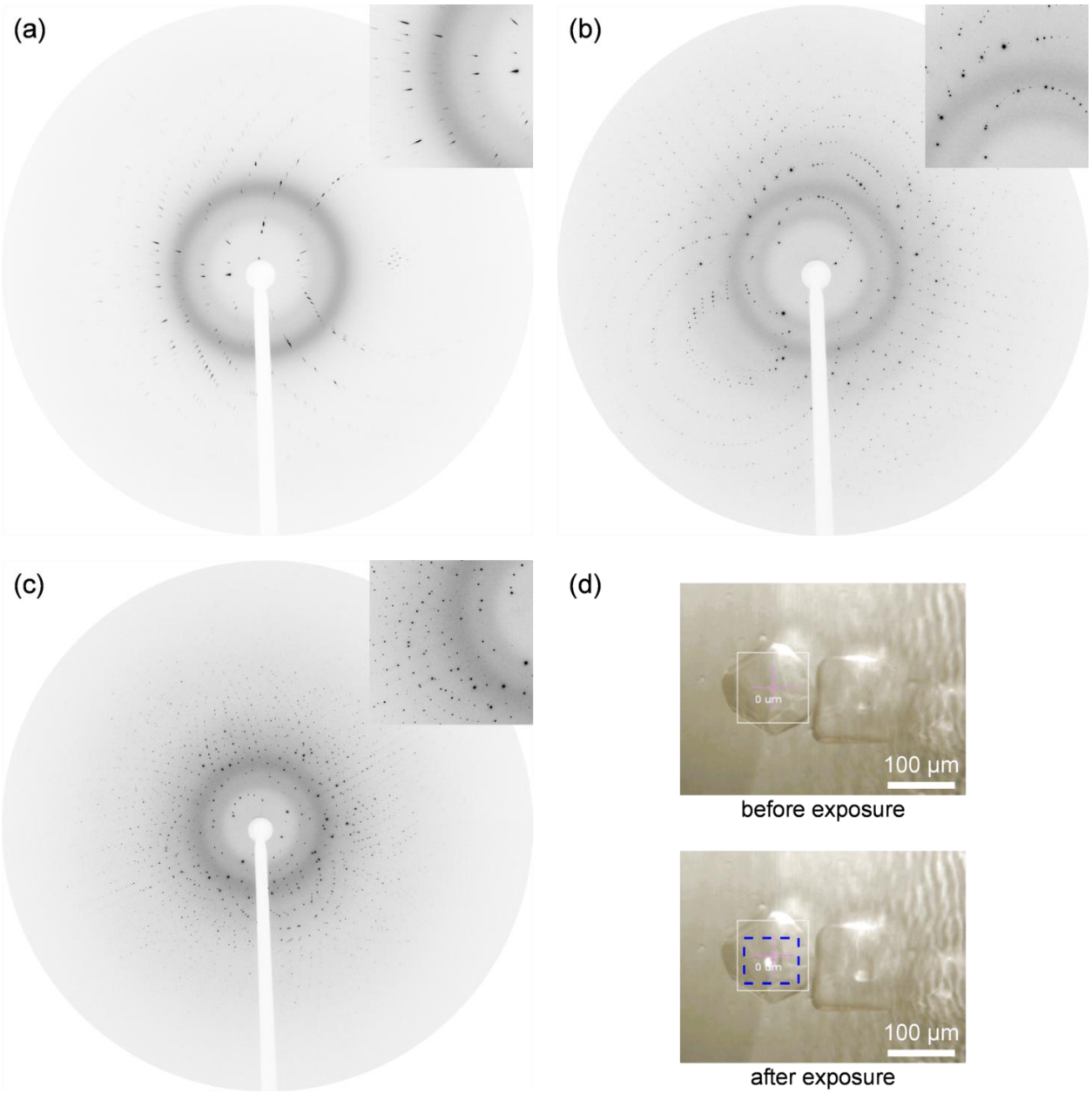

Figure 6.3. Polychromatic diffraction data collected *in situ* from lysozyme crystals grown in a simple large well device. **(a)** Laue diffraction from a highly mosaic crystal, as indicated by the streaking and elongation of the spots. **(b)** High quality *in situ* Laue diffraction with the beam energy peaked at 12 keV (1.033 Å). **(c)** High quality *in situ* Laue diffraction with the energy of the undulators offset by 2 keV (11.8 keV (1.05 Å) and 13.8 keV (0.898 Å)). A higher density of diffraction spots is observed here compared to **(b)** due to the increased range of X-ray energy present. Insets provide a closer view of spot quality. **(d)** Optical micrographs of crystals mounted for *in situ* analysis. Damage to the crystal due to X-ray exposure can be seen, as highlighted in the dashed rectangle.

Because of the sensitivity of the Laue method to radiation damage, a variety of data collection strategies have been developed to try and optimize the workable lifetime of a crystal. Gap-filling strategies where one pass through rotational space at large intervals followed by filling in with additional frames to sample between these intervals can be used to maximize the completeness of a dataset before radiation damage becomes too severe. In addition to gap-filling, a wider range of X-ray radiation can be

achieved by offsetting the peak of the beamline undulators to further increase the density of spots per frame, although there is a balance to be struck between an increase in data density and the ability to resolve individual spots.

Both the gap filling and increased spectrum of radiation were used to collect complete datasets from single crystals of lysozyme. A summary of the data collection statistics is given in Table 6.1. Whereas in monochromatic diffraction analysis the high resolution limit is determined typically based off of the level at which the signal-to-noise (I/σ) level falls below 3, for Laue crystallography a criterion of completeness in the highest resolution shell greater than 25% was used. However, as can be seen from the statistics in Table 6.1, the overall completeness of both datasets is very poor. Additionally, R_{sym} for the case of increased spot density per frame is very poor. A strategy to overcome the limitation of radiation damage during room temperature Laue data collection is discussed in Section 6.3.2.

Table 6.1. Crystallographic data statistics from the diffraction analysis of lysozyme crystals grown on chip using *in situ* Laue analysis of single crystals taken at different undulator settings. A gap filling method with 6° spacing was used with a narrower band of X-ray radiation achieved by peaked undulators. Simple data acquisition was used in 8° increments with the higher data density achieved by using offset undulators. All data collection was performed at room temperature. Reported values are for all hkls. Values shown in parenthesis represent the value for the highest resolution shell.

Parameter	Peaked Undulators 6° Gap Filling	Offset Undulators 8° Intervals
Resolution	100 – 2.20 Å	100 – 2.00 Å
R_{sym}	0.046	0.426
Mosaicity	0.028° – 0.116°	0.010° – 0.111°
Completeness	56.5% (26.6%)	70.2% (26.4%)
Frames of Data	7	9

6.3.2 *In Situ* Single-Shot Laue Structure Determination of Crystals Grown in a Microfluidic Chip

Due to the significant adverse effects of radiation damage on the crystals grown on chip, the collection of a high quality dataset from a single crystal grown on-chip proved to be difficult to achieve, as expected, despite the use of various data acquisition strategies. This observation is particularly striking given that the model system used, lysozyme, forms particularly robust high quality crystals such that radiation damage and mosaicity would be much more significant for crystals of most other proteins. However, microfluidic methods have the advantage of being able to prepare a large number of samples in parallel. Therefore a large array chip with 96 wells (Figure 6.4) was used to generate a large number of lysozyme crystals (Figure 6.5), enabling "single-shot" structure determination. Additionally, the path length through the crystal in these devices was increased relative to the total thickness of the device. In these devices the crystals were able to grow to ~50 μm in size and did not appear to have been significantly limited in their growth by the height of the chamber. This increase in the crystal size enabled the use of thicker device layers (a total path length of ~100 μm, including ~20 μm of PDMS) to yield more robust devices.

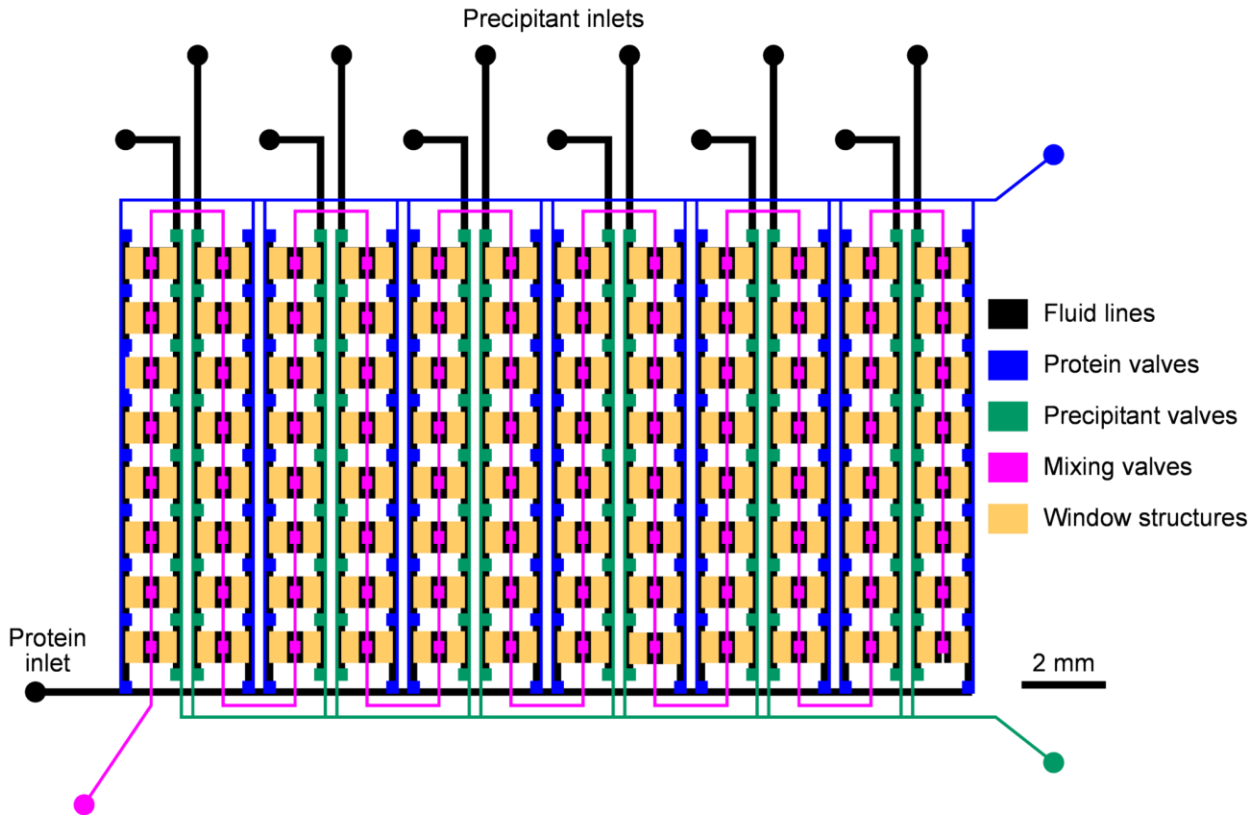

Figure 6.4. Schematic depiction of the design of a 96-well microfluidic array chip for the crystallization of soluble or detergent solubilized proteins. Protein and precipitant inlets are indicated. The fluid layer is shown in black while the various features of the control layer have been identified based on function. Valves for the loading of protein are shown in blue, precipitant valves in green, and the valves to connect chambers and allow for diffusion between the protein and precipitant chambers are pink. Window structures are shown in yellow. These structures are present in the control layer, but serve only to decrease the thickness of material present in the path of the X-ray beam.

Data collection by taking a single diffraction image of a large number of crystals is particularly attractive for microfluidic applications, provided that crystals can be grown without an orientational bias on-chip. One of the significant challenges for data collection in a planar microfluidic device is the need to maintain alignment of the crystal during rotation, coupled with geometric limitations for rotation of the device. For single-shot analysis the microfluidic chip can be mounted perpendicular to the X-ray beam and simply translated from well-to-well. The random orientation of crystals within the chip would then allow for a full survey of rotational space without having to rotate the sample itself. This type of a setup avoids difficulties with rotational and geometric limitations and eases difficulties with optically aligning a rotating crystal in the beam. This method was further enabled by the development of an automated method for marking the location of crystals within a microfluidic chip such that data collection could be performed automatically once all crystals have been located.

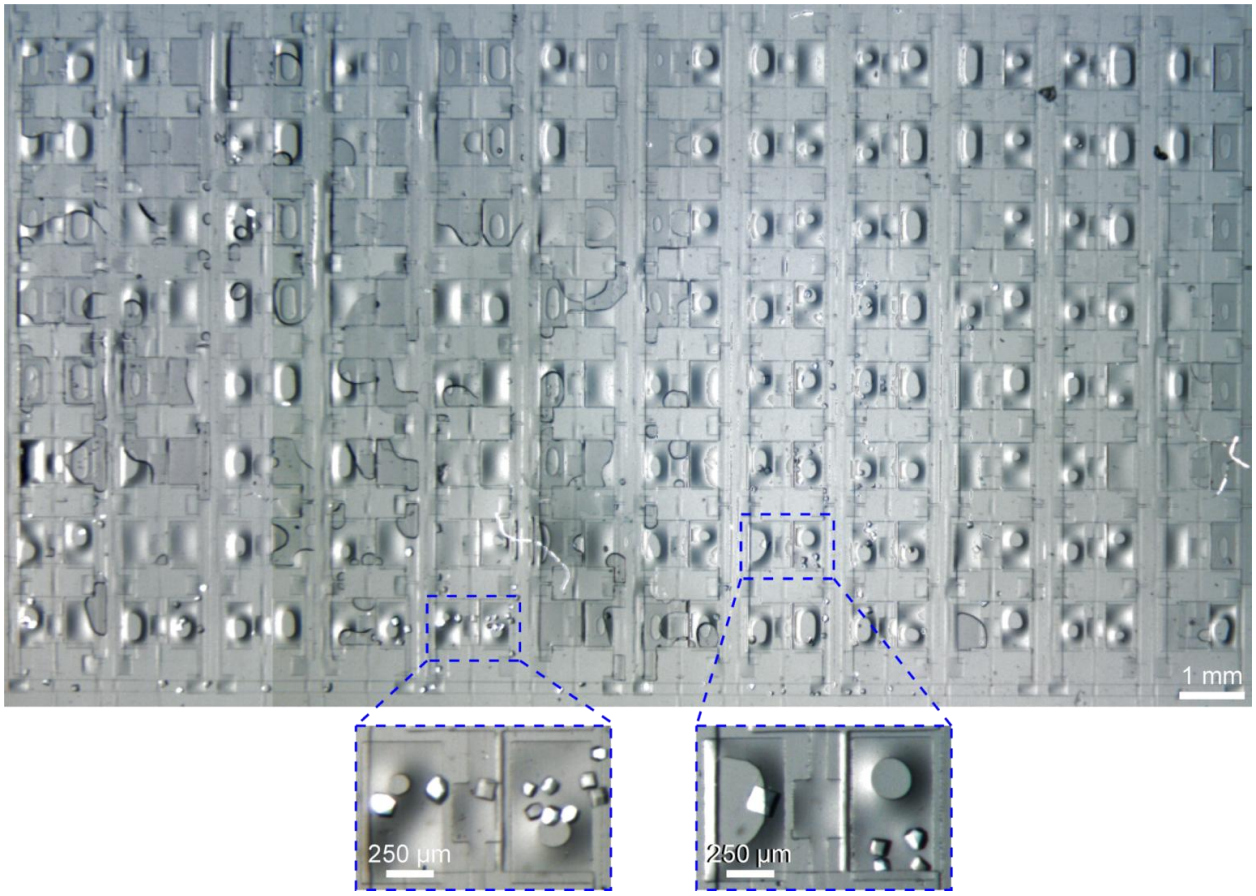

Figure 6.5. Composite optical micrograph of lysozyme crystals grown in a 96-well microfluidic array chip used for Laue X-ray diffraction experiments. Insets provide a magnified view of crystals in individual wells.

Diffraction analysis of crystals grown on a single chip resulted in 169 frames of data, of which 122 represented high quality data. Of the 34 frames taken where no diffraction was observed, the majority of these lost frames can be attributed to errors in controlling sample translation, the scripting for which was corrected during the course of data collection. Also, the accuracy of crystal marking coupled with fine control of sample translation over the entire dimensions of the chip (20 mm x 10 mm) were validated in that only a single frame of data was collected which showed overlapping diffraction patterns from multiple crystals, despite the close proximity of many crystals within wells.

Of the 122 frames of data obtained, 66 were merged to form a single dataset. While is possible that the quality and completeness of the final result could have been improved by including additional frames of data, scripting was used to analyze the entire dataset in an automated fashion so as to maintain the high throughput nature of this method. More careful analysis for inclusion of the excluded frames is beyond the scope of the current study.

The data obtained by "single-shot" Laue methods was then compared to an analogous dataset obtained by collecting small wedges of data from a large number of crystals using monochromatic diffraction, as presented in Chapter 5. Statistics associated with the data collection and model refinement

of the two datasets are given in Table 6.2. As can be seen in Table 6.2, the two datasets extend over similar resolution ranges and have comparable values for the linear R-factor (R_{sym}). One particularly observation is that significantly lower levels of mosaicity were seen for crystals analyzed by "single-shot" Laue methods as compared to an equivalent monochromatic method. However, despite the collection of high quality, low mosaicity data, the completeness of the Laue dataset is significantly lower than that of the monochromatic dataset. Although part of this difference could stem from the criteria used to establish resolution limits, this difference in completeness could account for differences seen in the resultant electron density maps (Figure 6.6) and the higher levels of R and R_{free} obtained during model refinement.

Table 6.2. Crystallographic data statistics from the room temperature diffraction analysis of lysozyme crystals grown on chip and analyzed *in situ* using (i) "single-shot" Laue methods (polychromatic) and (ii) "small wedge" monochromatic diffraction. Data was collected from a large number of crystals and merged to form a complete datasets. Reported values are for all hkls. Values shown in parenthesis represent the value for the highest resolution shell except in the case of R (R_{free}) statistics from model building and for the Ramachandran plot statistics where the number in parenthesis indicates the number of residues in a given region.

Parameter	Polychromatic	Monochromatic
Data Collection		
Resolution	50 – 1.62 Å	50 – 1.55 Å
R_{sym}	0.074	0.064 (0.362)
Mosaicity	0.006° – 0.062°	0.03° – 0.08°
Completeness	90.1% (39.1%)	98.1% (83.4%)
Frames of Data	66	363
Refinement		
R (R_{free})	0.281 (0.346)	0.164 (0.227)
Ramachandran Plot		
Most Favored	94.49% (120)	96.06% (122)
In Allowed Regions	5.51% (7)	3.94% (5)
Disallowed	0.00% (0)	0.00% (0)

As can be seen in Figure 6.6a-b1, the electron density maps generated from the "single-shot" Laue data are not capable of generating as clear a picture of amino acid side-chain conformations as was the more complete monochromatic dataset. The difference in quality of these two maps becomes even more apparent when a difference map comparing of the observed and calculated electron density of a single sidechain, tryptophan Trp 111 are made (Figure 6.6a-b2). The electron density map generated from Laue data shows discontinuous regions of electron density suggesting a difference in quality of the two maps. A comparison of the observed solvent molecules showed areas of both agreement and disagreement between the two datasets (Figure 6.6a-b3). Despite the differences of the two datasets, these results clearly demonstrate the capability of single-shot *in situ* data collection for structure determination using Laue methods.

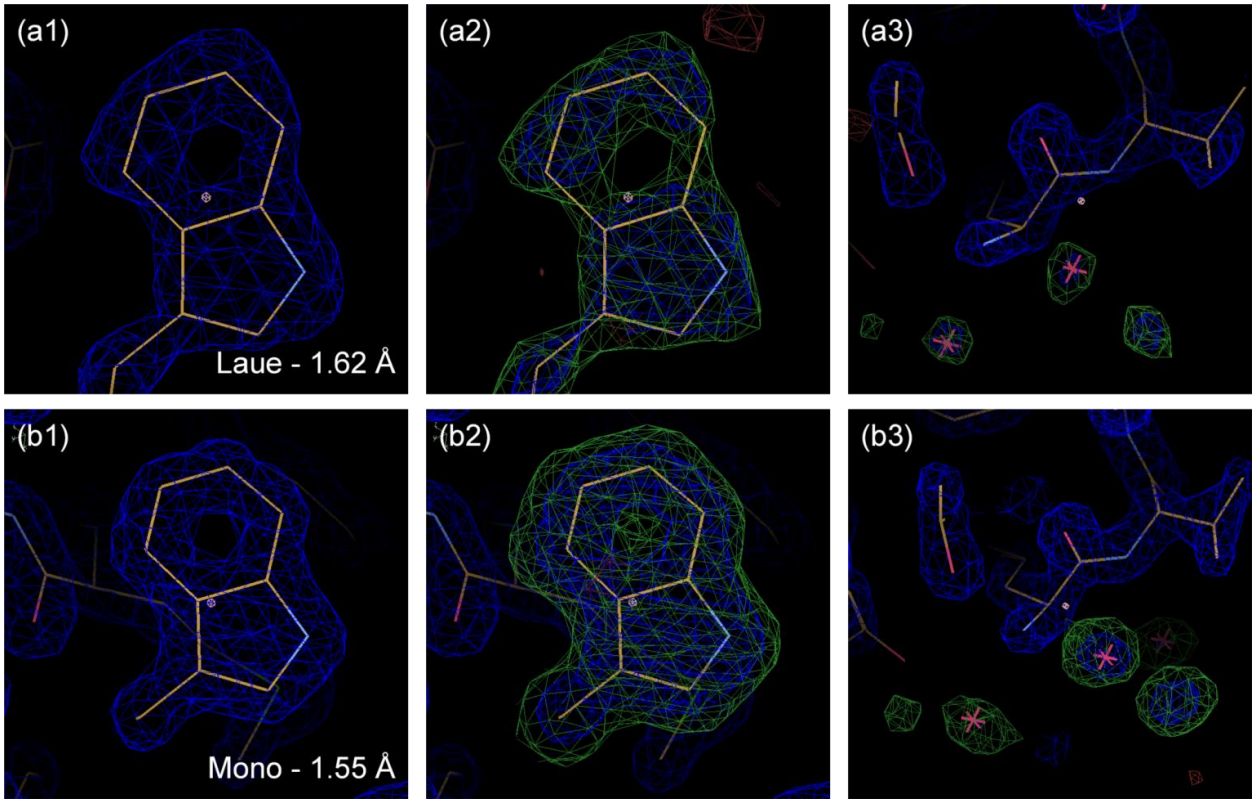

Figure 6.6. Electron density maps displaying various aspects of the structure of hen egg white lysozyme obtained by merging data from many crystals grown on-chip and analyzed at room temperature to **(a)** 1.62 Å using single-shot Laue diffraction, and **(b)** 1.55 Å obtained using monochromatic diffraction methods. **(1)** The calculated structure for Trp111 at a sigma level of 2.0. **(2-3)** Maps showing the difference between the calculated and observed structures for **(2)** Trp111 and **(3)** water molecules located near Lys1. The calculated map (blue) is displayed at a sigma level of 2.0, while the difference map (green) is displayed at a sigma level of 3.0.

6.4 Conclusions

In summary, the utility of the X-ray transparent device architecture developed in Chapter 5 has been extended to polychromatic Laue diffraction methods. The effects of sample and device geometry have been investigated and the relative path length through the crystal as compared to the device materials was shown to be significant. Taking advantage of the lack of sample manipulation during Laue data collection, an automated method for collecting "single-shot" diffraction data from a large number of crystals grown on chip has been developed in collaboration with the BioCARS team at the Advanced Photon Source at Argonne National Laboratory. Automated strategies for data processing are also in place to facilitate the high throughput analysis of the large number of frames of data which could result from this data collection strategy.

As in the case of monochromatic diffraction analysis, these X-ray transparent microfluidic platforms circumvent challenges associated with the growth and mounting fragile protein crystals. Fine control over the fluid transport on-chip enables reproducible crystallization of a large number of crystals with limited well-to-well variability. The ability to perform *in situ* X-ray analysis further decreases the potential for crystal-to-crystal variability that could occur as a result of physical handling and/or environmental shock.

While these strategies have been demonstrated with lysozyme as a model system, further validation of this approach with more challenging systems such as less strongly diffracting soluble protein targets, and/or membrane proteins crystallized both *in surfo* and *in meso* would be a truly powerful demonstration of the efficacy of this approach. The ability to efficiently perform Laue diffraction studies using a large number of crystals has the potential to enable the time resolved study of a large number of protein targets which have otherwise resisted analysis by Laue methods.

In addition to the static structural studies presented here, there is tremendous potential for developing microfluidic crystallization platforms for use in time resolved structural studies. In these more advanced studies the fluid handling capabilities of microfluidics and the fine control over transport phenomena could be utilized not only to grow a large array of crystals, but also to supply ligands or substrates to study structural changes associated with protein function, or more subtle changes associated with variations in pH, ionic strength, temperature, or other biologically relevant parameters. The majority of time resolved studies reported thus far have been limited to systems for which robust protein crystals can be grown. Eliminating the need for manual handling of crystals not only avoids the potential for physically damaging fragile crystals, it also enables the analysis of a significantly larger number of crystals. The development and validation of this technology for time resolved and dynamic crystallography studies would be extremely powerful and would provide a new niche area where microfluidic technologies can truly excel.

6.5 Acknowledgements

This work was funded by NIH (R01 GM086727) and a NIH Kirschstein Predoctoral Fellowship from the National Institute of Biomedical Imaging and Bioengineering (F31 EB008330). The collaborative efforts of the BioCARS group at the Advanced Photon Source at Argonne National Laboratory, and in particular Dr. Zhong Ren helped to make this work possible. Also, Sudipto Guha was invaluable in his assistance with the development and testing of X-ray transparent microfluidic chips. Dr. Satish Nair, Vinayak Argawal, and Dr. Tiik Luk were also tremendously helpful with their assistance in data analysis.

Use of the Advanced Photon Source was supported by the U.S. Department of Energy, Basic Energy Sciences, Office of Science, under Contract No. DE-AC02-06CH11357. Use of the BioCARS Sector 14 was supported by the National Institutes of Health, National Center for Research Resources, under grant number RR007707.

6.6 References

(1) Hansen, C.; Quake, S. R. *Current Opinion in Structural Biology* **2003**, *13*, 538.
(2) Ng, J. D.; Gavira, J. A.; Garcia-Ruiz, J. M. *Journal of Structural Biology* **2003**, *142*, 218.
(3) van der Woerd, M.; Ferree, D.; Pusey, M. *Journal of Structural Biology* **2003**, *142*, 180.
(4) Song, H.; Chen, D. L.; Ismagilov, R. F. *Angew Chem Int Edit* **2006**, *45*, 7336.
(5) Sauter, C.; Dhouib, K.; Lorber, B. *Crystal Growth and Design* **2007**, *7*, 2247.
(6) Salmon, J.-B.; Leng, J. *Comptes Rendus Chimie* **2009**, *12*, 258.
(7) Leng, J.; Salmon, J.-B. *Lab Chip* **2009**, *9*, 24.

(8) Perry, S. L.; Roberts, G. W.; Tice, J. D.; Gennis, R. B.; Kenis, P. J. A. *Cryst Growth Des* **2009**, *9*, 2566.

(9) Li, L.; Fu, Q.; Kors, C.; Stewart, L.; Nollert, P.; Laible, P.; Ismagilov, R. *Microfluid Nanofluid* **2009**, *8*, 789.

(10) Li, L.; Du, W.; Ismagilov, R. F. *J Am Chem Soc* **2009**.

(11) Zheng, B.; Roach, L. S.; Ismagilov, R. F. *J Am Chem Soc* **2003**, *125*, 11170.

(12) Zheng, B.; Tice, J. D.; Ismagilov, R. F. *Adv Mater* **2004**, *16*, 1365.

(13) Zheng, B.; Tice, J. D.; Ismagilov, R. F. *Anal Chem* **2004**, *76*, 4977.

(14) Zheng, B.; Tice, J. D.; Roach, L. S.; Ismagilov, R. F. *Angew Chem Int Edit* **2004**, *43*, 2508.

(15) Zheng, B.; Gerdts, C. J.; Ismagilov, R. F. *Current Opinion in Structural Biology* **2005**, *15*, 548.

(16) Zheng, B.; Ismagilov, R. F. *Angew Chem Int Edit* **2005**, *44*, 2520.

(17) Yadav, M. K.; Gerdts, C. J.; Sanishvili, R.; Smith, W. W.; Roach, L. S.; Ismagilov, R. F.; Kuhn, P.; Stevens, R. C. *J Appl Crystallogr* **2005**, *38*, 900.

(18) Chen, D. L.; Gerdts, C. J.; Ismagilov, R. F. *J Am Chem Soc* **2005**, *127*, 9672.

(19) Chen, D. L. L.; Ismagilov, R. F. *Curr Opin Chem Biol* **2006**, *10*, 226.

(20) Gerdts, C. J.; Tereshko, V.; Yadav, M. K.; Dementieva, I.; Collart, F.; Joachimiak, A.; Stevens, R. C.; Kuhn, P.; Kossiakoff, A.; Ismagilov, R. F. *Angew Chem Int Edit* **2006**, *45*, 8156.

(21) Li, L.; Mustafi, D.; Fu, Q.; Tereshko, V.; Chen, D. L. L.; Tice, J. D.; Ismagilov, R. F. *P Natl Acad Sci USA* **2006**, *103*, 19243.

(22) Chen, D. L. L.; Li, L.; Reyes, S.; Adamson, D. N.; Ismagilov, R. F. *Langmuir* **2007**, *23*, 2255.

(23) Laval, P.; Salmon, J. B.; Joanicot, M. *J Cryst Growth* **2007**, *303*, 622.

(24) Dombrowski, R. D.; Litster, J. D.; Wagner, N. J.; He, Y. *Chem Eng Sci* **2007**, *62*, 4802.

(25) Maki, S.; Murai, R.; Yoshikawa, H. Y.; Kitatani, T.; Nakata, S.; Kawahara, H.; Hasenaka, H.; Kobayashi, A.; Okada, S.; Sugiyama, S.; Adachi, H.; Matsumura, H.; Takano, K.; Murakami, S.; Inoue, T.; Sasaki, T.; Mori, Y. *J Synchrotron Radiat* **2008**, *15*, 269.

(26) Gerdts, C. J.; Elliott, M.; Lovell, S.; Mixon, M. B.; Napuli, A. J.; Staker, B. L.; Nollert, P.; Stewart, L. *Acta Crystallographica Section D* **2008**, *64*, 1116.

(27) Kreutz, J. E.; Li, L.; Roach, L. S.; Hatakeyama, T.; Ismagilov, R. F. *J Am Chem Soc* **2009**, *131*, 6042.

(28) Du, W.; Li, L.; Nichols, K. P.; Ismagilov, R. F. *Lab Chip* **2009**, *9*, 2286.

(29) Pang, Y.; Liu, J.; Li, H.; Lin, J. *Science in China Series B: Chemistry* **2009**, *52*, 1014.

(30) Luft, J. R.; Rak, D. M.; DeTitta, G. T. *J Cryst Growth* **1999**, *196*, 450.

(31) Steinert, C. P.; Mueller-Dieckmann, J.; Weiss, M.; Roessle, M.; Zengerle, R.; Koltay, P. In *Future Generation Communication and Networking* 2007, p 561.

(32) Zhou, X.; Lau, L.; Lam, W. W. L.; Au, S. W. N.; Zheng, B. *Anal. Chem.* **2007**.

(33) Lounaci, M.; Rigolet, P.; Casquillas, G. V.; Huang, H. W.; Chen, Y. *Microelectron Eng* **2006**, *83*, 1673.

(34) Lounaci, M.; Rigolet, P.; Abraham, C.; Le Berre, M.; Chen, Y. *Microelectron Eng* **2007**, *84*, 1758.

(35) Korczynska, J.; Hu, T. C.; Smith, D. K.; Jenkins, J.; Lewis, R.; Edwards, T.; Brzozowski, A. M. *Acta Crystallogr D* **2007**, *63*, 1009.

(36) Shim, J. U.; Cristobal, G.; Link, D. R.; Thorsen, T.; Fraden, S. *Cryst Growth Des* **2007**, *7*, 2192.

(37) Shim, J. U.; Cristobal, G.; Link, D. R.; Thorsen, T.; Jia, Y.; Piattelli, K.; Fraden, S. *J Am Chem Soc* **2007**, *129*, 8825.

(38) Hansen, C. L.; Classen, S.; Berger, J. M.; Quake, S. R. *J Am Chem Soc* **2006**, *128*, 3142.

(39) Lau, B. T. C.; Baitz, C. A.; Dong, X. P.; Hansen, C. L. *J Am Chem Soc* **2007**, *129*, 454.

(40) Lopez-Jaramillo, F. J.; Garcia-Ruiz, J. M.; Gavira, J. A.; Otalora, F. *J Appl Crystallogr* **2001**, *34*, 365.

(41) Garcia-Ruiz, J. M.; Otalora, F.; Novella, M. L.; Gavira, J. A.; Sauter, C.; Vidal, O. *J Cryst Growth* **2001**, *232*, 149.

(42) Garcia-Ruiz, J. M.; Gonzalez-Ramirez, L. A.; Gavira, J. A.; Otalora, F. *Acta Crystallogr D* **2002**, *58*, 1638.

(43) Gavira, J. A.; Toh, D.; Lopez-Jaramillo, J.; Garcia-Ruiz, J. M.; Ng, J. D. *Acta Crystallogr D* **2002**, *58*, 1147.

(44) Bolanos-Garcia, V. M. *J Cryst Growth* **2003**, *253*, 517.

(45) Ng, J. D.; Clark, P. J.; Stevens, R. C.; Kuhn, P. *Acta Crystallographica Section D* **2008**, *64*, 189.

(46) Ng, J. D.; Garcia-Ruiz, J. M.; Gavira-Gallardo, J. A.; Wells, M.; Jenkins, G. US, 2006.

(47) Dhouib, K.; Malek, C. K.; Pfleging, W.; Gauthier-Manuel, B.; Duffait, R.; Thuillier, G.; Ferrigno, R.; Jacquamet, L.; Ohana, J.; Ferrer, J.-L.; Theobald-Dietrich, A.; Giege, R.; Lorber, B.; Sauter, C. *Lab Chip* **2009**, *9*, 1412.

(48) Sugahara, M.; Kageyama, Y.; Kunishima, N. *J Appl Crystallogr* **2009**, *42*, 129.

(49) Sauter, C.; Otalora, F.; Gavira, J. A.; Vidal, O.; Giege, R.; Garcia-Ruiz, J. M. *Acta Crystallogr D* **2001**, *57*, 1119.

(50) Hansen, C. L.; Skordalakes, E.; Berger, J. M.; Quake, S. R. *P Natl Acad Sci USA* **2002**, *99*, 16531.

(51) Kothe, M.; Kohls, D.; Low, S.; Coli, R.; Cheng, A. C.; Jacques, S. L.; Johnson, T. L.; Lewis, C.; Loh, C.; Nonomiya, J.; Sheils, A. L.; Verdries, K. A.; Wynn, T. A.; Kuhn, C.; Ding, Y. H. *Biochemistry-Us* **2007**, *46*, 5960.

(52) Sugahara, M.; Asada, Y.; Morikawa, Y.; Kageyama, Y.; Kunishima, N. *Acta Crystallogr D* **2008**, *64*, 686.

(53) Li, L.; Ismagilov, R. F. *Ann Rev Biophys* **2010**.

(54) Ren, Z.; Bourgeois, D.; Helliwell, J. R.; Moffat, K.; Srajer, V.; Stoddard, B. L. *J Synchrotron Radiat* **1999**, *6*, 891.

(55) Garman, E. F.; Schneider, T. R. *J Appl Crystallogr* **1997**, *30*, 211.

(56) Alcorn, T.; Juers, D. H. *Acta Crystallographica Section D* **2010**, *66*, 366.

(57) Juers, D. H.; Matthews, B. W. *Q Rev Biophys* **2004**, *37*, 105.

(58) Bourgeois, D.; Schotte, F.; Brunori, M.; Vallone, B. *Photoch Photobio Sci* **2007**, *6*, 1047.

(59) Baxter, R. H. G.; Ponomarenko, N.; Å rajer, V.; Pahl, R.; Moffat, K.; Norris, J. R. *P Natl Acad Sci USA* **2004**, *101*, 5982.

(60) Schlichting, I. *Accounts of Chemical Research* **2000**, *33*, 532.

(61) Cornaby, S.; Szebenyi, D. M. E.; Smilgies, D.-M.; Schuller, D. J.; Gillilan, R.; Hao, Q.; Bilderback, D. H. *Acta Crystallographica Section D* **2010**, *66*, 2.

(62) Sophianopoulos, A. J.; Holcomb, D. N.; Vanholde, K. E.; Rhodes, C. K. *J Biol Chem* **1962**, *237*, 1107.

(63) BioCARS. http://cars9.uchicago.edu/biocars/

(64) Ren, Z. Precognintion User Guide with Reference and Tutorials. http://renzresearch.com/Precognition (2006).

(65) *Acta Crystallogr D* **1994**, *50*, 760.

(66) Langer, G.; Cohen, S. X.; Lamzin, V. S.; Perrakis, A. *Nat Protoc* **2008**, *3*, 1171.

(67) Murshudov, G. N.; Vagin, A. A.; Dodson, E. J. *Acta Crystallogr D* **1997**, *53*, 240.

(68) Evans, P.; McCoy, A. *Acta Crystallographica Section D* **2008**, *64*, 1.

(69) Vaney, M. C.; Maignan, S.; Ries-Kautt, M.; Ducruix, A. *Acta Crystallographica Section D* **1996**, *52*, 505.

(70) Emsley, P.; Cowtan, K. *Acta Crystallographica Section D* **2004**, *60*, 2126.

Chapter 7

Microfluidic Platforms for *In Situ* Analysis of Lipid Phase Behavior

Abstract

The X-ray transparent microfluidic device architecture developed in Chapters 5 and 6 for protein crystallography has been applied to the challenge of *in situ* small angle X-ray diffraction studies for the determination of the phase behavior of aqueous/lipid systems. The feasibility of analyzing very thin microfluidic samples was tested by examining the effect of sample thickness on the observed signal intensity and the effects X-ray irradiation on microfluidic samples. The use of these platforms for the collection of *in situ* phase diagram data was validated using microfluidic chambers as thin as 10 µm.

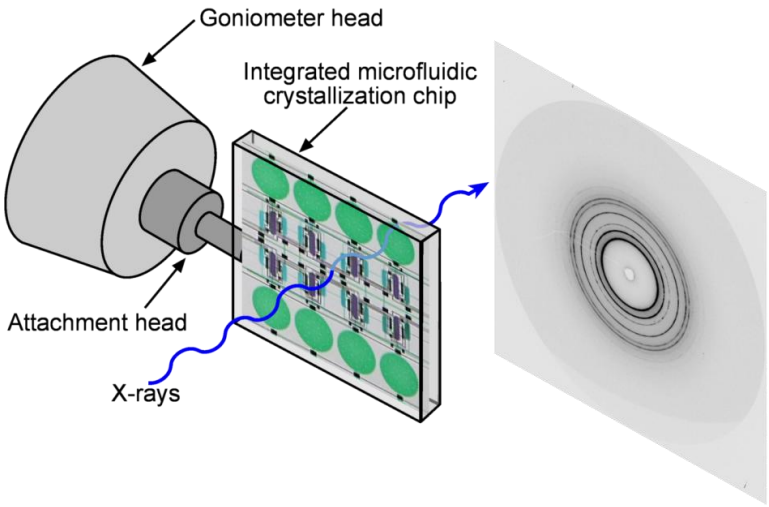

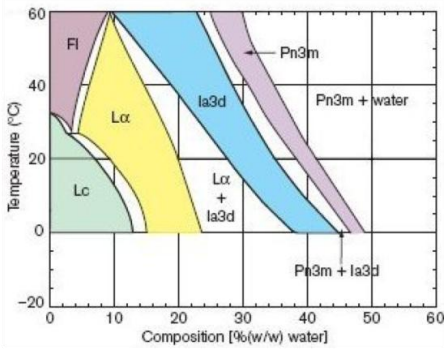

7.1 Introduction

As was discussed in Chapter 2, the *in meso* crystallization method relies on the self-assembly of liquid crystalline mesophase structures above a limiting concentration of certain lipids in water. Understanding the phase behavior of these self assembling aqueous/lipid systems is critical for the advancement of the *in meso* crystallization method. However, the preparation of highly viscous mesophase samples is non-trivial and mapping out the phase behavior of even a binary water/lipid mixture is both time and sample intensive. To understand crystallization systems it is necessary to not only understand the phase behavior of the simple lipid water system, but also to understand the effect that a wide variety of additives can have on phase behavior.

The preparation of aqueous/lipid mesophases, particularly at small volumes is challenging because of the high viscosity of the lipid solution (~30 times higher than the viscoity of water) and the non-Newtonian behavior and the extremely high viscosity (~10^5 times higher than the viscosity of water at the shear rates employed) of the resulting mixture.[1-4] Sample preparation in the literature has typically been done either by repeated centrifugation in a small tube along with extended periods of equilibration,[5-22] or through the use of two microsyringes that are coupled through a small bore connector.[3,22-32]

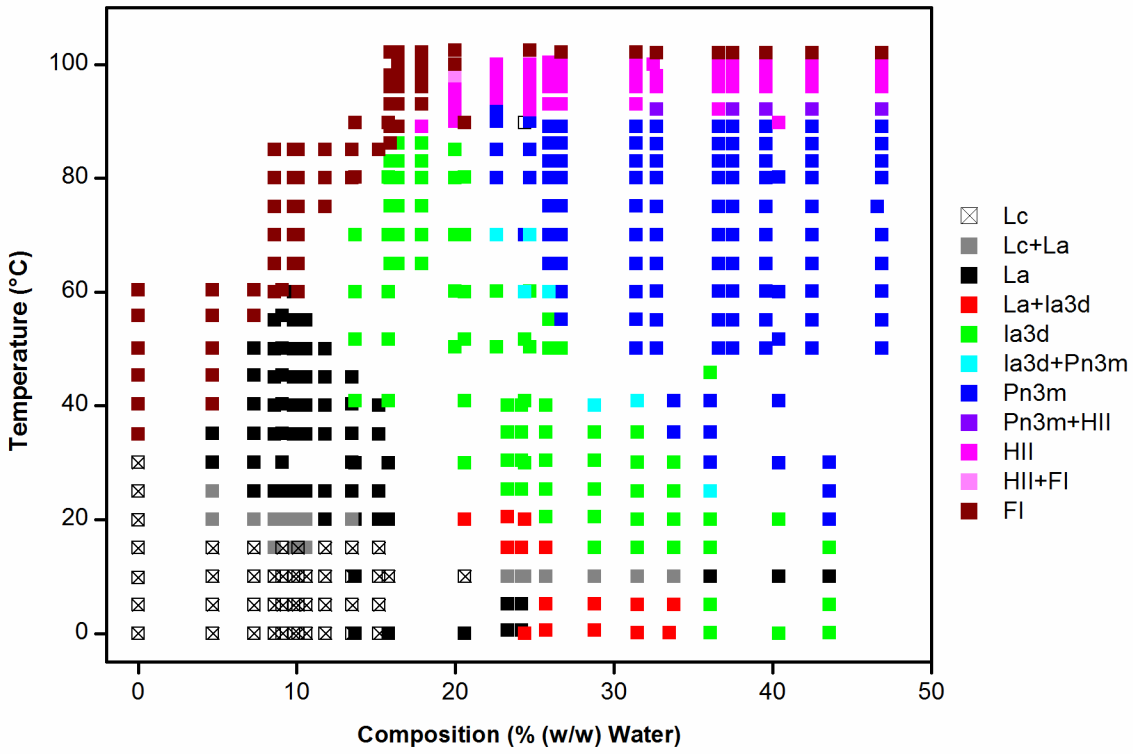

Figure 7.1. Equilibrium temperature/composition phase diagram for the binary monoolein/water system. Legend: Lc and La are lamellar phases, Ia3d and Pn3m are bicontinuous cubic phases, HII is an inverted hexagonal phase and FI is a fluid isotropic phase. 471 individual data points were needed for the construction of this phase diagram. (Figure adapted from Briggs and Caffrey, 1994).[33]

Determination of the phase diagram for an aqueous/lipid system is highly labor intensive, involving preparation of all individual compositions, followed by transfer into X-ray capillaries and analysis. For

example, determination of the equilibrium temperature/composition phase diagram for monoolein and water required nearly 500 separate measurements (Figure 7.1).[33] To determine a phase diagram, mesophase samples of specific concentrations are prepared. The phase identity of each sample is then analyzed by a variety of techniques including small angle X-ray diffraction.[32-36] X-ray analysis provides direct insight into the dimensions of the mesophases: for example, a fully hydrated cubic Pn3m phase of monoolein and water has a bilayer thickness of 32Å and water channels with a diameter of 40Å.[37] The metastable character of the various mesophases requires long incubation times in excess of 3 hours at each temperature increment to minimize these effects.[7,22,32,33,35-37] Temperature-controlled sample holders are also limited in the number of samples which can be mounted at one time. Actual diffraction data collection takes between 15 minutes to 24 hours using a 'bench-top' X-ray source[20,32,35] or on the order of seconds when a synchrotron source is used.[22,34]

In meso crystallization has thus far utilized the wealth of self-assembling phase behavior observed in aqueous/monoacylglycerol (MAG) systems, most commonly with the lipid monoolein (1-monooleoyl-*rac*-glycerol). While these aqueous/MAG systems form a variety of phases including lamellar phases, bicontinuous cubic and inverted hexagonal phases,[3,10,28,30,38-40] the lamellar and cubic phases are thought to be the most important for *in meso* crystallization.[3,8,31,41-46] Lamellar phases are locally planar lipid bilayer structures with varying degrees of inter-bilayer hydration. Cubic phases can be described as networks of interconnected aqueous channels surrounded by lipid bilayers with negative curvature. These phases are bicontinuous, allowing for diffusion in both the aqueous channels and the curved lipid bilayers.

Additives such as salts, detergents, lipids, other components of crystallization screens, biologically relevant molecules and cofactors, and the membrane proteins themselves have been shown to have a significant effect on not only the phase behavior of these aqueous/MAG systems, but also potentially on the related *in meso* crystallization trial.[3,8-13,15-17,19-22,26-31,41,45,47-53] Understanding the effect of these various additives, not only on the identity of a particular mesophase, but also on the lattice parameter and curvature of the phase is critical for developing a rational understanding of *in meso* crystallization. However, performing such a survey of the effects of even a small set of the additives typical in crystallization experiments would be an immense undertaking, particularly given current methods.

In Chapters 4 and 5 a microfluidic platform for the preparation of *in meso* crystallization samples with *in situ* analysis capabilities was introduced. This microfluidic platform decreased the preparative scale at which mesophase samples could be prepared by 1000x from traditional syringe-based methods and has the potential to be scaled out for high throughput screening. In this chapter the development and characterization of a microfluidic platform for the preparation and *in situ* X-ray analysis of mesophase samples for phase behavior studies is described. This work was truly enabled by the development of a small angle X-ray diffraction setup with advanced sample visualization capabilities by the Life Sciences Collaborative Access Team (LS-CAT) at the Advanced Photon Source at Argonne National Laboratory

(Section 7.3.1). The visualization capabilities of this setup were necessary to enable targeting of individual samples in an integrated microfluidic chip. Using this setup, an investigation into the effects of signal as a function of sample thickness for very thin microfluidic samples was done (Section 7.3.2). Several integrated microfluidic chips were developed to study various aspects of phase behavior, including the effects of additives (Section 7.3.3), and initial testing of *in situ* small angle X-ray diffraction analysis of mesophase samples in a microfluidic device validated the efficacy of this approach (Section 7.3.4).

7.2 Materials and Methods

7.2.1 Device Fabrication and Operation

The microfluidic chips used here were fabricated as described in Chapter 5. Briefly, microfluidic chips were fabricated by bonding a thin polydimethylsiloxane (PDMS, General Electric RTV 650) fluid layer with 10 µm features covered with a membrane thickness of ~20 µm. This fluid layer was chemically bonded to a molded cyclic olefin copolymer (COC, 4 mil 6013, from TOPAS Advanced Polymers Inc.) control layer and a flat COC substrate (2 mil 5013, TOPAS Advanced Polymers Inc.). A thick layer of PDMS with punched holes for the fluid and control lines was then bonded to the control layer. This layer of PDMS did not cover the areas of interest for analysis on the chip.

7.2.2 Chemicals and Solutions

Monoolein (1-monooleoyl-*rac*-glycerol, Fluka) was purchased and stored at -12°C. Mixtures of monoolein and β-octylglucoside (anagrade, Anatrace) were prepared by dissolution in chloroform followed by evaporation of the solvent first under a nitrogen stream and then by drying under vacuum at room temperature overnight. Mixtures with a ratio of 0.033 (w/w), 0.066 (w/w), and 0.099 (w/w) β-octylglucoside/monoolein were prepared. 1.3M KH_2PO_4 (Sigma), pH 5.5 was prepared gravimetrically, taking careful note not only of the mass of salt present, but also the mass of water added. Prior to use, solutions were filtered through 0.22 µm (Steriflip, Millipore) filters.

Mesophase preparation was done using a coupled syringe mixer.[3,22-32] The dry lipid or lipid/detergent mixture was carefully loaded into a 250 µL gastight syringe (Hamilton Co.) and weighed using a microbalance (Ohaus Discovery DV215CD). The aqueous solution was pipetted into a 100 µL gastight syringe and similarly weighed. The syringe mixer was then assembled, taking care to avoid trapping air in the syringes. Mixing was then achieved by driving the contents of the syringes back and forth until a uniform mixture was obtained. The resultant mesophase was inspected both visually and under crosspolarized light. Cubic phases are optically transparent and nonbirefringent while lamellar phases tend to be opaque and are birefringent.[3-6,8,20,24,26,35,39,40,42-45,54-65]

For sample thickness experiments a 50/50 (w/w) mixture of monoolein and water was prepared. This composition of monoolein and water forms a hydrated cubic phase at 25°C. A second mixture with lower water content was also prepared. The composition of this phase was unknown due to losses during

sample preparation. For *in situ* analysis of mesophases in microfluidic chips a mixture of 90/10 (w/w) mixture of monoolein and β-octylglucoside with 1.3M KH_2PO_4 pH 5.5 were prepared using different (w/w) ratios of monoolein and β-octylglucoside.

7.2.3 Sample Thickness Experiments

Testing of the signal intensity as a function of sample thickness was performed using both traditional capillary mounted samples, and also proof-of-concept structures to mimic the architecture of a microfluidic device. Cubic mesophase samples were prepared as in Section 7.2.2 and dispensed into thin-walled glass capillaries (Charles Supper) with a nominal wall thickness of 10 µm and nominal diameters of 200 µm, 300 µm, 500 µm, and 800 µm. The ends of the capillaries were sealed with Critoseal (Leica) and epoxy (Loctite Quick Set Epoxy, Henkel Consumer Adhesives) and stored at -12°C after preparation. Samples were allowed to equilibrate to room temperature (~25°C) for at least 4 hours prior to data collection.

For proof-of-concept experiments a mesophase sample was prepared and dispensed into both 900 µm glass capillaries (nominal thickness) as a control and test device structures ranging in thickness from 25 to 100 µm (nominal). Test structures were made from 2 mil (~50 µm) 5013 COC windows attached to double-sided adhesive films (3M) of varying nominal thicknesses (Table 7.1) with a small hole punched to form the sample compartment. The mesophase sample was dispensed directly into these devices and they were sealed immediately.

Table 7.1. Summary of 3M adhesive film spacers used to fabricate the test structures. Single sheets were used unless otherwise specified.

3M Adhesive Film	Nominal Film Thickness
9019	1 mil (~25 µm)
9628B	2 mil (~50 µm)
666	3 mil (~75 µm)
2 sheets of 9628B	2 x 2 mil (~100 µm)

7.2.4 *In Situ* Analysis of Phase Behavior on a Microfluidic Chip

Experiments were set up and visualized using a stereomicroscope (Leica, MZ12.5) with an attached digital camera (Leica, DFC295) operated using Leica Application Suite software. For visualization of mesophases, images were taken with the use of cross-polarizers.

For proof-of-concept experiments a mesophase sample was prepared as in Section 7.2.2 and flowed into a microfluidic device through 24 AWG polytetrafluoroethylene (PTFE) tubing (Cole-Parmer Instrument Co.) coupled with a thin metal tube connected to a syringe.

After filling, the inlet holes for both the fluid and control layers were sealed with Crystal Clear tape (Hampton Research). Samples were stored at -12°C after preparation and were allowed to equilibrate to room temperature (~25°C) for at least 4 hours prior to data collection.

7.2.5 Small Angle X-ray Diffraction Experiments

Synchrotron experiments were performed at the 21-ID-D beamline in collaboration with the Life Sciences Collaborative Access Team (LS-CAT) at the Advanced Photon Source at Argonne National Laboratory.[66] 21-ID-D operates over a wide energy range of 6.5 keV to 20 keV (1.91 Å to 0.62 Å). Thickness experiments were performed using an energy of 8.048 keV (1.54 Å, Cu-α edge). Experiments examining mesophases within microfluidic devices were performed using 8 keV radiation (1.55 Å). All 21-ID stations utilize MD-2 diffractometers (EMBL, with LS-CAT developed extensions) with on-axis sample viewing and automatic sample alignment. A MAR 300 CCD detector was used at a sample-to-detector distance of ~890 mm. Precise calibration of the sample-to-detector distance was performed using a silver behenate standard.[67] The X-ray beam was focused either in horizontal direction (singly-focused beam) or in both vertical and horizontal directions (doubly-focused beam) using a set of Kirkpatrick-Baez bimorph mirrors (ACCEL, Germany). The doubly-focused beam as used in the setup was about an order of magnitude more intense than a singly-focused beam. The beam was collimated with a set of slits and finally with a 20 µm or 50 µm pinhole aperture followed by a cleanup capillary with a pinhole (Figure 7.2). All experiments were performed using a vacuum flight tube with a mica window on the end closest to the sample and a Kapton window with an attached beamstop on the end closest to the detector. A base pressure on the order of 10^{-3} to 10^{-2} Torr was used to minimize air scatter from the X-ray beam (Figure 7.3a).

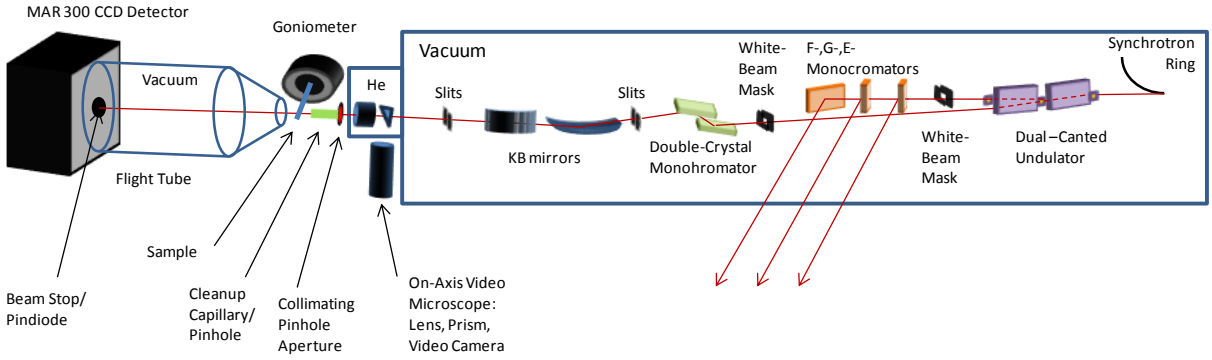

Figure 7.2. Diagram of the experimental configuration for small angle X-ray data collection on 21-ID-D. Figure was provided by Dr. Elena Kondrashkina from the Life Sciences Collaborative Access Team (LS-CAT) at the Advanced Photon Source at Argonne National Laboratory.

Capillary and samples for thickness measurements were mounted using a standard magnetic goniometer mount with an attached metal tube as a sample holder. Capillary samples were mounted into this holder using beeswax while a modified design with a slit and set-screw were used to mount samples for thickness measurements (Figure 7.3b – inset 1). Microfluidic chips were mounted in a plastic frame attached to an automated *x*-*y*-*z* translational stage (Physik Instrumente GmbH, Germany) (Figure 7.3b).

Sample visualization and alignment was achieved through the use of an on-axis video microscope. Data collection was performed at ambient conditions (~25°C).

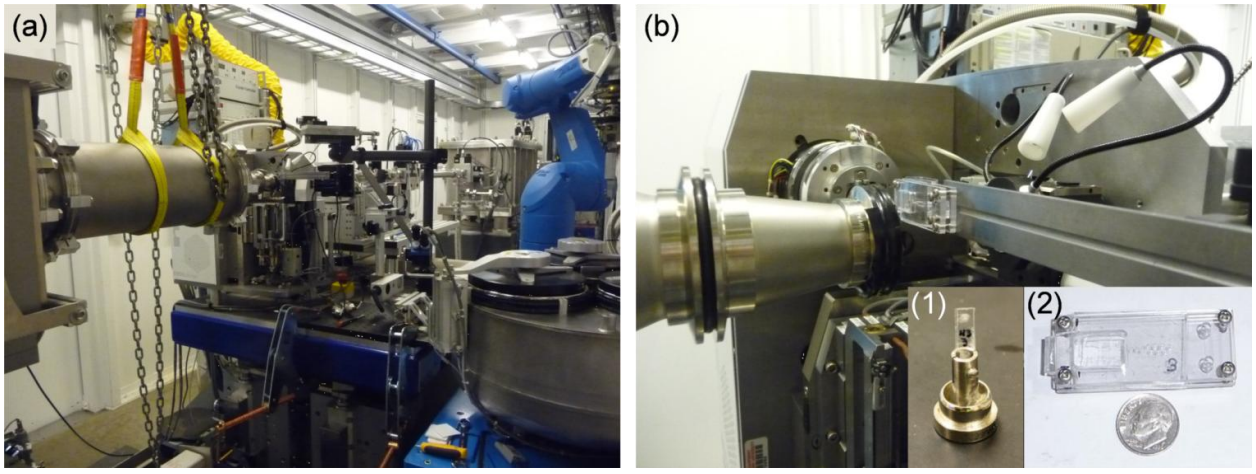

Figure 7.3. Photographs of **(a)** the small angle X-ray experimental setup at 21-ID-D and **(b)** a microfluidic chip for phase diagram determination mounted for *in situ* data collection. Inset **(1)** shows a thickness sample mounted on a magnetic cap. Inset **(2)** shows a microfluidic chip for phase diagram determination mounted in a plastic frame.

For thickness experiments, performed using a singly focused X-ray beam, exposure times ranging from 1s to 30s were used for the test structures, all taken at the same location within a sample. Exposure times for capillary samples were typically 10s. Two shots were taken sequentially at the same location in each capillary in order to investigate the effect of the X-ray beam on the sample. All samples were rotated 360° during the course of data collection to average out the effects of oriented grains. Images were captured for each sample as it was mounted on the beamline in order to facilitate determination of sample thicknesses.

For experiments on mesophases in microfluidic device structures exposure times of 1s to 5s were used without rotation. The corresponding capillary data was collected using a 1s exposure with a 180° rotation. The X-ray beam for these experiments was doubly focused, and thus more intense than in previous experiments.

7.2.6 Analysis of Small Angle X-ray Diffraction Data

Analysis of diffraction data obtained at the Advanced Photon Source was done using FIT2D software (ESRF)[68] and MATLAB.[69] Briefly, an automated script was used to integrate each diffraction image and identify peak locations and phase identities. These assignments were confirmed by manual inspection.

One of the difficulties in comparing samples of both different thickness and also different material properties is the variation in background. In an attempt to overcome this, a baselining procedure was used where the average signal value from values of q-spacing between 0.054 $Å^{-1}$ and 0.068 $Å^{-1}$ where no peaks were observed was calculated and subtracted from the entire spectrum.

In order to consider the signal intensity, the height of the main peak for the various phases present in a sample was determined using the MAX function in Excel over the appropriate range of data points. Most samples only had a single phase present, and while the information was collected for the second phase in the few cases were multiple phases were present, it was not included in the analysis.

Sample thickness was determined using image analysis in ImageJ software of the digital images taken of the various mounted samples. A scale of 0.377 pixels = 1 µm was determined from the embedded scalebar. The sample thickness was taken to be the vertical distance from the edges of the capillary at the point where the X-ray beam passed through the sample, as indicated by the crosshairs in the photograph (Figure 7.4) minus an assumed nominal value for the wall thickness of the capillary (2 x 10µm). This value does not correspond to the actual diameter of the capillary in some cases when the sample was not perfectly horizontal. The diameter of the capillaries was found to be significantly different from the nominal value and varied along the length of the capillary. These nonuniformities were also evident upon visual inspection of the capillaries. Similar measurements were attempted on the test-structures, but difficulties in imaging the edge of a planar device made this an ineffective method.

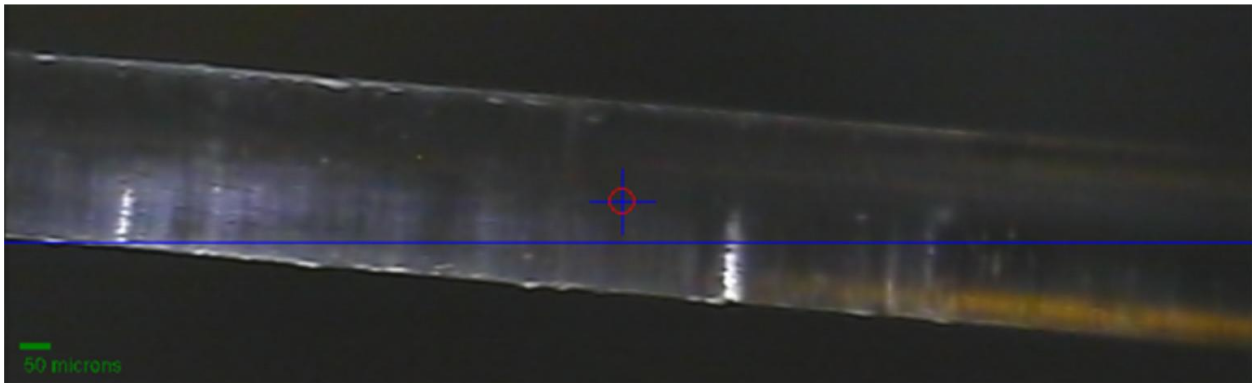

Figure 7.4. Photograph of a 200 µm (nominal) capillary containing a mesophase sample mounted on LS-CAT beamline 21-ID-D at the Advanced Photon Source at Argonne National Laboratory.

7.3 Results and Discussion

7.3.1 Development of Small Angle X-ray Analysis Capabilities at LS-CAT with High Resolution Sample Visualization Capabilities

While small angle X-ray analysis setups are common at synchrotron sources, they typically lack the ability to clearly visualize the sample. In developing microfluidic platforms to study the phase behavior of mesophase systems it is critical to be able to target specific microfluidic wells for analysis. The experimental setup at LS-CAT at the Advanced Photon Source is designed for high quality macromolecular crystallography.[66] To this end it employs high resolution sample visualization along the same axis as the X-ray beam coupled with precise sample targeting strategies. A collaboration with LS-CAT, headed by Dr. Elena Kondrashkina was established to enable the development and testing of microfluidic devices to study phase behavior and to establish and expand the capabilities of the LS-CAT setup for potentially new and exciting areas of research.

Examples of the visualization capabilities of the experimental setup at LS-CAT are shown in Figure 7.5. These optical micrographs clearly visualize not only the location of the microfluidic chip, but also the targeting area of the 20 µm X-ray beam used in these experiments (Figure 7.5a), and changes in the sample as a result of exposure to the X-ray beam (Figure 7.5b). This level of visualization is critical for the use of *in situ* analysis in highly integrated microfluidic devices in order to clearly identify the target area of interest.

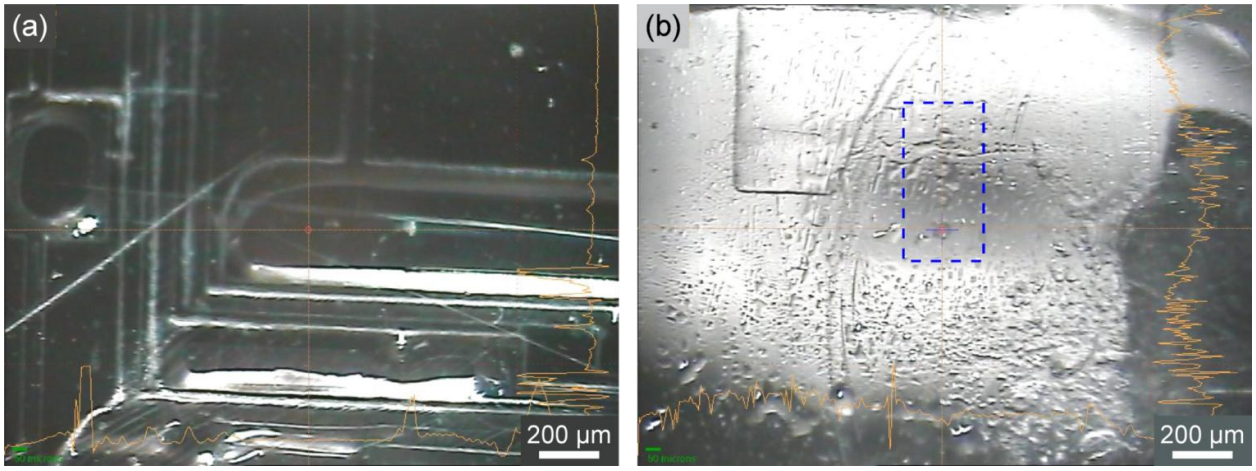

Figure 7.5. Optical micrographs demonstrating the visualization capabilities of the on-axis camera at the LS-CAT beamline 21-ID-D. **(a)** A microfluidic chip for phase diagram determination. Targeting for the X-ray beam can be seen by the red cross-hairs indicating that a sample in the side chamber of a mixer is to be sampled. **(b)** A series of small circles within a microfluidic mesophase sample resulting from multiple exposures to the beam are highlighted, providing visual evidence for radiation damage.

7.3.2 Proof-of-Concept Experiments: Signal Intensity as a Function of Sample Thickness

7.3.2.1 Phase Identification and Lattice Parameter Determination

Small angle X-ray diffraction analysis of the 50/50 (w/w) monoolein/water samples prepared in capillaries confirmed the presence of a Pn3m cubic phase. Analysis of capillary samples prepared with a monoolein/water mixture of unknown composition resulted in the formation of either an Ia3d cubic phase or a L_α lamellar phase. Identification of the various phases was done based on the location of the observed diffraction rings. Lamellar phases are characterized by a single strong diffraction signal while cubic phases display two main diffraction peaks as well as other smaller peaks at higher values of q-spacing (Figure 7.6).

The location of the various peaks is defined by Bragg's Law where λ is the wavelength of the incident and diffracted radiation, θ corresponds to the diffraction angle, and d is the interplanar spacing for a family of parallel planes in the crystal lattice.

$$\lambda = 2d \sin\theta \tag{7-1}$$

In crystallography the orientation of a particular set of planes is described via Miller indices (hkl) and the interplanar spacing is related to the unit cell dimensions (lattice parameter): The d-spacing of a particular

phase corresponds to the lattice parameter a based on the indices (hkl) of the observed peaks. For a lamellar phase $d = a$, while for a cubic phase:

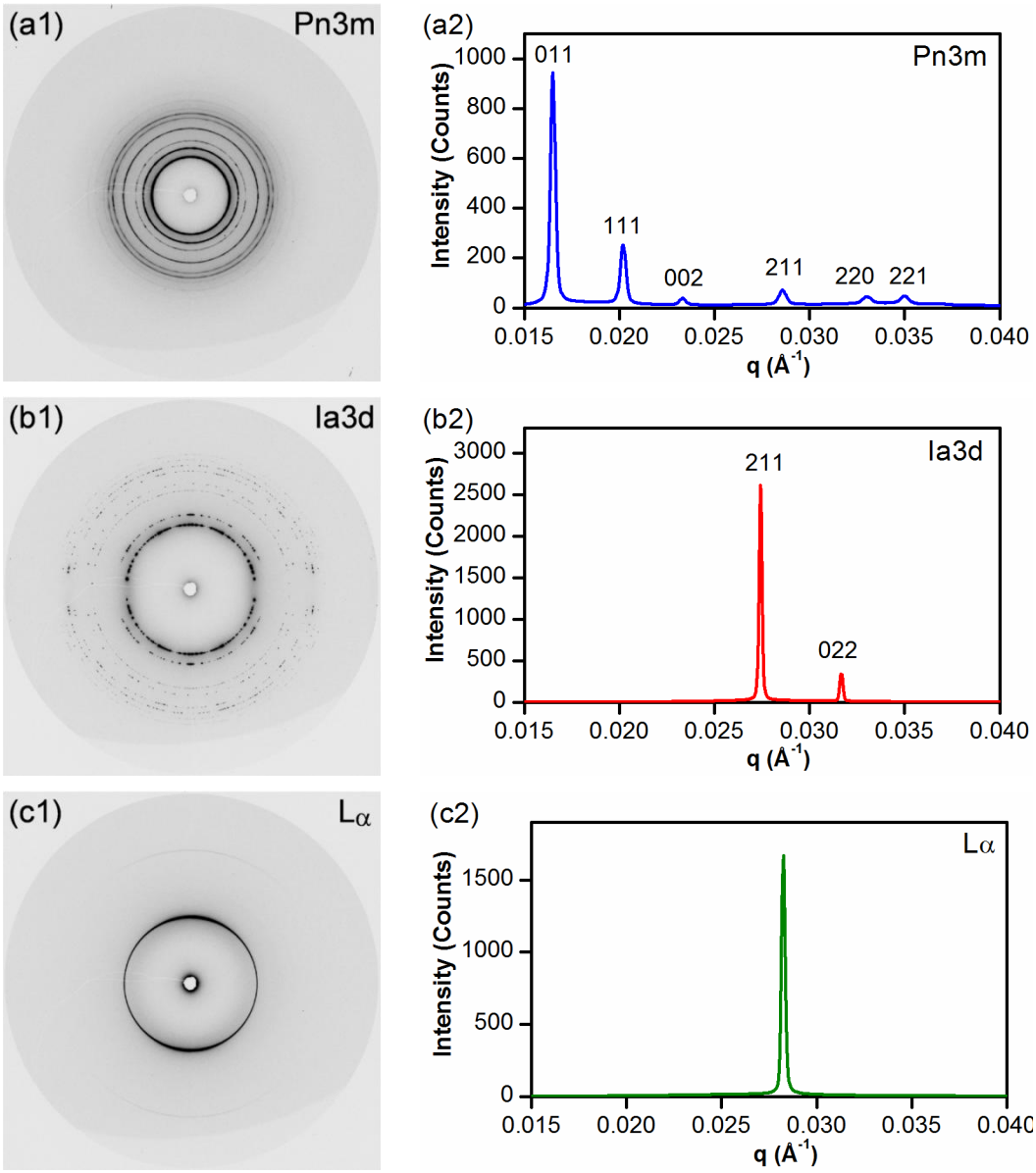

Figure 7.6. Small angle diffraction images collected in 200 µm (nominal thickness) glass capillaries. The diffraction image and the resultant diffractograms are shown for a **(a)** Pn3m cubic phase, **(b)** an Ia3d cubic phase, and **(c)** a L_α lamellar phase. The indices (hkl) of the various peaks observed for the cubic phases are indicated.

$$d = \frac{a}{\sqrt{h^2 + k^2 + l^2}} \tag{7-2}$$

Thus for the (100) peak of the lamellar phase:[70,71]

$$a = d = \frac{\lambda}{2\sin\theta} \tag{7-3}$$

For the (011) peak of the Pn3m cubic phase:[70,71]

$$a = d\sqrt{2} = \frac{\lambda\sqrt{2}}{2\sin\theta} \tag{7-4}$$

For the (211) peak of the Ia3d cubic phase:[70,71]

$$a = d\sqrt{6} = \frac{\lambda\sqrt{6}}{2\sin\theta} \tag{7-5}$$

For small angle diffraction the approximation $\theta = \sin(\theta)$ can be made. Using this approximation in Bragg's Law and substituting Eq. (7-2) gives:

$$\theta \approx \frac{\lambda}{2d} = \frac{\lambda\sqrt{h^2 + k^2 + l^2}}{2a} \tag{7-6}$$

For a Pn3m cubic phase the two main peaks in the diffraction pattern correspond to the (011) and (111) planes. For an Ia3d cubic phase the main peaks correspond to the (211) and (220) planes.[70,71] Thus knowing the indices of these peaks, a comparison of the relative spacing between the two main peak locations can be used to identify the two phases.

$$\frac{\theta_1}{\theta_2} \approx \frac{d_2}{d_1} = \frac{\sqrt{h_1^2 + k_1^2 + l_1^2}}{\sqrt{h_2^2 + k_2^2 + l_2^2}} \tag{7-7}$$

For the Pn3m phase, this ratio corresponds to $\sqrt{3/2} \approx 1.224$ while for an Ia3d phase the ratio is $\sqrt{4/3} \approx 1.157$.

However, the values of 2θ corresponding to the location of the observed diffraction rings varies as a function of wavelength. Therefore it is more common to report diffractograms in terms of q-spacing, where q is related to the momentum transfer between the incident and the scattered wave and is defined as:

$$q = \frac{2\pi}{d} = \frac{4\pi\sin\theta}{\lambda} \tag{7-8}$$

7.3.2.2 The Effects of Signal vs. Sample Thickness in Capillaries

To first examine the feasibility of analyzing thin microfluidic samples, an analysis of the observed signal intensity from the main diffraction peak of various mesophases as a function of sample thickness was performed using traditional capillary mounted samples. Signal was clearly observable over the range of sample thicknesses considered, and trends in both the signal intensity as a function of thickness and as a function of phase identity were observed. The lamellar L_α and the cubic Ia3d phases showed significantly higher intensity for the same sample thickness than did samples containing the cubic Pn3m

phase (Figure 7.7a). It is possible that this difference could be negated by considering the total area of all peaks in the spectrum, though this analysis was not performed.

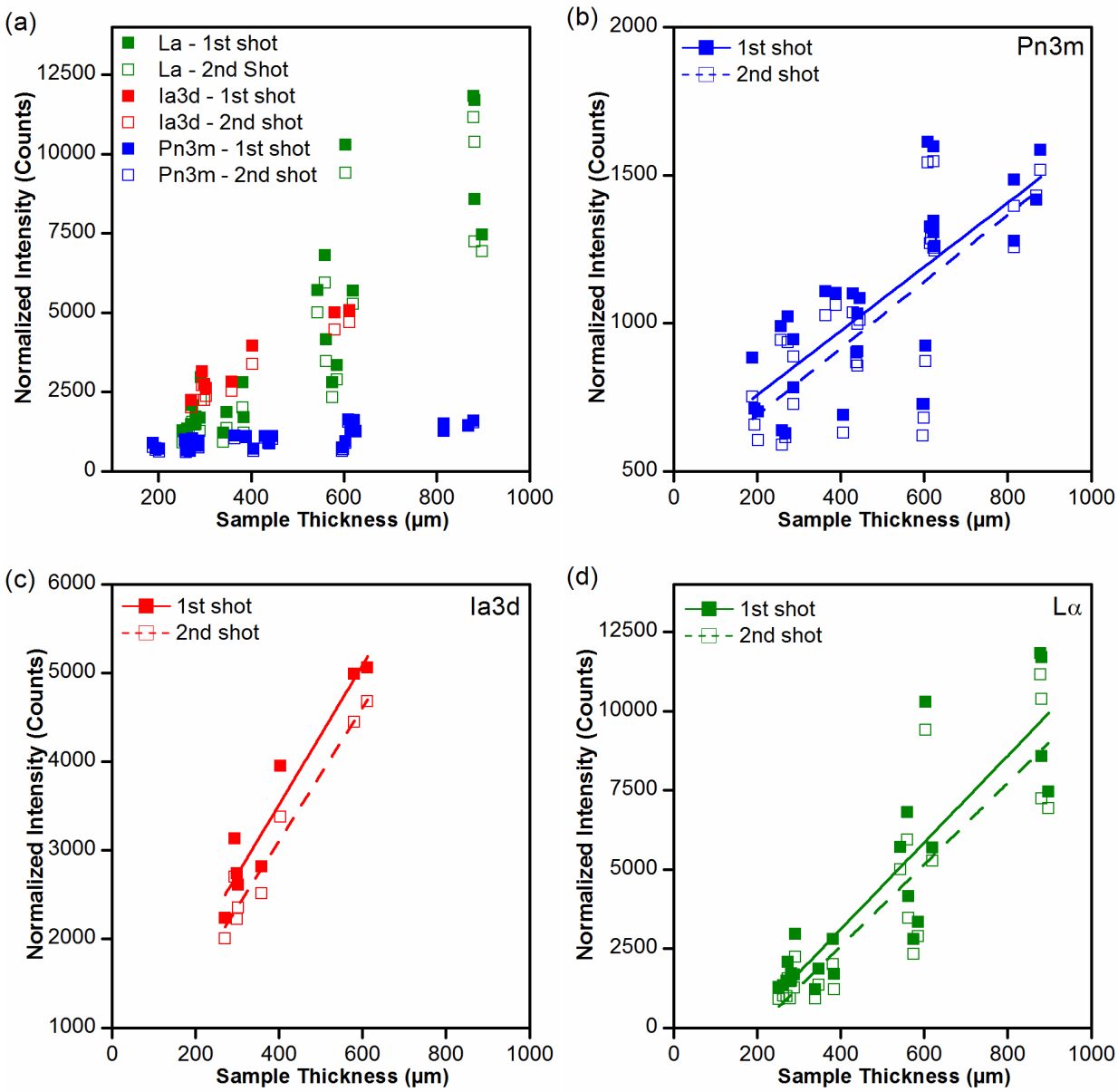

Figure 7.7. Plots of normalized intensity as a function of sample thickness for the diffraction of various mesophases prepared in capillaries. Two exposures of the mesophase were taken of the same location for each sample to investigate the effects of the X-ray beam on the sample, designated "1st shot" and "2nd shot." **(a)** A comparison of data for all three phases. **(b)** Pn3m cubic phase only. **(c)** Ia3d cubic phase only. **(d)** L_α lamellar phase only. Linear curve fits are shown in plots **(b-d)** for the individual phases for each shot.

7.3.2.3 The Impact of Radiation on Mesophase Samples in Capillaries

To investigate the effect of radiation on the samples, a comparison was made between the observed peaks resulting from two frames taken at the same location in quick succession. Both a slight decrease in intensity and a shift in the peak location were observed. The decrease in peak intensity can be clearly seen in Figure 7.7, both from the raw data and from the plotted trendlines. However, the total area under

the peak was estimated to remain the same by summing the intensities over a given range. These observations correspond to broadening of the observed diffraction peaks and could be evidence of radiation damage.[72] The shift in peak location translates to a slight decrease in the lattice parameter of the various phases (0.1 Å – 0.3 Å). These observations suggest that sample heating occurs as a result of X-ray exposure as the lattice parameter is known to decrease upon heating.[33]

7.3.2.4 The Effects of Signal vs. Sample Thickness in Test Structures

While experiments in traditional glass capillaries provided a useful baseline with which measurements could be compared, the length scale of microfluidics is an order of magnitude smaller than typical X-ray capillaries. Additionally, the high silicon content in the walls of glass capillaries might be expected to contribute significantly to signal attenuation for very thin samples. In order to circumvent these challenges, a test structure was fabricated using thin sheets of COC similar to what would be present in an actual microfluidic device. Adhesive spacers of varying thicknesses were then used to define wells in the range of 25 µm to 100 µm (Figure 7.3b – inset 1).

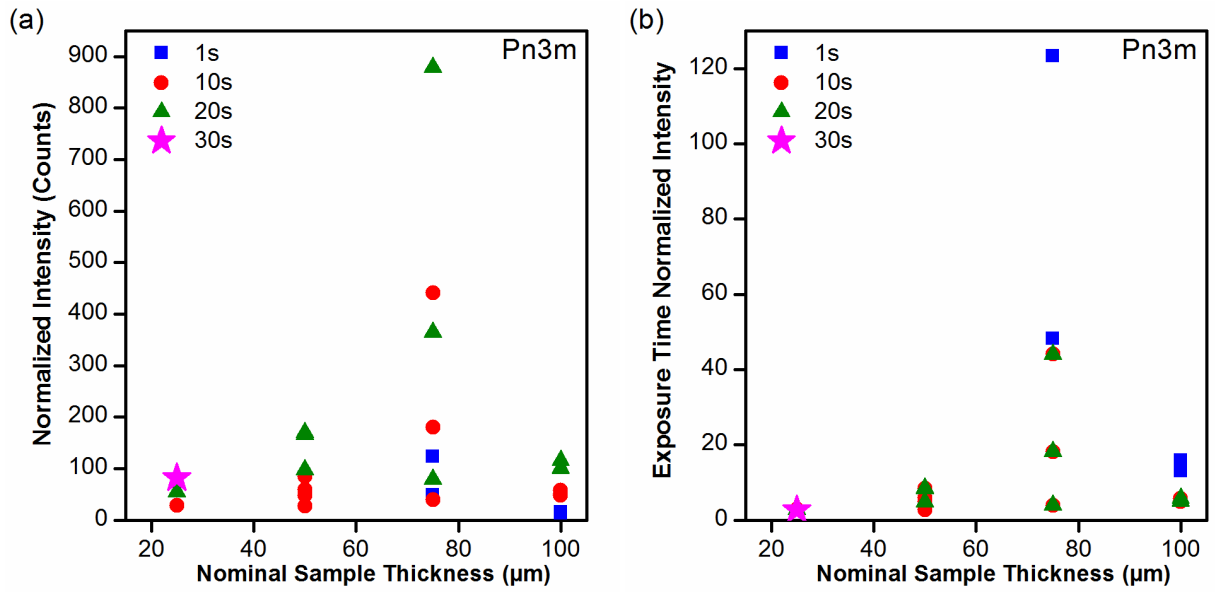

Figure 7.8. Plot of **(a)** baseline-normalized intensity and **(b)** exposure time-normalized intensity as a function of sample thickness and different exposure times for the diffraction of a Pn3m cubic phase in proof-of-concept test structures.

For these test-structures, reasonable signal was observed over the range of sample thicknesses and exposure times considered (Figure 7.8a). However, there was not an easily distinguishable trend in the data. Excepting the data points at 100 µm, the data could be fit reasonably well with an exponential curve. However, all of the data taken at 100 µm clearly shows a deviation from the trend. It is possible that this deviation comes from variations in the physical dimensions (other than thickness) of the device. Because the samples were rotated 360° during the course of data collection, a larger device could attenuate the signal more and artificially lower the observed signal.

Another observation from the data is that the signal intensity varies linearly with exposure time (Figure 7.8b). Thus it is possible to normalize the observed signal intensity by the exposure time. However, the effects of exposure to the X-ray beam as a function of sample thickness are not known. While it is not clear at this point where or how experimental variation has affected these results, these experiments have validated the potential for collecting small angle X-ray diffraction data on mesophases at microfluidic path lengths. At the shortest path length of 25 µm, the observed signal was significantly above the baseline over a range of exposure times.

7.3.3 Design of Microfluidic Chips for Phase Diagram Determination

In designing microfluidic chips to explore aqueous/lipid phase behavior, the simplest system to consider would be that of a binary mixture. To map out a phase diagram for a two component system it is merely necessary to vary the concentration of the two species across an integrated microfluidic chip based on the volume of the various microfluidic compartments (Figure 7.9). The arrangement of compartments on this chip was designed around the lipid mixing unit described in Chapter 4. The preparation of a large number of compositional samples in parallel would enhance the rate at which these experiments could be performed. In order to map out both the effects of concentration and temperature it would be necessary to either use a temperature-controlled sample holder, or to integrate heating/cooling elements onto the chip itself.

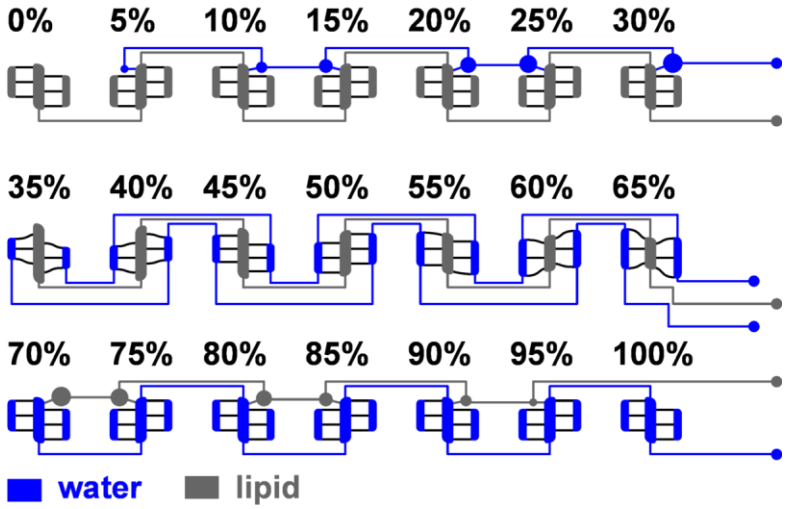

Figure 7.9. Schematic depiction of the fluid layer for a microfluidic array chip for the screening of a binary lipid/water mixture. Lipid and water are filled into the device through the specified lines. For systems with either a low water or lipid content and injection of the contents of the small outer chamber would precede mixing within the three main chambers.

Exploring the effect of a particular contaminant would most likely be performed at a particular lipid content or hydration level. For instance, the chip shown in Figure 7.10 was designed to test the effect of a particular contaminant in a mesophase that is 50/50 (v/v) aqueous phase/lipid. This chip takes advantage of not only the parallel processing capabilities of microfluidics, but also the ability to generate solutions of known concentration on-chip. During filling, this chip is designed first to flow lipid into the

center chambers of each mixing unit. A diluent solution such as water or buffer is then metered into the circular blue wells. A valve located over each of these diluent chambers is then used to meter this volumetrically defined quantity of liquid into the side chamber of the mixer. Following a rinsing step, the side chambers are then filled the rest of the way with a solution of concentrated additive. The previously metered diluent thus creates a variation in the concentration of the additive from the stock solution (100%), to one half of this concentration. The design could be altered or expanded to change this range.

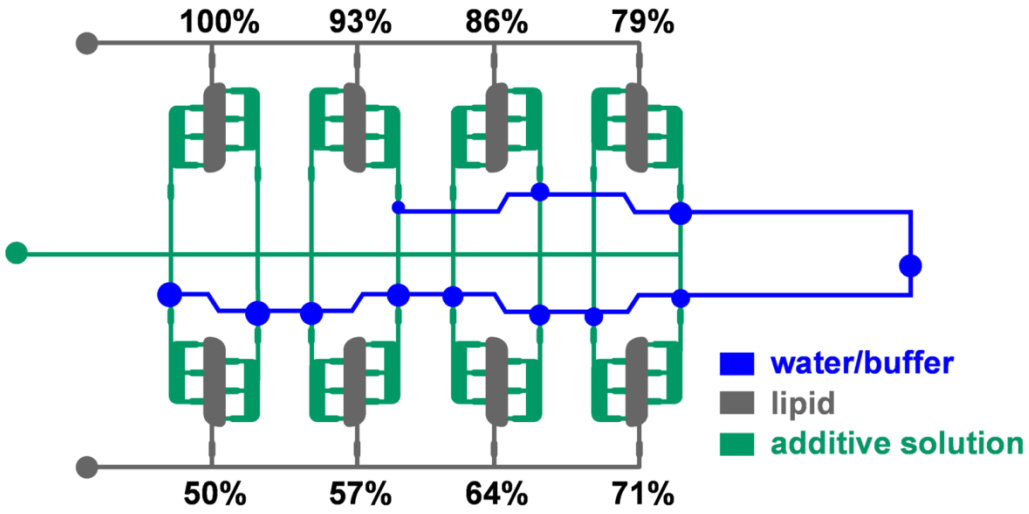

Figure 7.10. Schematic depiction of the fluid layer for a microfluidic array chip for the screening of contaminant effects on a 50/50 (v/v) mixture of lipid and aqueous phase. Lipid is metered into the center chambers. The aqueous phase is metered first by the filling of the blue line with water or buffer. Actuation of valves over the circular chambers depicted meters a specified volume of water or buffer into the side chamber. After rinsing of this line, the side chambers are filled with a concentrated solution of the additive of interest. The buffer metered into the side chamber previously serves to dilute the concentrated solution by the amount indicated.

7.3.4 Validation of Platform by *In Situ* Analysis of Phase Behavior

While proof-of-concept experiments with test structures were able to demonstrate the potential for data collection in a microfluidic device, it was important to extend this work to an actual device. For simplicity, and to allow for direct comparison with a known sample, various mesophases were prepared using a traditional syringe mixer. The mesophases were loaded into both traditional capillaries and a series of X-ray transparent PDMS/COC microfluidic devices (Figure 7.5). Both of these samples were stored at -12°C, both to eliminate metastable phase behavior, and for improved stability during storage.

One of the concerns related to preparing and analyzing mesophase samples on-chip is the potential for evaporation and solvent loss. As was discussed in Chapter 5, the PDMS/COC hybrid device architecture provides significantly lower evaporative losses than traditional PDMS devices. However, the loss of even small amounts of water could produce a significant change in the observed phase behavior of a sample, particularly for water poor samples. To test this, a sample containing a 0.033 (w/w) mixture of monoolein and β-octylglucoside combined in a 90/10 (w/w) ratio with 1.3M KH_2PO_4 pH 5.5 was prepared. Because of the low water content, this mixture was expected to form a L_α lamellar phase. Analysis of small angle diffraction from both traditional capillaries and samples loaded into PDMS/COC

microfluidic devices confirms the lamellar nature of this phase (Figure 7.11). The average lattice parameter calculated for both the capillary samples and measurements taken on-chip was 37.5 Å. Although the lattice parameter of lamellar phases can be moderately insensitive to changes in hydration, these values validate the capability of this PDMS/COC X-ray transparent device architecture to deal with mesophase samples with a very low water content.

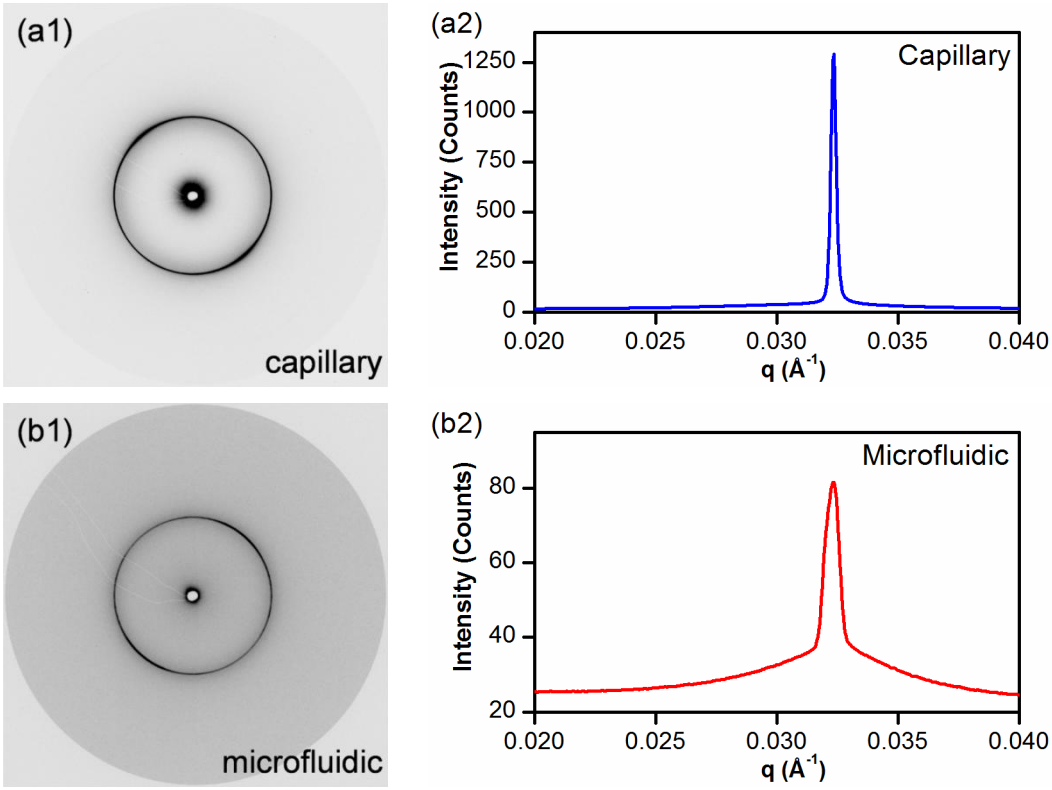

Figure 7.11. Small angle diffraction images and diffractograms of a sample containing a 0.033 (w/w) mixture of monoolein and β-octylglucoside combined in a 90/10 (w/w) ratio with 1.3M KH_2PO_4 pH 5.5 collected in **(a)** a glass X-ray capillary and **(b)** a PDMS/COC X-ray transparent microfluidic device.

While the use of a lamellar phase allowed for compatibility testing of the PDMS/COC device with low water content samples, the diffraction from lamellar phases is relatively strong and it would be interesting to also observe a cubic phase on chip. To accomplish this, a hydrating solution of 1.3M KH_2PO_4 pH 5.5 was injected into a chip that was originally loaded with a lamellar phase and allowed to equilibrate. As discussed in Chapter 2, the use of a concentrated salt solution helps to stabilize the formation of a cubic phase, and the injection of this solution enabled the recovery of a cubic phase from the initially lamellar sample.

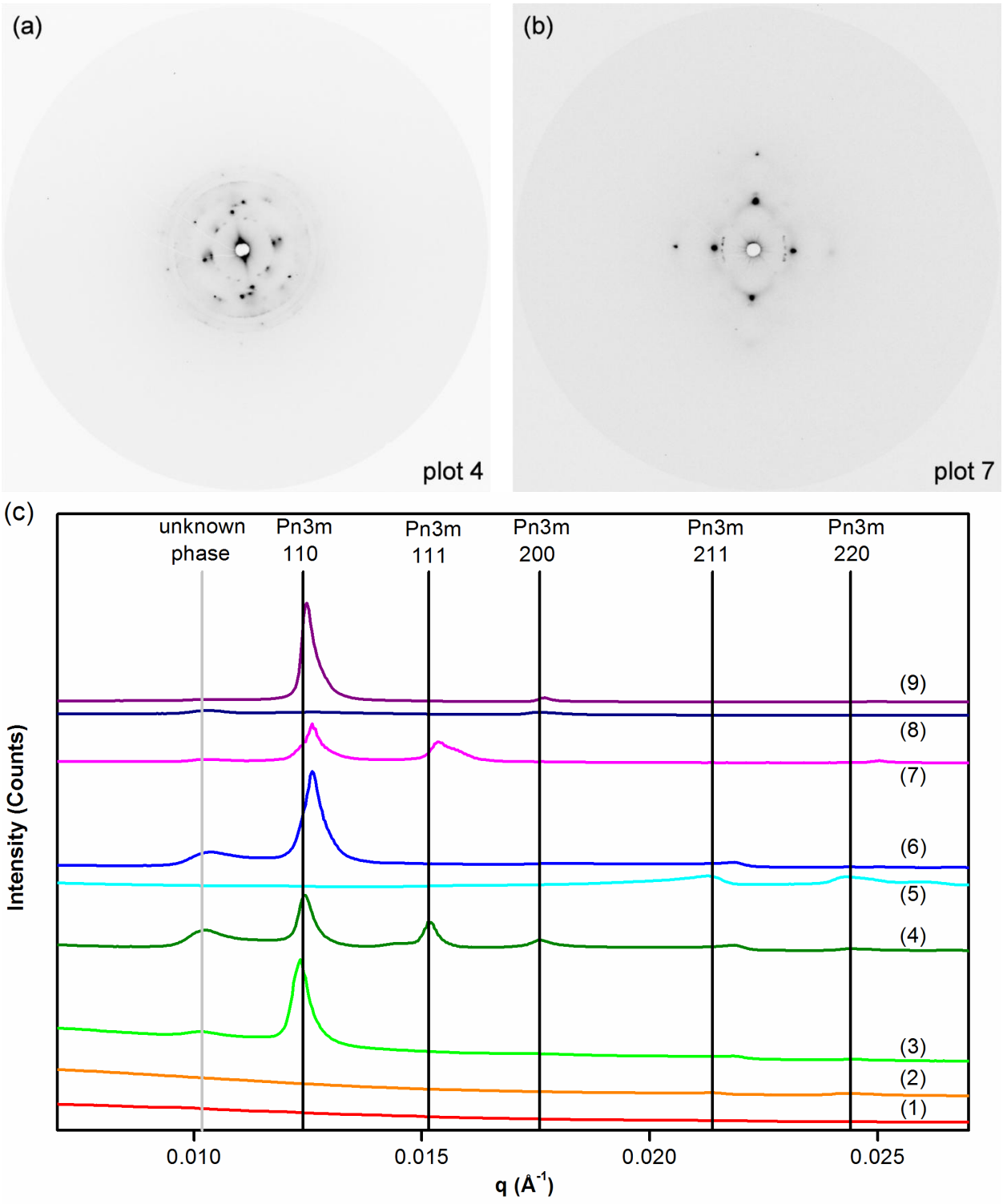

Figure 7.12. **(a-b)** Small angle diffraction images from different points in a hydrated crystalline cubic phase in a PDMS/COC X-ray transparent microfluidic device. Images correspond to traces (4) and (7). **(c)** Diffractograms from various different points in the hydrated crystalline cubic phase. Depending on location, different diffraction planes (hkl) for the same cubic phase are observed. Vertical lines serve as a guide for the eye, defining the various peaks and their corresponding (hkl) values. Traces (1 – 6) were taken with a 5s exposure, (7 – 9) with a 1s exposure.

One particularly interesting aspect of the observed cubic phase was that instead of obtaining a powder diffraction ring, single crystal diffraction spots were seen (Figure 7.12a-b). An analysis of diffraction data collected at different points throughout the device displayed both a peak corresponding to an unknown phase at low values of 2θ, but also different (hkl) reflections corresponding the same Pn3m cubic phase (Figure 7.12c). In this sense, collecting data at multiple points in a crystalline mesophase could be treated similarly to collecting "single-shot" data on multiple crystals as in Chapters 5 and 6. However, rotation of the sample during data collection would help to restore the observed powder diffraction patterns and could assist in unambiguously identifying phases.

7.3.4.1 The Effect of the X-ray Beam on Microfluidic Mesophase Samples

In Section 7.3.2.1 the X-ray beam was shown to have a significant effect on capillary-mounted samples. Another aspect of *in situ* X-ray analysis of mesophase behavior in microfluidic chips is the potential for radiation damage and/or local heating to have an adverse effect on the very thin sample. As seen in Figure 7.5b, the X-ray beam produced a visual change in the sample, however it was unclear from these observations how the visual change in the sample corresponded to the actual identity and lattice parameter of the mesophase.

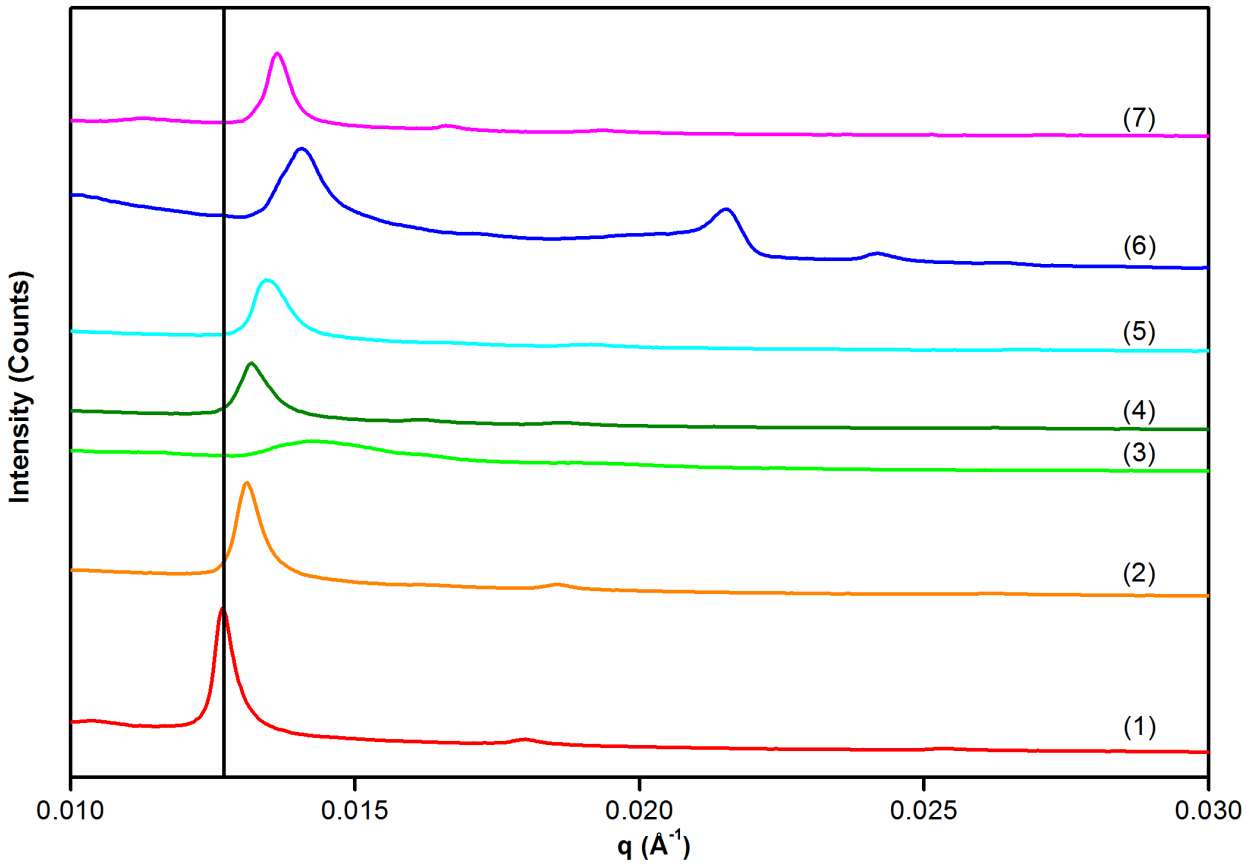

Figure 7.13. Plot (offset) of diffractograms for multiple exposures of the same location on a microfluidic device, labeled (1) to (7). From the initial diffractogram (1), continued exposure to the X-ray beam results in both the broadening of the diffraction signal and also a shift to higher values of q. However, if the sample is allowed to cool, the location of the peak upon subsequent testing shifts back to lower values of q (curve 7). A vertical line is drawn as a guide to the eye for the locations of the various peaks in comparison to the initial diffractogram.

To investigate the effects of prolonged exposure to the X-ray beam on the sample a series of frames were taken in the same location (Figure 7.13) with approximately 30 s intervals except frames #6 and #7 that were taken with a 7 minute interval.. Starting from the initial image (1), continued exposure to the X-ray beam produces two effects: (i) a broadening of the diffraction peak and (ii) a shift in the peak location to higher values of q. As discussed in Section 7.3.2.1, peak broadening has been reported in the literature as evidence for radiation damage in mesophase samples,[72] although these effects appear to be somewhat reversible. The shift in the peak location indicates a decrease in the lattice parameter of the phase, and could easily be the result of heating due to the X-ray beam. The idea of local heating is supported by the reversibility of this peak shift if the sample is allowed to cool for a time between exposures (6) and (7).

The sensitivity of these very thin microfluidic mesophase samples is a potential challenge for *in situ* analysis, particularly because without a standard for comparison, there is no way of knowing if the first observation is actually an accurate representation of the original phase. However, a straightforward method for decreasing the sensitivity of these samples would be to simply increase the height of the device features.

7.4 Conclusions

In summary, the X-ray transparent microfluidic device architecture applied in Chapters 5 and 6 for protein crystallography has been validated for use in small angle X-ray diffraction studies for the determination of the phase behavior of aqueous/lipid systems. Studies of the observed signal intensity from samples of varying thickness validated the possibility of *in situ* data collection from microfluidic chambers as thin as 10 μm, though several issues related to X-ray irradiation were identified and should be studied further.

Understanding these mesophase systems is critical for the development of a rational understanding of the *in meso* crystallization method, however studies of phase behavior are tremendously sample intensive. The integrated microfluidic platforms discussed here have the potential to streamline the preparation and analysis of samples by utilizing nanoliter-scale preparation of multiple samples in parallel followed by *in situ* analysis of the resultant phase behavior.

7.5 Acknowledgements

This work was funded by NIH (R01 GM086727) and a NIH Kirschstein Predoctoral Fellowship from the National Institute of Biomedical Imaging and Bioengineering (F31 EB008330). Use of the Advanced Photon Source was supported by the U. S. Department of Energy, Office of Science, Office of Basic Energy Sciences, under Contract No. DE-AC02-06CH11357. Use of the LS-CAT Sector 21 was supported by the Michigan Economic Development Corporation and the Michigan Technology Tri-Corridor for the support of this research program (Grant 085P1000817).

The collaborative efforts of the Life Sciences Collaborative Access Team (LS-CAT) at the Advanced Photon Source at Argonne National Laboratory, and in particular Dr. Elena Kondrashkina helped to make this work possible. Also, Daria Khvostichenko was invaluable in her assistance in the study of lipidic phase behavior and Sudipto Guha was invaluable in his assistance with the development and testing of X-ray transparent microfluidic chips.

7.6 References

(1) Bonacucina, G.; Palmieri, G. F.; Craig, D. Q. M. *J Pharm Sci-Us* **2005**, *94*, 2452.

(2) Mezzenga, R.; Meyer, C.; Servais, C.; Romoscanu, A. I.; Sagalowicz, L.; Hayward, R. C. *Langmuir* **2005**, *21*, 3322.

(3) Caffrey, M. *Ann Rev Biophys* **2009**, *38*, 29.

(4) Perry, S. L.; Roberts, G. W.; Tice, J. D.; Gennis, R. B.; Kenis, P. J. A. *Cryst Growth Des* **2009**, *9*, 2566.

(5) Nollert, P. *Methods* **2004**, *34*, 348.

(6) Persson, G.; Edlund, H.; Amenitsch, H.; Laggner, P.; Lindblom, G. *Langmuir* **2003**, *19*, 5813.

(7) Persson, G.; Edlund, H.; Lindblom, G. *European Journal of Biochemistry* **2003**, *270*, 56.

(8) Sparr, E.; Wadsten, P.; Kocherbitov, V.; Engstrom, S. *Bba-Biomembranes* **2004**, *1665*, 156.

(9) Vargas, R.; Mateu, L.; Romero, A. *Chem Phys Lipids* **2004**, *127*, 103.

(10) Takahashi, H.; Matsuo, A.; Hatta, I. *Phys Chem Chem Phys* **2002**, *4*, 2365.

(11) Takahashi, H.; Matsuo, A.; Hatta, I. *Mol Cryst Liq Cryst* **2000**, *347*, 475.

(12) Awad, T. S.; Okamoto, Y.; Masum, S. M.; Yamazaki, M. *Langmuir* **2005**, *21*, 11556.

(13) Caboi, F.; Nylander, T.; Razumas, V.; Talaikyte, Z.; Monduzzi, M.; Larsson, K. *Langmuir* **1997**, *13*, 5476.

(14) Engblom, J.; Miezis, Y.; Nylander, T.; Razumas, V.; Larsson, K. In *Surface and Colloid Science*; Springer: Berlin / Heidelberg, 2000; Vol. 116, p 9.

(15) Engström, S.; Alfons, K.; Rasmusson, M.; Ljusberg-Wahren, H. *Progress in Colloid and Polymer Science* **1998**, *108*, 93.

(16) Li, S. J.; Yamashita, Y.; Yamazaki, M. *Biophys J* **2001**, *81*, 983.

(17) Masum, S. M.; Li, S. J.; Awad, T. S.; Yamazaki, M. *Langmuir* **2005**, *21*, 5290.

(18) Murgia, S.; Lampis, S.; Angius, R.; Berti, D.; Monduzzi, M. *The Journal of Physical Chemistry B* **2009**, *113*, 9205.

(19) Okamoto, Y.; Masum, S. M.; Miyazawa, H.; Yamazaki, M. *Langmuir* **2008**, *24*, 3400.

(20) Razumas, V.; Larsson, K.; Miezis, Y.; Nylander, T. *J Phys Chem-Us* **1996**, *100*, 11766.

(21) Razumas, V.; Talaikyte, Z.; Barauskas, J.; Larsson, K.; Miezis, Y.; Nylander, T. *Chem Phys Lipids* **1996**, *84*, 123.

(22) Caffrey, M. *Biochemistry-Us* **1987**, *26*, 6349.

(23) Cherezov, V.; Caffrey, M. *J Appl Crystallogr* **2005**, *38*, 398.

(24) Caffrey, M.; Cherezov, V. **2009**, *4*, 706.

(25) Cheng, A. H.; Hummel, B.; Qiu, H.; Caffrey, M. *Chem Phys Lipids* **1998**, *95*, 11.

(26) Misquitta, Y.; Caffrey, M. *Biophys J* **2003**, *85*, 3084.

(27) Ai, X.; Caffrey, M. *Biophys J* **2000**, *79*, 394.

(28) Cherezov, V.; Fersi, H.; Caffrey, M. *Biophys J* **2001**, *81*, 225.

(29) Boyle-Roden, E.; Hoefer, N.; Dey, K. K.; Grandinetti, P. J.; Caffrey, M. *J Magn Reson* **2007**, *189*, 13.

(30) Cherezov, V.; Clogston, J.; Misquitta, Y.; Abdel-Gawad, W.; Caffrey, M. *Biophys J* **2002**, *83*, 3393.

(31) Liu, W.; Caffrey, M. *Journal of Structural Biology* **2005**, *150*, 23.

(32) Qiu, H.; Caffrey, M. *Biomaterials* **2000**, *21*, 223.

(33) Briggs, J.; Chung, H.; Caffrey, M. *J Phys Ii* **1996**, *6*, 723.

(34) Briggs, J.; Caffrey, M. *Biophys J* **1994**, *66*, 573.

(35) Misquitta, Y.; Caffrey, M. *Biophys J* **2001**, *81*, 1047.

(36) Misquitta, Y.; Cherezov, V.; Havas, F.; Patterson, S.; Mohan, J. M.; Wells, A. J.; Hart, D. J.; Caffrey, M. *Journal of Structural Biology* **2004**, *148*, 169.

(37) Misquitta, L. V.; Misquitta, Y.; Cherezov, V.; Slattery, O.; Mohan, J. M.; Hart, D.; Zhalnina, M.; Cramer, W. A.; Caffrey, M. *Structure* **2004**, *12*, 2113.

(38) Caffrey, M.; Cheng, A. *Current Opinion in Structural Biology* **1995**, *5*, 548.

(39) Caffrey, M. *Current Opinion in Structural Biology* **2000**, *10*, 486.

(40) Caffrey, M. *Journal of Structural Biology* **2003**, *142*, 108.

(41) Caffrey, M. *Cryst Growth Des* **2008**, *8*, 4244.

(42) Grabe, M.; Neu, J.; Oster, G.; Nollert, P. *Biophys J* **2003**, *84*, 854.

(43) Cherezov, V.; Caffrey, M. *Faraday Discussions* **2007**, *136*, 195.

(44) Nollert, P.; Qiu, H.; Caffrey, M.; Rosenbusch, J. P.; Landau, E. M. *Febs Lett* **2001**, *504*, 179.

(45) Sennoga, C.; Heron, A.; Seddon, J. M.; Templer, R. H.; Hankamer, B. *Acta Crystallogr D* **2003**, *59*, 239.

(46) Qutub, Y.; Reviakine, I.; Maxwell, C.; Navarro, J.; Landau, E. M.; Vekilov, P. G. *J Mol Biol* **2004**, *343*, 1243.

(47) Cherezov, V.; Rosenbaum, D. M.; Hanson, M. A.; Rasmussen, S. G. F.; Thian, F. S.; Kobilka, T. S.; Choi, H. J.; Kuhn, P.; Weis, W. I.; Kobilka, B. K.; Stevens, R. C. *Science* **2007**, *318*, 1258.

(48) Kors, C. A.; Wallace, E.; Davies, D. R.; Li, L.; Laible, P. D.; Nollert, P. *Acta Crystallographica Section D* **2009**, *65*, 1062.

(49) Saturni, L.; Rustichelli, F.; Di Gregorio, G. M.; Cordone, L.; Mariani, P. *Phys Rev E* **2001**, *6404*.

(50) Bitan-Cherbakovsky, L.; Yuli-Amar, I.; Aserin, A.; Garti, N. *Langmuir* **2009**.

(51) Clogston, J.; Caffrey, M. *J Control Release* **2005**, *107*, 97.

(52) Yaghmur, A.; Kriechbaum, M.; Amenitsch, H.; Steinhart, M.; Laggner, P.; Rappolt, M. *Langmuir* **2010**, *26*, 1177.

(53) Hunte, C.; Richers, S. *Current Opinion in Structural Biology* **2008**, *18*, 406.

(54) Chiu, M. L.; Nollert, P.; Loewen, M. C.; Belrhali, H.; Pebay-Peyroula, E.; Rosenbusch, J. P.; Landau, E. M. *Acta Crystallogr D* **2000**, *56*, 781.

(55) Johansson, L. C.; Wöhri, A. B.; Katona, G.; Engström, S.; Neutze, R. *Current Opinion in Structural Biology* **2009**, *19*, 372.

(56) Liu, W.; Hanson, M. A.; Stevens, R. C.; Cherezov, V. *Biophys J* **2010**, *98*, 1539.

(57) Nollert, P.; Royant, A.; Pebay-Peyroula, E.; Landau, E. M. *Febs Lett* **1999**, *457*, 205.

(58) Nollert, P.; Navarro, J.; Landau, E. M. *Method Enzymol* **2002**, *343*, 183.

(59) Rouhani, S.; Facciotti, M. T.; Woodcock, G.; Cheung, V.; Cunningham, C.; Nguyen, D.; Rad, B.; Lunde, C. S.; Glaeser, R. M. *Biopolymers* **2002**, *66*, 300.

(60) Rummel, G.; Hardmeyer, A.; Widmer, C.; Chiu, M. L.; Nollert, P.; Locher, K. P.; Pedruzzi, I.; Landau, E. M.; Rosenbusch, J. P. *Journal of Structural Biology* **1998**, *121*, 82.

(61) Wadsten, P.; Wo?hri, A. B.; Snijder, A.; Katona, G.; Gardiner, A. T.; Cogdell, R. J.; Neutze, R.; Engström, S. *J Mol Biol* **2006**, *364*, 44.

(62) Wöhri, A. B.; Johansson, L. C.; Wadsten-Hindrichsen, P.; Wahlgren, W. Y.; Fischer, G.; Horsefield, R.; Katona, G.; Nyblom, M.; Öberg, F.; Young, G.; Cogdell, R. J.; Fraser, N. J.; Engström, S.; Neutze, R. *Structure* **2008**, *16*, 1003.

(63) Kissick, D. J.; Gualtieri, E. J.; Simpson, G. J.; Cherezov, V. *Anal Chem* **2009**, *82*, 491.
(64) Katona, G.; Andreasson, U.; Landau, E. M.; Andreasson, L.-E.; Neutze, R. *J Mol Biol* **2003**, *331*, 681.
(65) Porcar, L.; Hamilton, W. A.; Butler, P. D. *Langmuir* **2003**, *19*, 10779.
(66) Life Sciences Collaborative Access Team (LS-CAT). http://ls-cat.org/
(67) Huang, T. C.; Toraya, H.; Blanton, T. N.; Wu, Y. *J Appl Crystallogr* **1993**, *26*, 180.
(68) Hammersley, A. P. *FIT2D: An Introduction and Overview*, 1997.
(69) 7.6.0.234 ed.; Mathworks Inc.: Natick, MA, 2008.
(70) Larsson, K. *Nature* **1983**, *304*, 664.
(71) International Tables for Crystallography. http://it.iucr.org/ (August 4, 2010).
(72) Cherezov, V.; Riedl, K. M.; Caffrey, M. *J Synchrotron Radiat* **2002**, *9*, 333.

Chapter 8

Summary of Accomplishments and Future Directions

8.1 Introduction

The development of microfluidic platforms for a variety of applications including protein crystallization has increased dramatically in the last decade. These platforms take advantage of not only decreases in volume at the microscale, but also enhancements in the level of control over fluid handling, concentrations, and local gradients. However, the efficacy of these platforms is limited without the potential for performing analysis on-chip. The work presented in the previous chapters represents significant advancements in the field of microfluidics for protein crystallization and *in situ* X-ray analysis. Challenges associated with the mixing of highly viscous and non-Newtonian fluids were overcome, and an X-ray transparent device architecture was developed which enabled both protein crystallography and small angle X-ray studies of lipidic mesophases.

8.2 Microfluidic Platforms for Protein Crystallization

8.2.1 Microfluidic Platforms for the Crystallization of Solubilized Proteins

During the course of developing an X-ray transparent device architecture for protein crystallography, a series of array chips utilizing actuate-to-open valves were designed. These chips have tremendous potential for the screening and optimization of crystallization conditions for both soluble proteins and detergent solubilized membrane proteins, and should be applied in structural biology efforts on novel protein targets. Collaborative efforts with the Gennis and Nair labs at the University of Illinois for the crystallization of various heme-copper oxidases and other novel proteins using these X-ray transparent chips are ongoing at this time (Nov 2010).

The various 24- and 96-well array chips reported in Chapters 5 and 6 were fabricated for various different applications and the total number of wells per chip in these designs did not necessarily reflect the actual number of crystallization conditions which were screened per device. For crystallography experiments where the goal is to analyze a large number of crystals on chip a large array of identical wells is desirable. However, for crystallization screening efforts a chip design such as the one reported in Chapter 5 in which the volumetric ratios of protein and precipitant solution are varied for a given condition are more useful. A powerful aspect of microfluidics is the ease whereby modifications can be made to an

existing design to enhance its efficacy or tailor it to a specific application. For instance, using microfluidics one has the ability to generate solutions of a desired composition on chip. For the optimization of screening conditions, the automated generation of a concentration grid would improve the efficiency associated with the use of a microfluidic platform. For instance, coupling a gradient-tree[1,2] with an array chip could have significant utility for optimization trials.

8.2.2 Microfluidic Platforms for the *In Meso* Crystallization of Membrane Proteins

The development of microfluidic platforms capable of preparing *in meso* crystallization trials was a significant advancement. However, in order to further advance this technology to the stage where it could be used for crystallization trials with novel proteins it is necessary to optimize the design in a scaled out array chip format.

In addition to these efforts, the effect of a microfluidic geometry on a protein crystallization trial has not been fully investigated. It has been suggested in the literature that the geometry of the interaction between a mesophase bolus and the precipitant solution can have a significant impact on the crystallization trial,[3] but this hypothesis remains to be tested. The effects of geometry, however, could be particularly significant in very thin microfluidic chambers where relatively long lateral diffusion distances exist. This chamber geometry should be optimized for the growth of a few large crystals, rather than potentially favoring the nucleation of a large number of small crystals due to long diffusion distances.

The ability to prepare a large number of samples with varying compositions also has tremendous potential to open up new variables for crystallization screening efforts. The nanoliter preparative scale of these crystallization platforms can easily be applied to the preparation of *in meso* crystallization trials with varying concentrations of protein and lipid, or combinations of different lipids. While the role of the lipid during *in meso* crystallization has not been explored extensively, studies using different monoacylglycerols for the formation of the lipidic mesophase for crystallization have clearly demonstrated the significance of lipidic composition as a variable.[4-8]

The preparation of lipidic mesophases on-chip can also be utilized for mechanistic studies of how *in meso* crystallization occurs. For instance, *in meso* crystallization is thought to involve a local phase change from a cubic to a lamellar phase where crystal nucleation takes place.[3,9-16] Crystal growth is then thought to occur via a lamellar conduit connecting the bulk cubic phase and the growing crystal.[3,5,8,10,11,14,16-19] Microfluidic mixers could be used to prepare two different mesophase samples, one containing protein and the other without. Bringing these two mesophases into contact, fluorescence microscopy could then be used to track the gradient diffusion of the embedded membrane proteins over time (Figure 8.1). Coupling this knowledge with information about the identity and curvature of the various mesophases could then be used to facilitate the rational design of *in meso* crystallization experiments. This work is continuing in the group through the efforts of Daria Khvostichenko.

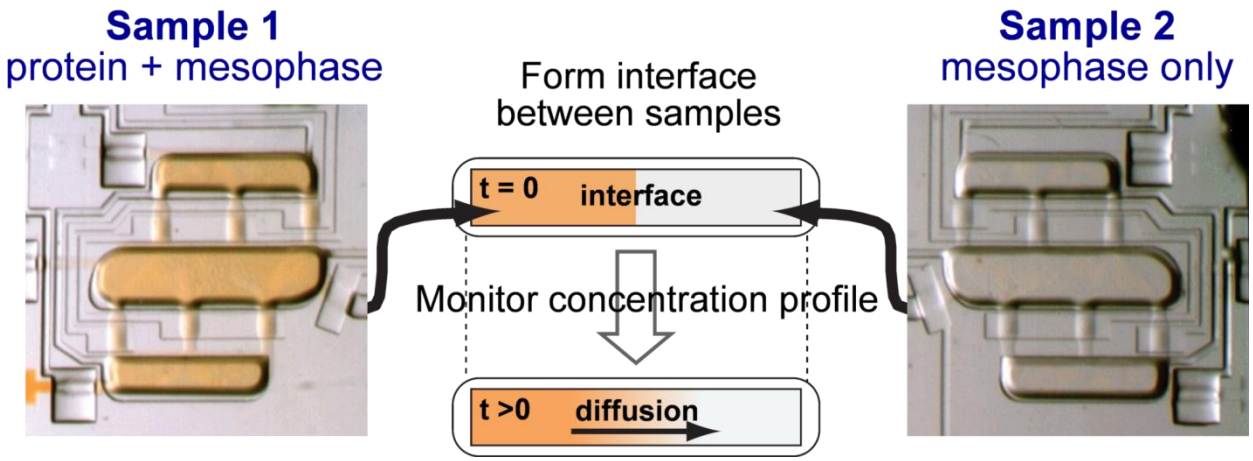

Figure 8.1. Schematic depiction of two coupled lipidic mixers for use in studying the diffusion of reconstituted membrane proteins between various lipidic mesophases. Figure contributed by Daria Khvostichenko.

8.3 X-ray Transparent Microfluidic Devices for *In Situ* Protein Crystallography

While the ability to grow protein crystals in a microfluidic environment has inherent benefits, coupling of *in situ* analysis methods with microfluidic platforms has the potential to side-step many challenges associated with crystal handling and damage. However, the integration of these devices with current X-ray beamline setups is still a challenge. Depending upon the experiment it will be necessary to tailor not only the architecture and geometry of the microfluidic device, but also the method for mounting this device for *in situ* analysis and the surrounding experimental setup.

8.3.1 Microfluidic Platforms for Crystal Quality Screening and Structure Determination

The results presented in Chapter 5 demonstrated a variety of device geometries for protein crystallization and validated a series of *in situ* data collection strategies ranging from the analysis of a few frames of diffraction data to extract information on crystal quality to the collection of an entire dataset from a single crystal under cryogenic conditions or by combining diffraction data from numerous crystals. However, these experiments were performed using model proteins such as lysozyme, thaumatin, and ribonuclease A. The challenge remains to apply these methods to both novel soluble and membrane protein targets to truly evaluate the quality of diffraction data which can be collected from a more challenging system.

8.3.2 Microfluidic Platforms for Laue Crystallography

The potential applications for microfluidic crystallization platforms with *in situ* analysis capabilities in the field of Laue crystallography and time resolved structural studies are tremendous and could have a significant impact on the field. The work presented in Chapter 6 validated the microfluidic device architecture for performing Laue crystallography and demonstrated several data collection strategies for static structure determination. However, the next logical step in this area is to extend this work to include time resolved and dynamic crystallography studies.

A variety of studies in the field of time resolved and dynamic crystallography can be envisioned, including photo-activated structural studies, dynamic studies of the effects of an environmental change such as pH, temperature, or an applied electric field, and also ligand binding studies. For each of these studies developments in the device architecture and/or capabilities can be made alongside structural biology efforts. For instance, during time resolved studies where laser light is used to trigger a structural change, a method for preventing the scattered light from the triggering of one crystal from affecting other crystals within the device would be critical for the success of the experiment. Ligand binding or pH studies would require the validation of a method for controllably introducing a chemical species to the various crystals and synchronizing the timing of fluid handling steps on the microfluidic chip with X-ray data collection. Several efforts in this area are ongoing in collaboration with the BioCARS team at the Advanced Photon Source at Argonne National Laboratory and scientists from the University of Chicago.

8.4 Microfluidic Platforms for the Preparation and *In Situ* Analysis of Aqueous/Lipid Phase Behavior

As in crystallization screening experiments where microfluidics provides the benefit of a large number of parallel trials while using a small volume of material and efficient preparative methods, the examination of the phase behavior of aqueous/lipid mesophases is very sample intensive. Scaled-out microfluidic chips coupled with *in situ* small angle X-ray analysis capabilities have tremendous potential to broaden the range of conditions which can be screened and the rate at which data can be collected. However, further validation of these platforms is still needed.

A logical first test of an array chip to study the phase behavior of mesophase systems would be the reproduction of an existing dataset. In order to accomplish this goal, a variety of challenges need to be overcome, including optimization of device design and operation, and further characterization of the effects of radiation damage and heating due to exposure the X-ray beam. Having achieved this milestone, subsequent experiments can be designed to either characterize new lipidic systems, or to try and understand the effect of additives and/or other contaminants on the phase behavior of an existing system. On the one hand, study of a novel lipid could enable its use in future *in meso* crystallization trials. On the other, an improved understanding of the effects of various contaminants could bring a very powerful understanding as to the mechanism behind *in meso* crystallization, and could be used to rationally design future crystallization trials.

8.5 Conclusions

In summary, the work presented here is a significant first step in a project which has tremendous potential for impacting the field of protein crystallography. The development of microfluidic platforms for *in meso* membrane protein crystallization that allow for subsequent *in situ* analysis has overcome several bottlenecks for the study of these systems in microfluidic systems. This project can continue to grow in many directions, taking advantage of not only the capabilities of preparing highly viscous mesophase samples on chip, but also a variety of strategies for on-chip crystallization and *in situ* analysis. Hopefully

the use of these platforms in the structure determination of a novel protein target will occur in the near future, and their use will rapidly improve the success rates of structural biology efforts everywhere.

8.6 References

(1) Dertinger, S. K. W.; Jiang, X. Y.; Li, Z. Y.; Murthy, V. N.; Whitesides, G. M. P Natl Acad Sci USA 2002, 99, 12542.

(2) Dertinger, S. K. W.; Chiu, D. T.; Jeon, N. L.; Whitesides, G. M. Anal Chem 2001, 73, 1240.

(3) Caffrey, M. Cryst Growth Des 2008, 8, 4244.

(4) Cherezov, V.; Clogston, J.; Misquitta, Y.; Abdel-Gawad, W.; Caffrey, M. Biophys J 2002, 83, 3393.

(5) Misquitta, L. V.; Misquitta, Y.; Cherezov, V.; Slattery, O.; Mohan, J. M.; Hart, D.; Zhalnina, M.; Cramer, W. A.; Caffrey, M. Structure 2004, 12, 2113.

(6) Misquitta, Y.; Caffrey, M. Biophys J 2001, 81, 1047.

(7) Misquitta, Y.; Cherezov, V.; Havas, F.; Patterson, S.; Mohan, J. M.; Wells, A. J.; Hart, D. J.; Caffrey, M. Journal of Structural Biology 2004, 148, 169.

(8) Cherezov, V.; Yamashita, E.; Liu, W.; Zhalnina, M.; Cramer, W. A.; Caffrey, M. J Mol Biol 2006, 364, 716.

(9) Grabe, M.; Neu, J.; Oster, G.; Nollert, P. Biophys J 2003, 84, 854.

(10) Cherezov, V.; Caffrey, M. Faraday Discussions 2007, 136, 195.

(11) Nollert, P.; Qiu, H.; Caffrey, M.; Rosenbusch, J. P.; Landau, E. M. Febs Lett 2001, 504, 179.

(12) Sennoga, C.; Heron, A.; Seddon, J. M.; Templer, R. H.; Hankamer, B. Acta Crystallogr D 2003, 59, 239.

(13) Sparr, E.; Wadsten, P.; Kocherbitov, V.; Engstrom, S. Bba-Biomembranes 2004, 1665, 156.

(14) Liu, W.; Caffrey, M. Journal of Structural Biology 2005, 150, 23.

(15) Qutub, Y.; Reviakine, I.; Maxwell, C.; Navarro, J.; Landau, E. M.; Vekilov, P. G. J Mol Biol 2004, 343, 1243.

(16) Caffrey, M. Ann Rev Biophys 2009, 38, 29.

(17) Caffrey, M. Journal of Structural Biology 2003, 142, 108.

(18) Misquitta, Y.; Caffrey, M. Biophys J 2003, 85, 3084.

(19) Cherezov, V.; Clogston, J.; Papiz, M. Z.; Caffrey, M. J Mol Biol 2006, 357, 1605.

Appendix

Overcoming the Challenge of Pumping Viscous Fluids at the Microscale*

Appendix A.1 Typical Values of β for Microfluidic Channels

Table A.2 - Table A**.4** give calculated values for β for a variety of microfluidic geometries assuming a Young's modulus of E = 1000 MPa, a Poisson's ratio of σ = 0.5, and a value for the numerical constant c = 1.

Table A.2. Calculated values for β as a function of channel width and applied pressure assuming an initial channel height of h_0 = 10 µm.

h_0 (µm)	10	w (µm)				
		50	100	250	500	1000
P_{in} (kPa)	6.89	3.4E-02	6.9E-02	1.7E-01	3.4E-01	6.9E-01
	34.5	1.7E-01	3.4E-01	8.6E-01	1.7E+00	3.4E+00
	68.9	3.4E-01	6.9E-01	1.7E+00	3.4E+00	6.9E+00
	103	5.2E-01	1.0E+00	2.6E+00	5.2E+00	1.0E+01
	138	6.9E-01	1.4E+00	3.4E+00	6.9E+00	1.4E+01
	172	8.6E-01	1.7E+00	4.3E+00	8.6E+00	1.7E+01
	207	1.0E+00	2.1E+00	5.2E+00	1.0E+01	2.1E+01

Table A.3. Calculated values for β as a function of channel width and applied pressure assuming an initial channel height of h_0 = 20 µm.

h_0 (µm)	20	w (µm)				
		50	100	250	500	1000
P_{in} (kPa)	6.89	1.7E-02	3.4E-02	8.6E-02	1.7E-01	3.4E-01
	34.5	8.6E-02	1.7E-01	4.3E-01	8.6E-01	1.7E+00
	68.9	1.7E-01	3.4E-01	8.6E-01	1.7E+00	3.4E+00
	103	2.6E-01	5.2E-01	1.3E+00	2.6E+00	5.2E+00
	138	3.4E-01	6.9E-01	1.7E+00	3.4E+00	6.9E+00
	172	4.3E-01	8.6E-01	2.2E+00	4.3E+00	8.6E+00
	207	5.2E-01	1.0E+00	2.6E+00	5.2E+00	1.0E+01

Table A.4. Calculated values for β as a function of channel width and applied pressure assuming an initial channel height of h_0 = 50 µm.

* This work has been published: S.L. Perry, J.J.L. Higdon, and P.J.A. Kenis, *Design Rules for Pumping and Metering of Highly Viscous Fluids*, Lab on a Chip 2010 Vol. 10(22), 3112-3124.

h_0 (μm)	50	w (μm)				
		50	100	250	500	1000
P_{in} (kPa)	6.89	6.9E-03	1.4E-02	3.4E-02	6.9E-02	1.4E-01
	34.5	3.4E-02	6.9E-02	1.7E-01	3.4E-01	6.9E-01
	68.9	6.9E-02	1.4E-01	3.4E-01	6.9E-01	1.4E+00
	103	1.0E-01	2.1E-01	5.2E-01	1.0E+00	2.1E+00
	138	1.4E-01	2.8E-01	6.9E-01	1.4E+00	2.8E+00
	172	1.7E-01	3.4E-01	8.6E-01	1.7E+00	3.4E+00
	207	2.1E-01	4.1E-01	1.0E+00	2.1E+00	4.1E+00

Appendix A.2 Determination of Constants for 2nd Order Polynomial Fit for Time

In the development of a universal relationship in Chapter 3 to relate the steady-state lag volume as a function of β an effective time was defined based on a 2nd order polynomial scaling of the dimensionless diffusive time, as in Eq. (3-21). The fit parameters A and B were obtained by matching values of the effective time for each value of β to the case of β = 0.001 when the lag volume parameter = 0.4 and 0.9. Expressions for the fit parameters A and B can be obtained from solutions to the system of two 2nd order polynomials from Eq. (3-21) evaluated at β = 0.001 and the value of interest. τ^*_{ref} refers to the value for β = 0.001 whereas τ^* refers to the value of β of interest. The subscript (1) indicates that the time was evaluated for a lag time parameter V_{lag}/V_{lagss} = 0.4, while the subscript (2) indicates that the time was evaluated for a lag time parameter of V_{lag}/V_{lagss} = 0.9.

$$A = \frac{\tau^*_{ref\,1}}{\tau^{*2}_1} - \frac{B}{\tau^*_1} \tag{A-1}$$

$$B = \frac{\tau^*_{ref\,2} - \tau^*_{ref\,1}\left[\frac{\tau^*_2}{\tau^*_1}\right]^2}{\tau^*_2\left[1-\frac{\tau^*_2}{\tau^*_1}\right]} \tag{A-2}$$

Appendix A.3 Determination of a Graduated Mesh

A graduated mesh was used in the numerical solution for the partial differential equation in order to account for the sharp changes in the slope of the function near the outlet. To form the graduated mesh the change in the separation from point-to-point will be modified by a constant factor of λ such that Δx_n = $\lambda \Delta x_{n-1}$. Thus the value s of the N^{th} point considering an initial spacing difference of Δx_0 is:

$$s = \left(1 + \lambda + \lambda^2 + \lambda^3 + \ldots + \lambda^N\right)\Delta x_0 \tag{A-3}$$

We can also write:

$$\lambda s = \left(\lambda + \lambda^2 + \lambda^3 + \ldots + \lambda^N + \lambda^{N+1}\right)\Delta x_0 \tag{A-4}$$

Subtracting Eqs. (A-3) and (A-4) gives:

$$(1-\lambda)s = \left(1-\lambda^{N+1}\right)\Delta x_0 \tag{A-5}$$

Rearranging Eq. (A-5) thus gives an expression for the value of the N^{th} point s:

$$s = \frac{\left(1-\lambda^{N+1}\right)}{(1-\lambda)}\Delta x_0 \tag{A-6}$$

Appendix A.4 Development of a Differential Equation with an Analytical Solution for Code Debugging

In the course of testing the MATLAB code presented in Appendix 1F it is useful to be able to compare the results of the numerical solution to a partial differential equation with an exact solution. While an analytical expression can be obtained for Eq. (3-17) for the case of β = 0, it is an Eigenfunction expansion and is inconvenient for testing purposes. Instead it is simple to develop an expression which is bounded in time and which satisfies the desired boundary conditions (U = 1 at Z = 0 and U = 0 at Z = 1).

$$U_{exact} = (1-Z) + Z(Z-1)\exp\left(-\tau^*\right) \tag{A-7}$$

It is then possible to force this expression to be a solution to Eq. (3-17) with β = 0 through the addition of a source term and a modification of the initial conditions.

$$\frac{\partial U}{\partial \tau^*} = \frac{\partial^2 U}{\partial Z^2} + \left(-2+Z-Z^2\right)\exp\left(-\tau^*\right) \tag{A-8}$$

Substitution of Eq. (A-7) into Eq. (A-8) demonstrates that this expression does in fact satisfy the differential equation. Evaluation of Eq. (A-8) at τ^* = 0 shows that $U = Z^2 - 2Z + 1$ is an appropriate initial condition.

Appendix A.5 Derivation of the Displacement of an Infinite Slab from a Point Pressure Source

A detailed treatment of the theory elasticity and deformation of materials has been presented by Love.[1] In Chapter 3, Eq. (3-4) describing the deformation of a channel due to pressure effects was developed from the theory associated with the displacement of an infinite slab resulting from a point pressure source. Here the derivation of this equation is presented.

The displacement Δh of an infinite slab resulting from a point source of pressure P located at a point (x_0,y_0,0) and evaluated on the plane z and at a point located a distance r from the point of pressure application is:

$$\Delta h = \frac{P}{4\pi\mu}\frac{z^2}{r^3} + \frac{P(\lambda+2\mu)}{4\pi\mu(\lambda+\mu)}\frac{1}{r} \tag{A-9}$$

with

$$r = \sqrt{(x-x_0)^2 + (y-y_0)^2 + z^2} \tag{A-10}$$

where μ and λ are the Lamé parameters and can be related to the Young's modulus E and Poisson's ratio σ.

$$\mu = \frac{E}{2(1+\sigma)} \tag{A-11}$$

$$\lambda = \frac{E\sigma}{1-2\sigma}\left[\frac{1}{1+\sigma}\right] \tag{A-12}$$

Because the Poisson's ratio for PDMS is $\sigma = 0.5$, it can be seen that $\lambda \to \infty$. Thus Eq. (A-9) reduces to:

$$\Delta h = \frac{P}{4\pi\mu}\frac{z^2}{r^3} + \frac{P}{4\pi\mu}\frac{1}{r} \tag{A-13}$$

Evaluating Eq. (A-13) on the surface of the slab ($z = 0$) and substitution for the remaining Lamé parameter gives:

$$\Delta h = \frac{P(1+\sigma)}{2\pi E r} \tag{A-14}$$

While Eq. (A-14) describes the displacement as a result of a point pressure source, a distributed pressure source can be described as the superposition of the effects of point contributions over the area of interest. Thus for deformation over a circle of radius a, integration of Eq. (A-14) gives:

$$\Delta h = \frac{P(1+\sigma)}{2\pi E}\int_0^a\int_0^{2\pi}\left(\frac{1}{r}\right) r\,d\theta\,dr \tag{A-15}$$

$$\Delta h = \frac{Pa(1+\sigma)}{E} \tag{A-16}$$

For a rectangular area defined by $-a \le x \le a$ and $-b \le y \le b$ where $\hat{x} = x - x_0$ and $\hat{y} = y - y_0$, the expression for displacement becomes:

$$\Delta h = \frac{P(1+\sigma)}{2\pi E}\int_{-b}^{b}\int_{-a}^{a}\frac{d\hat{x}\,d\hat{y}}{\sqrt{\hat{x}^2+\hat{y}^2}} \tag{A-17}$$

$$\Delta h = \frac{P(1+\sigma)}{\pi E}\left[a\log\left(\frac{\frac{b}{a}+\sqrt{1+\left(\frac{b}{a}\right)^2}}{\frac{-b}{a}+\sqrt{1+\left(\frac{b}{a}\right)^2}} \right) + b\log\left(\frac{\frac{a}{b}+\sqrt{1+\left(\frac{a}{b}\right)^2}}{\frac{-a}{b}+\sqrt{1+\left(\frac{a}{b}\right)^2}} \right) \right] \quad \text{(A-18)}$$

Comparing the expression used in Eq. (3-4) with the results from Eqs. (A-16) and (A-18) shows that Eq. (3-4) is a general expression which can be applied to a variety of geometries. In Eq. (3-4) the displacement is defined in terms of the Poisson's ratio σ, the ratio of the applied pressure to the Young's modulus of the material P/E, a characteristic length w, and a geometric constant c. In the case of deflection over a circle the characteristic length is the radius a, and the geometric constant c = 1. For the case of a rectangular geometry it is much more difficult to identify a specific the characteristic length and the expression for the geometric constant is more complicated.

Appendix A.6 MATLAB Code

```
function ChannelSwellingPDE
clear
clear global

% This code uses the Matlab function pdepe to provide a numerical solution
% for the nonlinear "diffusion" equation that describes pressure driven
% laminar flow in an infinite slit that swells based on the applied
% pressure.

% The problem is coded in subfunctions PDEX1PDE, PDEX1IC, and PDEX1BC.
% Additional subfunctions VFlowRate and Volume are coded for data analysis.

% Physical parameters defined here
Pappl = 207; % (kPa, equivalent to 30 psi)
sigma = 0.5; % (Poisson's ratio)
w = 100; % (µm, channel width)
h0 = 10; % (µm, initial channel height)
L = 1e4; % (µm, channel length)
eta = 0.001/1000; % (kPa-s, viscosity)

Vdotrigid = h0^3*w*Pappl/(12*eta*L)*1e-6; % (nL/s Vdot in a rigid channel)
c1 = 1; % (geometric parameter, order of magnitude 1)
beta = 1;

Vdotref = L^3*Pappl/eta*1e-6; % (nL/s core variable non-dimensionalization for Vdot)
Vref = L^3*1e-6; % (nL) core variable non-dimensionalization for volume

% Define the timepoints for evaluation of the function
tfinalND = 1; % includes a factor of gamma to make things happen at 1
Nt = 201; % (number of time steps save for plotting)
Ntdisplay = (Nt-1)/10; % (time interval to take for plot displays)
```

```
dt = tfinalND/(Nt-1);
t = (0:dt:tfinalND);

% Define the number of spatial discretizations
N = 201;

% Establish x using a variable mesh
lambda = 0.95;
x(1)=0;
x(2)=0.05;
for i=3:N
    delta_x = x(i-1) - x(i-2);
    x(i)=x(i-1)+lambda*delta_x;
end
x(N)=1;

m = 0; % Sets the geometry as a slab
sol = pdepe(m,@pdex1pde,@pdex1ic,@pdex1bc,x,t);
% Extract the first solution component as u.  This is not necessary
u = sol(:,:,1);
u_ss = 1/beta*((x*(1-(1+beta)^4)+(1+beta)^4).^(1/4)-1);
% u_exact = (1-x)+x.*(x-1)*exp(-tfinalND); % exact solution for debugging with beta =
0

% Evaluation of dudx
dudx = Derivative(u,Nt,N,x);
dudx_ss = 1/(4*beta)*(x*(1-(1+beta)^4)+(1+beta)^4).^(-3/4)*(1-(1+beta)^4);
Error = dudx(Nt,:) - dudx_ss;
% dudx_exact = -1 + (2*x-1)*exp(-tfinalND); % exact solution for debugging with beta =
0

% Evaluation of Vdot from dudx
Vdot = VFlowRate(u,dudx,Nt,N,beta,Vdotrigid,Vdotref);
% Vdot_exact = -dudx_exact; % exact solution for debugging with beta = 0 at tfinal
% Vdot_exact_t = -(-1 + (2*x(N)-1)*exp(-t)); % exact solution for debugging with beta
= 0 at
       outlet

% Evaluation of Total Volume Flowed
a=1;
Vin = Volume(Vdot,a,t);
Vout = Volume(Vdot,N,t);
% V_exact = -tfinalND-(2*x-1)*exp(-tfinalND)+2*x-1;% exact solution for debugging with
beta = 0 at tfinal
% V_exact_t = t+(2*x(N)-1)*exp(-t)-2*x(N)+1; % exact solution for debugging with beta
= 0 at
       outlet

% Evaluation of h(z)
h = Height(u,Nt,N,beta,h0);
```

```
% h_exact = h0; % exact solution for debugging with beta = 0

% Evaluation of the final channel volume (nL)
Vchannel = ChannelVolume(h,x,Nt,N,w,L);
% Vchannel_exact = h0*w*L; % exact solution for debugging with beta = 0

%-------------------------------------------------------------------------
% Plots

% set the default line color order to follow a rainbow pattern starting
% with red and ending with black
set(0,'DefaultAxesColorOrder',[1 0 0 ; 1 0.69 0.39 ; 1 1 0 ;...
    0 1 0 ; 0.17 0.51 0.34 ; 0.39 0.47 0.64 ; 0.08 0.17 0.55 ;...
    0.48 0.06 0.89 ; 1 0 1 ; 0.5 0.5 0.5 ; 0 0 0]);

% Plots for Debugging

% figure(1)
% subplot(3,2,1);
% plot(x,u(1,:),'LineWidth',2);
% title('Non-dimensionalized Pressure vs. Distance over Time')
% xlabel('Distance'), ylabel('Pressure')
% hold all
% for ii=2:Ntdisplay:Nt
%     subplot(3,2,1);
%     plot(x,u(ii,:),'LineWidth',2);
% end
% subplot(3,2,1);
% plot(x,u_exact(:),'kd');
% xlim([0 1])
% ylim([0 1])
% hold off
%
% figure(2)
% subplot(3,2,2);
% plot(x,dudx(1,:),'LineWidth',2);
% title('Non-dimensionalized dP/dx vs. Distance over Time')
% xlabel('Distance'), ylabel('dP/dx')
% hold all
% for ii=2:Ntdisplay:Nt
%     subplot(3,2,2);
%     plot(x,dudx(ii,:),'LineWidth',2);
% end
% subplot(3,2,2);
% plot(x,dudx_exact(:),'kd');
% xlim([0 1])
% hold off
%
% figure(3)
```

```
% subplot(3,2,3);
% plot(x,Vdot(1,:),'LineWidth',2);
% title('Non-dimensionalized Volumetric Flowrate vs. Distance over Time')
% xlabel('Distance'), ylabel('Volumetric Flowrate')
% hold all
% for ii=2:Ntdisplay:Nt
%     subplot(3,2,3);
%     plot(x,Vdot(ii,:),'LineWidth',2);
% end
% subplot(3,2,3);
% plot(x,Vdot_exact(:),'kd');
% xlim([0 1])
% ylim([0 Vdot(2,1)*1.5])
% hold off
%
% figure(4)
% subplot(3,2,4);
% plot(t,Vdot(:,N),'LineWidth',2);
% hold all
% subplot(3,2,4);
% plot(x,Vdot_exact_t(:),'kd');
% hold off
% title('Non-dimensionalized Volumetric Flowrate at the Outlet vs. Time')
% xlabel('Time'), ylabel('Volumetric Flowrate')
% xlim([0 tfinalND])
%
% figure(5)
% subplot(3,2,5);
% plot(t,V,'LineWidth',2);
% hold all
% subplot(3,2,5);
% plot(x,V_exact_t(:),'kd');
% title('Non-dimensionalized Total Volume at the Outlet vs. Time')
% xlabel('Time'), ylabel('Volume')
% xlim([0 tfinalND])
% hold off
%
% figure(6)
% subplot(3,2,6);
% plot(x,h(1,:),'LineWidth',2);
% title('Channel Height vs. Distance over Time')
% xlabel('Distance'), ylabel('Channel Height (μm)')
% hold all
% for ii=2:Ntdisplay:Nt
%     subplot(3,2,6);
%     plot(x,h(ii,:),'LineWidth',2);
% end
% subplot(3,2,6);
% plot(x,h_exact,'kd');
```

```
% xlim([0 1])
% hold off

% Plots for Real Data

figure(1)
subplot(3,2,1);
plot(x,u(1,:),'LineWidth',2);
title('Non-dimensionalized Pressure vs. Distance over Time')
xlabel('Distance'), ylabel('Pressure')
hold all
for ii=2:Ntdisplay:Nt
    subplot(3,2,1);
    plot(x,u(ii,:),'LineWidth',2);
end
plot(x,u_ss,'kd');
xlim([0 1])
ylim([0 1])
hold off

% figure(2)
subplot(3,2,2);
plot(t,dudx(:,N),'LineWidth',2);
title('Non-dimensionalized dP/dx at the Outlet vs. Time')
xlabel('Time'), ylabel('dPdx')
xlim([0 tfinalND])
% ylim([-1 0.1])

% figure(3)
subplot(3,2,3);
plot(x,Vdot(1,:),'LineWidth',2);
title('Non-Dimensionalized Volumetric Flowrate vs. Distance over Time')
xlabel('Distance'), ylabel('Volumetric Flowrate')
hold all
for ii=2:Ntdisplay:Nt
    subplot(3,2,3);
    plot(x,Vdot(ii,:),'LineWidth',2);
end
xlim([0 1])
% ylim([0 Vdot(2,1)*1.5])
hold off

% figure(4)
subplot(3,2,4);
plot(t,Vdot(:,N),'LineWidth',2);
title('Non-dimensionalized Volumetric Flowrate at the Outlet vs. Time')
xlabel('Time'), ylabel('Volumetric Flowrate')
xlim([0 tfinalND])
% ylim([-0.1 1])
```

```
% figure(5)
subplot(3,2,5);
plot(t,Vout,'LineWidth',2);
title('Non-dimensionalized Total Volume at the Outlet vs. Time')
xlabel('Time'), ylabel('Volume')
xlim([0 tfinalND])

% figure(6)
subplot(3,2,6);
plot(x,h(1,:),'LineWidth',2);
title('Channel Height vs. Distance over Time')
xlabel('Distance'), ylabel('Channel Height (μm)')
hold all
for ii=2:Ntdisplay:Nt
    subplot(3,2,6);
    plot(x,h(ii,:),'LineWidth',2);
end
xlim([0 1])
hold off

%--------------------------------------------------------------------------
% Exporting data to Excel
u_out = [x' u'];
dudx_out = [x' dudx'];
Vdot_out = [x' Vdot'];
Vdot_end_out = [t' Vdot(:,1) Vdot(:,N)];
V_end_out = [t' Vin Vout];
h_out = [x' h'];
Vchannel_out = [t' Vchannel'];
Error_out = [x' Error'];

filename=['Beta-' num2str(beta) '.xls'];
filename=['Output.xls'];

warning off MATLAB:xlswrite:AddSheet
xlswrite(filename, beta, 'Beta', 'B1');

warning off MATLAB:xlswrite:AddSheet
xlswrite(filename, 't', 'ND Pressure', 'B1');
xlswrite(filename, 'd', 'ND Pressure', 'A2');
xlswrite(filename, t, 'ND Pressure', 'B2');
xlswrite(filename, u_out, 'ND Pressure', 'A3');

xlswrite(filename, 't', 'ND dPdx', 'B1');
xlswrite(filename, 'd', 'ND dPdx', 'A2');
xlswrite(filename, t, 'ND dPdx', 'B2');
xlswrite(filename, dudx_out, 'ND dPdx', 'A3');
```

```
xlswrite(filename, 't', 'ND Vdot', 'B1');
xlswrite(filename, 'd', 'ND Vdot', 'A2');
xlswrite(filename, t, 'ND Vdot', 'B2');
xlswrite(filename, Vdot_out, 'ND Vdot', 'A3');

xlswrite(filename, 't', 'ND Vdot ends', 'A1');
xlswrite(filename, '1', 'ND Vdot ends', 'B1');
xlswrite(filename, 'N', 'ND Vdot ends', 'C1');
xlswrite(filename, Vdot_end_out, 'ND Vdot ends', 'A2');

xlswrite(filename, 't', 'ND V ends', 'A1');
xlswrite(filename, '1', 'ND V ends', 'B1');
xlswrite(filename, 'N', 'ND V ends', 'C1');
xlswrite(filename, V_end_out, 'ND V ends', 'A2');

xlswrite(filename, 't', 'Channel Height', 'B1');
xlswrite(filename, 'd', 'Channel Height', 'A2');
xlswrite(filename, t, 'Channel Height', 'B2');
xlswrite(filename, h_out, 'Channel Height', 'A3');

xlswrite(filename, 't', 'Channel Volume', 'A1');
xlswrite(filename, 'V', 'Channel Volume', 'B1');
xlswrite(filename, Vchannel_out, 'Channel Volume', 'A2');

xlswrite(filename, 'x', 'dudx Error', 'A1');
xlswrite(filename, Error_out, 'dudx Error', 'A2');

%--------------------------------------------------------------------------

function [c,f,s] = pdex1pde(x,t,u,DuDx)

% Physical parameters defined here
beta = 1;

c = 1;
f = (1+beta*u)^3*DuDx;
% s = (-2+x-x^2)*exp(-t); % source term for debugging with beta = 0
s = 0;

% --------------------------------------------------------------------------

function u0 = pdex1ic(x)

% Physical parameters defined here
beta = 1;

u0 = 0; % initial condition of P = 0
% u0 = x^2 - 2*x + 1; % initial condition for debugging with beta = 0
% u0 = 1/beta*((x*(1-(1+beta)^4)+(1+beta)^4).^(1/4)-1); % initial condition of P = Pss
```

```
% --------------------------------------------------------------------------

function [pl,ql,pr,qr] = pdex1bc(xl,ul,xr,ur,t)

pl = ul-1; % u = 1 at x = 0
ql = 0;
% pl = 0; % u = 0 at x = 0
% ql = 1; % dudx = 0 at x = 0
pr = ur; % u = 0 at x = 1
qr = 0;

% --------------------------------------------------------------------------

function dudx = Derivative(u,Nt,N,x)

for tt = 1:Nt

    % Differentiation done with parabolic fit for derivative such that
    % u = ax^2+bx+c and dudx = 2ax+b because of unequal mesh spacings.
    % A first point fit is used for the inlet, a center point fit is used
    % for the interior points, and a 3rd point fit is used for the outlet.

    % For the interior points
    for ii = 2:N-1
        x1 = x(ii-1);
        x2 = x(ii);
        x3 = x(ii+1);
        b1 = ((u(tt,ii)-u(tt,ii+1))*(x1^2-x2^2)-(u(tt,ii-1)-u(tt,ii))*...
             (x2^2-x3^2))/((x2-x1)*(x2^2-x3^2)+(x2-x3)*(x1^2-x2^2));
        a1 = (u(tt,ii-1)-u(tt,ii)+b1*(x2-x1))/(x1^2-x2^2);
        dudx(tt,ii) = 2*a1*x2+b1;
    end

    % For the inlet condition
    x1 = x(1);
    x2 = x(2);
    x3 = x(3);
    b1 = ((u(tt,2)-u(tt,3))*(x1^2-x2^2)-(u(tt,1)-u(tt,2))*(x2^2-x3^2))/...
         ((x2-x1)*(x2^2-x3^2)+(x2-x3)*(x1^2-x2^2));
    a1 = (u(tt,1)-u(tt,2)+b1*(x2-x1))/(x1^2-x2^2);
    dudx(tt,1) = 2*a1*x1+b1;

    % For the outlet condition
    x3 = x(N);
    x2 = x(N-1);
    x1 = x(N-2);
    bN = ((u(tt,N-1)-u(tt,N))*(x1^2-x2^2)-(u(tt,N-2)-u(tt,N-1))*(x2^2-x3^2))/...
         ((x2-x1)*(x2^2-x3^2)+(x2-x3)*(x1^2-x2^2));
```

```
    aN = (u(tt,N-2)-u(tt,N-1)+bN*(x2-x1))/(x1^2-x2^2);
    dudx(tt,N) = 2*aN*x3+bN;

end

% ------------------------------------------------------------------------

function Vdot = VFlowRate(u,dudx,Nt,N,beta,Vdotrigid,Vdotref)

for tt = 1:Nt

    for xx = 1:N
        Vdot(tt,xx) = -Vdotrigid/Vdotref*(1+beta*u(tt,xx))^3*dudx(tt,xx);
    end
end

% ------------------------------------------------------------------------

function V = Volume(Vdot,N,t)

% Integration done using the trapezoid rule
% Result is gamma*V-ND
    V = cumtrapz(t,Vdot(:,N));

% ------------------------------------------------------------------------

function h = Height(u,Nt,N,beta,h0)
h(Nt,N) = zeros;

for tt = 1:Nt

    for xx = 1:N
        h(tt,xx) = h0*(1+beta*u(tt,xx));
    end
end

% ------------------------------------------------------------------------
function Vchannel = ChannelVolume(h,x,Nt,N,w,L)
h_integ(N)=zeros;
z=x*L;
%Integration done using the trapezoid rule
for tt = 1:Nt

    for xx = 1:N
        h_integ(xx) = h(tt,xx);
        Vchannel(tt) = w*trapz(z,h_integ)*1e-6;
    end
end
```

References

(1) Love, A. E. H. *A Treatise on the Mathematical Theory of Elasticity*; 4th ed.; Cambridge University Press: Cambridge, 1934.